Statistical Coherence of Large-Scale Circulation in Turbulent Rayleigh-Bénard Convection

A thesis submitted
in partial fulfilment of the requirements
for the degree of

Doctor of Philosophy

in

Mechanical Engineering

by

Vishnu Venugopal T.

Department of Mechanical Engineering,
Indian Institute of Technology Guwahati,
Guwahati - 781039,
Assam, India.
January 2021

Dedicated to my Ammamma.

Certificate

This is to certify that the work presented in this thesis entitled "**Statistical Coherence of Large-Scale Circulation in Turbulent Rayleigh-Bénard Convection**" is carried out by **Vishnu Venugopal T.** for the award of Doctor of Philosophy in the Department of Mechanical Engineering from Indian Institute of Technology Guwahati. The thesis embodies the result of original work and studies carried out by the student himself under my supervision and has not been submitted elsewhere for a degree.

29/1/2021

Dr. Arnab Kumar De,
Associate Professor,
Department of Mechanical Engineering,
Indian Institute of Technology Guwahati,
Guwahati, Assam, Pin - 781039, India.

Date: 29/01/2021
Place: Guwahati

Acknowledgements

First and foremost, I express my deep sense of gratitude to my thesis supervisor, Dr. Arnab Kumar De, for his extraordinary support and guidance. I have been lucky to learn a lot from him. I am also thankful for his inspiration and the trust he showed in me, which gave me a lot of confidence and helped me to establish an overall direction of research. I am deeply grateful for his valuable comments and suggestions.

I acknowledge my fruitful collaboration with Dr. Pankaj Kumar Mishra. I thank him for sharing his rich experience in different fields and enlightening me on the physical aspects of turbulent flows. I am immensely thankful to him for giving me an opportunity to work as a JRF under him. I express my sincere gratitude to my Doctoral Committee members, Prof. Anoop K. Dass, Dr. Ganesh Natarajan, Prof. Dipankar Bandyopadhyay, and Prof. Vinayak Kulkarni, for their valuable insights during research. I am also grateful to Indian Institute of Technology Guwahati for providing the ideal infrastructure, especially the 'Param-Ishan' supercomputing facility, to accomplish my research successfully.

During my stay in IIT Guwahati, I came across several friends who made the journey very pleasant and colourful. I acknowledge all the love and cooperation that I have received from them at different stages of my PhD. I thank Sajith, Anoop, Jiss, Vivek, Vijith, Sooraj, Arun, Vasu, Pankaj, Sailen and many other friends whose company I really cherished during my PhD and whose memories will always be an integral part of my life. My special thanks to Arjun for always showing his great interests to discuss several aspects of CFD and heat transfer. I am thankful to my lab mates in PGC and CFD lab for their continuous support and encouragement. Special thanks to Mukesh, who was my go-to person during all the hurdles related to Linux

and latex. Also Peter, Krishan and Mukesh for the fruitful discussions and funny talks. I thank Suvin and Amrutha for all the help in statistics, MATLAB, and those delicious meals. Thanks to Dileepettan for all the discussions on everything under the sun.

Above everything, this PhD would not have been possible without the constant support, encouragement, blessings and good wishes of my family members. I am grateful to my parents for their continuous support and affection through this journey and beyond. I would always be thankful for their enormous sacrifices made for me to make my dream into reality. Special thanks to Vinu, Reshma and Ayan for keeping me motivated during my bad days.

Vishnu Venugopal T.

Abstract

Rayleigh-Bénard convection (RBC) is one of the classical problems in fluid dynamics, in which a fluid layer is heated from below and cooled from the top. In this thesis, various aspects of turbulent RBC inside a Cartesian box and cylindrical cell are studied, using direct numerical simulations (DNS). Our prime focus is to identify and characterize large-scale circulation (LSC), which is an organization of thermal plumes to form a large-scale coherent structure. For rotating RBC inside a cylindrical container, we identify different flow regimes based on the Fourier modes and flow structures. At low rotation rates, LSC is observed, while at higher rotation rates, wall-bounded flow structures, namely quadrupolar and sextupolar are obtained. The reorientations of LSC are identified as rotation-led and cessation-led based on their nature of occurrence, and as partial and complete reversal depending on the azimuthal drift. In addition to the previously reported rare events like cessations and double-cessations, an interesting event of multiple-cessation is observed in the present study. We observe that similar to non-rotating RBC, the probability distribution of the reorientations exhibits a power-law behaviour. Further, the significance of Prandtl number (Pr) on the flow structure and heat transport in rotating convection is investigated. We report an intermediate Pr regime where the increase in heat transfer occurs at low rotation rates. Moreover, the enhancement in heat transfer rate is observed in the region where the flow structure changes from quadrupolar to dipolar state.

For turbulent RBC inside a cubic cell, we have been able to attain a high Rayleigh number (Ra) range, up to $Ra = 10^9$, and study various characteristics of the flow, especially thermal plumes and LSC. We observe that the volume fraction of the plume decreases, while that of the turbulent background increases with Ra. Comparisons with the theoretical predictions show

that the dissipation from the plume region follows the Grossmann-Lohse scaling, while considerable deviations are observed in the background contribution. By comprehensive analysis of the flow behaviour in different planes, a mechanism of flow reversals is proposed. Our analyses show that the corner-rolls present in the plane containing LSC play a key role in destabilizing the LSC, and thus, resulting in reversals. We notice that partial reversals are a common occurrence across all Ra, while complete reversals are rare occurrences and restricted to low Ra. The evaluation of turbulent kinetic energy (TKE) budget across the LSC and non-LSC planes indicate that the production of TKE occurs at localized pockets in both the planes, while dissipation of TKE largely happens near the plane containing LSC.

Abbreviations and symbols

Abbreviations

BiCGSTAB	Bi-Conjugate Gradient Stabilized
BL	Boundary layer
CV	Control volume
CW	Clock-wise
CCW	Counter clock-wise
DNS	Direct numerical simulation
FVM	Finite volume method
ILU	Incomplete LU factorization
LES	Large-eddy simulation
LSC	Large-scale circulation
MLE	Maximum likelihood estimation
MPI	Message passing interface
PDF	Probability distribution function
PSD	Power spectral density
rms	Root mean square
RBC	Rayleigh-Bénard convection
RRBC	Rotating Rayleigh-Bénard convection
SIP	Strongly implicit procedure
TKE	Turbulent kinetic energy

Symbols

α	Thermal diffusivity
β	Thermal expansion coefficient
Γ	Aspect ratio of cylinder
θ	Non-dimensional temperature
δ_θ	Thermal boundary layer thickness
δ_u	Viscous boundary layer thickness
η_k	Kolmogorov length scale
η_t	Kolmogorov time scale
ϵ_θ	Thermal dissipation rate
ϵ_u	Viscous dissipation rate
$\mathbf{\Omega}$	Angular velocity
ϕ	Azimuthal angle
Φ_k	Phase of Fourier mode
ρ	Density of fluid
σ	Standard deviation
τ	Time interval between reorientations
ν	Kinematic viscosity of fluid
μ	Dynamic viscosity of fluid
μ_τ	Mean time interval between reorientations
A_k	Amplitude of Fourier mode
C_t	Cutoff value for plume and background decomposition
D	Diameter of cylinder
$\hat{\boldsymbol{e}}$	Unit vector in vertical direction
E_k	Energy of Fourier mode
Ek	Ekman number
g	Acceleration due to gravity
H	Height of container
K	Thermal conductivity
Nu	Nusselt number
P	Dimensional pressure

p	Non-dimensional pressure
Pr	Prandtl number
q	Heat flux
R	Radius of cylinder
Re	Reynolds number
Ra	Rayleigh number
Ro	Rossby number
$\boldsymbol{r}$	Position vector
S_{LSC}	Strength of LSC
T	Dimensional temperature
T_{eddy}	Eddy turn over time
t	Time
Δt	Time increment
ΔT	Temperature difference between hot and cold surfaces
T_c	Temperature of cold surface
T_h	Temperature of hot surface
Ta	Taylor number
$\boldsymbol{u}$	Velocity vector
$\boldsymbol{u_R}$	Velocity vector in rotating frame
$\boldsymbol{u_I}$	Velocity vector in inertial frame
V^f	Free-fall velocity
V^{ref}	Reference velocity
V	Volume

Contents

List of figures

List of tables

1 Introduction

1.1 Significance of Rayleigh-Bénard convection

Rayleigh-Bénard convection (RBC) is a bottom-heated and top-cooled configuration of a fluid layer confined between two horizontal surfaces. RBC has been of keen interest to the scientific community due to its pivotal role in many natural phenomena and technological applications. For example, solar and stellar systems depend principally on the convective heat transport from their outer core to the surface [1, 2]. Convective motions inside Earth's mantle result in tectonic drift and volcanic activities [3–8]. Further, oceanic convection, coupled with the atmospheric convection [9], assists in the transport of heat and moisture around the planet, which are cardinal in determining the climate. Figure 1.1 shows a schematic representation of some of these natural phenomena where RBC plays a crucial role. Apart from these, RBC finds applications in various engineering fields such as cooling of electronic equipment [10], metal solidification processes, fluid storage applications, heat exchangers, nuclear reactors, and solar heating devices. Even heating a pan of water is also a classic example of Rayleigh-Bénard convection.

The addition of rotation to the Rayleigh-Bénard system makes it more complex, but relevance to the physical world is unparalleled, as rotation is an important ingredient in all the aforementioned situations. When a fluid layer is rotated, it introduces two extra forces into the system, namely the Coriolis force and the centrifugal force. Further, if the rotation is time-dependent, the Euler force is also introduced. Rotating convection is a common phenomenon in many natural flows and various engineering applications. For planetary and stellar objects,

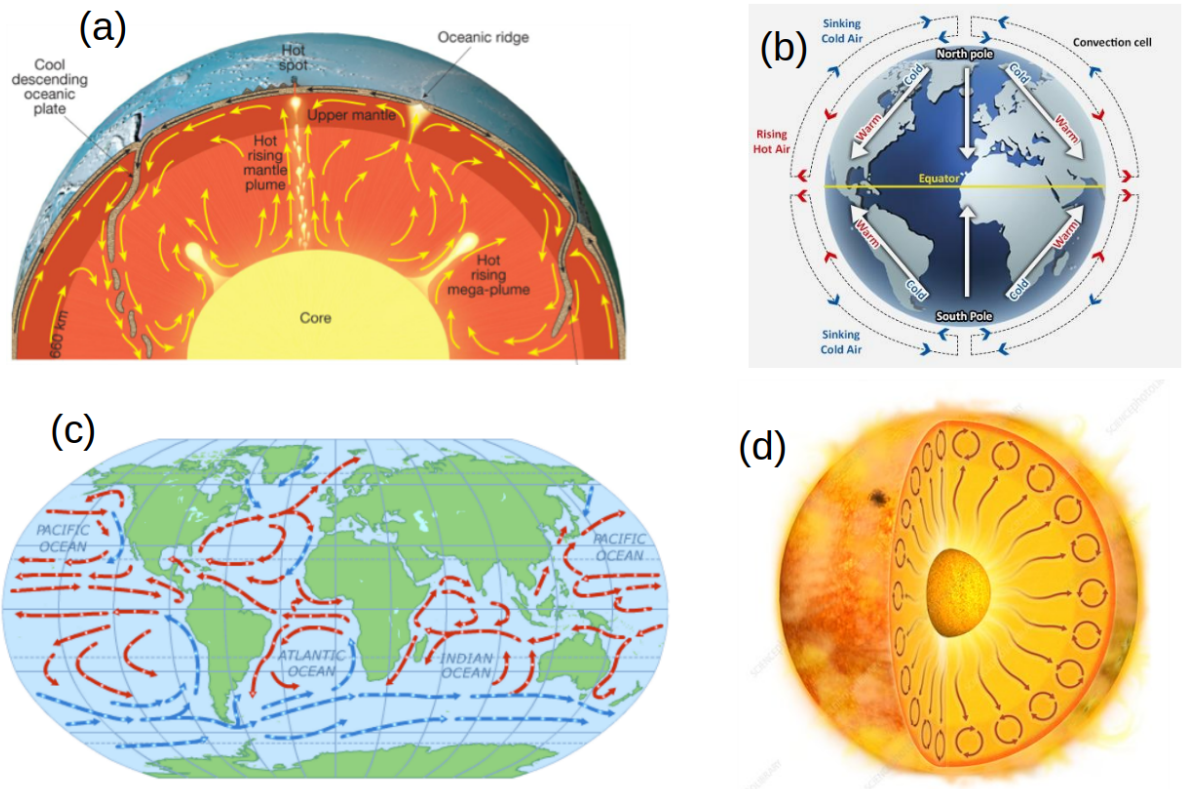

Figure 1.1: Schematic representation of (a) convection dynamics inside the Earth [11], (b) atmospheric convection [12], (c) oceanic convection [13], and (d) stellar convection [14].

many large-scale fluid motions are driven by thermal convection, and the length scales of these phenomena are large enough to be influenced by their respective rotation [15, 16]. The magnetic fields, atmospheric jets, and emitted heat flux patterns of planets are controlled by the turbulent rotating convective movements of molten metals within the planets [17, 18]. The rotating convection of molten metals inside the Earth's core plays a crucial role in the generation of geomagnetic field and its reversals, which resultantly shields the Earth from solar winds [19]. Further, the atmospheric [9], oceanic [20], and the global thermohaline convections [21] are largely affected by Earth's rotation, which in turn influence the climate. The interplay between the rotation and convective motions is the root cause of trade-winds [22], which are extremely important in weather predictions. Rotating thermal convection is also a key concept in various industrial applications like convective cooling in turbomachinery [23], centrifugal phase separation in gas exploration [24], crystallization processes, and many material processing fields. Thus, modelling of these flows is essential from the astronomical, geological, climatological, industrial, and technological point of views. In the next section, some general aspects of RBC and an overview of the existing state of literature on it is provided. After this general introduc-

tion, a detailed introduction specific to each chapter of the thesis is also presented.

1.2 Rayleigh-Bénard instability and flow transitions

Rayleigh-Bénard instability occurs when a fluid layer is subjected to an adverse vertical temperature gradient (bottom-heated and top-cooled). Due to thermal expansion, the fluid at the bottom (hot side) becomes lighter than the fluid at the top (cooler side). This top-heavy and bottom-light configuration is potentially unsteady, and the fluid has a natural tendency to redistribute itself to counter this destabilizing effect. But the viscosity of the fluid acts as a stabilizing force against this redistribution. Initially, there exists a balance between these forces, and the fluid remains in a stratified and motionless stage, which is the static conduction state. Once the temperature gradient exceeds the critical one, the destabilizing force overshadows the stabilizing force and instabilities set in [25]. The strength of the thermal driving in RBC is quantified by the Rayleigh number, Ra, which indicates the dimensionless temperature difference across the system. It is the ratio of the destabilizing buoyancy force to the stabilizing viscous force. Another non-dimensional quantity that comes in to picture is the Prandtl number, Pr, which is the ratio of momentum diffusivity (kinematic viscosity) to thermal diffusivity. Prandtl number is a property of the fluid and varies from 10^{-8} for the Sun's convective zone to 10^{23} for the Earth's mantle. In addition to these two control parameters, the aspect ratio of the container, Γ, which is the ratio of the horizontal to the vertical extent of the flow domain, also determines the dynamics of RBC.

The first quantitative experiment on convective motion of a fluid layer was performed by Bénard [26], more than a century ago. He studied the dynamics of a thin fluid layer heated from below and open to ambient air on a levelled metallic plate. Initially, the fluid layer remained static with the mode of heat transfer as conduction only. As time progressed, rolls of fluid started to appear, as convection begins. Bénard observed hexagonal patterns with a slight depression at the center on the upper free surface of the fluid layer, called Bénard cells. He studied the structure and periodicity of these cells. Bénard's work laid the foundation for Rayleigh-Bénard convection, the buoyancy-driven flow of a fluid layer between two surfaces of which the bottom one is heated, and the top is cooled; and Bénard-Marangoni convection,

surface tension driven flow of a fluid layer heated from below and open to free surface at the top. Rayleigh [27] in 1916 theoretically investigated the Bénard experiment. He used Boussinesq approximation and assumed the top and bottom walls with no temperature disturbance (infinite conductivity). Rayleigh quantified the appearance of rolls of fluid using the Rayleigh number. The minimum value of Ra for which the first convective rolls appear is called the critical Rayleigh number (Ra_c) [28–30]. Jeffreys [31, 32] and Low [33] carried out further on Rayleigh's observations. Jeffreys extended it to other boundary combinations and generalized the occurrence of instabilities using revised theoretical results. For $Ra > Ra_c$, the flow patterns are highly non-linear and depend strongly on both the fluid properties and aspect ratio of the container [34–38]. As the Rayleigh number is increased beyond the critical value, flow transition occurs from static periodic state to chaotic leading to the turbulent state [39].

The transitions between the convective states with the increase in Rayleigh number for different fluids were studied by Krishnamurthi and Howard [40]. For all Pr, the transition from conduction to convection states occurs at $Ra_c \approx 1707$. For moderate Prandtl number ($Pr \approx 1$) and high Prandtl number ($Pr > 1$) fluids, steady two-dimensional rolls are observed at low Rayleigh numbers (up to $Ra \approx 2 \times 10^4$). Beyond this, three-dimensional steady roll patterns are observed [41]. The structure of these three-dimensional rolls strongly depends on the shape (geometry) and size (aspect ratio) of the container. Generally, symmetric or asymmetric square patterns are observed in Cartesian box configurations, while in cylindrical domains, spiral or hexagonal patterns are noticed. As the Rayleigh number is increased, the flow transits to periodic/quasi-periodic state as a result of various time-dependent instabilities in the system [41, 42]. This is followed by a transition to a chaotic state, where the temporal coherence of the flow is lost. With further increase in the Rayleigh number, the flow loses its spatial coherence also and thus exhibits spatio-temporal chaos, i.e., turbulent state. Here the flow shows random characteristics in both space and time. However, under certain parameter range, the statistical coherence of the flow is restored. Here, on an average, the thermal plumes organize to form a large-scale convection roll with hot and cold fluid rising and dipping, respectively, along opposite sides of the container [40]. Such an organization of the flow is termed as 'large-scale circulation' (LSC) or the 'mean-wind' [43–47]. The length scale of LSC is comparable to the size of the container, and the time-scale is of the order of the eddy turn-over time of the flow.

1.3 Large-scale circulation and its dynamics

LSC is a coherent structure of the flow wherein hot and cold fluid, by their impending motion, create an organized state amidst background or neighbouring chaos. Generally, two types of domains are used to study LSC and its dynamics in the RBC system, such as (a) rectangular box and (b) cylindrical container. An important aspect to investigate is how does the shape of the container affect the convection dynamics? A prominent work in this direction was carried out by Daya and Ecke [48], where they showed a direct comparison between the convective flow inside cylindrical and cubic convection cells of equal volume and height. They observed that both the magnitudes and scalings of fluctuations as a function of Ra depend strongly on the geometry of the container. Further, they noted that the features of the boundary layers and LSC are different for both the geometries. Similar observations were made in the DNS study by Wagner *et al.* [49]. The simulations were carried out in a cube and a cylinder with equal diameter and height, to investigate the main responses of the system. They observed significant differences in the heat flux and the kinetic energy between both the geometries. An apparent difference between cylindrical and cubic containers is that the former provides an azimuthal symmetry, while the latter does not. Figure 1.2 shows the schematic representation of LSC inside a Cartesian box and cylindrical cell, where the dashed line indicates the direction of circulation. Note that in both the configurations, the bottom plate is heated while the top one is cooled, and the lateral walls are adiabatic. The hot plumes erupt from the boundary layer at the bottom and rise along the lateral wall, while the cold plumes sink along the opposite side.

Generally, the dynamics of the mean wind is investigated in cylindrical geometries. For cylindrical containers with unit aspect ratio ($\Gamma \approx 1$), mostly a single-roll structure (LSC) is noticed [50, 51]. However, for larger or smaller aspect ratio containers, two or more circulation rolls can be present, which are aligned either next to each other or one roll stacked on top of the other [52]. It has been observed in laboratory experiments that the vertical plane containing LSC undergoes diffusive motion in the azimuthal direction of the cylindrical container [53]. Sometimes, in the course of its motion, the plane of LSC changes swiftly by a significant angle. This phenomenon is called the "reorientation of LSC" [43, 54]. Previous studies have shown that reorientations occur in two ways: (i) rotation-led, in which reorientation takes place without changing the amplitude of the LSC, and (ii) cessation-led, where the amplitude of LSC vanishes

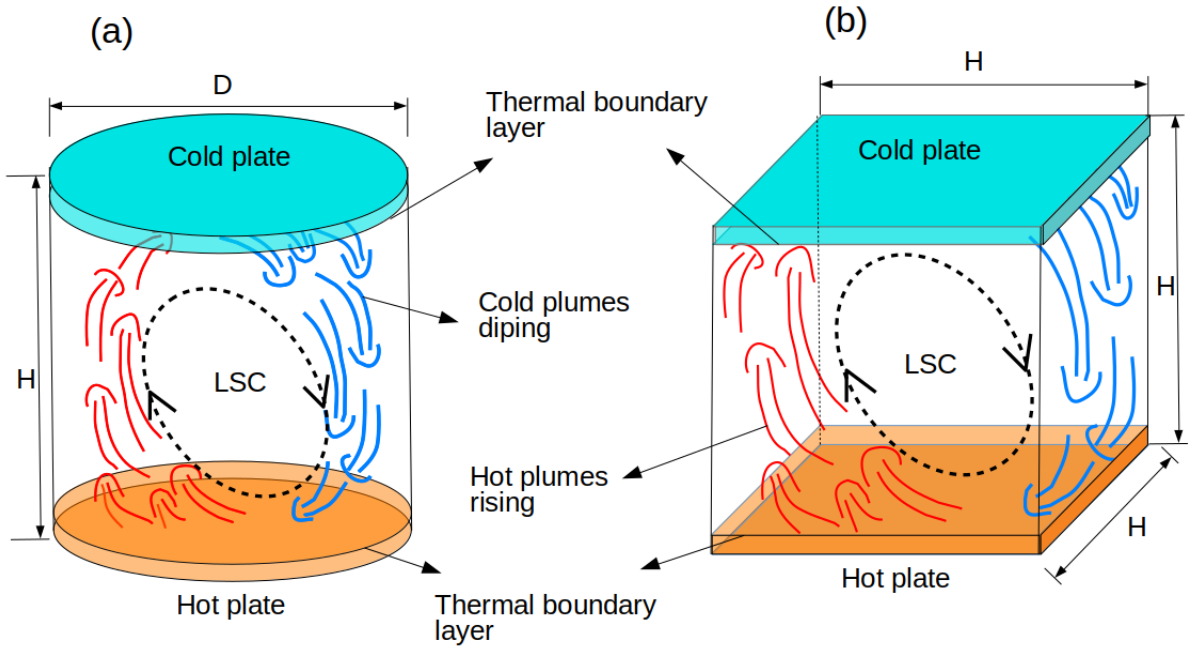

Figure 1.2: Schematic representation of turbulent thermal convection inside (a) cylindrical cell and (b) Cartesian box. The hot thermal plumes arise from the boundary layer at the bottom and the cold plumes descend from the top boundary layer, thus forming an LSC.

during the reorientation [51, 54–57]. These issues are of major interest to the community at present. Several experimental studies have identified these reorientations and quantified them based on various statistical measures [43, 45, 54, 56, 58–60]. Brown and Ahlers [56] and Xi and Xia [60] carried out experiments with water inside cylindrical cells to investigate the dynamics and statistics of reorientations. Both rotations and cessations were identified, and they followed Poisson statistics in time. It is important to note that a similar attempt to study the statistics of reorientation using numerical simulations has never been made.

Interestingly, most of the studies on the dynamics of LSC have been carried out in cylindrical cells, while those for cubic (or cuboid) enclosures are few. In contrast to the cylindrical domain, the azimuthal symmetry is absent in cubic configurations, and hence, the reversal of flow is non-trivial [61]. The experimental works by Zocchi *et al.* [62] and Qiu and Xia [63] with water as the working fluid showed that LSC aligns along the diagonal direction in cubic containers. Qiu and Xia [63] also reported that there exist secondary flows that sometimes have opposite directions to the LSC, which could affect the stability of the LSC. Sun *et al.* [64] performed similar experiments in rectangular convection cell and observed that the LSC is aligned with the largest diagonal of the system. In addition, it was seen that the rectangular

geometry has the most stable flow structure compared to cylindrical and cubical cells. Recently, Foroozani *et al.* [65] used large-eddy simulations to investigate the dynamics of LSC inside a cubic box and reported that the plane of LSC is confined along one of the diagonals of the box. They observed reorientations of LSC as a result of lateral rotation, and the LSC spent some finite time in a transition state between the two diagonals. During the transition stage, the large-scale flow becomes parallel to the sidewalls of the container. Further, they proposed that there exist four possible orientations of LSC in cubic cells, such as along the two diagonal planes with clockwise and counter-clockwise rotations. Similar observations were made in the DNS by Giannakis *et al.* [66] in turbulent RBC, using Koopman eigenfunction analysis. They observed that the LSC persists along the diagonal planes as long as a thousand convective free-fall time units. The first few eigenfunctions quantify the long-term switching of LSC between these different orientations while higher eigenfunction pairs identify the secondary structures such as corner rolls.

LSC and its dynamics are interconnected with the characteristics of heat transport and boundary layers. Wang and Xia [67] experimentally studied the positional dependence of the thermal boundary layer thickness along the direction of LSC in a cubic box. They observed an asymmetric distribution of the thermal boundary layer thickness (δ_θ) with a minimum near the central region. Similar observations were made by Werne [68] in his numerical study of RBC inside a two-dimensional (2D) square cell. At higher Rayleigh numbers, δ_θ remained nearly constant except near the sidewalls. This is in accordance with the observations made by Lui and Xia [69] in a cylindrical convection cell. Qiu and Xia [70] studied the spatial structure of the velocity field in the boundary layer region for RBC of water in a cubic cell. They observed that the magnitude of the mean flow, the shear rate, and the velocity boundary layer thickness change considerably in the directions both along and perpendicular to the orientation of LSC. Further, they noted that the spatial structure of the velocity field in the boundary layer region does not change with Ra. Foroozani *et al.* [71] studied the heat flux distribution at the top and bottom isothermal plates in connection with the alignment of LSC. They observed that the heat flux at the horizontal plates is distributed non-homogeneously, where the heat flux at one corner (where the flow impinges on the wall) is much larger than that at the center and on opposite corners. Numericall simulations by Chandra and Verma [72] observed that heat transport in 2D Rayleigh-Bénard systems is interlinked with flow reversals. In their simulations, they ob-

served anomalous fluctuations in the Nusselt number during flow reversals. After introducing the large-scale flow behaviour and its associated characteristics in turbulent convection, in the next section, we move on to the global heat transport and associated flow regimes in RBC.

1.4 Heat transport in turbulent convection

A recurring theme in both theoretical descriptions and phenomenological pictures of Rayleigh-Bénard convection is how does the heat transport which is generally characterized by a non-dimensional parameter, the Nusselt number (Nu), depends on the other non-dimensional parameters (Ra, Pr, and Γ). In RBC, the dynamics of the system are determined by the dimensionless control parameters, the Rayleigh number, Prandtl number, and the aspect ratio, while the response to the system is measured by the heat flux and kinematic energy, quantified by the Nusselt number and Reynolds number, respectively. Nusselt number is the ratio of the heat transport by convection mechanism to conduction alone. It thus quantifies the heat transport due to fluid motion and is of significant importance in the conceptual and application point of view.

In turbulent RBC, the scaling relation between Nusselt number and Rayleigh number has been subject to extensive study over the years [73–75]. The scaling laws of these quantities have been widely used to identify different flow regimes [76–78]. The early studies on the Nusselt number scaling were based on single exponent, $Nu \propto Ra^{\beta}$ [73, 75, 79]. For fully turbulent thermal convection, Malkus [73] proposed the so-called "classical" scaling of Nusselt number with Rayleigh number as $Nu \propto Ra^{1/3}$. The scaling was based on the assumptions that the opposing boundary layers do not interact, and the height of the fluid layer, therefore, does not enter into the heat transfer scaling. It is often argued that the $n = 1/3$ scaling is suitable for geophysical systems, where the boundary layers are relatively isolated, such that when they are much thinner than the convective fluid layer. Recently, using DNS, Iyer *et al.* [80] showed that for turbulent RBC inside slender ($\Gamma = 1/10$) cylindrical cells, the Nusselt number follows the classical scaling up to $Ra = 10^{15}$.

Using the mixing length theory, Kraichnan [81] proposed the scalings for Nusselt number as $Nu \propto Ra^{1/3}$ for large Prandtl number ($Pr > 1$), $Nu \propto (PrRa)^{1/3}$ for small Prandtl number

($Pr < 1$), and $Nu \propto 1$ for very small Pr. Further, at very large Rayleigh numbers or the so-called "ultimate regime", a scaling behaviour of $Nu \propto [Ra/ln(Ra)]^{1/2}$ was proposed. The half scaling is valid only at high Rayleigh number regime ("ultimate" or asymptotic regime), where the boundary layers undergo a transition from laminar to turbulent, and the heat flux and turbulent intensity become independent of the kinematic viscosity and thermal diffusivity. The numerical studies by Lohse and Toschi [82] and Calzavarini *et al.* [83] also observed similar scaling in the so-called homogeneous RBC, i.e., in the bulk region. Similar half scaling was obtained by Cholemari and Arakeri [84, 85], in their experiments on turbulent flow in a long vertical tube that is axially homogeneous, and sustained purely by buoyancy. They separated the bulk and the boundary layer effects in turbulent convection, by eliminating the boundary layers and proposed that the bulk mechanisms cause the $Nu \sim Ra^{1/2}$ scaling. Chilla *et al.* [86] showed that the thermal conductivity and the heat capacity of the horizontal plates play a crucial role in attaining the ultimate regime in RBC.

Different experimental results at different Ra and Pr ranges reported a wide variety in exponents for the Nusselt number scaling. This prompted Grossmann and Lohse [76–78] to propose a unifying theory that consists of different regimes with different exponents. They identified different flow regimes in the parameter space $Ra - Pr$, and established the Nusselt number and Reynolds number scalings ($Nu \propto Ra^m Pr^n$ and $Re \propto Ra^a Pr^b$) at these regimes. The main idea of the theory is to decompose the volume-averaged kinetic (ϵ_u) and thermal dissipation rate (ϵ_θ) into their respective bulk and boundary layer contributions, i.e.,

$$\epsilon_u = \epsilon_{u,BL} + \epsilon_{u,bulk}, \tag{1.1}$$

$$\epsilon_\theta = \epsilon_{\theta,BL} + \epsilon_{\theta,bulk}, \tag{1.2}$$

where the subscripts BL and $bulk$ denote the boundary layer and bulk regions, respectively. Four different regimes are characterized based on the domination of ϵ_u and ϵ_θ inside the boundary layer and the bulk region. The different regimes are:

(I) both ϵ_u and ϵ_θ are dominated by their BL contributions.

(II) ϵ_θ is dominated by $\epsilon_{\theta,BL}$ and ϵ_u is dominated by $\epsilon_{u,bulk}$.

(III) ϵ_u is dominated by $\epsilon_{u,BL}$ and ϵ_θ is dominated by $\epsilon_{\theta,bulk}$.

(IV) both ϵ_u and ϵ_θ are bulk dominated.

Table 1.1: Power laws for Nu in different flow regimes.

Regime	Dominance of regime	BL	Nu
I_l	$\epsilon_{u,BL}$,$\epsilon_{\theta,BL}$	$\delta_u < \delta_\theta$	$0.27Ra^{1/4}Pr^{1/8}$
I_u		$\delta_u > \delta_\theta$	$0.33Ra^{1/4}Pr^{-1/12}$
II_l	$\epsilon_{u,bulk}$,$\epsilon_{\theta,BL}$	$\delta_u < \delta_\theta$	$0.97Ra^{1/5}Pr^{1/5}$
II_u		$\delta_u > \delta_\theta$	$(\sim Ra^{1/5})$
III_l	$\epsilon_{u,BL}$,$\epsilon_{\theta,bulk}$	$\delta_u < \delta_\theta$	$6.43 \times 10^{-6}Ra^{2/3}Pr^{1/3}$
III_u		$\delta_u > \delta_\theta$	$3.43 \times 10^{-3}Ra^{3/7}Pr^{-1/7}$
IV_l	$\epsilon_{u,bulk}$,$\epsilon_{\theta,bulk}$	$\delta_u < \delta_\theta$	$4.43 \times 10^{-4}Ra^{1/2}Pr^{1/2}$
IV_u		$\delta_u > \delta_\theta$	$0.038Ra^{1/3}$

The $Ra - Pr$ phase diagram identifying different flow regimes is shown in Fig. 1.3. Each regime is further divided into two sub-regimes based on the velocity (δ_u) and thermal (δ_θ) boundary layer thickness. Depending on whether δ_u is lesser or larger than δ_θ, the sub-regimes are identified, where the subscript 'u' stands for $\delta_u > \delta_\theta$ and 'l' for $\delta_u < \delta_\theta$. The Nusselt number scaling observed in the respective regimes are shown in Table 1.1.

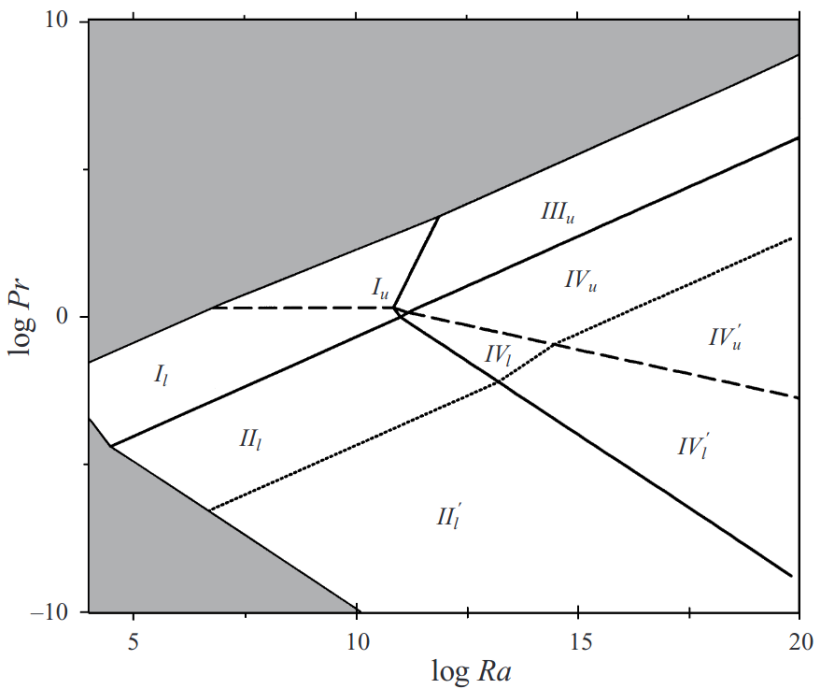

Figure 1.3: Phase diagram in $Ra-Pr$ plane indicating the different flow regimes by Grossmann and Lohse theory [76]. The dashed line represents $\delta_u = \delta_\theta$. The shaded regime for large Pr is where $Re \leq 50$, and the shaded regime for low Pr is where $Nu = 1$.

Generally, from a scaling point of view, detached thermal plumes are considered as a part of the thermal boundary layers. Thus, instead of BL and $bulk$ decomposition, one may also con-

sider the contribution of dissipation rates from the plume (BL-like regions) and background regions separately. Plumes are coherent structures and play a crucial role in heat transport in turbulent convection. Mostly, they consist of a mushroom cap with a sharp temperature gradient and a stem that is relatively diffuse [87, 88]. Over the years, researchers have used different techniques to identify plumes. Although these structures are seen directly in experiments (shadow-graph and particle-image velocimetry (PIV) techniques) [89], identification and quantification of thermal plumes are not straight forward in numerical simulations. Some of the prominent works in this direction have been carried out by Belmonte and Libchaber [90], Julien *et al.* [91], Zhou and Xia [92], Alexandre *et al.* [93], Shishkina and Wagner [94], and Emran and Schumacher [95]. In most of the studies, plumes are identified based on some correlation between temperature and velocity fluctuations. The experimental study by Xi *et al* [89] showed that plumes cluster together to form large vortices that lead to the formation of LSC. Similar observations were made in the numerical studies by Poel *at al.* [96] and Parodi *et al.* [97]. As a result of the clustering of thermal plumes, heat transport across the system becomes highly inhomogeneous, both temporally and spatially [98]. Investigation of the morphology, evolution, and characteristics of these coherent structures is essential to the understanding of turbulent flows in many natural and industrial systems.

1.5 Rotating Rayleigh-Bénard convection

Rotating Rayleigh-Bénard convection (RRBC) is a phenomenon that is observed all around us. The addition of rotation to the RBC system makes it more complex. Nevertheless, several experiments have been conducted in this direction. RRBC was first studied by Chandrasekhar [99] in 1953. Chandrasekhar [25, 99] extended Rayleigh's analysis on RBC to the rotating case. He examined the stability of a fluid layer heated from below, subjected to gravity and Coriolis force. It was shown that the effect of the Coriolis force was to inhibit the onset of convection. The extent of the inhibition depends on different non-dimensional parameters. From linear stability theory he found out that for any Prandtl number greater than one, the critical Rayleigh number for the onset of convection (Ra_c) depends only on the rotation rate, quantified by the Taylor number Ta (alternatively the Rossby number Ro or the Ekman number Ek are also used). But for lower Pr, the critical Rayleigh number depends on both Pr and

Ta. This was later experimentally confirmed by Nakagawa *et al.* [100]. Chandrasekhar [25] observed that for non-rotating case viscosity has a stabilizing effect on the fluid layer, but when rotation is introduced, viscosity plays a destabilizing role. This was explained using Taylor-Proudman theorem [101–103]. A similar stabilizing effect of rotation on the convection system was observed by Veronis [104]. In the non-rotating case, Ra_c was constant for given boundary conditions, but in the rotating counterpart, it depends on the Ta and the Pr. He found out that viscosity here plays a dual role, i.e., the familiar role of dissipating kinetic energy and a special role of releasing energy due to rotational effects. In a different study, Veronis [105] extended his analysis to a wide range of Prandtl numbers and Taylor numbers with stress-free boundary conditions. He observed an early onset of instability for low Prandtl numbers, as compared to those predicted by the stability analysis. The onset of thermal convection and pattern formation in RRBC have been subject to several experimental [106–109] and numerical [110–114] investigations.

A detailed experimental study on rotating convection was carried out by Rossby [115] in 1969. He observed an increase in heat transport (of about 10%) at low rotation rates compared to the non-rotating case. However, for higher rotation rates, a stronger reduction in heat transport was noticed, due to the suppression of vertical velocity fluctuations by the rotation. This behaviour has been later confirmed by several experiments [116–118]. Niemela *et al.* [119] conducted experiments on RRBC at very high Rayleigh numbers ($10^{11} < Ra < 4.3 \times 10^{15}$). For steady rotation, no heat transport enhancement was observed. However, as the rotation rate varied periodically, an enhancement in heat transfer was reported.

Over the past few decades, numerical simulations have made significant progress in the field of rotating convection [120–122]. The DNS study by Julien *et al.* [91, 116, 123], Kunnen *et al* [124–126] and King *et al* [18] investigated the heat transport and resulting flow patterns under the influence of rotation, for a range of Ra and Ro. Kunnen *et al.* [124] observed that for RRBC at low rotation rates, heat transfer increases with Nusselt number increasing up to 5%. The increase in heat transport was described by the phenomenon of Ekman pumping [127], which creates a vertical heat flux. However, as the rotation rate increases, the heat transfer drops. This is due to the suppression of fluctuations in vertical velocity as a result of increased rotation rate (Taylor-Proudman theorem). Furthermore, Kunnen *et al* [128–130] performed experimental and numerical investigations of turbulent rotating convection inside cylindrical

domain and made direct comparisons between the two. They observed a domain filling large-scale circulation at low rotation rates, where the hot plumes gather and rise along one side of the domain while the cold plumes gather and sink along the other side of the container. When the rotation rate was increased slightly, the LSC was replaced by dispersed vertical local thermal plumes as the dominant flow structure. At very high rotation rates, the stabilizing effect of rotation was clearly demonstrated. Oresta *et al.* [131] studied the transitional regimes and mean flow structures for thermally driven flow with background rotation in a cylindrical cell. They observed that at strong rotation rates, it is a very effective way to inhibit vertical motions and to prevent horizontal thermal gradients, which is a highly desirable outcome in solidification and crystal growth processes where thermally induced motions cause material defects and crystal inhomogeneities. Schmitz and Tilgner [132, 133] carried out numerical simulations inside a horizontally periodic domain with no-slip and stress-free boundary conditions at the horizontal plates. The enhancement in transport under the influence of rotation was observed only when a no-slip boundary condition is used at the horizontal plates.

Previous studies have shown that based on the rotation rate and its effect on global heat transport, different flow regimes can be identified [134–137]. At weak rotation regime, heat transport remains nearly constant, but as soon as the rotation rate is increased above a critical value, an increase in Nusselt number is observed for moderate rotation rate. After the Nu has reached its peak value, it marks the transition to the next regime, which is dominated by rotation. Here the heat transfer rate drops steeply with an increase in rotation rates. Note that this classification is valid only for $Pr \gtrsim 1$. For low Prandtl numbers ($Pr \lesssim 1$), no enhancement in heat transport is observed at any rotation rate [138]. Horn and Shishkina [139] used a method based on the decomposition of the velocity field into toroidal and poloidal parts to identify different flow regimes and transitions in rotating convection, without any restriction to certain Prandtl numbers or aspect ratios.

1.6 Motivation and objectives

It has been established that thermal plumes, which are the major carriers of heat, triggers the onset of LSC in turbulent RBC [89]. Understanding the characteristics of plumes, their morphology, and evolution in connection to LSC is of significant importance, as these coherent

structures play a crucial role in many physical systems. Despite the fact that there are many experimental works that have studied LSC and its dynamics over the years, comprehensive numerical studies in this direction are less, especially for convective flow inside a Cartesian box. Moreover, the effect of rotation on this large-scale structure is also less explored. Some of the critical questions that arise in the study of these large-scale structures in the presence of rotation are: (a) how rotation affects the overall flow dynamics, particularly the appearance and orientation of LSC? And (b) how it changes the characteristics of heat transport, dissipation rates, and boundary layers? In this thesis, DNS of 3D turbulent RBC inside cubic and cylindrical cells are carried out with a prime focus on LSC, its characteristics, and dynamics. In addition, a detailed investigation of the effect of rotation and Prandtl number and statistics of thermal plumes on RBC is performed. Although there are many experimental and numerical works in rotating convection, we observe that there is much more to be explored in RRBC, particularly when the flow is significantly dominated by rotation. In spite of the fact that identification of flow regimes and their transitions in rotating convection have been studied extensively, such attempts in low Prandtl number flows are less, where no increment in heat transport with rotation is observed. These issues are also addressed in this thesis. The results of the thesis can be broadly classified into two sections. Chapters 3-5 constitute the first part where DNS of rotating convection inside cylindrical confinement is presented. In the second part, which comprises chapters 6 and 7, the results pertaining to highly turbulent flow inside a cubic cell are discussed. The main objectives of the thesis are as follows:

1. To study the effect of rotation in RBC, and thereby identify different flow regimes, characterize the flow structures and quantify them based on the Fourier modes.

2. Investigate the dynamics and statistics of LSC in turbulent rotating RBC inside a cylindrical cell.

3. Study the effect of Prandtl number on the heat transport and flow structures in rotating RBC.

4. Identify and characterize thermal plumes, their contribution to thermal dissipation and study their statistics for highly turbulent RBC.

5. Understanding the dynamics of LSC in a cubic cell and thereby propose a mechanism of flow reversal.

1.7 Outline of the thesis

The remainder of the thesis is organized as follows. In the next chapter (chapter 2), the details of mathematical modelling, numerical strategies adopted, parallelization techniques, and code validation with previous results are presented. In chapter 3, the effect of rotation on turbulent Rayleigh-Bénard convection inside a cylindrical cell of unit aspect ratio is studied. We primarily focus on the flow structures, heat transport, and boundary layer dynamics and evaluate the effect of rotation on these aspects. Based on the flow modes and heat transfer characteristics, different flow regimes are identified. At low rotation rates, a coherence at large-scale is observed, resulting in LSC, while at higher rotation rates, wall-bounded flow structures, namely quadrupolar and sextupolar modes are obtained. This is followed by chapter 4, where the focus is entirely on LSC, its characteristics, dynamics, and statistical measures. Reorientations of LSC are identified, and they are quantified using the Fourier mode analysis of the vertical velocity along the cylinder azimuth. We identify the so-called cessation-led and rotation-led reorientations of LSC and present their statistics. Further, the effect of LSC on heat transfer, dissipation rates, and boundary layers are also evaluated. After investigating the effect of rotation, in chapter 5, we study the effect of Prandtl number in RBC. Based on the Fourier mode decomposition, different flow states are quantified, and their association with the heat transport and boundary layer dynamics are evaluated. Additionally, the flow dynamics at extremely high rotation rates are evaluated, and the transition to conduction stage is studied along with its dependence on the change in Prandtl number.

In chapter 6 we study highly turbulent flow inside a cubic cell in the Rayleigh number range $2 \times 10^6 \leq Ra \leq 10^9$. Thermal plumes are identified and quantified based on the correlation between the vertical velocity and temperature fluctuations, and their statistics are discussed in detail. The entire cell volume is decomposed into plume and background dominated regions, and the thermal dissipation rate contribution from each of these subsets are evaluated, and scaling laws are established. Additionally, temperature and velocity fluctuations, their skewness, flatness, and turbulent kinetic energy budget are evaluated to asses the statistical behaviour of the flow. Then we proceed to chapter 7, where LSC, its characteristics, and dynamics inside cubic confinement are discussed in detail. Flow dynamics in different planes are analyzed comprehensively, and a mechanism of flow reversals in cubic cells is proposed. Further, the effect

of LSC on the boundary layer, dissipation rate, and turbulent kinetic energy budget is evaluated. Finally, chapter 8 presents a panorama of the salient contributions and conclusions of this thesis and suggests some possible directions for future research.

2

Mathematical modelling

This chapter presents the details of mathematical modelling and numerical strategies adopted to perform the simulations. We first introduce the governing equations and details of the flow domain with boundary conditions. This is followed by a detailed discussion on the finite volume formulations, linear solver, and the solution algorithm used. Further, the grid generation and parallelization techniques employed in the present study are taken up. Finally, comparison with a few previous literatures is presented.

2.1 Problem description and mathematical formulation

Physically Rayleigh-Bénard convection can be described as thermo-convective instability of an incompressible Newtonian fluid confined in a container in which the bottom surface is heated and the top surface is cooled. In this work, two different geometries are considered, namely (a) cylindrical cell and (b) cubic box, as shown in Fig. 2.1. For both the flow domains, isothermal boundary conditions are implemented on the horizontal surfaces. The bottom plate is hot (T_H) and the top plate is cold (T_C), and thus a temperature difference of $\Delta T = T_H - T_C$ is applied across the surfaces. All the lateral walls are adiabatic. For velocity, no-slip conditions are applied on all the surfaces.

Mathematically the problem is described using the momentum, mass, and energy conser-

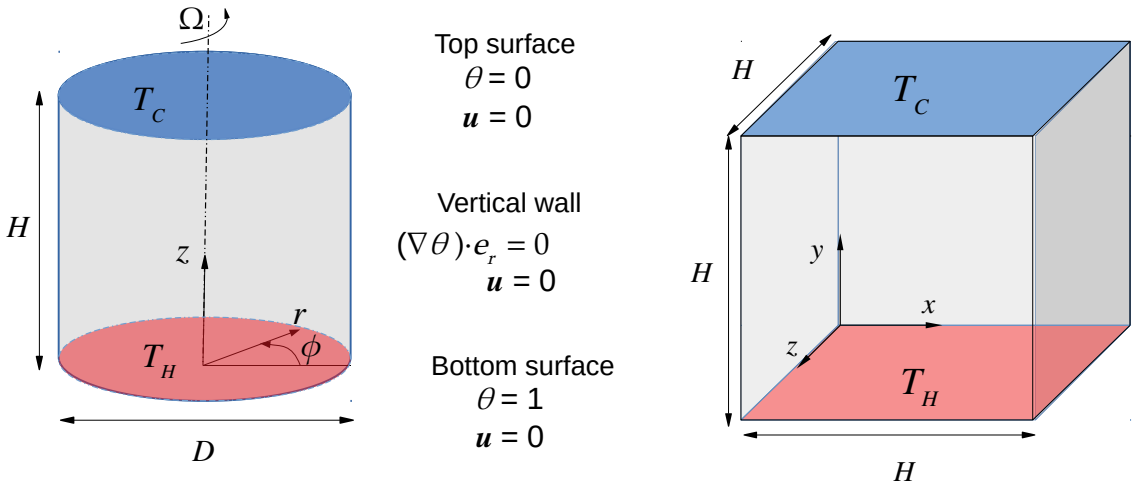

Figure 2.1: Schematic diagram of cylindrical cell and Cartesian cubic box with boundary conditions.

vation equations using the Boussinesq approximation, written in the normalized form as

$$\frac{\partial \boldsymbol{u}}{\partial t} + \boldsymbol{u}\cdot\nabla\boldsymbol{u} = -\nabla p + \sqrt{\frac{Pr}{Ra}}\nabla^2\boldsymbol{u} + \theta\hat{\boldsymbol{e}} - \frac{1}{Ro}(\hat{\boldsymbol{e}}\times\boldsymbol{u}), \tag{2.1}$$

$$\nabla\cdot\boldsymbol{u} = 0, \tag{2.2}$$

$$\frac{\partial \theta}{\partial t} + \boldsymbol{u}\cdot\nabla\theta = \frac{1}{\sqrt{PrRa}}\nabla^2\theta, \tag{2.3}$$

where $\boldsymbol{u}$ is the velocity vector, p the pressure, $\hat{\boldsymbol{e}}$ the unit vector in the vertical direction and θ [$= (T - T_C)/\Delta T$] the non-dimensional temperature. Note, $\hat{\boldsymbol{e}}$ is the unit vector in y and z directions for Cartesian and cylindrical geometries, respectively. Here Ra, Pr and Ro are the Rayleigh, Prandtl and Rossby number, respectively, where

$$Ra = \frac{g\beta\Delta T H^3}{\nu\alpha}, \quad Pr = \frac{\nu}{\alpha}, \quad Ro = \frac{\sqrt{g\beta\Delta T H}}{2\Omega H}.$$

The last term on the right-hand side of Eq. 2.1 represents the Coriolis force, which appears in case of rotating convection. The effect of rotation is studied in cylindrical domain, where rotation is applied about the vertical axis of the cylinder. The effect of rotation is embedded inside the Rossby number which, by its form, implies inverse of the rotation rate. In literature, different non-dimensional numbers are used to quantify rotation rate [125, 140]. Alternatively Taylor number (Ta), or Ekman number (E_k) are also used [124], given as

$$Ta = \left(\frac{2\Omega H^2}{\nu}\right)^2 \quad \text{and} \quad Ek = \frac{\nu}{\Omega L^2}, \quad \text{where} \quad Ro = \sqrt{\frac{Ra}{PrTa}}.$$

We use height of the container H, free-fall velocity $V^f = \sqrt{g\beta\Delta T H}$, and ΔT as the scales for normalization of length, velocity, and temperature, respectively. The aspect ratio of the cylinder is defined as $\Gamma = D/H$, where D is the diameter of the cylinder. In case of rotating convection, the governing equations are solved in rotating frame of reference. A detailed discussion on frame transformation, Boussinesq approximation, and normalization of the governing equations are presented below.

2.1.1 Rotating frame of reference

A frame of reference is a framework consisting of a coordinate system, an observer, and a clock, used in the description of a physical phenomenon. There exist two kinds of frame of reference, namely, the inertial frame and the non-inertial frame. A reference frame that is either at rest or in uniform motion (without rotation) is termed an inertial frame of reference or a Newtonian frame of reference. On the other hand, a frame of reference accelerating with respect to an inertial frame is called the non-inertial frame of reference. A special case of non-inertial frame is a rotating frame of reference, where the frame is rotating with respect to the inertial frame. It is more reasonable to work in the non-inertial (or rotating) frames for geophysical and astrophysical applications where everything is in relative motion. Under such situations, it is customary to fix the frame to the planet (or any celestial body) rotating with a particular angular velocity. In the case of RRBC, the governing equations are solved in a rotating frame of reference.

The dimensional mass, momentum and energy conservation equations in the inertial or laboratory frame of reference are given by

$$\frac{\partial \boldsymbol{u_I}}{\partial t} + \boldsymbol{u_I}\cdot\nabla\boldsymbol{u_I} = -\frac{1}{\rho}\nabla P + \nu\nabla^2\boldsymbol{u_I}, \tag{2.4}$$

$$\frac{\partial \rho}{\partial t} + \rho\nabla\cdot\boldsymbol{u_I} = 0, \tag{2.5}$$

$$\frac{\partial T}{\partial t} + \boldsymbol{u_I}\cdot\nabla T = \alpha\nabla^2 T, \tag{2.6}$$

where $\boldsymbol{u_I}$ is the velocity vector in the inertial frame, T the dimensional temperature, and P the dimensional pressure. Now, let us consider the rotation of a position vector $\boldsymbol{x}$ with angular velocity $\boldsymbol{\Omega}$ (=$0i + 0j + \Omega k$). The rate of change of the position vector in inertial frame of reference is written as

$$\left(\frac{d\boldsymbol{x}}{dt}\right)_I = \left(\frac{d\boldsymbol{x}}{dt}\right)_R + \boldsymbol{\Omega} \times \boldsymbol{x}, \tag{2.7}$$

where $\left(\frac{d\boldsymbol{x}}{dt}\right)_R$ indicates the rate of change of $\boldsymbol{x}$ in the rotating frame and $\boldsymbol{\Omega} \times \boldsymbol{x}$ captures the dynamics due to frame rotation. As the rate of change of position vector gives the velocity, Eq. 2.7 can be written as

$$\boldsymbol{u_I} = \boldsymbol{u_R} + \boldsymbol{\Omega} \times \boldsymbol{x}, \tag{2.8}$$

where $\boldsymbol{u_R}$ is the velocity vector in the rotating frame. Similarly, the rate of change of velocity (acceleration) in the inertial frame can be written as

$$\left(\frac{d\boldsymbol{u_I}}{dt}\right)_I = \left(\frac{d\boldsymbol{u_I}}{dt}\right)_R + \boldsymbol{\Omega} \times \boldsymbol{u_I}. \tag{2.9}$$

Substituting Eq. 2.8 in the above equation results in

$$\left(\frac{d\boldsymbol{u_I}}{dt}\right)_I = \left(\frac{d\boldsymbol{u_R}}{dt}\right)_R + \left(\frac{d\boldsymbol{\Omega}}{dt}\right)_R \times \boldsymbol{x} + \boldsymbol{\Omega} \times (\boldsymbol{\Omega} \times \boldsymbol{x}) + 2(\boldsymbol{\Omega} \times \boldsymbol{u_R}). \tag{2.10}$$

If we consider a constant rate of rotation, the second term in the right-hand side becomes zero. The last two terms represent the centripetal acceleration [$\boldsymbol{\Omega} \times (\boldsymbol{\Omega} \times \boldsymbol{x})$] and Coriolis acceleration [$2(\boldsymbol{\Omega} \times \boldsymbol{u_R}) = 2\Omega(\hat{\boldsymbol{e}} \times \boldsymbol{u_R})$]. The Coriolis acceleration acts in the direction perpendicular to the rotation vector and the velocity in rotating frame. The centripetal acceleration can be expressed as the gradient of a scalar as $\boldsymbol{\Omega} \times (\boldsymbol{\Omega} \times \boldsymbol{x}) = -\frac{1}{2}\nabla(\Omega^2 R_p^2)$, where R_p radial distance of the projection of the vector $\boldsymbol{x}$ on to the horizontal plane. Note that the total derivative of any scalar quantity is the same in both inertial and rotating frames. Thus, the continuity equation and the energy equation remain unaffected by the frame rotation. Also, the pressure gradient remains unaltered as the spatial gradients are identical in both the frames. The unsteady Navier-stokes equation in the rotating frame of reference can be written as

$$\frac{\partial \boldsymbol{u_R}}{\partial t} + \boldsymbol{u_R} \cdot \nabla \boldsymbol{u_R} + 2\Omega(\hat{\boldsymbol{e}} \times \boldsymbol{u_R}) - \frac{1}{2}\nabla(\Omega^2 R_p^2) = -\frac{1}{\rho}\nabla P + \nu \nabla^2 \boldsymbol{u_R} - g\hat{\boldsymbol{e}}.$$

The Coriolis acceleration and the centripetal acceleration terms can be taken to the right hand side of the momentum equation to become the Coriolis force and the centrifugal force respectively. Thus, one obtains

$$\frac{\partial \boldsymbol{u_R}}{\partial t} + \boldsymbol{u_R}\cdot\nabla\boldsymbol{u_R} = -\frac{1}{\rho}\nabla P + \nu\nabla^2\boldsymbol{u_R} - g\hat{\boldsymbol{e}} - 2\Omega(\hat{\boldsymbol{e}}\times\boldsymbol{u_R}) + \frac{1}{2}\nabla(\Omega^2 R_p^2). \tag{2.11}$$

2.1.2 Boussinesq approximation and pressure modification

We assume Boussinesq approximation under which the density variations are neglected except for the buoyancy term. It is an approach to model buoyancy-driven flows at not-so-high temperature difference, without solving the complete variable-density Navier-Stokes equation. All the properties (ν, α, μ) of the fluid are considered to be independent of temperature, and the fluid is considered to be incompressible except for the buoyancy term. Here the density variation occurs only due to temperature difference. Its variation, thus, can be written as $\rho = \rho_o[1-\beta(T-T_o)]$, where ρ_o is any reference density corresponding to a reference temperature T_o that may be of any boundary or the mean temperature in the flow. Note that Boussinesq approximation is applicable only for low Mach number flows. For high-speed flows, the density variations caused by velocity divergence cannot be neglected. Similarly, the approximation cannot be used when the vertical scale of flow is large enough to cause significant changes in density due to hydrostatic pressure variations. After applying the Boussinesq approximations, the momentum equation (Eq. 2.11) is written

$$\rho_o(\frac{\partial \boldsymbol{u_R}}{\partial t}+\boldsymbol{u_R}\cdot\nabla\boldsymbol{u_R}) = -\nabla P+\mu\nabla^2\boldsymbol{u_R}-g\rho_o\hat{\boldsymbol{e}}+g\rho_o\beta(T-T_o)\hat{\boldsymbol{e}}-2\Omega(\hat{\boldsymbol{e}}\times\boldsymbol{u_R})\rho_o+\frac{1}{2}\nabla(\Omega^2R^2)\rho_o \tag{2.12}$$

The gravity force (third term on RHS) and the centrifugal force are conservative forces and can be expressed as the gradient of some potential function, which has similar effects as the pressure gradient. In incompressible flow calculations, it is convenient to bury such terms inside the modified pressure [127, 135, 141] which results in

$$\frac{\partial \boldsymbol{u_R}}{\partial t} + \boldsymbol{u_R}\cdot\nabla\boldsymbol{u_R} = -\frac{1}{\rho_o}\nabla p + \nu\nabla^2\boldsymbol{u_R} + g\beta(T-T_o)\hat{\boldsymbol{e}} - 2\Omega(\hat{\boldsymbol{e}}\times\boldsymbol{u_R}). \tag{2.13}$$

Thus, the dimensional mass, momentum and energy conservation equations in rotating

Table 2.1: Normalization scales and the non-dimensional variables.

Variable	Scale	Normalized variable
length	H	$x^* = x/H$
velocity	$V^f = \sqrt{g\beta\Delta T H}$	$\boldsymbol{u^*} = \boldsymbol{u}/\sqrt{g\beta\Delta T H}$
time	H/V^f	$t^* = t\sqrt{g\beta\Delta T H}/H$
pressure	$\rho_c(V^f)^2$	$p* = p/(\rho_o g\beta\Delta T H)$
temperature	$\Delta T = T_H - T_C$	$\theta = T - T_C/(T_H - T_C)$

frame of reference (dropping subscript $_{\boldsymbol{R}}$ for simplicity), incorporating the Boussinesq approximation is written as

$$\frac{\partial \boldsymbol{u}}{\partial t} + \boldsymbol{u}\cdot\nabla\boldsymbol{u} = -\frac{1}{\rho_o}\nabla p + \nu\nabla^2\boldsymbol{u} + g\beta(T - T_o)\hat{\boldsymbol{e}} - 2\Omega(\hat{\boldsymbol{e}}\times\boldsymbol{u}), \tag{2.14}$$

$$\nabla\cdot\boldsymbol{u} = 0, \tag{2.15}$$

$$\frac{\partial T}{\partial t} + \boldsymbol{u}\cdot\nabla T = \alpha\nabla^2 T. \tag{2.16}$$

On normalization of the above equations (Eqs. 2.14-2.16) using the scales shown in Table 2.1 and discarding $*$ for convenience, we obtain the non-dimensional form of the governing equations as shown in Eqs. 2.1-2.3. Note that the reference temperature is taken at the cold plate; hence, $\rho_o = \rho_c$ and $T_o = T_C$.

The governing equations (Eqs. 2.1-2.3) are solved using finite volume formulations with collocated arrangement of variables [142–144]. Each term of the continuity, momentum, and energy equation is integrated over a hexahedral volume V. Figure 2.2 depicts typical control volumes (CV) considered to integrate each term in the Cartesian and cylindrical domain. The variables u, v, w (u_r, u_ϕ, u_z), p and θ are defined at the centroid of the hexahedral volume (point P). The integrals are approximated as given below.

Continuity equation: The volume integration of Eq. 2.2 is simplified using the divergence theorem, followed by second order approximation (denoted as $\approx$ here onwards) of the surface integrals, as

$$\int_V \nabla\cdot\boldsymbol{u}dV = \int_S \boldsymbol{u}\cdot\hat{\boldsymbol{n}}dS \approx \sum_f \boldsymbol{u_f}\cdot\boldsymbol{S_f} = \sum_f F_f$$

where $F_f = \boldsymbol{u}\cdot\hat{\boldsymbol{n}}\ dS$ denotes the mass flux through the face f and $\hat{\boldsymbol{n}}$ ($\hat{n}_i$ in index notation)

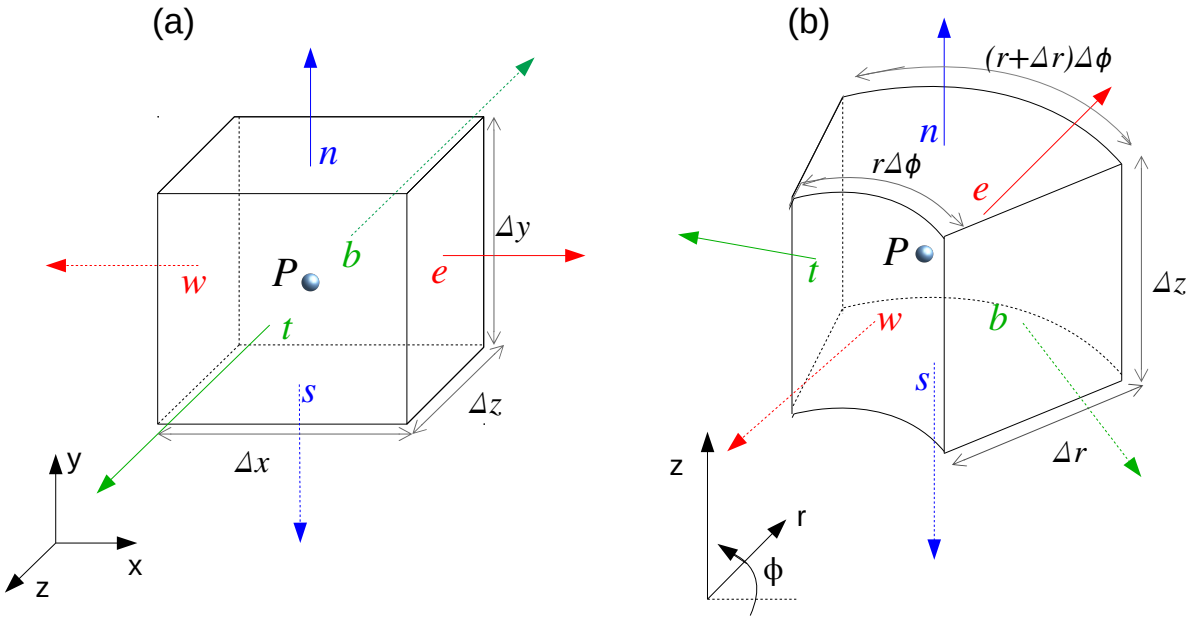

Figure 2.2: Schematic diagram of a hexahedral control volume centered at P, showing all six faces, for (a) Cartesian and (b) cylindrical geometries. Here n, w, e, s, t, and b represent the north, west, east, south, top, and bottom faces of the CV, respectively, required for the identification of neighbours in the linear equations.

is the outward unit normal vector to the surface S. Here $\boldsymbol{u_f}$ and $\boldsymbol{S_f}$ are the velocity at a face center and the area vector, respectively.

Momentum equation: Integral approximation of different terms in the momentum equation is shown below. Here n, $n+1$ correspond to n^{th} and $(n+1)^{th}$ time step, respectively, and Δt is the time increment used for time marching solution. Note that i in general corresponds to three linearly independent directions which need not be orthogonal. Such a distinction is felt through the unit outward normals, surface and volume construction. Here u_i represents the velocity components in $i = x, y, z$ (or r, ϕ, z) directions, and $u_{i,f}$ indicates their face interpolated counterparts.

1. Unsteady term:

$$\int_V \frac{\partial \boldsymbol{u}}{\partial t} dV \approx \frac{u_{i,P}^{n+1} - u_{i,P}^{n}}{\Delta t} V_P$$

The above integral is approximated by considering u_i, P at the cell center while V_P represents the volume of the control volume.

2. Convective term:

$$\int_V \boldsymbol{u}\cdot\nabla\boldsymbol{u}dV = \int_V \nabla\cdot(u_i u_j)dV = \int_S u_i(u_j\cdot\hat{n}_j dS) \approx \int_S u_i dF = \sum_f u_{i,f}F_f$$

3. Diffusive term:

$$\int_V \nabla\cdot\nabla\boldsymbol{u}dV = \int_V \nabla\cdot\nabla u_i dV = \int_S \nabla u_i.\hat{\boldsymbol{n}}dS \approx \sum_f (\nabla u_i\cdot\boldsymbol{S})_f = \sum_f F_{df u_i}$$

where $F_{df u_i} = (\nabla u_i\cdot\boldsymbol{S})_f$ represents the diffusion flux at face f.

4. Pressure term:

$$\int_V \nabla p\cdot\hat{n}_i dV = \int_V (\hat{n}_i\cdot\nabla p + p\nabla\cdot\hat{n}_i)dV = \int_V \nabla\cdot(p\hat{n}_i)dV = \int_S p(\hat{n}_i\cdot\hat{n}_j dS) \approx \sum_f p_f S_{f,i}$$

where $S_{f,i}$ represents the i^{th} component of the area vector at the face f and p_f is the face interpolated pressure.

5. Buoyancy Term:

$$\int_V \theta dV \approx \theta_P V_P$$

6. Coriolis term:

$$\int_V (\hat{\boldsymbol{e}}\times\boldsymbol{u})dV \approx (\hat{\boldsymbol{e}}\times\boldsymbol{u})_P V_P$$

Energy equation: The terms in the energy equation are approximated in a similar way as in the momentum equation.

1. Unsteady term:

$$\int_V \frac{\partial\theta}{\partial t}dV \approx \frac{\theta_P^{n+1}-\theta_P^n}{\Delta t}V_P$$

2. Convective term:

$$\int_V \boldsymbol{u}\cdot\nabla\theta dV = \int_S \theta(\boldsymbol{u}\cdot\hat{\boldsymbol{n}}dS) = \int_S \theta dF \approx \sum_f \theta_f F_f$$

3. Diffusive term:

$$\int_V \nabla\cdot\nabla\theta dV = \int_S \nabla\theta\cdot\hat{\boldsymbol{n}}dS = \sum_f (\nabla\theta\cdot\boldsymbol{S})_f \approx \sum_f F_{df\theta}$$

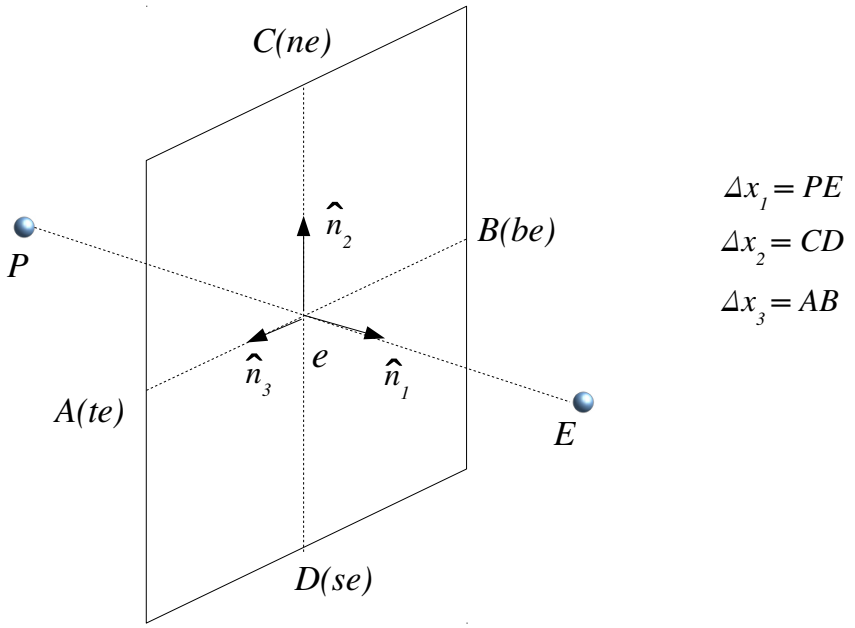

Figure 2.3: Geometrical features showing the edge centers and three unit vectors required for the integral of the Laplacian at the east face.

Next, the computation of the diffusive flux $F_{df u_i}$ is illustrated. Figure 2.3 shows the east face of a typical CV with centroid P having the neighbouring east centroid E. Here, $se, ne, be,$, and te denote the centers of the edges that this face shares with its neighbouring cells located in the south, north, bottom, and top, respectively. Outward normal vector of a face can be written as

$$\boldsymbol{S_f} = \alpha_1 \hat{\boldsymbol{n}}_{\boldsymbol{1}} + \alpha_2 \hat{\boldsymbol{n}}_{\boldsymbol{2}} + \alpha_3 \hat{\boldsymbol{n}}_{\boldsymbol{3}} \tag{2.17}$$

where $\hat{\boldsymbol{n}}_{\boldsymbol{1}},\ \hat{\boldsymbol{n}}_{\boldsymbol{2}},\ \hat{\boldsymbol{n}}_{\boldsymbol{3}}$ are three linearly independent vectors (not necessarily orthogonal). Thus

$$\nabla u_i \,.\, \boldsymbol{S_f} = \alpha_1 \nabla u_i \,.\, \hat{\boldsymbol{n}}_{\boldsymbol{1}} + \alpha_2 \nabla u_i \,.\, \hat{\boldsymbol{n}}_{\boldsymbol{2}} + \alpha_3 \nabla u_i \,.\, \hat{\boldsymbol{n}}_{\boldsymbol{3}}$$

If $\Delta x_1,\ \Delta x_2$ and Δx_3 are three line segments in the three directions mentioned in Eq. 2.17 and $\Delta u_{i1},\ \Delta u_{i2}$ and Δu_{i3} are differential change in u_i along them, then

$$\Delta u_{i1} = \nabla u_i \,.\, \hat{\boldsymbol{n}}_{\boldsymbol{1}} \Delta x_1,\ \Delta u_{i2} = \nabla u_i \,.\, \hat{\boldsymbol{n}}_{\boldsymbol{2}} \Delta x_2,\ \Delta u_{i3} = \nabla u_i \,.\, \hat{\boldsymbol{n}}_{\boldsymbol{3}} \Delta x_3$$

Thus

$$(\nabla u_i \,.\, \boldsymbol{S})_f = \alpha_1 \frac{\Delta u_{i1}}{\Delta x_1} + \alpha_2 \frac{\Delta u_{i2}}{\Delta x_2} + \alpha_3 \frac{\Delta u_{i3}}{\Delta x_3}$$

Table 2.2: Calculation of surface areas and volume for a finite volume cell in Cartesian and cylindrical domains.

Surface area/ Volume	Cartesian	cylindrical
$\boldsymbol{S_e}$	$\Delta y \Delta z$	$(r+\Delta r)\Delta\phi\Delta z$
$\boldsymbol{S_w}$	$\Delta y \Delta z$	$r\Delta\phi\Delta z$
$\boldsymbol{S_n}$	$\Delta x \Delta z$	$0.5(r\Delta\phi+(r+\Delta r)\Delta\phi)\Delta r$
$\boldsymbol{S_s}$	$\Delta x \Delta z$	$0.5(r\Delta\phi+(r+\Delta r)\Delta\phi)\Delta r$
$\boldsymbol{S_t}$	$\Delta x \Delta y$	$\Delta r \Delta z$
$\boldsymbol{S_b}$	$\Delta x \Delta y$	$\Delta r \Delta z$
V_P	$\Delta x \Delta y \Delta z$	$0.5(r\Delta\phi+(r+\Delta r)\Delta\phi)\Delta r\Delta z$

If $\hat{\boldsymbol{n}}_1,\ \hat{\boldsymbol{n}}_2,\ \hat{\boldsymbol{n}}_3$ have the components $(\hat{n}_{11},\hat{n}_{12},\hat{n}_{13}),\ (\hat{n}_{21},\hat{n}_{22},\hat{n}_{23})$ and $(\hat{n}_{31},\hat{n}_{32},\hat{n}_{33})$, respectively, then Eq. 2.17 can be written in matrix form

$$\begin{bmatrix} \hat{n}_{11} & \hat{n}_{12} & \hat{n}_{13} \\ \hat{n}_{21} & \hat{n}_{22} & \hat{n}_{23} \\ \hat{n}_{31} & \hat{n}_{32} & \hat{n}_{33} \end{bmatrix}^T \begin{Bmatrix} \alpha_1 \\ \alpha_2 \\ \alpha_3 \end{Bmatrix} = \begin{bmatrix} S_{f1} \\ S_{f2} \\ S_{f3} \end{bmatrix}$$

Using the above matrix equation $\alpha_1,\ \alpha_2,\ \alpha_3$ can be solved for each face of a finite volume. Note as $\hat{\boldsymbol{n}}_1,\ \hat{\boldsymbol{n}}_2,\ \hat{\boldsymbol{n}}_3$ are assumed to be linearly independent, the above matrix is always non-singular.

Calculation of surface area and volume

Next, we discuss the computation of the volume and surface areas of the control volume. Table 2.2 shows the calculation of the surface areas at six faces ($\boldsymbol{S_e}, \boldsymbol{S_w}, \boldsymbol{S_n}, \boldsymbol{S_s}, \boldsymbol{S_t}$ and $\boldsymbol{S_b}$) and volume (V_P) for a finite volume cell in both Cartesian and cylindrical domains. Here $\Delta x, \Delta y$, and Δz are the elemental length in x, y, and z directions, respectively, for Cartesian domain, as shown in Fig. 2.2. Similarly, $\Delta r, r\Delta\phi$ [or $(r+\Delta r)\Delta\phi$], and Δz are respectively the elemental length in r, ϕ, and z directions, in cylindrical domain.

Discretized equations

The governing equations are solved using a cell-centered finite volume method with the variables defined in a non-staggered fashion. Using the finite volume approximations discussed

above, the continuity equation, i^{th} momentum equation and the energy equation can be written in discrete form as

$$\sum_f F_f^{n+1} = 0 \tag{2.18}$$

$$\frac{u_{i,P}^{n+1} - u_{i,P}^{n}}{\Delta t} V_P + (\frac{3}{2}\sum_f F_f^n u_{i,f}^n - \frac{1}{2}\sum_f F_f^{n-1} u_{i,f}^{n-1}) = -\frac{1}{2}\sum_f \left(p_f^{n+1} + p_f^n\right) S_{f,i}$$
$$+\frac{1}{2}\sqrt{\frac{Pr}{Ra}}(\sum_f F_{df u_i}^{n+1} + \sum_f F_{df u_i}^{n}) + \frac{1}{2}(\theta_P^{n+1} + \theta_P^n)V_P - \frac{1}{2Ro}(3\varepsilon_{ijk} n_j u_k^n - \varepsilon_{ijk} n_j u_k^{n-1})_P V_P \tag{2.19}$$

$$\frac{\theta_P^{n+1} - \theta_P^n}{\Delta t} V_P + (\frac{3}{2}\sum_f F_f^n \theta_f^n - \frac{1}{2}\sum_f F_f^{n-1}\theta_f^{n-1}) = \frac{1}{2\sqrt{RaPr}}(\sum_f F_{df\theta}^{n+1} + \sum_f F_{df\theta}^{n}) \tag{2.20}$$

Note that the convective term is discretized using 2^{nd}-order Adams Bashforth scheme, while the diffusive, pressure, and buoyancy terms are handled by implicit 2^{nd}-order Crank-Nicolson scheme to retain the stability and robustness of the time marching procedure. The extra source term arising due to the Coriolis force is approximated by the Adams Bashforth scheme. However, the buoyancy term in the momentum equation is handled implicitly as the temperature field can be obtained by solving the energy equation at the beginning of a time step. Now that we have obtained the fully discretized form of the governing equations, we move on to the solution algorithm.

2.1.3 Solution algorithm and predictor corrector method

The solution algorithm is based on a predictor-corrector method [145]. Since the latest pressure p^{n+1} associated with the velocity field u_i^{n+1} is unknown, Eq. 2.19 cannot be solved directly. In the predictor-corrector method, first, a provisional velocity field u_i^* is predicted without accounting for the pressure term. The pressure field is later calculated by invoking momentum interpolation in the mass balance equation, which is then used to refine the initially approximated velocity field. As the pressure field at the $(n+1)^{th}$ time level is not known, the provisional

velocities are calculated excluding pressure term as given below

$$\frac{u^*_{i,P} - u^n_{i,P}}{\Delta t} V_P + (\frac{3}{2}\sum_f F^n_f u^n_{i,f} - \frac{1}{2}\sum_f F^{n-1}_f u^{n-1}_{i,f}) = \frac{1}{2}\sqrt{\frac{Pr}{Ra}}(\sum_f F^*_{dfi} + \sum_f F^n_{dfi}) + \frac{1}{2}(\theta^{n+1}_P + \theta^n_P)V_P - \frac{1}{2Ro}(3\varepsilon_{ijk} n_j u^n_k - \varepsilon_{ijk} n_j u^{n-1}_k)_P V_P \tag{2.21}$$

The face velocities are then estimated by enforcing the pressure gradient on to the linearly interpolated face values from the provisional velocities ($\boldsymbol{u}^*_f$) [142]. This is called momentum interpolation, which invokes a velocity-pressure coupling. This is essential as collocated formulations lead to velocity-pressure decoupling since both the variables (pressure and velocity) are defined at the same point. The face velocities are estimated as

$$\boldsymbol{u_f} = \boldsymbol{u}^*_f - \Delta t(\nabla p)_f. \tag{2.22}$$

The face velocities are then used to calculate the mass flux, which when inserted into the mass balance equation, gives the pressure Poisson equation. Thus, the mass flux is given by

$$F_f = \rho \boldsymbol{u_f} \cdot \boldsymbol{S_f} = \rho \boldsymbol{u^*_f} \cdot \boldsymbol{S_f} - \Delta t(\nabla p)_f \cdot \boldsymbol{S_f} = F^*_f - \Delta t(\nabla p)_f \cdot \boldsymbol{S_f}, \tag{2.23}$$

where

$$F^*_f = \rho \boldsymbol{u^*_f} \cdot \boldsymbol{S_f}. \tag{2.24}$$

Now, if Eq. 2.23 is inserted into the mass balance expression, Eq. 2.18, the following equation for the pressure is obtained

$$\sum_f F^{n+1}_f = \sum_f F^*_f - \Delta t \sum_f (\nabla p)_f \,.\, \boldsymbol{S_f} = 0 \implies \sum_f (\nabla p)_f \,.\, \boldsymbol{S_f} = \frac{1}{\Delta t}\sum_f F^*_f \tag{2.25}$$

Equation 2.25 is the counterpart of the Poisson equation for pressure-correction in SIMPLE-like formulation. It should be noted here that solution of Eq. 2.25 takes the center stage of this entire algorithm as the resulting matrix usually is a poorly conditioned one. The converged pressure field obtained from Eq. 2.25 is used in Eq. 2.23 to calculate new estimate of mass flux. The converged mass flux along with the pressure field that estimates it correspond to the divergence-free velocity field. These quantities are then used to solve Eq. 2.19 for the desired

velocity field u_i^{n+1}.

The solution algorithm for solving the finite volume approximated, 3-D unsteady governing equations using the predictor-corrector method is explained below. Before initializing the computations, the grid is generated, the flow domain is decomposed for parallelization and the geometric parameters are calculated.

- 1. Initialize the variables and prescribe boundary conditions. Start with u, v, w, p, θ (at n^{th} time level) and the mass flux F_f^n and F_f^{n-1}.
- 2. Solve the energy equation (Eq. 2.20) and get the temperature filed θ^{n+1}, so that it can be treated implicitly in the momentum equation.
- 3. Using θ^{n+1} and u^n, v^n, w^n, θ^n, find the provisional velocity field $u_{i,P}^*$ using Eq. 2.21.
- 4. Compute the Flux F_f^* from this provisional velocities using Eq. 2.24.
- 5. With the available provisional flux F_f^*, solve the pressure Poisson equation Eq. 2.25 for p^{n+1}.
- 6. Estimate the new mass flux F_f from Eq. 2.23
- 7. Using p^{n+1} and F_f, solve the Eq. 2.19 to obtain the corrected velocities $u_{i,P}^{n+1}$.
- 8. Set $n = n + 1$ and repeat the steps 2-7 for the next time step and thus time march.

2.2 Linear solver

As a result of the finite volume numerical approximation of the governing equations and boundary conditions, they are reduced to a set of simultaneous algebraic equations. A general form of these equations is

$$a_S\phi_S + a_B\phi_B + a_W\phi_W + a_P\phi_P + a_E\phi_E + a_T\phi_T + a_N\phi_N = b_P, \tag{2.26}$$

where a_P is the coefficient at point P, shown in Fig. 2.2 and $a_S, a_B, a_W, a_E, a_T, a_N$ correspond to coefficients of the neighbouring south, bottom, west, east, top, and north cells, respectively (also see Fig. 2.4). These are to be solved at each and every grid point within the computational domain, resulting in a system of algebraic equations.

$$A\boldsymbol{\phi} = \boldsymbol{b}, \tag{2.27}$$

where A is the coefficient matrix, $\boldsymbol{\phi}$ is the column of unknown vectors, and $\boldsymbol{b}$ the column of known vectors. The matrix A is sparse and banded due to the local nature of the approximations. For the sparse system considered here, A has seven diagonals, i.e., six from its immediate neighbours and one from itself. In a generic form, any iterative scheme can be written as

$$M\boldsymbol{\phi}^{l+1} = N\boldsymbol{\phi}^{l} + \boldsymbol{b}, \tag{2.28}$$

where M and N are iteration matrices, and l is the iteration count. Since at the convergence, $\boldsymbol{\phi}^{l+1} \longrightarrow \boldsymbol{\phi}^{l} \longrightarrow \boldsymbol{\phi}$ the above equation yields

$$M\boldsymbol{\phi} = N\boldsymbol{\phi} + \boldsymbol{b} \Longrightarrow (M - N)\boldsymbol{\phi} = \boldsymbol{b} \tag{2.29}$$

Thus, for consistency of Eqs. 2.27 and 2.29, $A = M - N$, which is the relation between the original coefficient matrix and the iteration matrices. The Eq. 2.28 can be cast into the residual form by subtracting $M\boldsymbol{\phi}^{l}$ from both the sides as

$$M\boldsymbol{\phi}^{l+1} - M\boldsymbol{\phi}^{l} = \boldsymbol{b} - (M - N)\boldsymbol{\phi}^{l} \Longrightarrow M(\boldsymbol{\phi}^{l+1} - \boldsymbol{\phi}^{l}) = \boldsymbol{b} - A\boldsymbol{\phi}^{l} \Longrightarrow M\boldsymbol{\delta}^{l+1} = \boldsymbol{\rho}^{l}$$

where $\boldsymbol{\delta}^{l+1} = \boldsymbol{\phi}^{l+1} - \boldsymbol{\phi}^{l}$ is an update in $\boldsymbol{\phi}$ at $(l+1)$ iteration level and $\boldsymbol{\rho}^{l} = \boldsymbol{b} - A\boldsymbol{\phi}^{l}$ is the residual after l iterations. Note $\boldsymbol{\phi}^{l+1}$ can be found by first solving $\boldsymbol{\delta}^{l+1} = M^{-1}\boldsymbol{\rho}^{l}$ followed by the update $\boldsymbol{\phi}^{l+1} = \boldsymbol{\phi}^{l} + \boldsymbol{\delta}^{l+1}$. Clearly, the choice of M is driven by this step, and a suitable form of M is required for a cheap inversion. Moreover, as M approaches A, Eqs. 2.27 and 2.28 become equivalent and expectedly less efforts go in iterations. Thus, the choice of M should be such that it is easily invertible and is close to A.

One of the better ways of splitting A is the LU factorization. However, complete or direct

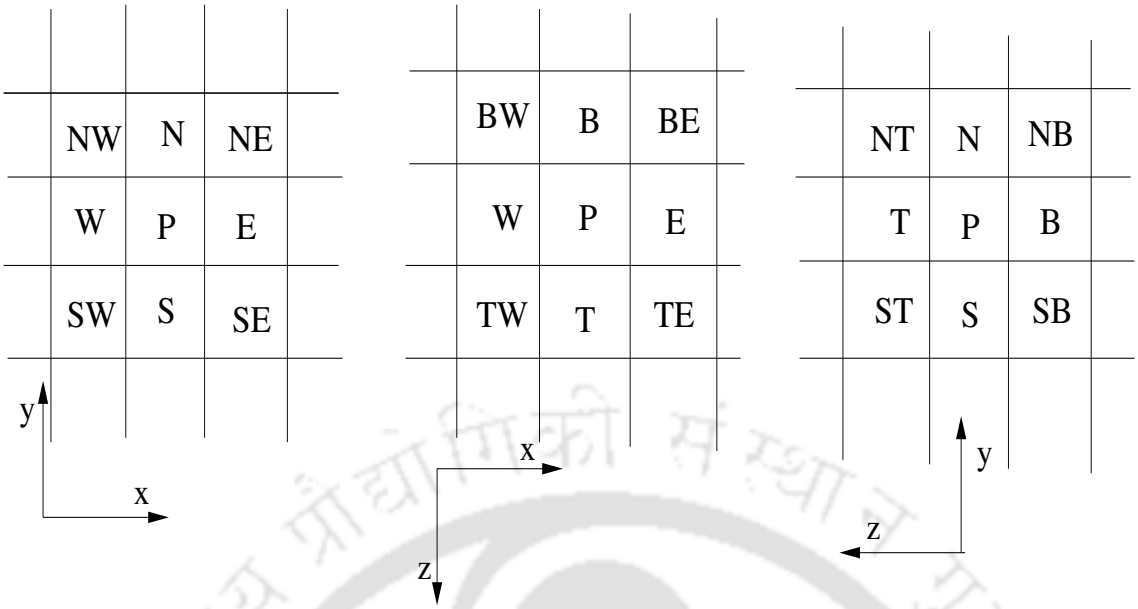

Figure 2.4: Planar view of the finite volume cells and their neighbours.

factorization has two main drawbacks. Firstly, the level of additional calculations can be quite high if the size of A is large. In addition to this, though A is sparse, one can not ensure the same for L and U. This spoils the basic structure of A, which should be exploited for a faster technique. In view of this, L and U are actually chosen form A though subsequent multiplication LU does not give back A, and this is the reason this class of methods are known as **incomplete LU factorization**, in short, **ILU** [146].

Stone's strongly implicit procedure [147] (SIP) is a variant of ILU factorization originally proposed for pentadiagonal sparse matrix obtained in two-dimensional Cartesian grid. For three-dimensional flows in Cartesian grids, numerical approximations result in algebraic equation with seven point stencil (refer to Eq. 2.26). In the SIP method, the original matrix is LU factorized. In doing so, the seven diagonal matrix can be factorized into the following L and U factors as

$$A = [\, L_P \;\; L_W \;\; L_S \;\; L_B] \, [\, I \;\; U_E \;\; U_T \;\; U_N]$$

The main diagonal of U is chosen as unity. L_P, L_W, L_S, L_B and U_E, U_T, U_N are non-zero diagonals of L and U. Thus the original system (Eq. 2.27) can be written as

$$[\, L_P \;\; L_W \;\; L_S \;\; L_B] \, [\, I \;\; U_E \;\; U_T \;\; U_N] \, \boldsymbol{\phi} = b.$$

Note that the L factors are always the diagonals corresponding to locations which is already traversed during the iteration sweep. Writing the above equation for node P,

$$[\, L_P \;\; L_W \;\; L_S \;\; L_B]\, [\phi_P \;\; U_E\phi_E \;\; U_T\phi_T \;\; U_N\phi_N] \;\; = \;\; b_P$$

On expansion it becomes,

$$\begin{aligned}
\Big(L_S\phi_S + \boxed{L_S U_{E_{j-1}}\phi_{SE}} + \boxed{L_S U_{T_{j-1}}\phi_{ST}} + L_S U_{N_{j-1}}\phi_P\Big) \;\; + \\
\Big(L_B\phi_B + \boxed{L_B U_{E_{k-1}}\phi_{BE}} + L_B U_{T_{k-1}}\phi_P + \boxed{L_B U_{N_{k-1}}\phi_{NB}}\Big) \;\; + \\
\Big(L_W\phi_W + L_W U_{E_{i-1}}\phi_P + \boxed{L_W U_{T_{i-1}}\phi_{TW}} + \boxed{L_W U_{N_{i-1}}\phi_{NW}}\Big) \;\; + \\
(L_P\phi_P + L_P U_E\phi_E + L_P U_T\phi_T + L_P U_N\phi_N) \;\; = \;\; b_p
\end{aligned} \tag{2.30}$$

Note that only the locations which differ from i, j or k are mentioned in Eq. 2.30, i.e., $U_{E_{i-1}} = U_{E_{i-1,j,k}}$ and $L_W = L_{W_{i,j,k}}$. It can be observed that the matrix obtained after multiplication is less sparse than the original matrix A. The extra terms arising from LU multiplication is highlighted in the above equation. As the iteration matrix M is factorized as $M = LU$, the diagonals of M can be written from Eq. 2.30 as

$$\begin{aligned}
&M_S = L_S, \;\; M_W = L_W, \;\; M_B = L_B, \;\; M_N = L_P U_N, \;\; M_T = L_P U_T, \;\; M_E = L_P U_E \\
&M_P = L_P + L_W U_{Ei-1} + L_S U_{Nj-1} + L_B U_{Tk-1} \\
&M_{NW} = L_W U_{Ni-1}, \;\; M_{SE} = L_S U_{Ej-1}, \;\; M_{TW} = L_W U_{Ti-1} \\
&M_{ST} = L_S U_{Tj-1}, \;\; M_{BE} = L_B U_{Ek-1}, \;\; M_{NB} = L_B U_{Nk-1}
\end{aligned} \tag{2.31}$$

As the iteration matrix M is given by $M = A + N$, the diagonals of M or the product LU have to be distributed keeping in mind N should be as small as possible for faster convergence. In the standard ILU decomposition, N carries only the extra diagonals (highlighted in Eq. 2.30). However, in the SIP method, N is assumed to have non-zero diagonals corresponding to the non-zero locations of M; i.e., in addition to extra diagonals of M (M_{NW}, M_{SE}, M_{TW}, M_{ST}, M_{BE} and M_{NB}), N also has non-zero diagonals N_S, N_W, N_B, N_P, N_T, N_E, N_N. Thus, in view of faster convergence

$$N\,\boldsymbol{\phi} \;\approx\; 0 \Longrightarrow N_S\phi_S + N_B\phi_B + N_W\phi_W + N_P\phi_P + N_E\phi_E + N_T\phi_T + N_N\phi_N +$$

$$M_{NW}\phi_{NW} + M_{SE}\phi_{SE} + M_{TW}\phi_{TW} + M_{ST}\phi_{ST} + M_{BE}\phi_{BE} + M_{NB}\phi_{NB} \approx 0, \quad (2.32)$$

which implies effect of extra diagonals is nullified by the non-zero diagonals of N. This can be written in the equivalent form as

$$\begin{aligned} &M_{NW}(\phi_{NW} - \phi^*_{NW}) + M_{SE}(\phi_{SE} - \phi^*_{SE}) + M_{TW}(\phi_{TW} - \phi^*_{TW}) + \\ &M_{ST}(\phi_{ST} - \phi^*_{ST}) + M_{BE}(\phi_{BE} - \phi^*_{BE}) + M_{NB}(\phi_{NB} - \phi^*_{NB}) \approx 0, \end{aligned} \quad (2.33)$$

where the ϕ^* quantities can be expressed implicitly in terms of neighbouring nodal values as

$$\begin{aligned} \phi^*_{NW} &\approx \alpha(\phi_N + \phi_W - \phi_P), \quad \phi^*_{SE} \approx \alpha(\phi_S + \phi_E - \phi_P), \\ \phi^*_{TW} &\approx \alpha(\phi_T + \phi_W - \phi_P), \quad \phi^*_{ST} \approx \alpha(\phi_S + \phi_T - \phi_P), \\ \phi^*_{BE} &\approx \alpha(\phi_B + \phi_E - \phi_P), \quad \phi^*_{NB} \approx \alpha(\phi_N + \phi_B - \phi_P), \end{aligned} \quad (2.34)$$

where α implicitly relates the nodal values to the locations corresponding to the extra diagonals of M. It has been seen from numerical exercises that $\alpha \approx 0.9$ gives the best convergence, though there is no universal value of it which ensures the best convergence for a range of grid structures having different aspect ratios. When the implicit relations of Eq. 2.34 are inserted in Eq. 2.33, the resulting equations is

$$\begin{aligned} &M_{NW}(\phi_{NW} - \alpha\phi_N - \alpha\phi_W + \alpha\phi_P) + M_{SE}(\phi_{SE} - \alpha\phi_S - \alpha\phi_E + \alpha\phi_P) + \\ &M_{TW}(\phi_{TW} - \alpha\phi_T - \alpha\phi_W + \alpha\phi_P) + M_{ST}(\phi_{ST} - \alpha\phi_S - \alpha\phi_T + \alpha\phi_P) + \\ &M_{BE}(\phi_{BE} - \alpha\phi_B - \alpha\phi_E + \alpha\phi_P) + M_{NB}(\phi_{NB} - \alpha\phi_N - \alpha\phi_B + \alpha\phi_P) \approx 0. \end{aligned} \quad (2.35)$$

Thus, by comparing Eqs. 2.32 and 2.35, the non-zero diagonals of N can be obtained as

$$\begin{aligned} N_S &= -\alpha(M_{ST} + M_{SE}) \\ N_B &= -\alpha(M_{BE} + M_{NB}) \\ N_W &= -\alpha(M_{NW} + M_{TW}) \\ N_P &= \alpha(M_{NW} + M_{ST} + M_{SE} + M_{BE} + M_{TW} + M_{NB}) \\ N_E &= -\alpha(M_{SE} + M_{BE}) \end{aligned} \quad (2.36)$$

$$N_T = -\alpha(M_{ST} + M_{TW})$$
$$N_N = -\alpha(M_{NW} + M_{NB})$$

The matrix relation $A + N = M$ can now be written in terms of their individual diagonals, taking diagonals of N and M from Eqs. 2.36 and 2.31, respectively

$$\begin{aligned}
&a_S - \alpha L_S U_{Tj-1} - \alpha L_S U_{Ej-1} = L_S \\
&a_B - \alpha L_B U_{Ek-1} - \alpha L_B U_{Nk-1} = L_B \\
&a_W - \alpha L_W U_{Ni-1} - \alpha L_W U_{Ti-1} = L_W \\
&a_P + \alpha L_W U_{Ni-1} + \alpha L_S U_{Tj-1} + \alpha L_S U_{Ej-1} + \alpha L_B U_{Ek-1} + \\
&\quad \alpha L_W U_{Ti-1} + \alpha L_B U_{Nk-1} = L_P + L_W U_{Ei-1} + L_S U_{Nj-1} + L_B U_{Tk-1} \\
&a_E - \alpha L_S U_{Ej-1} - \alpha L_B U_{Ek-1} = L_P U_E \\
&a_T - \alpha L_S U_{Tj-1} - \alpha L_W U_{Ti-1} = L_P U_T \\
&a_N - \alpha L_W U_{Ni-1} - \alpha L_B U_{Nk-1} = L_P U_N
\end{aligned} \tag{2.37}$$

By solving seven relations written in Eq. 2.37 for seven diagonals (L_S, L_B, L_W, L_P, U_E, U_T and U_N), they can be computed in the order given below

$$L_S = \frac{a_S}{1 + \alpha(U_{Tj-1} + U_{Ej-1})}$$
$$L_B = \frac{a_B}{1 + \alpha(U_{Ek-1} + U_{Nk-1})}$$
$$L_W = \frac{a_W}{1 + \alpha(U_{Ni-1} + U_{Ti-1})}$$
$$L_P = a_P + \alpha(L_W U_{Ni-1} + L_W U_{Ti-1} + L_S U_{Tj-1} + L_S U_{Ej-1} + L_B U_{Ek-1} + L_B U_{Nk-1})$$
$$-L_W U_{Ei-1} - L_S U_{Nj-1} - L_B U_{Tk-1}$$
$$U_E = \frac{a_E - \alpha(L_S U_{Ej-1} + L_B U_{Ek-1})}{L_P}$$
$$U_T = \frac{a_T - \alpha(L_S U_{Tj-1} + L_W U_{Ti-1})}{L_P}$$
$$U_N = \frac{a_N - \alpha(L_W U_{Ni-1} + L_B U_{Nk-1})}{L_P}$$

After obtaining the L and U factors the residual form, Eq. 2.30, can be solved in two steps

$$\begin{aligned} &\implies && M\boldsymbol{\delta}^{k+1} = \boldsymbol{\rho}^k \\ &\implies && LU\boldsymbol{\delta}^{k+1} = \boldsymbol{\rho}^k \\ &\implies && \text{step 1: forward substitution:} \quad L\boldsymbol{s} = \boldsymbol{\rho}^k \\ &\implies && \text{step 2: backward substitution:} \quad U\boldsymbol{\delta}^{k+1} = \boldsymbol{s} \end{aligned} \tag{2.38}$$

Pre-conditioned Bi-Conjugate Gradient Stabilized method

Pre-conditioning can be considered as any form of modification of the original linear system, which makes it easier to solve by a given iterative method [146]. During solution, either the coefficient matrix or the right-hand side vector can pick-up errors. A well-conditioned matrix is less affected by this accumulation of errors. Moreover, conditioning of a matrix refines its spectral radius in such a way that its eigen values improve the convergence behaviour. Pre-conditioning of the original matrix A is done by pre-multiplying the original linear system by an inverse of the pre-conditioning matrix (P^{-1}). Thus instead of solving the equation $A\boldsymbol{\phi} = \boldsymbol{b}$ we solve for $P^{-1}A\boldsymbol{\phi} = P^{-1}\boldsymbol{b}$. The resulting system may become easier to solve than the original system as $\overline{A}\boldsymbol{\phi} = \overline{\boldsymbol{b}}$. For better convergence, P should be easier to compute, and it should be a close approximation of A. If P is taken as the identity matrix I, it is easier to compute but the system remains same ($A\boldsymbol{\phi} = \boldsymbol{b}$). On the other hand, if P is considered as A, then solution is obtained in one shot as $\boldsymbol{\phi} = A^{-1}\boldsymbol{b}$ since $P^{-1}A = I$. However, computing A^{-1} is not trivial. Thus, we usually choose P between these two extreme choices, which facilitates a faster convergence without adding significant computations for P^{-1}.

Here BiCGSTAB algorithm proposed by Zhang [148] is used as the linear solver. As this technique does not ensure a monotonic convergence, use of pre-conditioners not only ensure more smother convergence behaviour, but also accelerate the convergence dramatically. We use SIP splitting to obtain the pre-conditioner. As M in the SIP method is constructed by splitting decomposition (LU), its inversion is cheap and thus can be used as a pre-conditioner, i.e., $P = M$. As a result, the preconditioned system is $M^{-1}A\boldsymbol{\phi} = M^{-1}\boldsymbol{b}$, i.e., $\overline{A}\boldsymbol{\phi} = \overline{\boldsymbol{b}}$. Thus, a matrix-vector multiplication $A\boldsymbol{x}$ should be replaced by $M^{-1}A\boldsymbol{x}$ which can be achieved as

$$\boldsymbol{x_1} = M^{-1}A\boldsymbol{x} \implies M\boldsymbol{x_1} = A\boldsymbol{x} \implies Ls = A\boldsymbol{x},\ U\boldsymbol{x_1} = s \text{ and finally } A\boldsymbol{x} = \boldsymbol{x_1}$$

The algorithm for the BiCGSTAB technique [148] is written below. The optional pre-conditioner steps are written in red colour.

1. Initialize: $\boldsymbol{\phi} = \boldsymbol{\phi_{in}}$, $\boldsymbol{r} = \boldsymbol{b} - A\boldsymbol{\phi_{in}}$, $Mr_1 = r$, $r = r_1$, $\boldsymbol{r_0} = \boldsymbol{r}$, ρ_0, α, ξ any large value, $k = 0$

2. Compute $M\boldsymbol{p_1} = A\boldsymbol{p}$, $A\boldsymbol{p} = \boldsymbol{p_1}$, $\boldsymbol{p} = \boldsymbol{r} + \beta(\boldsymbol{p} - \xi A\boldsymbol{p})$

3. $\alpha = \dfrac{||\boldsymbol{r} \cdot \boldsymbol{r_0}||}{||A\boldsymbol{p} \cdot \boldsymbol{r_0}||}$

4. Compute $\boldsymbol{z} = \boldsymbol{r} - \alpha A\boldsymbol{p}$

5. $M\boldsymbol{z_1} = A\boldsymbol{z}$, $A\boldsymbol{z} = \boldsymbol{z_1}$, $\xi = \dfrac{||A\boldsymbol{z} \cdot \boldsymbol{z}||}{||A\boldsymbol{z} \cdot A\boldsymbol{z}||}$

6. $\boldsymbol{\phi} = \boldsymbol{\phi} + \alpha\boldsymbol{p} + \xi\boldsymbol{z}$
   $\boldsymbol{r} = \boldsymbol{z} - \xi A\boldsymbol{z}$
   $\beta = \dfrac{\alpha||\boldsymbol{r_0} \cdot \boldsymbol{r}||}{\xi||\boldsymbol{r_0} \cdot \boldsymbol{r}||_{k-1}}$

7. If $||\boldsymbol{b} - A\boldsymbol{\phi}||_{l_2} < \epsilon$, exit;
   else, $k \longrightarrow k + 1$ and return to step 2 and continue.

2.3 Grid generation and parallelization

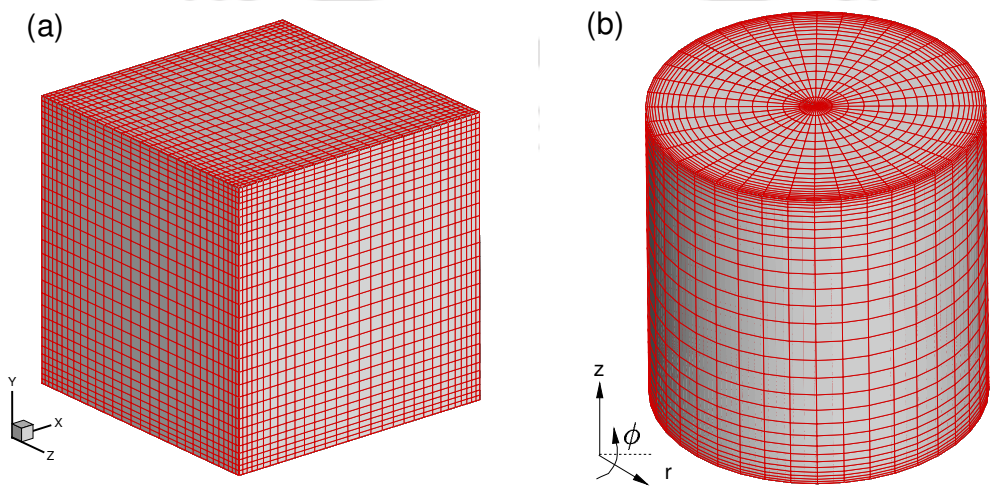

Figure 2.5: Sample grid for (a) Cartesian box and (b) cylindrical domain.

We use a structured and non-uniform grid with refinement near the walls. In the case of Cartesian box, the refinement is done in x, y, and z directions, i.e., near the top and bottom isothermal plates and near all the lateral walls. However, for the cylindrical domain, grid is refined in the radial and axial directions only. Here, the azimuthal direction is periodic (no wall appears along the azimuthal direction), and hence no refinement is required. We use an analytical function [149] for the generation of grid. Let x be the coordinate along a particular direction and L be the maximum length along the same, which is to be divided into different sizes, then

$$x_{i+1} = L\frac{(\beta+2\alpha)(\frac{\beta+1}{\beta-1})^{\frac{\eta-\alpha}{1-\alpha}} - \beta + 2\alpha}{(1+2\alpha)(1+(\frac{\beta+1}{\beta-1})^{\frac{\eta-\alpha}{1-\alpha}})}$$

provides the $(i+1)^{th}$ coordinate where $\eta = \dfrac{(i-1)}{(N_x-1)}$, α and β are the refinement parameters. Here i is the index and N_x represents the total number of grid points in x direction. β is always greater than 1 and the closer β is to 1, more refined the mesh is. α decides the region of refinement with $\alpha = 0$ gives refinement only near $x = L$ and $\alpha = 0.5$ gives refinement near both $x = 0$ and L. Figure 2.5 shows sample grid for Cartesian box and cylindrical cell. For Cartesian box, $\alpha = 0.5$ is used in all the directions as solid walls appear on both sides in each direction, as shown in Fig. 2.5(a). However, for cylindrical domain, we use $\alpha = 0.5$ in the vertical direction (z direction) and $\alpha = 0$ in the radial direction. Note that in the radial direction, the lateral wall appears only at $r = R$ [see Fig. 2.5(b)]. In the azimuthal direction, the mesh is taken as uniform.

In the case of cylindrical domain, a complexity arises at the center of the domain, i.e., $r = 0$. The grid converges towards the center of the cylinder, and there exists a point (vertical line in 3-D) of singularity. This region hence requires special attention while solving the algebraic equations. Figure 2.6(a) shows a schematic representation of the horizontal section of a cylindrical grid. A sample elemental grid cell at the center and a normal cell are also shown in Fig. 2.6 for reference. It is visible that the cells which are aligned along the center will have one face degenerated, which makes them one neighbour less. Thus, the algebraic equations must be modified accordingly. All the flux calculations for this face are trivial since the area is zero, and they are simply assigned zero. After obtaining a converged solution, the average value of the variables at the centroid of these cells in a horizontal plane is taken and assigned to the center point ($r = 0$) in that plane. This is essential in order to facilitate a smooth variation

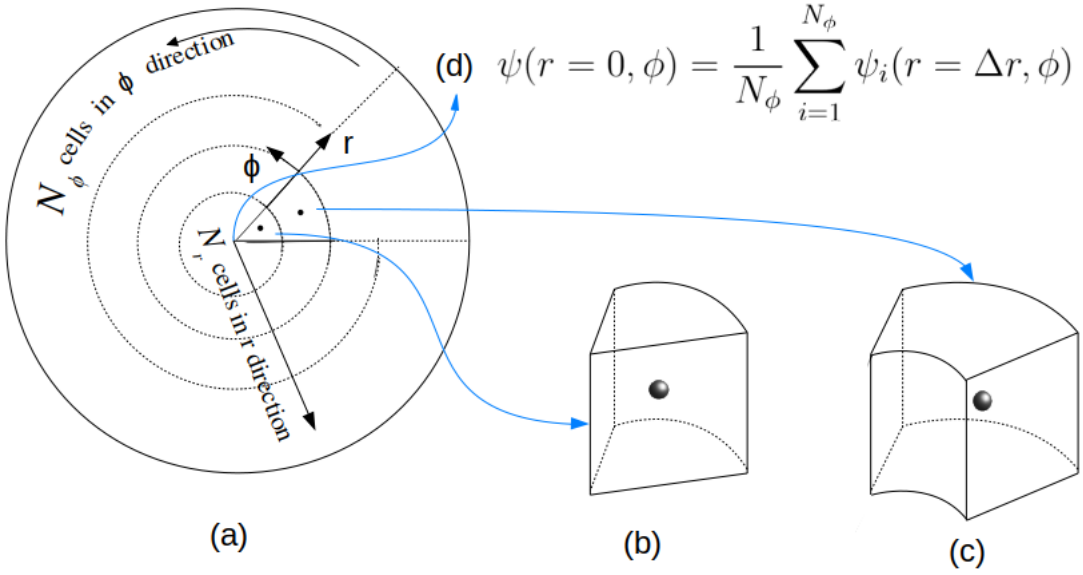

Figure 2.6: Graphical representation of (a) horizontal section of the grid in cylindrical domain, (b) degenerated cell at the center, and (c) a normal cell. (d) Computation of any variable ψ at $r = 0$.

of the variables without any discontinuity at the center owing to the singularity at the center. However, this value is never required in calculations. This procedure is depicted in Fig. 2.6, where ψ represents any variable (u_r, u_ϕ, u_z, p, or θ).

Parallelization

The numerical code is parallelized based on distributed memory allocation. The computational domain is decomposed into a number of sub-domains, and each of them is assigned to a processor. At the interfaces of these sub-domains, communication of solution variables is performed using Message Passing Interface (MPI) environment to synchronize computations among the processors. A sample grid distributed among 27 processors is shown in Fig. 2.7 for both the Cartesian box and cylindrical domain. Generally, processors are denoted as “rank," which starts from 0. In Fig. 2.7, note that the processors are distributed in the order of coordinate directions, i.e., x, y, z in Cartesian and r, ϕ, z in cylindrical coordinate systems. Here we have used three processors each in all three directions, and hence a total of 27 processors. All the processors are assigned equal number of computing cells, so that the load on each one of them is as identical as possible. Computations are performed in all processors simultaneously,

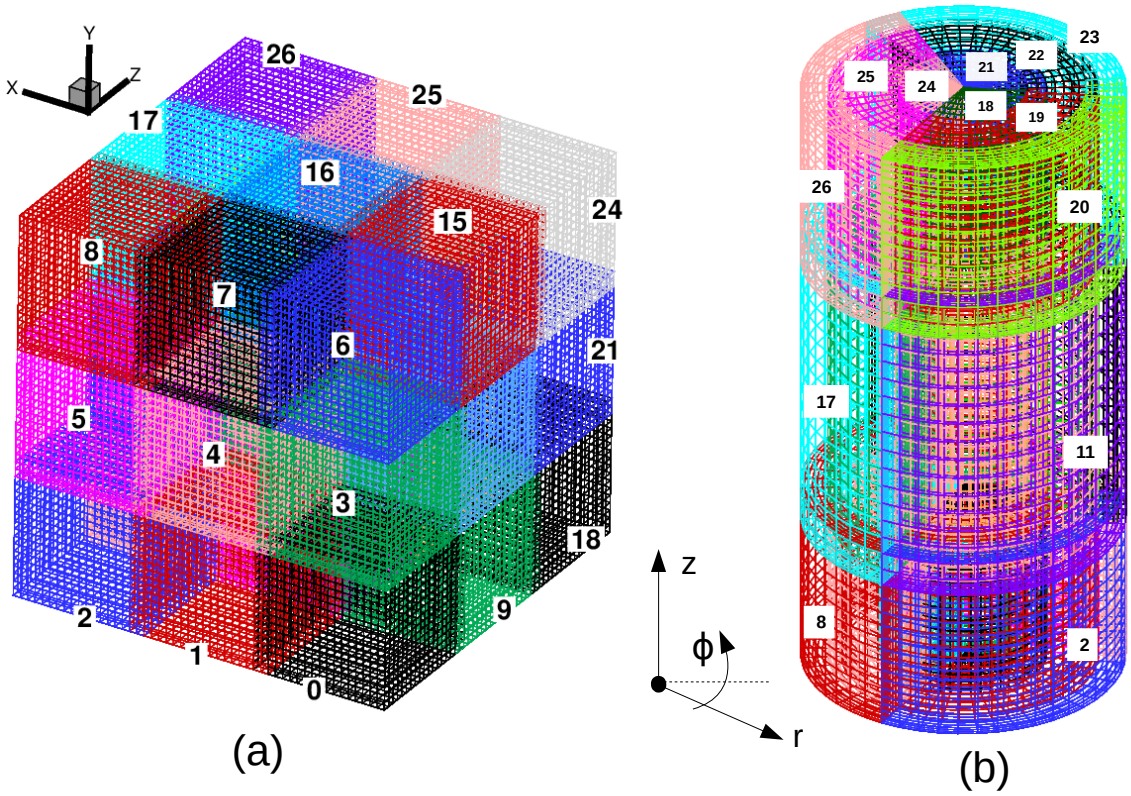

Figure 2.7: Sample grid decomposed into 27 sub-domains (3 in each direction) for (a) Cartesian box and (b) cylindrical domain. The processors are distributed in coordinate directions x, y, z (or r, ϕ, z).

and communications with other processors are carried out as per requirement. As each processor only deals with its own data and has no knowledge about its neighbours, communication is necessary along an interprocessor boundary. Suitable MPI libraries are used to facilitate this. In this work, the most demanding simulation has been the $Ra = 10^9$ case in Cartesian box which required nearly 134 million computing cells spread over 512 processors.

An important performance metric in parallelization is scalability (also referred to as the scaling efficiency). This measurement indicates how efficient an application is when using increasing numbers of parallel processing elements (CPUs / threads / processes/ cores / etc.). There are two basic ways to measure the parallel performance of a given application. These depend on whether or not the application is cpu-bound or memory-bound. The former method is generally called strong scaling, while the latter is weak scaling. In the present computations, we observe a scaling efficiency of about 75% and 55% based on strong and weak scalings, respectively.

2.4 Code validation and comparison with existing literature

The present numerical set-up has been validated with data from a number of existing literature. The comparisons are made in different flow situations such as (a) laminar and turbulent flow regimes, (b) rotating and non-rotating RBC, and (c) inside Cartesian box and cylindrical flow domains. For laminar flow situations, we primarily analyze the flow structures and average Nusselt number to evaluate the flow both qualitatively and quantitatively. In turbulent flows, in addition to the Nusselt number, statistical measures such as mean and root mean square (rms) of temperature and velocity are examined.

Table 2.3: Average Nusselt number at the hot wall for different Ra compared with Li *et al.* [41].

Ra (Initial condition)	Nu_S	Flow structure	Nu_S (Li *et al.*[41])	Error %
1800(0)	1.0	Conduction stage	1.0	0
3500(0)	1.32	Straight 2-roll Down	1.26	5
3500(c)	1.32	Straight 2-roll Up	1.26	5
10000(0)	2.35	Upward 2-roll	2.27	4
10000(c)	2.35	Downward 2-roll	2.27	4
15000(0)	2.67	Upward 2-roll	2.6	3
15000(c)	2.67	Downward 2-roll	2.6	3
20000(0)	2.97	Upward 2-roll	2.86	4
20000(c)	2.97	Downward 2=roll	2.86	4
45000(0)	3.2	4-spot kind	3.36	5

For validating non-rotating RBC at low Rayleigh numbers, simulations have been carried out for $1.8 \times 10^3 \leq Ra \leq 4.5 \times 10^5$ and $Pr = 7$ inside a cylindrical cell of aspect ratio $\Gamma = 2$ and the results are compared with those obtained by Li *et al.* [41]. A non-uniform grid of $40 \times 120 \times 40$ (which was used by Li *et al.* [41]) with near-wall refinement has been used with dimensionless time-step varying from 10^{-3} to 10^{-4}. Note that here we have used the diffusion scale α/H as the scale for normalizing velocity. We observe that the critical Rayleigh number for the onset of convection ($Ra_c \approx 1.8 \times 10^3$) is in good agreement with previous studies [35, 36, 41]. Further, different flow states are identified based on different initial conditions. Figure 2.8 shows the vertical velocity at the horizontal mid-plane along with the temperature iso-surfaces obtained for different Ra, compared with those obtained by Li *et al.* [41]. For $Ra = 3.5 \times 10^3$, we obtain the so-called straight two-roll patterns (both upward and downward), as shown in Figs. 2.8(a)- 2.8(d). In addition, the downward two-roll

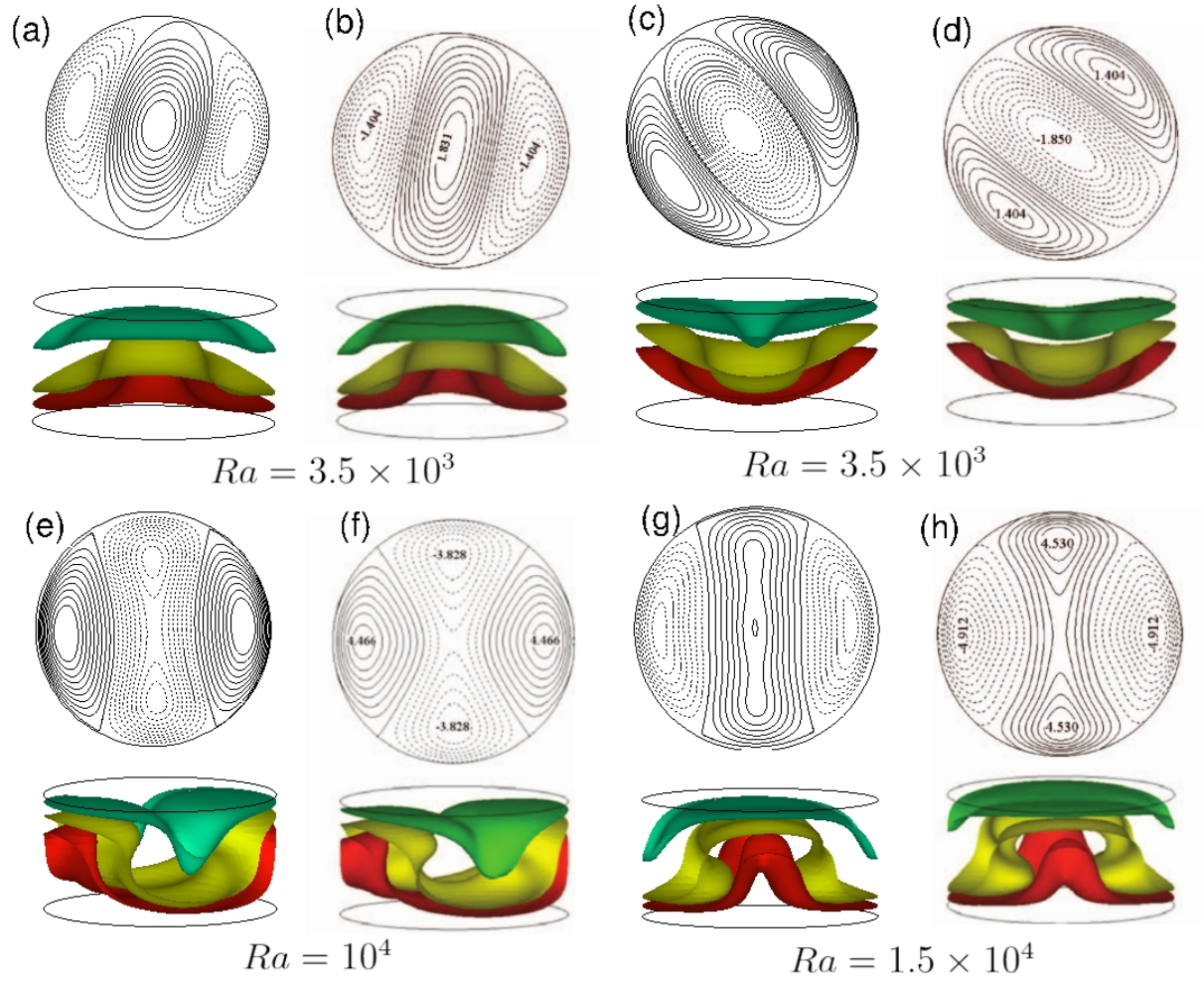

Figure 2.8: Flow patterns at different Rayleigh numbers compared with the numerical study by Li *et al.* [41]. Upper plots show the vertical velocity at horizontal mid plane, where solid and dashed lines indicate positive and negative values, respectively. Lower plots show the temperature iso-surfaces at θ = -0.3 (green) , 0 (yellow), +0.2 (red). Flow Patterns observed in the present study are shown in frames (a,c,e,g), while those obtained by Li *et al.* [41] are shown at the right hand side, i.e., frames (b,d,f,h). The frames correspond to (a,b) $Ra = 3.5 \times 10^3$ (straight two-roll downwards), (c,d) $Ra = 3.5 \times 10^3$ (straight two-roll upwards), (e,f) $Ra = 10^4$ (downward two-roll), and (g,h) $Ra = 1.5 \times 10^4$ (upward two-roll).

and upward two-roll patterns are obtained for $Ra = 10^4$ and $Ra = 1.5 \times 10^4$, respectively. It is apparent that the flow structures are in good agreement with those obtained by Li *et al.* [41]. Further, for quantitative validation of the numerical code, the average Nusselt number at the bottom wall is computed and compared with Li *et al.* [41], as shown in Table 2.3. The associated flow structure and the initial conditions used are also shown in Table 2.3, where 0 indicates zero initial value for all the variables, while c represents a static conductive stage (converged solution from $Ra = 1800$). The results are observed to close to the ones reported

in the literature.

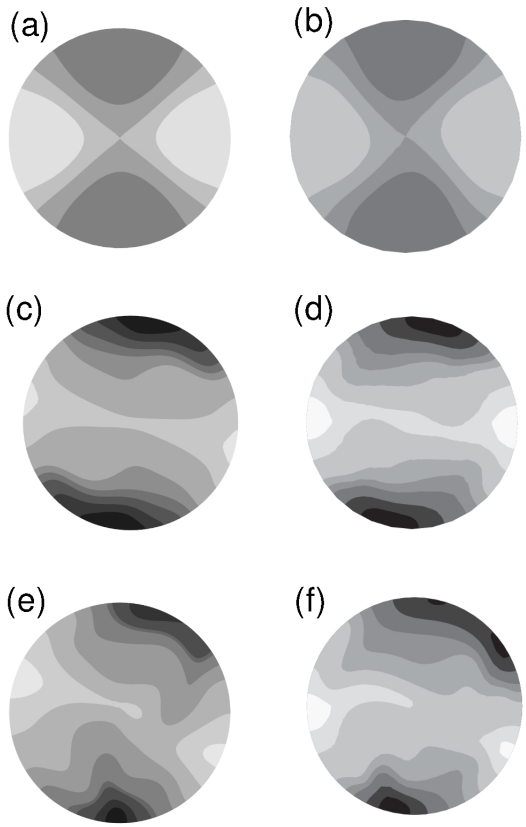

Figure 2.9: Mid-plane temperature deviation θ' for different Rayleigh numbers. Dark (light) regions indicate $\theta' < 0$ ($\theta' > 0$) representing cold descending (warm ascending) fluid. The patterns on the left and right represent those obtained in the present study and by R$\ddot{u}$diger and Knobloch [150], respectively, for (a,b) $Ra = 3.6 \times 10^3$, (c,d) $Ra = 3 \times 10^4$, and (e,f) $Ra = 5 \times 10^4$.

For validating RRBC at low Rayleigh numbers, simulations are performed in a cylindrical container ($\Gamma = 0.5$) at $Pr = 6.80$ and $Ro = 0.00245$ for a Rayleigh number range $3.6 \times 10^3 \leq Ra \leq 5.2 \times 10^4$ and the results are compared with the DNS study by R$\ddot{u}$diger and Knobloch [150]. Figure 2.9 shows the mid-plane temperature deviation θ' ($= \theta - \theta_{con}$) for different Rayleigh numbers which are closest to the reported ones, where θ_{con} is the linear conduction temperature profile. Dark (light) regions indicate $\theta' < 0$ ($\theta' > 0$) representing cold descending (warm ascending) fluid. We observe that the flow patterns are in excellent agreement.

Next, we validate the heat transfer rate in RBC and RRBC by evaluating the Nusselt number at the bottom wall. The simulations are carried out for $Pr = 0.7$ in a cylinder of aspect ratio $\Gamma = 0.5$ for different Ra, and the results are compared with those obtained by Oresta *et al.*

[131]. The critical Rayleigh number for the onset of convection and unsteady regimes agree well in both the studies. We obtain a critical Rayleigh number near $Ra_c \approx 2.35 \times 10^4$, where the Nusselt number departs from unity. The flow remains steady up to $Ra = 2 \times 10^5$ and changes to periodic with further increase in Ra. The Comparison of average Nusselt number at the bottom wall (Nu_S) with Oresta *et al.* [131] is shown in Fig. 2.10(a). The results match well with the error less than 5% in every case. Rotating convection is also validated with the above study for $Ra = 9 \times 10^5$ at different rotation rates. Figure 2.10(b) shows the variation of Nu_S with rotation rate compared with Oresta *et al.* [131], which is again observed to be in good agreement.

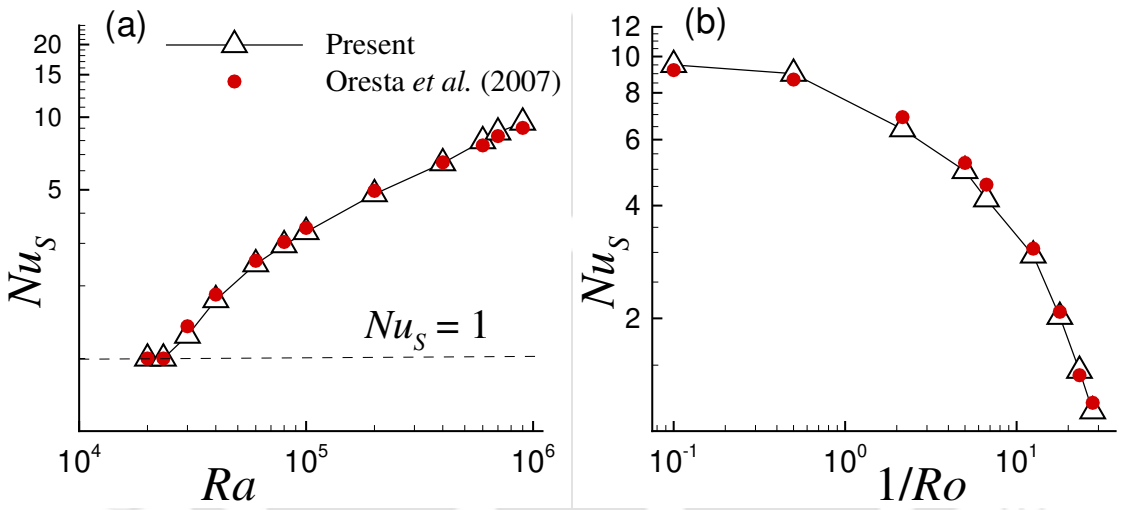

Figure 2.10: The variation of average Nusselt number at the bottom wall Nu_S with (a) Rayleigh number and (b) rotation rate expressed in $1/Ro$ at $Ra = 9 \times 10^5$, compared with Oresta *et al.* [131].

For turbulent convection inside a Cartesian box, we have carried out simulation for a wide range of Ra. To validate the numerical code, the Nusselt number is computed by three different methods: (a) using the mean heat flux at the horizontal surfaces ($Nu_S = \langle \partial\theta/\partial y \rangle_{A,t}$), (b) from the thermal dissipation rate ($Nu_{\epsilon_\theta} = (RaPr)^{1/2}\langle \epsilon_\theta \rangle$), and (c) from the viscous dissipation rate ($Nu_{\epsilon_u} = (RaPr)^{1/2}\langle \epsilon_u \rangle + 1$). Here $\langle .. \rangle$ denotes volume and time averaging, while $\langle .. \rangle_{A,t}$ represents horizontal surface and time averaging. The simulations are carried out inside a cubic cell with $Pr = 0.7$ and $5 \times 10^5 \leq Ra \leq 10^8$, and the results are compared with the most recently conducted DNS study [151]. Figure 2.11 shows the variation of Nusselt number computed using different methods with the Rayleigh number. Nusselt numbers computed using different methods are almost equal, suggesting the simulations are well resolved. It is apparent

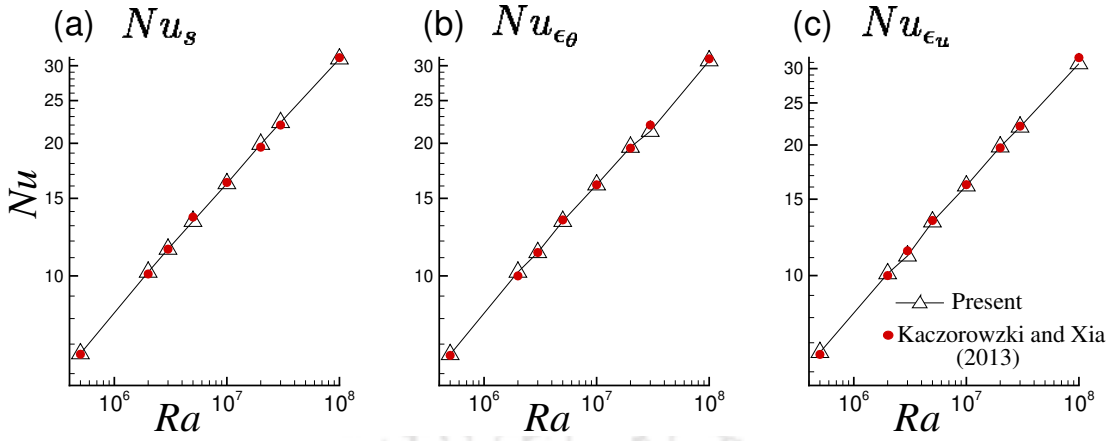

Figure 2.11: Variation of Nusselt number with Rayleigh number compared with the DNS by Kaczorowski and Xia [151]. (a) Surface averaged Nusselt number at the bottom plate Nu_S, (b) Nusselt number computed using the thermal dissipation rate Nu_{ϵ_θ}, and (c) Nusselt number computed using the viscous dissipation rate Nu_{ϵ_u}.

from Fig. 2.11 that the results are in excellent agreement with those reported by Kaczorowski and Xia [151]. Further, we observe a scaling relation of $Nu = 0.16Ra^{0.2857}$, which is also in excellent agreement with previous results [71, 151].

In addition to the flow structure and Nusselt number, we have also evaluated a few turbulent statistics such as mean and rms of velocity and temperature. Generally, the vertical variation of these statistical measures is used to analyze the characteristics in different regions of the flow domain. Here, we compare the mean and rms values of temperature and velocity with the numerical study by Kunnen *et al.* [124]. The simulations are performed at $Ra = 2.5 \times 10^6$ and $Pr = 1.0$ on a square domain with dimension $2 \times 2 \times 1$. We consider three cases, such as a non-rotating case ($Ro^{-1} = 0$), a low rotation rate ($Ro^{-1} = 0.75$) and at a moderate rotation rate ($Ro^{-1} = 3$). The computations have been carried out using a non-uniform mesh of grid size $128 \times 128 \times 64$ in x, y and z directions respectively. A dimensionless time step of 10^{-3} is used. Figure 2.12 shows the root-mean-square and mean profiles of temperature and velocity along the vertical direction. The rms of temperature is computed as $\theta_{rms} = \sqrt{\langle(\theta - \langle\theta\rangle_{A,t})^2\rangle_{A,t}}$. Similarly the rms of vertical ($v_{rms} = \sqrt{\langle v^2\rangle_{A,t}}$) and horizontal velocity ($u^H_{rms} = \sqrt{\langle u^2 + w^2\rangle_{A,t}}$) are also computed. We observe that with increasing rotation rate, the temperature gradient in the bulk region becomes more pronounced, as shown in Fig. 2.12(a). For the non-rotating case, there is hardly any temperature difference near the central region. Further, the vertical and horizontal velocity fluctuations reduce considerably with the

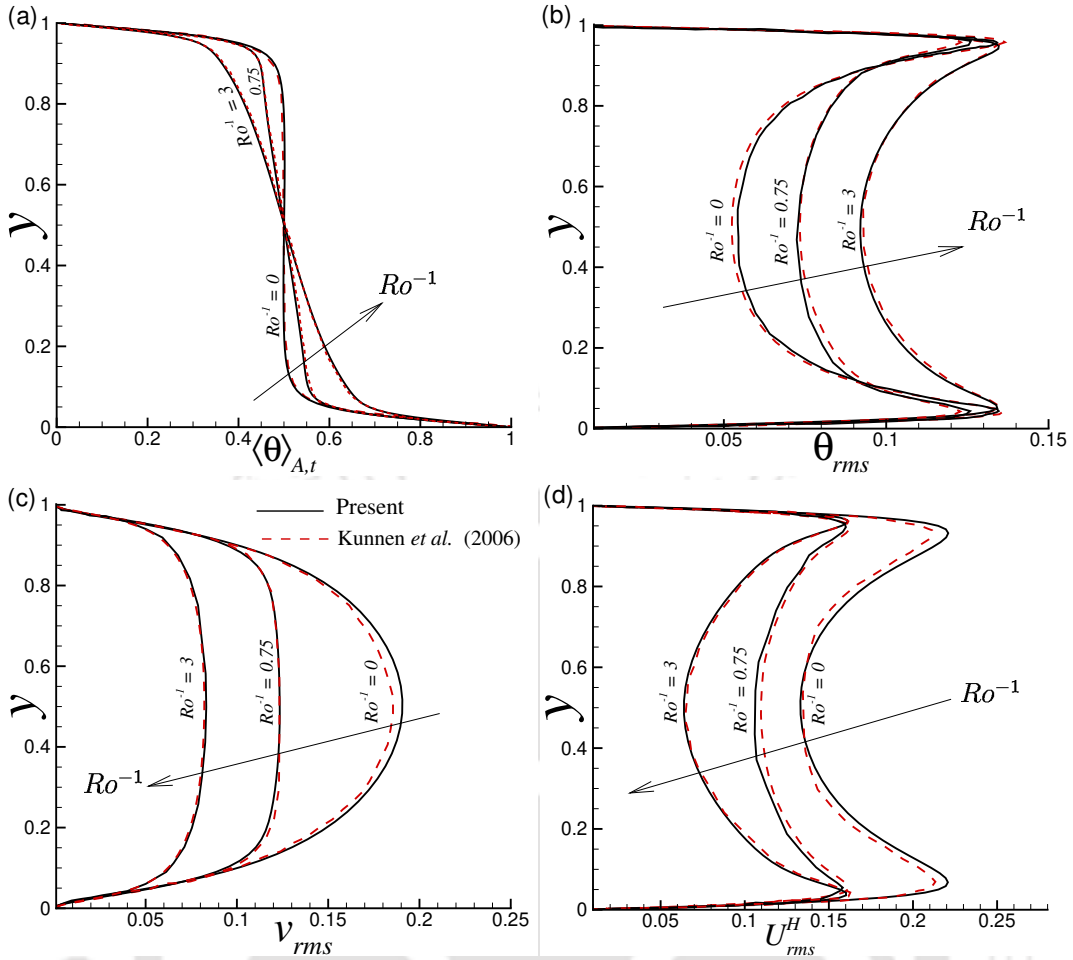

Figure 2.12: Variation of (a) mean temperature (b) rms of temperature (c) rms of vertical velocity and (d) rms of horizontal velocity along the vertical direction at different rotation rates compared with Kunnen *et al.* [124]. The arrow indicates the direction of increasing rotation rate. The solid black lines and red dashed lines represent the results obtained in the present study and those obtained by Kunnen *et al.* [124], respectively.

increase in rotation. However, the rms of temperature increases with rotation rate. It is evident that the results are in excellent agreement with those obtained by Kunnen *et al.* [124].

In the following chapters, we present the results of the thesis. First, we take up rotating turbulent convection inside a cylindrical container. In chapter 3, the flow structures and turbulent statistics are analysed, and different flow regimes are identified. This is followed by chapter 4, where a detailed investigation of LSC, its characteristics, dynamics and statistics is carried out. Then we study the effect of Prandtl number in RRBC in chapter 5. Finally, in chapters 6 and 7, the statistics and dynamics of turbulent convection inside cubic confinement are investigated, with a prime focus on thermal plumes and LSC.

3

Effect of rotation on turbulent Rayleigh-Bénard convection inside a cylindrical cell

In this chapter, the effect of rotation on turbulent Rayleigh-Bénard convection inside a cylindrical cell of unit aspect ratio is studied. Three-dimensional direct numerical simulations are performed at Rayleigh numbers 2×10^6 and 2×10^7, for a wide range of rotation rate ($0 \leq Ro^{-1} \leq 30$) with air ($Pr = 0.7$) as the working fluid. Using the Fourier mode analysis of time series data obtained from a number of probes placed in the azimuthal direction of the container at the mid-plane, different flow modes are identified, and these are used to quantify the flow regimes. At low rotation rates ($Ro^{-1} \lesssim 1$), a coherence at large scale is observed, resulting in a large-scale circulation. As the rotation rate increases, the fluctuations in the flow are damped out, and the observed coherence is lost. At even higher rotation rates ($Ro^{-1} \gtrsim 10$), wall-bounded flow structures, namely quadrupolar and sextupolar are obtained. In addition, the influence of rotation on the flow structures, heat transport, dissipation rates, and boundary layer dynamics are studied in detail. Overall, rotation has an effect of flow stabilization, and thus a reduction in heat transfer rate is observed.

3.1 Introduction

Rotation plays a crucial role in many natural flows and industrial applications. For a better understanding of these systems, it is necessary to investigate the influence of rotation on turbulent convection. Rotating Rayleigh-Bénard convection (RRBC) combines the effects of thermal

buoyancy and rotation-induced Coriolis and centrifugal forces. Heat transport and corresponding changes in the flow structure are some of the most studied aspects in turbulent convection. As discussed in chapter 1, the heat transfer rate in RBC depends on three control parameters, namely the Rayleigh number Ra, the Prandtl number Pr, and the aspect ratio Γ. In the case of rotating convection, the rotation rate also affects the heat transport. Generally, rotation has an inhibiting effect on heat transport. Since the experimental study by Rossby [115], it is understood that rotation (moderate rotation) can also enhance the heat transport in RRBC. Following this, several experimental [116–118] and numerical [18, 91, 116, 123–126] studies have been carried out in this direction. In contrast to an experimental set-up, the addition of rotation is rather straight forward in numerical simulations.

In RRBC, different flow regimes are characterized based on the behaviour of heat transfer rates. At low rotation rates, there exists a regime of no heat transfer increment where Nu remains same as the non-rotating case [134]. However, at moderate rotation rates ($Ro \approx 0.5$), heat transfer rate increases with rotation depending on Ra and Pr [134, 135]. Kunnen *et al.* [124] numerically studied RRBC for $Ra = 2.5 \times 10^6$ and $Pr = 1$ by varying the Rossby numbers ($0.33 < Ro < \infty$), and found that at low rotation rates, heat transfer increases with Nusselt number increasing up to 5%. In addition to this, Kunnen *et al.* [128, 129] performed numerical and experimental investigations on the flow structures in turbulent RRBC and identified different flow regimes. They observed that for low rotation rates ($Ro \geq 2$) flow behaviour is dominated by LSC. The azimuthal dynamics of LSC was found to be dependent on Ro. For $0.1 \leq Ro \leq 2$, LSC was replaced by vortical columns as dominant flow structure. For higher rotation rates ($Ro \leq 0.1$), the stabilizing effect of rotation was clearly observed. The statistics of turbulent intensities and root mean square fluctuations showed steeper dependence on Ro. Weiss and Ahlers [137] identified four regimes based on the Ro-dependence of Nu for $Pr = 4.38$ and a range of Rayleigh numbers $2.3 \times 10^9 \leq Ra \leq 7.2 \times 10^{10}$. In the first regime at low rotation rates, Nu remains constant or increases slowly (depending on Ra) with the increase in rotation. At $Ro \approx 2$, a second regime was observed where the increase in Nu was even slower (or decrease for higher Ra). A third regime was identified at $Ro \approx 1.18$, where Nu increases significantly with rotation as a result of Ekman vortices. This was followed by the fourth regime ($Ro \lesssim 0.33$), where Nu decreases with rotation rate due to the suppression of convective motion [134].

It is important to note that such classification of regimes based on the rotation rates is valid only for $Pr \gtrsim 1$. For low Prandtl numbers ($Pr \lesssim 1$), no enhancement in heat transport is observed at any rotation rate [138]. Horn and Shishkina [139] introduced an alternative method (which is independent of Γ and Pr) for the identification of the distinct flow regimes in RRBC, based on the decomposition of the velocity field into toroidal and poloidal parts. They identified different flow regimes such as buoyancy dominated, rotation influenced, rotation dominated, and geostrophic turbulence.

Though there are many existing studies in rotating convection, a profound identification of different flow regimes in RRBC is less attempted, particularly at low Prandtl numbers were the increase in heat transport with rotation is not observed. In this study, we attempt to identify different flow regimes based on the Fourier mode decomposition and evaluate the flow structures, heat transfer, dissipation rates, boundary layer dynamics and other turbulent statistics for a fluid with $Pr = 0.7$. Three-dimensional direct numerical simulations are performed at two different Rayleigh numbers, namely $Ra = 2 \times 10^6$ and 2×10^7 in a cylindrical cell. The cylindrical domain is rotated about its vertical axis. Rotation is quantified in terms of Rossby number ($Ro = V/2\Omega H$). As Ro is inversely proportional to Ω, Ro^{-1} directly measures the rotation rate. A wide rage of rotation rate is considered, starting from non-rotating case ($Ro^{-1} = 0$) to extremely high rotation rate ($Ro^{-1} \approx 30$).

The present chapter is organized as follows. The next section discusses the overall problem setup and the details of the computational grid. This is followed by a comprehensive analysis of the effect of rotation on turbulent RBC and identification of different flow regimes based on the flow structure and Fourier mode decomposition. Further, the characteristics of heat transport, dissipation rates, boundary layers, and other turbulent statistics are studied in subsequent sections.

3.2 Numerical details

In this section, we briefly describe the mathematical formulations of the problem followed by grid independence study. The problem deals with the investigation of thermo-convective instability of an incompressible Newtonian fluid inside a cylindrical cell of unit aspect ratio,

Table 3.1: Different grids with corresponding number of grid points within the thermal boundary layer N_{BL}, the critical grid parameters l_{max}/η_k, $\Delta z_{max}/\eta_k$, and Δ_{max}/η_k followed by volume averaged Nusselt number Nu_{vol}, Nusselt number at the bottom wall Nu_S and ratio of numerical to analytical dissipation rates, $\epsilon_u^r = \langle\epsilon_u^{num}\rangle/\langle\epsilon_u^{th}\rangle$ and $\epsilon_\theta^r = \langle\epsilon_\theta^{num}\rangle/\langle\epsilon_\theta^{th}\rangle$, at $Ra = 2 \times 10^6$ and 2×10^7 for non-rotating and high rotation case.

Ra	Ro^{-1}	$N_r \times N_\phi \times N_z$	N_{BL}	l_{max}/η_k	$\Delta z_{max}/\eta_k$	Δ_{max}/η_k	Nu_{vol}	Nu_S	ϵ_u^r	ϵ_θ^r
2×10^6	0	$43 \times 101 \times 85$	9	0.804	0.515	0.455	10.75	10.71	0.981	0.987
	10	$43 \times 101 \times 85$	13	0.715	0.457	0.404	3.68	3.69	0.978	0.990
2×10^6	0	$50 \times 101 \times 101$	11	0.804	0.432	0.409	10.68	10.66	0.990	0.983
	10	$50 \times 101 \times 101$	15	0.715	0.384	0.363	3.68	3.69	0.990	0.982
2×10^6	0	$60 \times 101 \times 115$	13	0.804	0.380	0.367	10.65	10.60	0.991	0.984
	10	$60 \times 101 \times 115$	19	0.715	0.338	0.326	3.67	3.68	0.985	0.984
2×10^7	0	$93 \times 175 \times 185$	12	0.968	0.492	0.492	20.47	20.42	0.978	0.986
	10	$93 \times 175 \times 185$	27	0.724	0.368	0.350	6.49	6.50	0.984	0.989
2×10^7	0	$101 \times 175 \times 201$	13	0.968	0.453	0.453	20.46	20.46	0.980	0.988
	10	$101 \times 175 \times 201$	30	0.724	0.339	0.331	6.37	6.38	0.986	0.992
2×10^7	0	$115 \times 175 \times 229$	15	0.968	0.391	0.391	20.42	20.39	0.982	0.988
	10	$115 \times 175 \times 229$	32	0.724	0.293	0.304	6.39	6.40	0.989	0.993

$\Gamma = D/H = 1$. A schematic diagram of the flow domain with relevant boundary conditions used is shown in Fig. 3.1(a). No-slip boundary conditions are implemented on all the surfaces. For temperature, horizontal surfaces are iso-thermal and the lateral wall is adiabatic. Rotation is applied about the vertical axis of the cylinder.

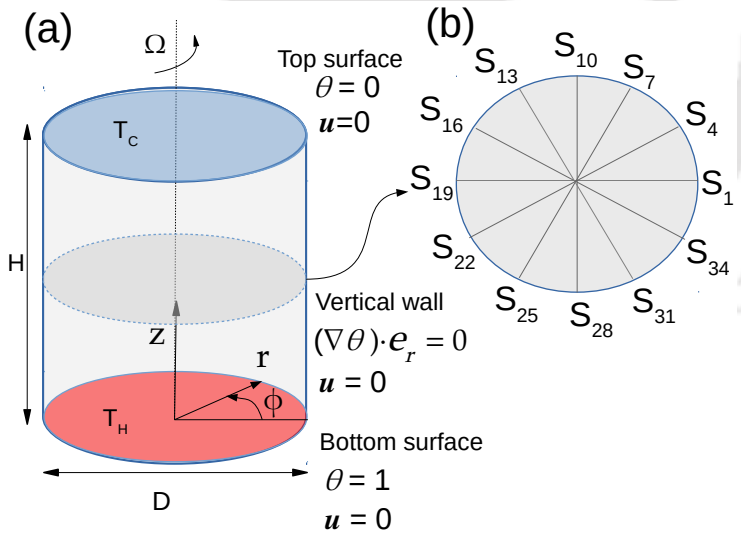

Figure 3.1: (a) Schematic diagram of the flow domain with relevant boundary conditions. (b) Schematic representation of the location of numerical probes at horizontal mid-plane of the cylinder used for signal analysis.

While reporting direct numerical simulations an important requirement is that the grid is resolved adequately to capture the flow physics correctly, and at the same time it consumes optimum computational resources. Two criteria are imposed for calculating the grid sizes.

Firstly, the boundary layers are properly resolved, for which we necessitate that at least 10 grid points are present within the boundary layers (both near horizontal and lateral walls). As a result $\Delta z_{min} \approx \delta_\theta/10$ and $\Delta z_{min} \approx \Delta r_{min}$. Here, δ_θ is the thermal boundary layer thickness, while Δz_{min} and Δr_{min} are the minimum grid size in the vertical and radial directions, respectively. Secondly, the mesh size is taken to be of the order less than or equal to the Kolmogorov scale (η_k). We implement the conditions $\Delta_{max} \lesssim \eta_k$, $l_{max}(= 2\pi r/N_\phi) \lesssim \eta_k$, $\Delta z_{max} < \eta_k$ and $\Delta r_{max} \approx \Delta z_{max}$, where l_{max}, Δr_{max}, and Δz_{max} represent the maximum grid size in the azimuthal, radial, and vertical directions, respectively. Here Δ_{max} indicates the maximum of mean grid size calculated as $(r\Delta\phi\Delta r\Delta z)^{1/3}$ and η_k is the Kolmogorov scale estimated using the analytical formula $\eta_k \approx \pi(Pr^2/RaNu)^{1/4}$ given by Grötzbach [152]. Table 3.1 shows the different computational grids with corresponding number of grid points within the boundary layer followed by the maximum grid size in the azimuthal and axial direction, and the maximum mean grid size, normalized with the Kolmogorov scale at Rayleigh numbers $Ra = 2 \times 10^6$ and 2×10^7 for non-rotating ($Ro^{-1} = 0$) and high rotation ($Ro^{-1} = 10$) case. Time increments of $\Delta t = 10^{-3}$ and 5×10^{-4} are used for $Ra = 2 \times 10^6$ and 2×10^7, respectively.

The Nusselt number at the bottom wall is computed as $Nu_S = \langle \partial\theta/\partial z \rangle_{A,t}$, where $\langle .. \rangle_{A,t}$ represents averaging over horizontal plane and time. Further, the volume averaged Nusselt number over the entire domain $Nu_{vol} = 1 + \sqrt{RaPr}\langle w\theta \rangle$ is also calculated, where $\langle .. \rangle$ denotes averaging over volume and time. Both values agree well and the difference between the Nu_{vol} (or Nu_S) values computed at the coarsest and finest grid for both Ra is less than 2%, which indicates a good grid convergence. To further confirm the spacial resolution, ratio of the numerical to the theoretical estimate of viscous ($\langle \epsilon_u^{num} \rangle / \langle \epsilon_u^{th} \rangle$) and thermal dissipation rates ($\langle \epsilon_\theta^{num} \rangle / \langle \epsilon_\theta^{th} \rangle$) are calculated for both non-rotating and sufficiently high rotation rate $Ro^{-1} = 10$. Here $\langle \epsilon_u^{num} \rangle = \nu V^2 H^{-2} \langle |\nabla \boldsymbol{u}|^2 \rangle$ and $\langle \epsilon_\theta^{num} \rangle = \alpha(\Delta T)^2 H^{-2} \langle |\nabla\theta|^2 \rangle$ are the numerically calculated values of viscous and thermal dissipation rates, respectively, while $\langle \epsilon_u^{th} \rangle = \nu^3(Nu-1)RaPr^{-2}H^{-4}$ and $\langle \epsilon_\theta^{th} \rangle = \alpha(\Delta T)^2 NuH^{-2}$ are their analytical counterparts [75]. Note that the theoretical estimates of the dissipation rates are functions of Nusselt number, for which we substitute the corresponding numerically obtained value [51, 153]. The ratios are always close to unity (minimum ≈ 0.978), suggesting that the present grid is well resolved to perform the proposed numerical calculations. Considering the computational cost and the accuracy of the above mentioned parameters, a grid size of $50 \times 101 \times 101$ and $101 \times 175 \times 201$

are chosen for $Ra = 2 \times 10^6$ and 2×10^7, respectively.

To study the temporal behaviour of the flow, time signals of velocity and temperature are recorded at different locations of the cell. Figure 3.1(b) shows a geometric construction of the locations of the numerical probes (shown only every third) that are used to record the field time signals. The signals are recorded from 36 equidistant locations (marked as probes S_1 to S_{36}) at the horizontal mid-plane ($z = 0.5H$) close to the lateral wall ($r = 0.4R$). These are used to identify different flow regimes and flow periodicity/reversals. In addition, the time traces are used to analyze large-scale circulation and its dynamics, which are to be taken up in the next chapter.

In the following sections, the results of the present work are discussed in detail. At the outset, we examine the flow topology in turbulent rotating RBC using a number of visualization methods, such as instantaneous contours, temperature iso-surfaces, and Q structures. Then different flow regimes are identified based on the rotation rates, using Fourier mode analysis of the time signals of vertical velocity. This is followed by a comprehensive analysis of heat transport, dissipation rates, and boundary layer dynamics in different flow regimes. In addition, planar statistics such as mean and variance of temperature and vertical velocity are evaluated to identify the flow characteristics in different regions of the flow.

3.3 Topology of the flow

In fluid dynamics, flow visualizations are used to make the flow patterns visible which helps construct the required qualitative or quantitative description. Generally, they provide necessary pieces of information about the whole flow field immediately understandable without the need for extensive data processing [154]. Flow visualizations in previous experimental and numerical studies have shown that in turbulent RBC, thermal plumes erupt from the top and bottom plates/boundary layers and traverse towards the opposite plate. Under certain parameter range, these plumes organize to form an LSC, where hot and cold fluid rises and falls, respectively, along opposite sides of the lateral wall [40, 61].

The instantaneous temperature iso-surfaces along with the vertical velocity (w or u_z) contours at horizontal mid-plane ($z = 0.5H$) at $Ra = 2 \times 10^6$ and 2×10^7 are shown in Figs. 3.2

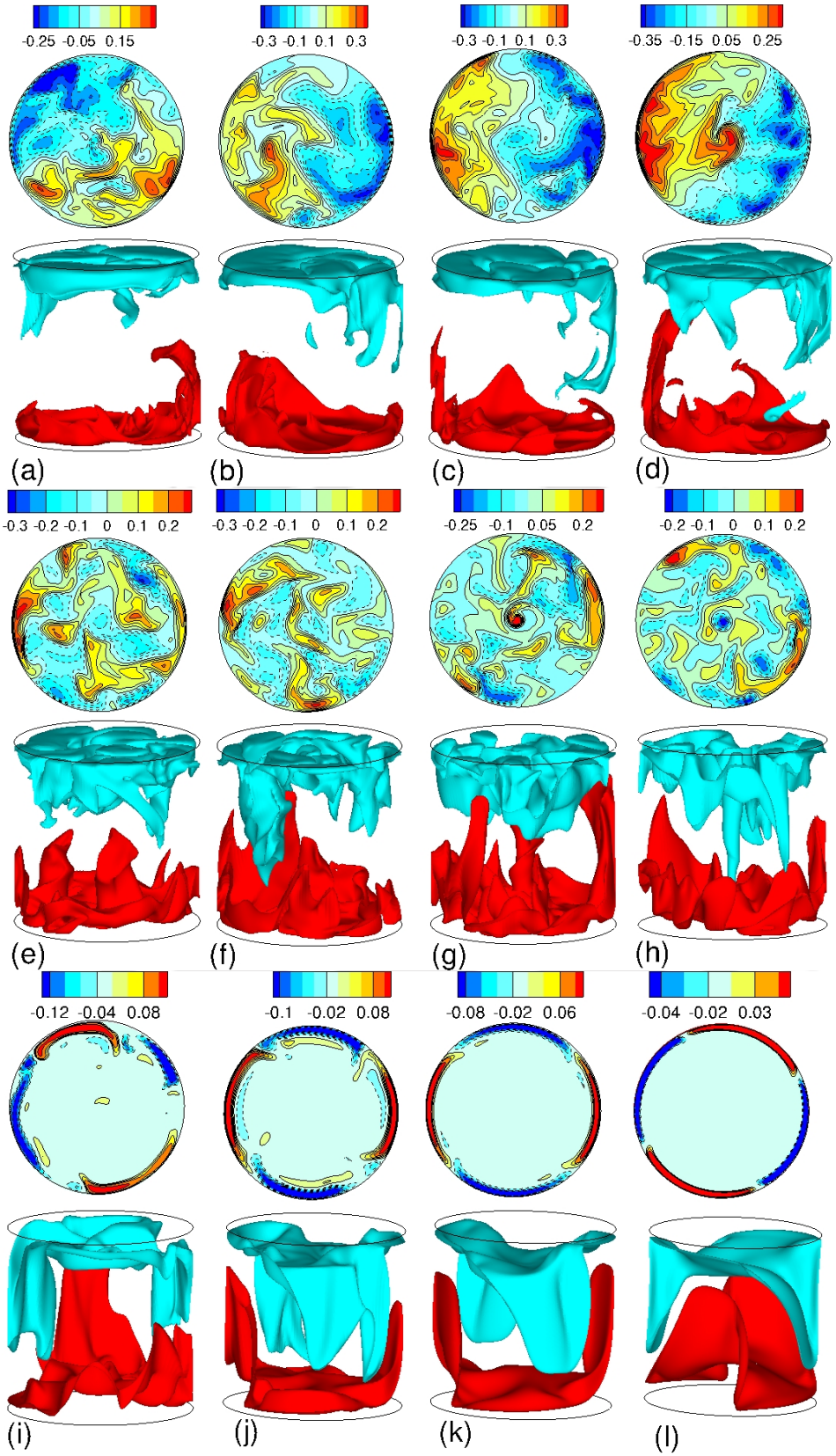

Figure 3.2: Flow structures for $Ra = 2 \times 10^7$ at (a) $Ro^{-1} = 0$, (b) $Ro^{-1} = 0.1$, (c) $Ro^{-1} = 0.2$, (d) $Ro^{-1} = 0.3$, (e) $Ro^{-1} = 2$, (f) $Ro^{-1} = 3$, (g) $Ro^{-1} = 4$, (h) $Ro^{-1} = 5.7$, (i) $Ro^{-1} = 10$, (j) $Ro^{-1} = 13.3$, (k) $Ro^{-1} = 20$ and (l) $Ro^{-1} = 30$. Top row: vertical velocity contour at the horizontal mid-plane ($z = 0.5H$). Bottom row: temperature iso-surfaces at $\theta = 0.35$ (blue) and $\theta = 0.65$ (red). For frames (a)-(d) : $\theta = 0.4$ (blue) and $\theta = 0.6$ (red).

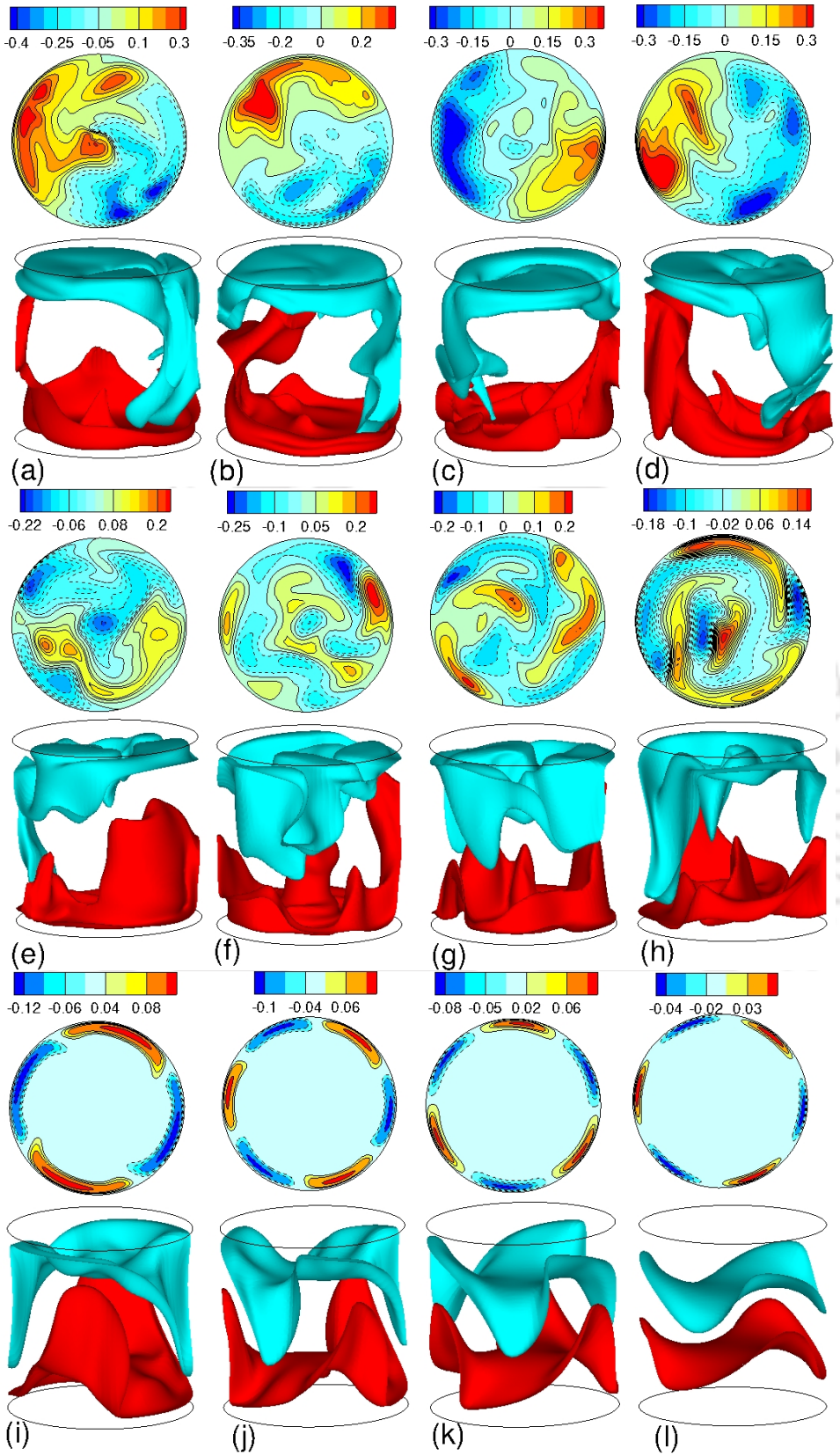

Figure 3.3: Flow structures for $Ra = 2 \times 10^6$ at (a) $Ro^{-1} = 0$, (b) $Ro^{-1} = 0.1$, (c) $Ro^{-1} = 0.2$, (d) $Ro^{-1} = 0.3$, (e) $Ro^{-1} = 2$, (f) $Ro^{-1} = 3$, (g) $Ro^{-1} = 4$, (h) $Ro^{-1} = 5.7$, (i) $Ro^{-1} = 10$, (j) $Ro^{-1} = 13.3$, (k) $Ro^{-1} = 20$ and (l) $Ro^{-1} = 30$. Top row: vertical velocity contour at the horizontal mid-plane ($z = 0.5H$). Bottom row: temperature iso-surfaces at $\theta = 0.35$ (blue) and $\theta = 0.65$ (red).

and 3.3, respectively, for different rotation rates. The iso-surfaces are drawn at $\theta = 0.35$ (blue) and 0.65 (red). At low rotation rates [frames (a)-(d)], the flow structures indicate the presence of LSC for both the Rayleigh numbers. The hot plumes erupt from the boundary layer and rise along the lateral wall, while the cold plumes sink along the opposite side. It is apparent from the vertical velocity contours that the hot and cold plumes are clustered around opposite sides of the sidewall, hence resulting in an approximate dipolar flow structure, a signature of LSC. Note that the up-flow ($+w$) and down-flow ($-w$) are clearly distinguished by the solid and dashed lines, respectively. As we increase the rotation rate, the coherence at large scale is lost and the large-scale flow structures are broken down to multiple small-scale structures, as shown in frames (e)-(h). Hence, at such intermediate rotation rates ($1 \lesssim Ro^{-1} \lesssim 10$), no specific organization of the flow is observed. Note that vertical velocity contours at the horizontal mid-plane show random fragmented plumes. Here hot and cold plumes appear without any particular organization.

It is apparent that up until now, thermal plumes appear all over the flow domain. The vertical velocity contours clearly show that convective flow scales almost the entire flow domain. However, at even higher rotation rates ($Ro^{-1} \gtrsim 10$), the plumes become localized and wall-bounded, as shown in frames (i)-(l). Here, vertical velocity contours indicate the presence of axial motion only near the walls. The stabilizing effect of rotation is evident at the higher rotation rate regime, as the bulk region becomes stabilized, and the convection rolls get organized and concentrated near the lateral walls. As the rotation rate is increased, the Coriolis force overshadows the buoyancy force. As a result, the buoyancy force becomes too small to sustain the convection rolls throughout the flow domain. The dominant Coriolis force pushes the convection rolls towards the lateral wall. This is called as wall-mode convection, where pairs of wall-bounded hot and cold plumes appear separately and alternatively [111, 155].

For $Ra = 2 \times 10^6$, at $Ro^{-1} = 10$ a quadrupolar [156] flow structure is observed, in which two pairs of hot and cold plumes are noticed which are separated azimuthally by approximately $\phi \approx \pi/2$, as shown in Fig. 3.3(i). At even higher rotation rates, $Ro^{-1} \geq 20$, a sextupolar structure [156] is seen as shown in Figs. 3.3(j)-3.3(l), where three pairs of hot and cold plumes appear that are separated azimuthally by $\phi \approx \pi/3$. Note that with the increase in rotation rate, the strength of the rolls diminishes and they become more localized near the lateral wall for both the Rayleigh numbers. At even higher rotation rates, all the temperature and velocity fluctua-

tions are suppressed, and the flow attains a conduction-like stage [155, 157]. Wall modes can be considered as a preceding step before approaching a conduction-like profile. The suppression of flow due to rotation first occurs near the bulk and then moves towards the walls. Wall modes are associated with a drastic drop in the heat transfer rates, which are discussed in a later section. Note that instantaneous snapshots do not necessarily give a comprehensive idea about the flow behaviour. Hence, we use different statistical measures for a better understanding of the same, which are carried out in the following sections.

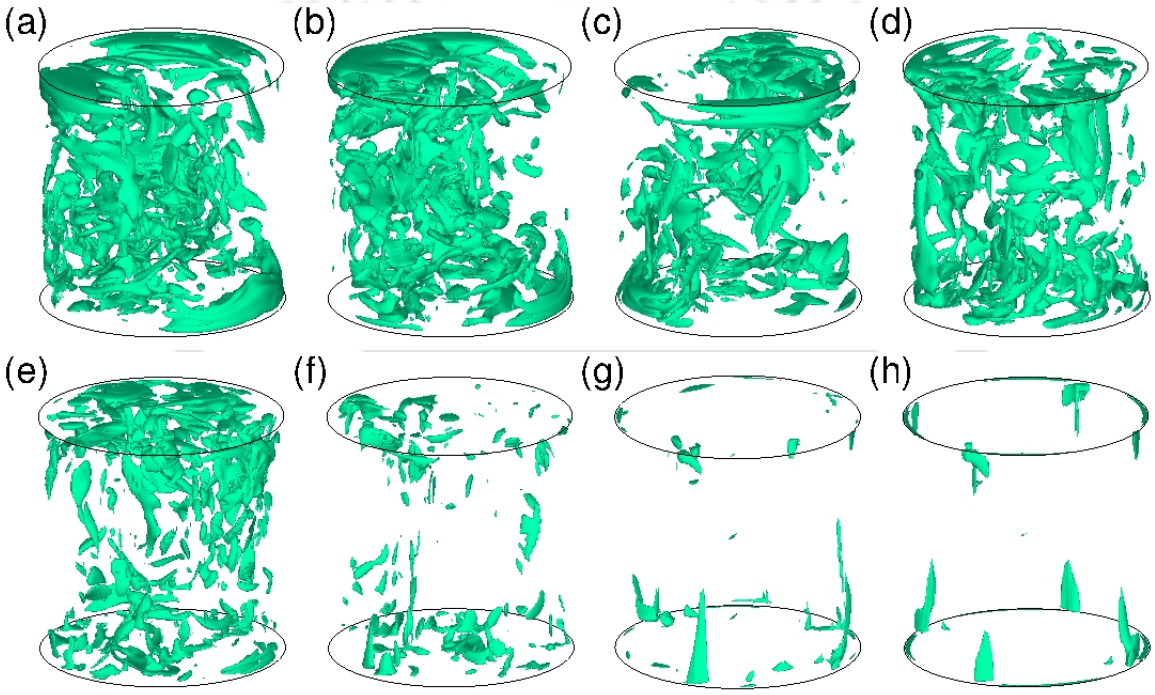

Figure 3.4: Q-structures for $Ra = 2 \times 10^7$ at (a) $Ro^{-1} = 0.1$, (b) $Ro^{-1} = 0.2$, (c) $Ro^{-1} = 0.5$, (d) $Ro^{-1} = 2$, (e) $Ro^{-1} = 3$, (f) $Ro^{-1} = 4$, (g) $Ro^{-1} = 10$, and (h) $Ro^{-1} = 20$. The iso-surfaces are drawn at 20% (for $0.1 \leq Ro^{-1} \leq 4$) and 10% (for $Ro^{-1} = 10$ and 20) of Q_{max}.

Turbulent flows are characterized by multi-scale and multi-layer nature [158]. Interestingly, it also features certain quasi-deterministic large-scale structures [159]. Such clearly organized structures in turbulent flows are generally referred to as coherent structures [160]. Identifying these vortical structures, their orientations, and distributions provide a deeper understanding of the flow dynamics. One of the most common methods for characterizing vortical structures is Q-criterion, which identifies the fluid regions with a positive second invariant of the velocity

gradient tensor $\nabla \boldsymbol{u}$. The second invariant is given by

$$Q = \frac{1}{2}(R_{ij}R_{ij} - S_{ij}S_{ij}), \tag{3.1}$$

$$\text{where } S_{ij} = \frac{1}{2}(\frac{\partial u_i}{\partial x_j} + \frac{\partial u_j}{\partial x_i}), \text{ and } R_{ij} = \frac{1}{2}(\frac{\partial u_i}{\partial x_j} - \frac{\partial u_j}{\partial x_i}). \tag{3.2}$$

Here S_{ij} and R_{ij} are the strain rate and rotational rate tensors, respectively. Q only takes into account the contribution by vortical motions, excluding the shearing motion. Thus regions with $Q > 0$ essentially represent strong local rotation. In Figs. 3.4 and 3.5, the Q-structures at different rotation rates are shown for both the Rayleigh numbers. Note that a wide range of values of Q are possible, and thus, an appropriate choice of Q is necessary to extract the relevant information [161]. The appropriate threshold value is based on the global maximum of Q over the entire flow field (Q_{max}). Here the levels are shown at about $10 - 20\%$ of the corresponding global maximum of Q. The structures are seen to become finer with the increase in Rayleigh number. At low rotation rates, the coherent structures are observed both near the lateral walls and bulk region. However, at higher rotation rates, the structures disappear in the bulk region and become localized near the lateral wall. As discussed previously, this indicates

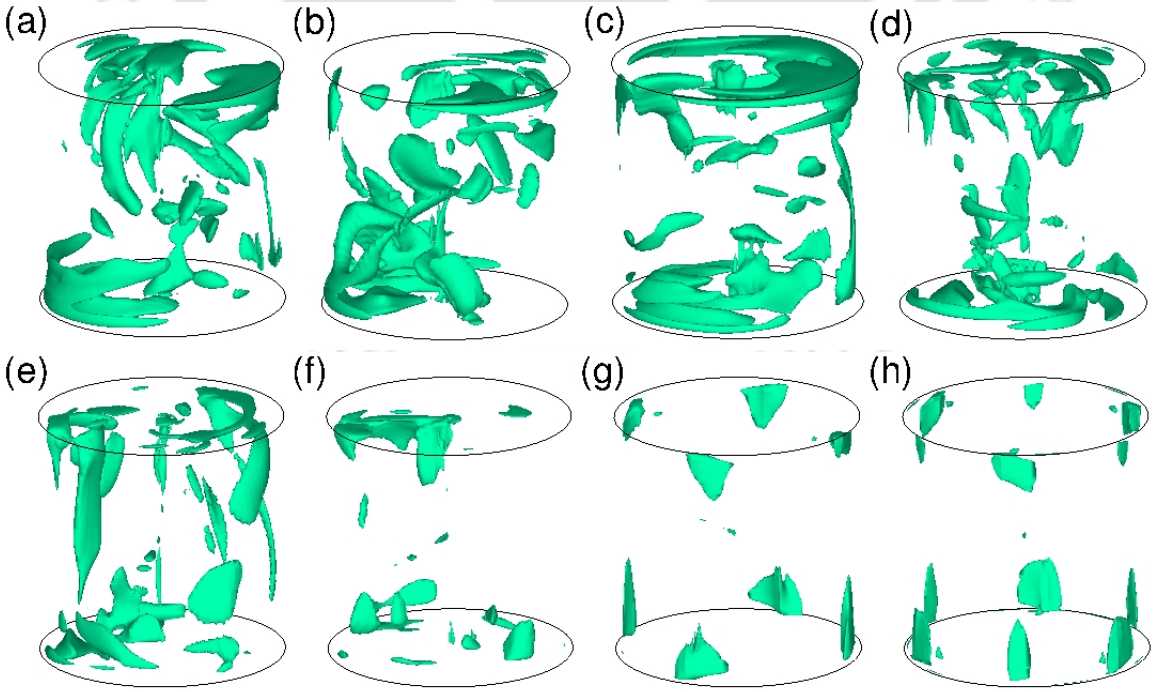

Figure 3.5: Q-structures for $Ra = 2 \times 10^6$ at (a) $Ro^{-1} = 0.1$, (b) $Ro^{-1} = 0.2$, (c) $Ro^{-1} = 0.5$, (d) $Ro^{-1} = 2$, (e) $Ro^{-1} = 3$, (f) $Ro^{-1} = 4$, (g) $Ro^{-1} = 10$, and (h) $Ro^{-1} = 20$. The iso-surfaces are drawn at 10% of Q_{max}.

the suppression of fluctuations in the bulk region due to flow stabilization at higher rotation rates and thus attainment of wall-mode convection.

3.4 Time evolution of the flow

In order to analyze the characteristics of unsteady flows, time signals are taken from 36 equidistant locations [Fig. 3.1(b)] which are $\pi/18$ apart along the azimuthal direction in the horizontal mid-plane ($z = 0.5$) at a radial distance of $r = 0.4R$ (close to the lateral wall). Time signals of vertical velocity from these probes are shown in Figs. 3.6 and 3.7, for $Ra = 2 \times 10^6$ and 2×10^7, respectively. These are helpful in identifying the flow periodicity and switching/flow reversals. Further, the time traces are used to recognize the azimuthal vertical velocity and temperature profiles, which in turn assists in quantifying the large-scale circulation and other flow behaviours.

Figures 3.6 and 3.7 show the vertical velocity signals at different locations in the mid-horizontal plane. In particular, we analyze the signal probes S_1, S_7, S_{10}, and S_{19}, which are located azimuthally at $\phi = 0$, $\pi/3$, $\pi/2$, and π, respectively. At low rotation rates $Ro^{-1} \lesssim 1$, the time traces are anti-correlated and fluctuate around a finite mean value, which indicates the presence of LSC. Note that in the LSC regime, the signals are shown at either end of a diametrical plane ($0 - \pi$), i.e., S_1 and S_{19}, to appropriately capture the dipolar nature of the flow. We observe that the finite mean of the time traces switches after a particular interval of time. These are identified as reorientations of LSC. Detailed discussion on the dynamics and statistics of reorientations of LSC are presented in the next chapter. Interestingly, with increase in rotation rate, the time span for which the LSC persists in a particular diametrical plane reduces for both Ra.

At higher rotation rates, the dipolar nature of the flow is lost and the time signals fluctuate around zero mean value, as shown in Figs. 3.6(f-i) and 3.7(f-i). This is a clear indication that the flow behaviour is far from LSC, as observed in the flow structures in the previous section, where at intermediate rotation rates random plume behaviour was noted without any particular flow organization [see Figs. 3.2 and 3.3]. At even higher rotation rates ($1 \lesssim Ro^{-1} \lesssim 10$), a

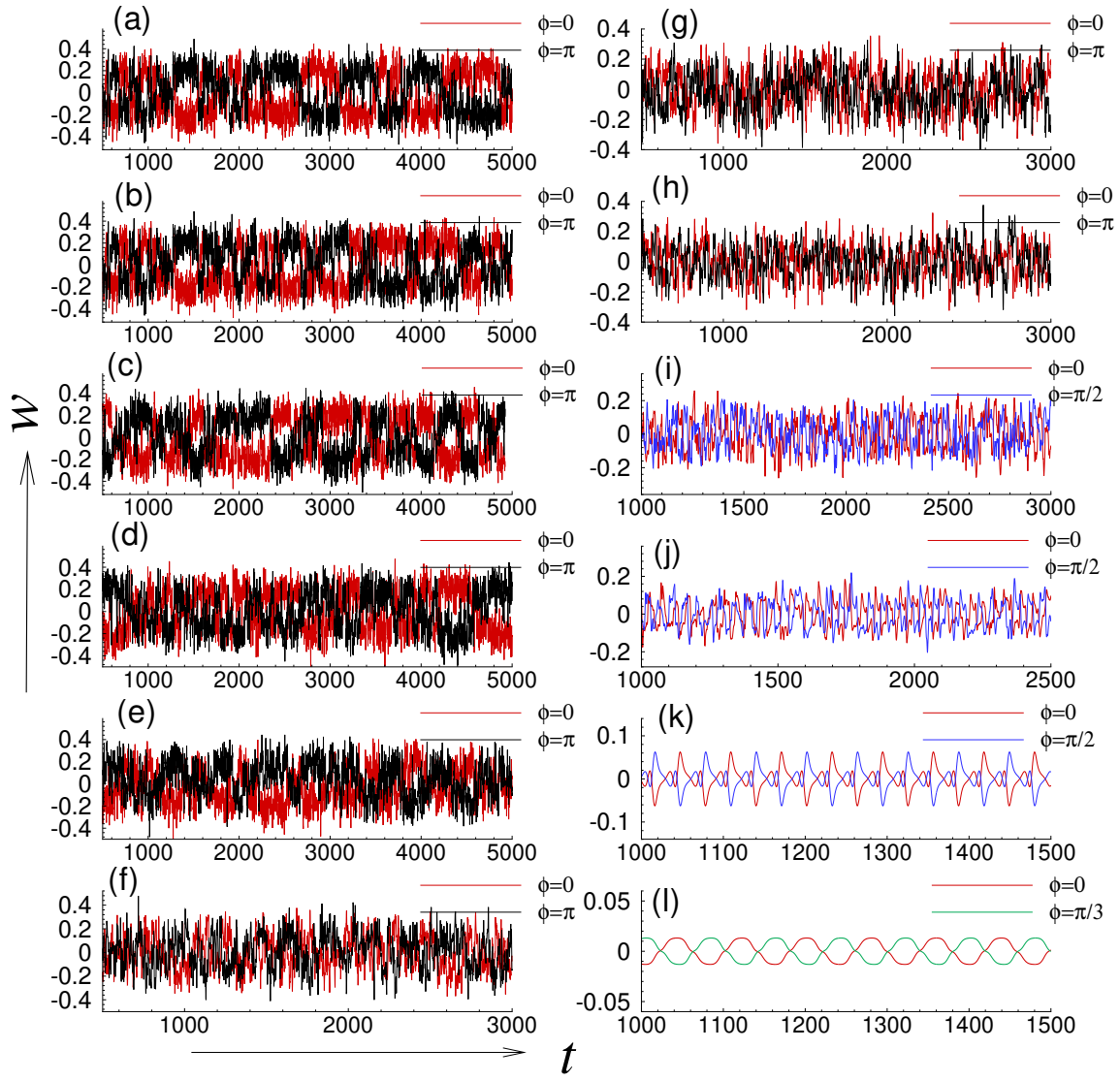

Figure 3.6: Time traces of vertical velocity for $Ra = 2\times10^6$ at (a) $Ro^{-1} = 0.1$, (b) $Ro^{-1} = 0.2$, (c) $Ro^{-1} = 0.3$, (d) $Ro^{-1} = 0.5$, (e) $Ro^{-1} = 1$, (f) $Ro^{-1} = 1.33$, (g) $Ro^{-1} = 2$, (h) $Ro^{-1} = 3$, (i) $Ro^{-1} = 4$, (j) $Ro^{-1} = 5.7$, (k) $Ro^{-1} = 10$, and (l) $Ro^{-1} = 20$.

significant reduction in the amplitude of the time traces is observed, as shown in Figs. 3.6(j)-3.6(k) and 3.7(j)-3.7(k). As we observe a quadrupolar flow behaviour for $Ra = 2 \times 10^6$ at $Ro^{-1} = 10$ [shown in Fig. 3.2(i)], the time signals from locations that are $\pi/2$ apart are expected to be anti-correlated, and hence the signals from these probes are shown in Fig. 3.6(k). Similarly, to identify the sextupolar nature of the flow for $Ra = 2 \times 10^6$ at $Ro^{-1} = 20$, the time signals are shown at $\phi = 0$ and $\pi/3$ in Fig. 3.6(l). Note that at higher rotation rates, the amplitude of the signals drops significantly, accompanied by a considerable reduction in the frequency content, which apparently shows the stabilizing effect of the rotation.

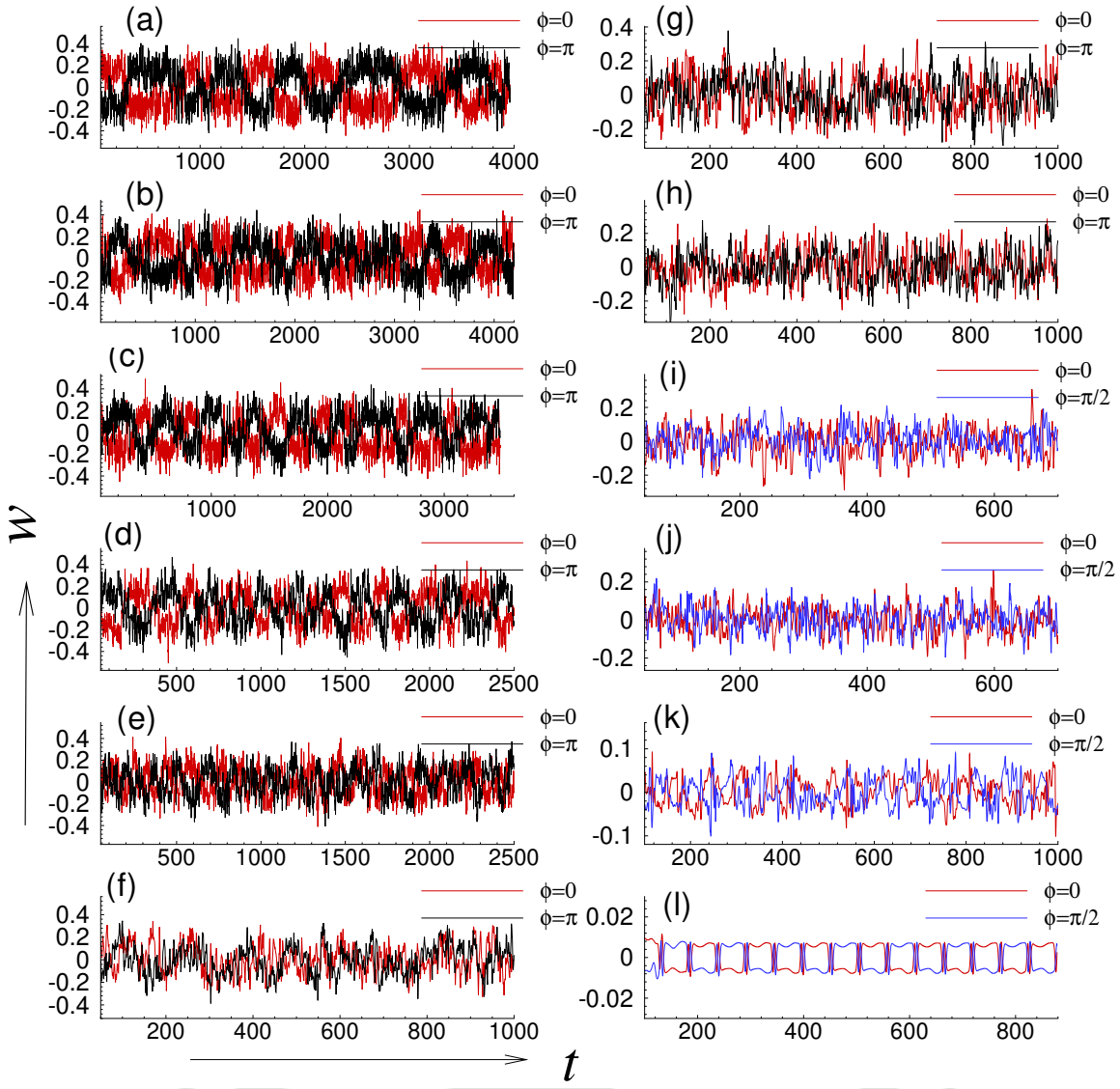

Figure 3.7: Time traces of vertical velocity for $Ra = 2\times10^7$ at (a) $Ro^{-1} = 0.1$, (b) $Ro^{-1} = 0.2$, (c) $Ro^{-1} = 0.3$, (d) $Ro^{-1} = 0.5$, (e) $Ro^{-1} = 1$, (f) $Ro^{-1} = 1.33$, (g) $Ro^{-1} = 2$, (h) $Ro^{-1} = 3$, (i) $Ro^{-1} = 4$, (j) $Ro^{-1} = 5.7$, (k) $Ro^{-1} = 10$, and (l) $Ro^{-1} = 20$.

The time-averaged vertical velocity from the above mentioned azimuthally equispaced numerical probes is shown in Figs. 3.8 and 3.9, where the averaging is carried out within a time over which the mean flow remains in a particular plane. At low rotation rates ($Ro^{-1} \lesssim 1$), the profiles show a cosine function with a single cycle spanning the entire (2π) domain [see Figs. 3.8(a)-3.8(b) and 3.9(a)-3.9(b)] which confirms the presence of LSC structure, and is consistent with previous studies [43, 56, 162, 163]. This particular nature of the flow in the azimuthal direction can be associated with the dipolar structure. This is consistent with the flow structures shown in the previous section [Figs. 3.2(a)-3.2(d) and 3.3(a)-3.3(d)], where

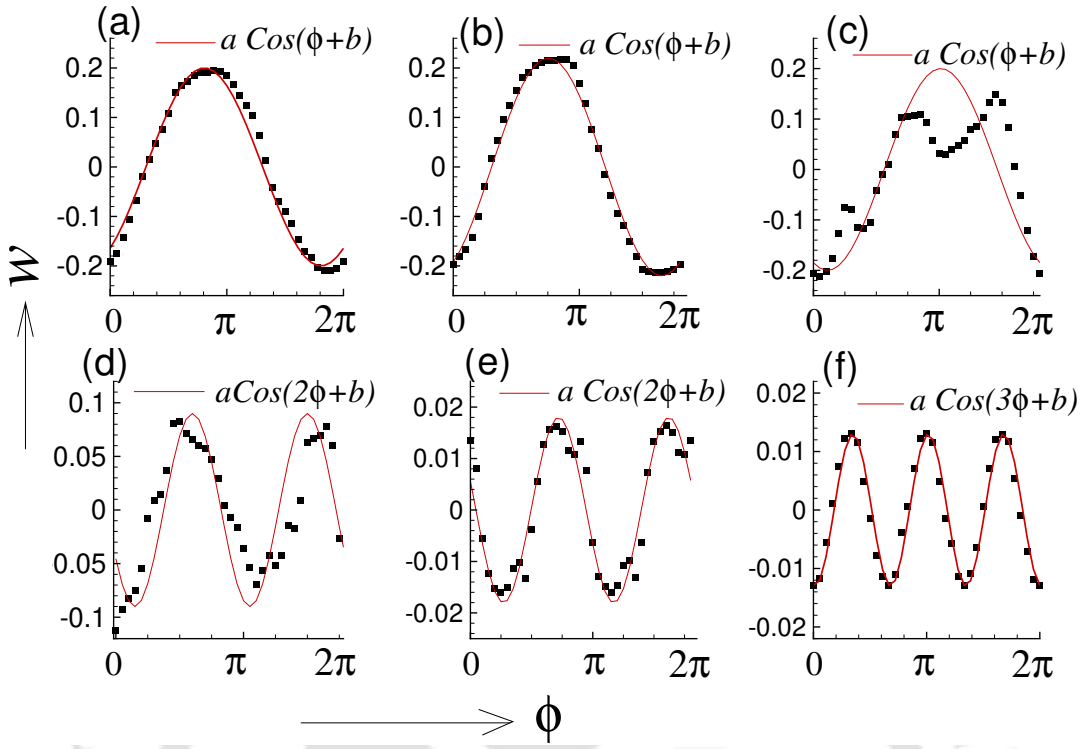

Figure 3.8: The temporal averaged vertical velocity profile along the azimuthal direction for $Ra = 2 \times 10^6$ at (a) $Ro^{-1} = 0$, (b) $Ro^{-1} = 0.1$, (c) $Ro^{-1} = 2$, (d) $Ro^{-1} = 5.7$, (e) $Ro^{-1} = 10$, and (f) $Ro^{-1} = 20$. The solid red line indicates the cosine fit.

the hot and cold plumes appear as segregated on opposite sides of the lateral wall. As rotation rate increases, we find a distortion from the cosine fit, as shown in Figs. 3.8(c)-3.8(d) and 3.9(c)-3.9(d). Recall that the flow structures at moderate rotation rates showed random plume behaviour without any specific organization. Hence the azimuthal profiles also do not show any specific arrangement. With further increase in rotation rate, the azimuthal velocity profiles approach the cosine function, but of higher periods such as period-two and period-three. For $Ra = 2 \times 10^6$ at $Ro^{-1} = 10$, the flow appears to be more close to the quadrupolar structure, indicated by two pairs of $+$ve and $-$ve peaks in the velocity profile [refer Fig. 3.8(e)]. At very high rotation rates ($Ro^{-1} = 20$), the vertical velocity profile appears to be more close to a sextupolar behaviour with $+$ve (up-flow) and $-$ve (down-flow) velocity separated azimuthally by $\pi/3$ [refer Fig. 3.8(f)]. For $Ra = 2 \times 10^7$, at high rotation rates ($Ro^{-1} \gtrsim 10$), the velocity profile shows a quadrupolar behaviour. Note that at lower and higher rotation rates we observe almost perfect cosine fits for the vertical velocity profile, while at intermediate rotation rates it deviates from the cosine fit.

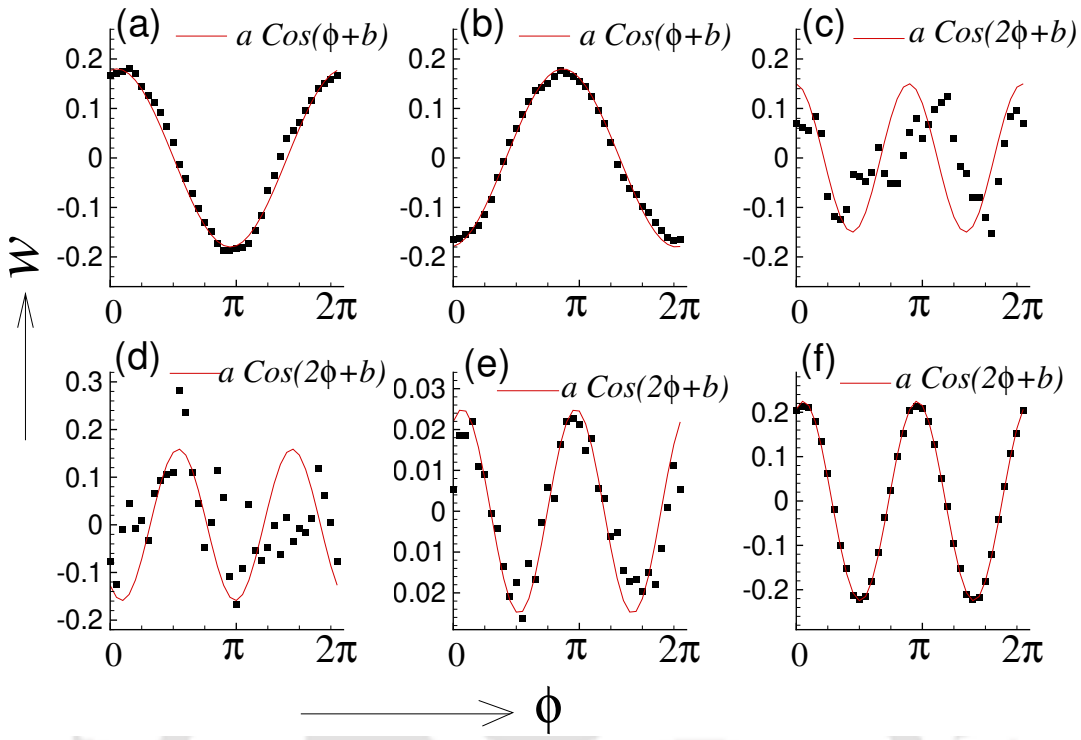

Figure 3.9: The temporal averaged vertical velocity profile along the azimuthal direction for $Ra = 2\times10^7$ at (a) $Ro^{-1} = 0$, (b) $Ro^{-1} = 0.1$, (c) $Ro^{-1} = 2$, (d) $Ro^{-1} = 4$, (e) $Ro^{-1} = 13.33$, and (f) $Ro^{-1} = 20$. The solid red line indicates the cosine fit.

3.5 Quantification of the flow based on the Fourier modes

After obtaining a qualitative picture of the flow structure and their temporal evolution, we now turn our focus on the quantification of the flow and thereby identification of different flow regimes based on the rotation rate. For this, the Fourier mode analysis of vertical velocity signals along the azimuthal direction of the cylindrical cell at mid-height is performed. We identify the dominant Fourier modes and connect these with the associated heat transfer and other turbulent statistics. Note that u_j is the velocity signal from N $(= 36)$ data points along the cylinder azimuth [refer Fig. 5.1(b)] and its Fourier transform is written as

$$\hat{u}_k = \sum_{j=1}^{N} u_j e^{-i2\pi kj/N} \tag{3.3}$$

where $\hat{u}_k$ represents the k^{th} Fourier mode and i the unit imaginary number. The first $(\hat{u}_1)$, second and third modes are associated with the dipolar, quadrupolar, and sextupolar structure of the flow, respectively [156]. Figure 3.10 shows a schematic diagram of different flow topology

at the horizontal mid-plane and the azimuthal velocity profile of the corresponding Fourier mode. Here, $+$ and $-$ signs indicate the hot and cold poles characterized by the aggregation of respective thermal plumes. The first Fourier mode represents LSC (dipolar structure) where hot and cold plumes traverse along opposite sides of the lateral wall, and hence the velocity profile shows a period-one cosine function. The vertical velocity is maximum near $\phi = 0$ ($+$ pole), drops to zero near $\phi = \pi/2$, reaches its minimum value at $\phi = \pi$ ($-$ pole), then attains zero at $\phi = 3\pi/2$ and finally completes the cycle by attaining the maximum value at 2π. The second Fourier mode identifies a period-two cosine function with two-pairs of maximum and minimum, hence constitute the quadrupolar structure. Similarly, the third mode corresponds to a period-three cosine function characterized by the sextupolar flow structure, as shown in Fig. 3.10. On performing the Fourier transform of the velocity signal along the azimuthal direction, the elemental Fourier modes are distinguished. Further, different flow regimes are quantified based on the dominance of these modes, which is characterized using the fraction of energy

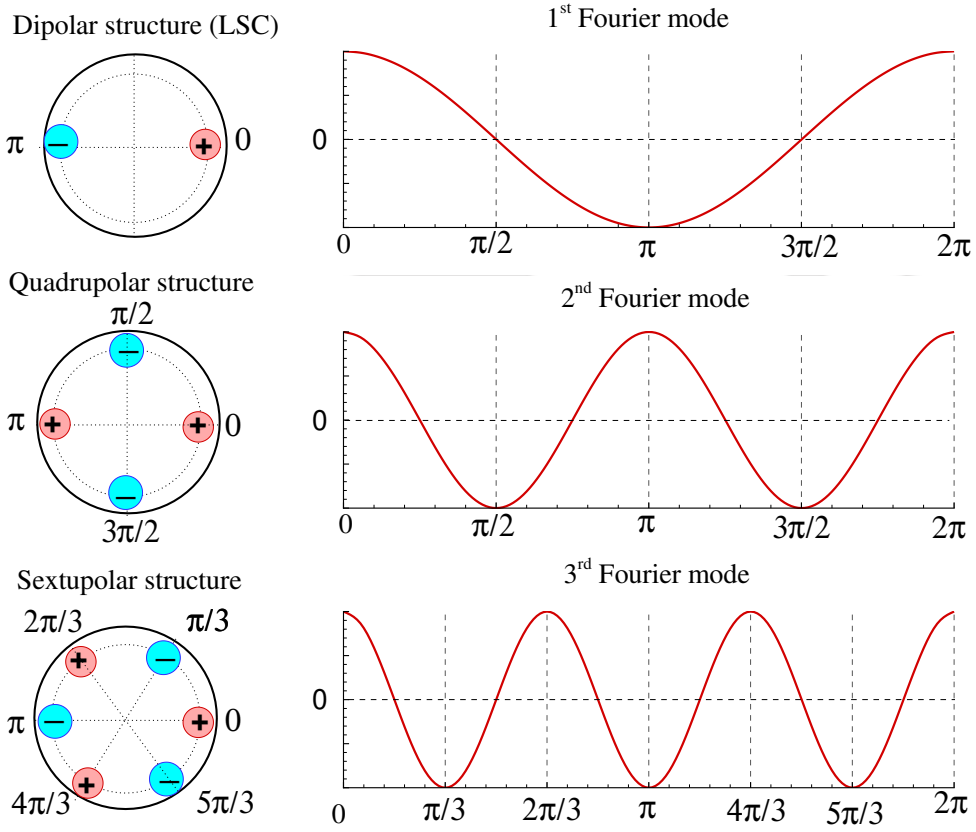

Figure 3.10: Schematic diagram of the flow behaviour at horizontal mid-plane along with the azimuthal velocity profile corresponding to the Fourier modes.

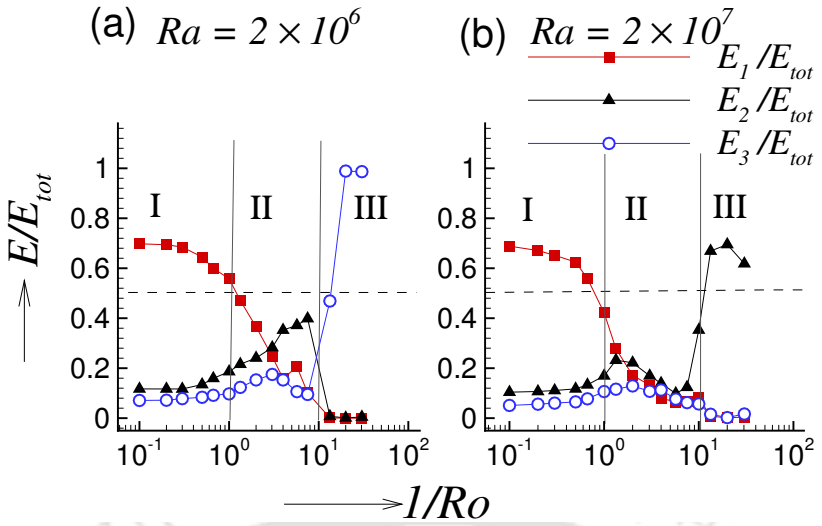

Figure 3.11: The variation of energy fraction of the first three Fourier modes with rotation rate for (a) $Ra = 2 \times 10^6$ and (b) $Ra = 2 \times 10^7$.

E_k/E_{tot}. Here $E_k = |\hat{u}_k|^2$ is the energy contained in the k^{th} Fourier mode and $E_{tot} = \sum_{k=1}^{N/2} E_k$ is the total energy. The evidence of LSC is often ascertained from the energy fraction of first Fourier mode (E_1/E_{tot}).

Figure 3.11 shows the variation of energy fraction of the first three Fourier modes with rotation rate. We identify different flow regimes based on the dominance of specific modes. In regime I ($0 \leq Ro^{-1} \lesssim 1$), the first Fourier mode is clearly dominant with $E_1/E_{tot} > 0.5$ and is identified as the LSC regime. Consequently, the average vertical velocity profile along the azimuthal direction clearly shows a perfect cosine fit [see Figs. 3.8(a)-3.8(b) and 3.9(a)-3.9(b)], as discussed in the previous section. A decrease in the energy fraction of the first Fourier mode accompanied by an increase in that of the second (E_2/E_{tot}) with increase in rotation rate is observed here. At high rotation rates, regime II ($1 \lesssim Ro^{-1} \lesssim 10$) is identified, where no dominance by any specific mode is observed as the fraction of energy carried by all the modes including the first mode is less than 0.5. As a result, the vertical velocity profiles in this regime are far from perfect cosine fit, as shown in Figs. 3.8(c)-3.8(d) and 3.9(c)-3.9(d). For $Ra = 2 \times 10^6$, although, the second mode marginally dominates at moderately high rotation rates ($5 < Ro^{-1} \lesssim 10$), it declines at extremely high rotation rates. Here, we even observe a third Fourier mode dominated flow for $Ro^{-1} \gtrsim 10$. This is identified as regime III, where the higher mode (second or third) shares more than 50% of the total energy. For $Ra = 2 \times 10^7$, the second Fourier mode dominates over the other modes in regime III.

3.6 Nusselt number and dissipation rates

Next, we discuss the behaviour of the Nusselt number and dissipation rates in different flow regimes. The Nusselt number quantifies the ratio of total heat flux through the system over the conductive heat flux (in absence of convection) [164, 165], i.e., $Nu = qH/K\Delta T$, where q is the total heat flux and K the thermal conductivity of the fluid. In RBC, the local Nusselt number at each spatial location is computed as $Nu(\boldsymbol{r}) = \sqrt{RaPr}w\theta - \dfrac{\partial\theta}{\partial z}$, where $\boldsymbol{r}$ is the position vector [166]. At the horizontal plates, where vertical velocity is zero the Nusselt number becomes $Nu(\boldsymbol{r}) = \dfrac{\partial\theta}{\partial z}$. Two quantities which play an important role in local and global heat transport process in RBC are the thermal dissipation and viscous dissipation rates. These two quantities represent the dissipation of thermal and kinetic energy due to the fluid thermal diffusivity and viscosity. The global averages of dissipation rates can be connected to the global heat transport via the exact relations $\langle\epsilon_u^{th}\rangle = \nu^3 H^{-4}(Nu-1)RaPr^{-2}$ and $\langle\epsilon_\theta^{th}\rangle = \alpha(\Delta T)^2 NuH^{-2}$ [75]. These two relations form the basis of the Grossmann-Lohse (GL) theory [76] [167] of turbulent heat transfer, where scaling laws for the Nusselt number and Reynolds number are established based on the decomposition of the dissipation rates into their bulk and boundary layer contributions (refer chapter 1).

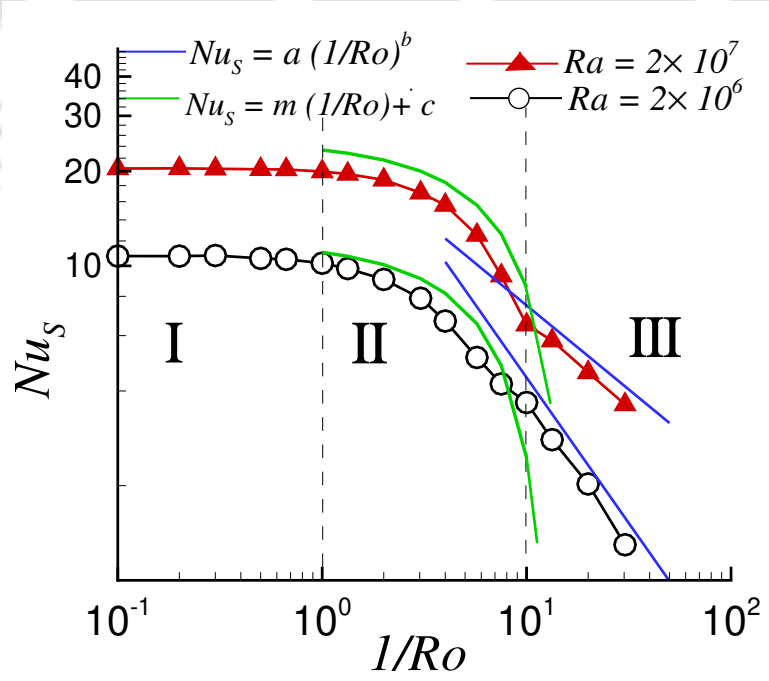

Figure 3.12: Variation of average Nusselt number with rotation rate at $Ra = 2 \times 10^6$ and 2×10^7. The solid green and blue lines indicate linear and power law fits, respectively.

Figure 3.12 shows the variation of area and time averaged Nusselt number at the bottom plate, $Nu_S = \langle \frac{\partial \theta}{\partial z} \rangle_{A,t}$, with rotation rate at different Rayleigh numbers. In regime I ($0 \leq Ro^{-1} \lesssim 1$) or LSC regime, heat transfer remains almost constant. As rotation rate increases Nusselt number drops linearly in regime II given by $1 \lesssim Ro^{-1} \lesssim 10$. However, in regime III ($Ro^{-1} \gtrsim 10$) Nusselt number shows a power law behaviour, $Nu_S \propto (1/Ro)^b$, with the exponent $b = -0.93$ and -0.53 for $Ra = 2 \times 10^6$ and 2×10^7, respectively. The solid green and blue lines in Fig. 3.12 represent the corresponding linear and power law fits at regimes II and III, respectively.

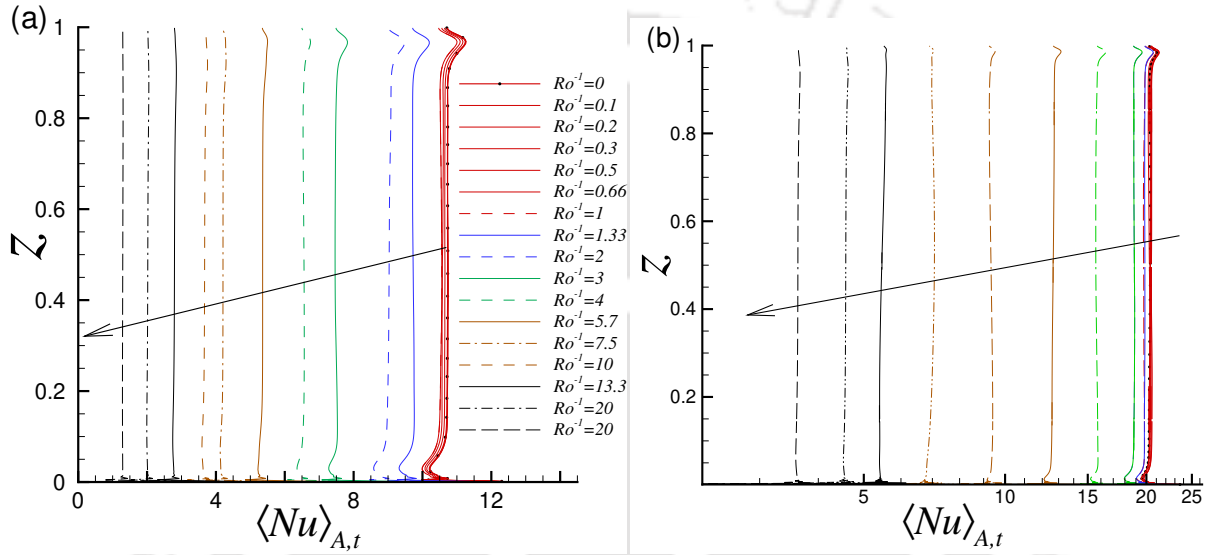

Figure 3.13: Variation of average Nusselt number along the vertical direction for (a) $Ra = 2 \times 10^6$ and (b) $Ra = 2 \times 10^7$ at different rotation rates. The arrows indicate the direction of increasing rotation rate.

The vertical variation of horizontal plane and time-averaged Nusselt number, $\langle Nu \rangle_{A,t} = \sqrt{RaPr} \langle w\theta \rangle_{A,t} - \langle \frac{\partial \theta}{\partial z} \rangle_{A,t}$, for different rotation rates is shown in Fig. 3.13. The profiles are almost similar in regime I, while the magnitude drops considerably at higher rotation rates (regimes II and III). Note that $\langle Nu \rangle_{A,t}$ remains nearly constant along the vertical direction as the the net vertical heat flux across two horizontal sections do not change. It is interesting to note that inside the boundary layer region (both at the top and bottom), the Nusselt number shows deviations from its mean profile, which can be attributed to the emissions of thermal plume. However, these deviations are suppressed with increase in rotation rates as the plume emissions diminish as a result of flow stabilization.

Next, we evaluate the viscous and thermal dissipation rates. Figure 3.14 shows the volume

and time averaged non-dimensional dissipation rates, $\langle \epsilon_u \rangle = \sqrt{Pr/Ra}\langle |\nabla \boldsymbol{u}|^2 \rangle$ and $\langle \epsilon_\theta \rangle = \sqrt{1/RaPr}\langle |\nabla \theta|^2 \rangle$, normalized by the corresponding non-rotating dissipation rates $\langle \epsilon_u^o \rangle$ and $\langle \epsilon_\theta^o \rangle$, respectively, for different rotation rates. In regime I where LSC is observed, both dissipation rates remain almost constant and close to the non-rotating value. However, at higher rotation rates a significant departure from the non-rotating case is noticed. At regime II, the dissipation rates decrease linearly with rotation rate, as observed for the Nusselt number. This is followed by rotation dominated regime III, where they follow a power law behaviour as $\langle \epsilon \rangle \propto (1/Ro)^b$, with exponent $b = -1.95$ and -0.68 for $Ra = 2 \times 10^6$ and 2×10^7, respectively, for $\langle \epsilon_u \rangle$, while $\langle \epsilon_\theta \rangle$ follows the same power law as that of Nu_S.

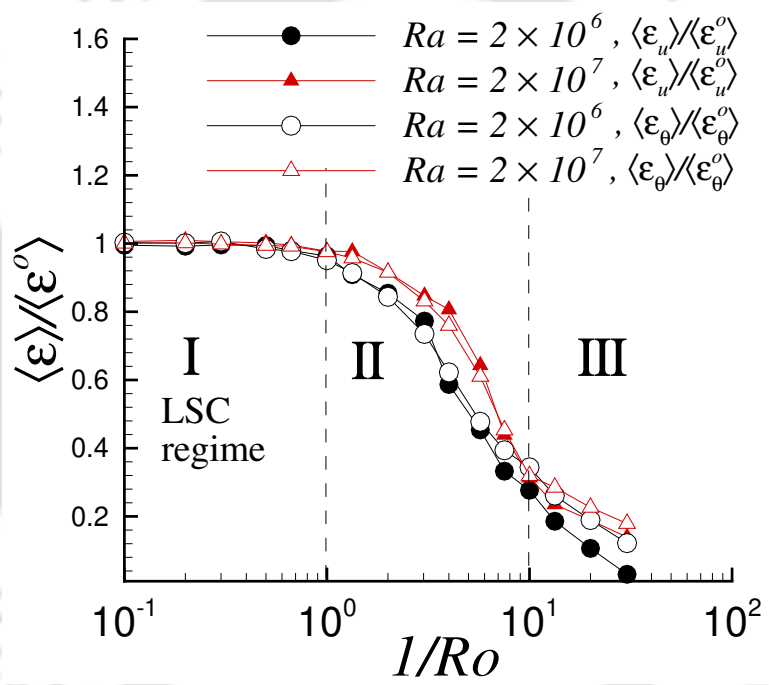

Figure 3.14: Variation of $\langle \epsilon_u \rangle / \langle \epsilon_u^o \rangle$ and $\langle \epsilon_\theta \rangle / \langle \epsilon_\theta^o \rangle$ with rotation rate for $Ra = 2 \times 10^6$ and 2×10^7.

In RBC, dissipation fields are often expected to follow a log-normal distribution [168]. However, considerable deviations due to the highly intermittent nature of the local dissipation have also been reported [169–172]. The spatial PDF of the thermal dissipation rate normalized by the respective rms values are shown in Fig. 3.15 for three different rotation rates ($Ro^{-1} = 0.1,\ 1.33$, and 20) corresponding to the three different flow regimes. We observe that at regimes I and II, both the PDFs show a long tail that fits well with a stretched exponential function $P(X) = C/\sqrt{X}\exp(-mX^\alpha)$. Here, C, m and α are the fitting parameters, and X corresponds to the values of $\epsilon_\theta/\epsilon_\theta^{rms}$. The fitting is done for the values which are greater than the abscissa

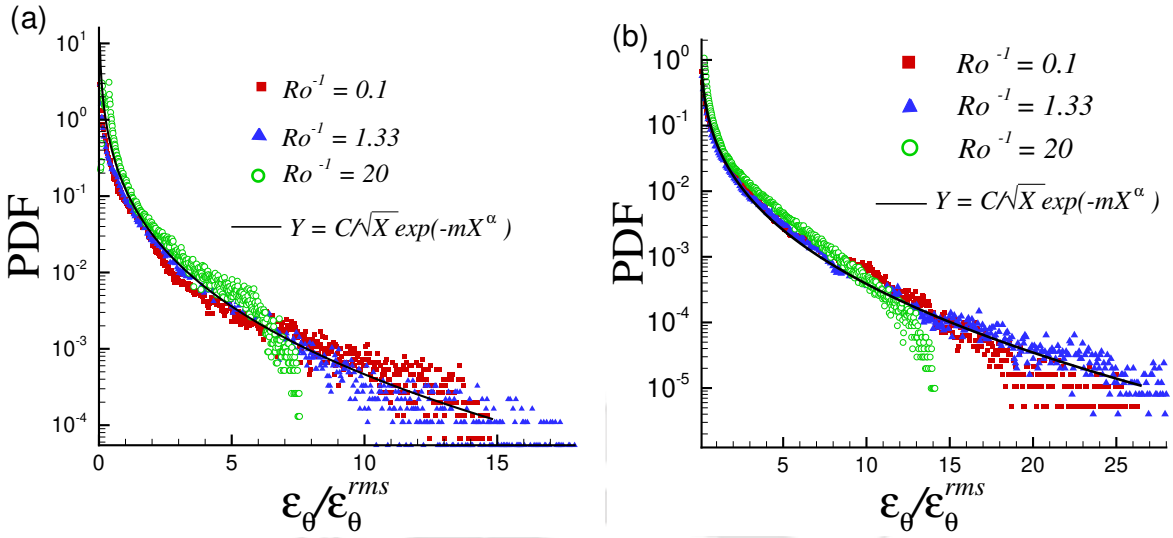

Figure 3.15: Spatial PDF of thermal dissipation rate normalized by the respective rms vales for (a) $Ra = 2 \times 10^6$ and (b) $Ra = 2 \times 10^7$ at different rotation rates. The solid lines indicate the best fits of stretched exponentials (at regime I).

of the most probable value. In both the regimes I and II, the fitting exponents are almost the same with $\alpha \approx 0.4$. These findings are consistent with earlier results [169, 170]. However, at high rotation rates (regime III), the tails of the PDFs get shortened indicating the reduction in high amplitude dissipation events due to flow stabilization.

Next, we analyze the temporal behaviour of dissipation rates. In Figs. 3.16 and 3.17, the temporal PDFs of thermal and viscous dissipation rates are represented in log-normal coordinates, where μ and σ indicate the mean and standard deviation of the logarithmic dissipation rates. The solid line represents normal distribution curve for reference. In the LSC regime, both viscous and thermal dissipation rates follow a log-normal behaviour. However, as the rotation rate increases, a clear departure from log-normality is noticed, especially in regime III ($Ro^{-1} = 10$). Further, the deviations are significant for ϵ_u than for ϵ_θ. For a better comparison between different rotation rates, the PDFs are collapsed under a single linear-logarithmic axes, as shown in Fig. 3.18. It is apparent that the tails of PDFs become shorter in regime III, implying a reduced probability of high-amplitude dissipation events. This is due to the flow stabilization at higher rotation rates, which reduces the fluctuations in the flow.

The spatial distribution of the viscous and thermal dissipation rates in different flow regimes are examined now. The variation of the horizontal plane and time-averaged dissipation rates along the vertical direction are shown in Figs. 3.19 and 3.20, where the complete profile of

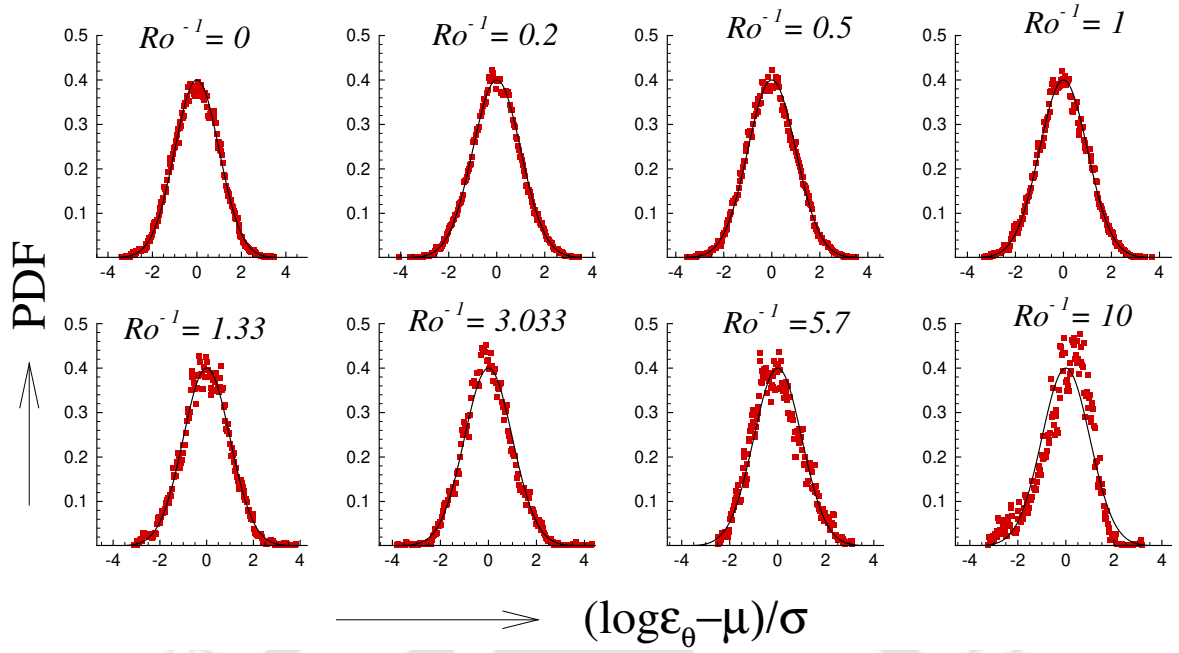

Figure 3.16: PDF of log ϵ_θ at $Ra = 2 \times 10^7$ for different Ro^{-1} in log-normal coordinates. As the rotation rate increases, the PDFs depart from log-normality.

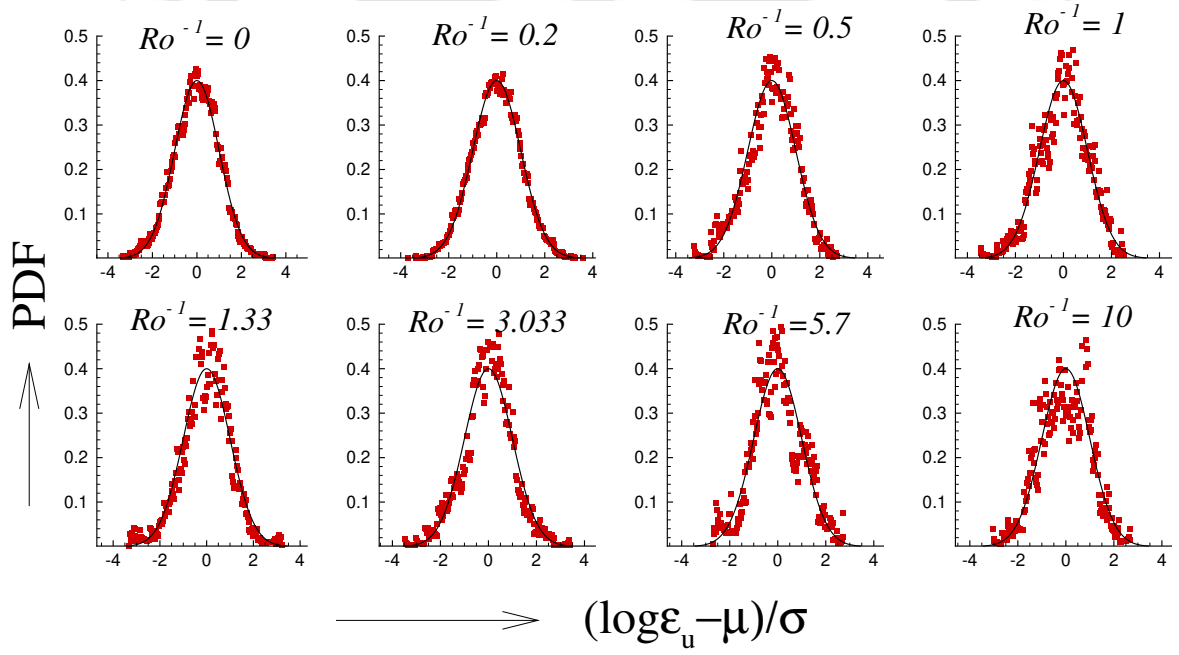

Figure 3.17: PDF of log ϵ_u at $Ra = 2 \times 10^7$ for different Ro^{-1} in log-normal coordinates. As the rotation rate increases, the PDFs depart from log-normality.

$\langle \epsilon_\theta \rangle_{A,t}$ is shown in the inset of frame (a). We observe that maximum value of the dissipation rates occurs at the top and bottom plates, which is consistent with the observations made by Zhang *et al.* [169] and Emran and Schumacher [95]. In the LSC regime, the bulk region shows negligible thermal dissipation (in comparison to boundary layers), indicating most of

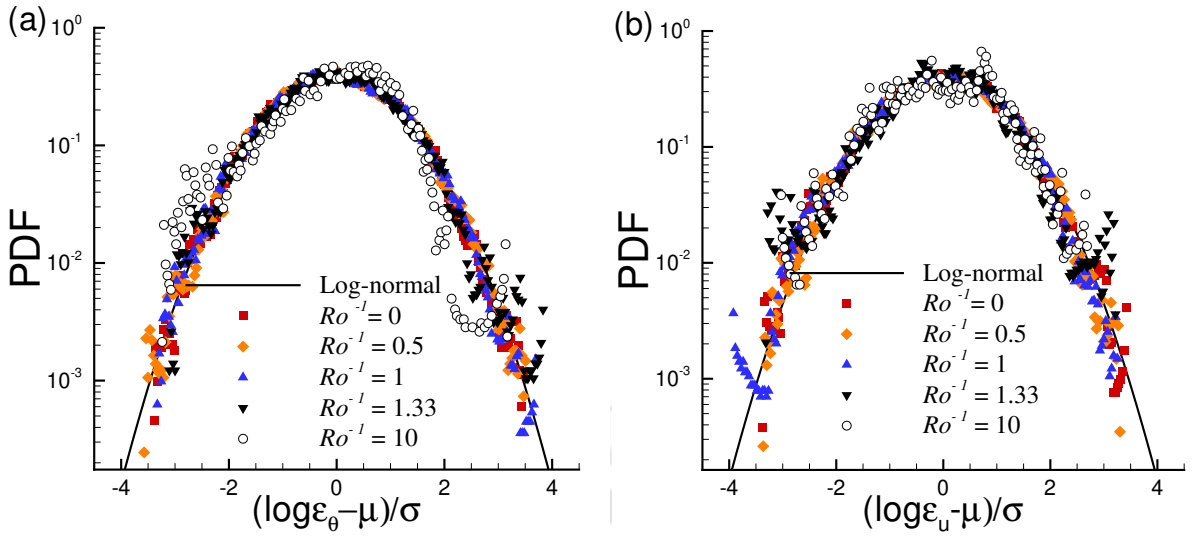

Figure 3.18: PDFs of log ϵ_θ and log ϵ_u at $Ra = 2 \times 10^7$ for different Ro^{-1} in log-normal coordinates. The tails of the PDFs become shorter at high rotation rates.

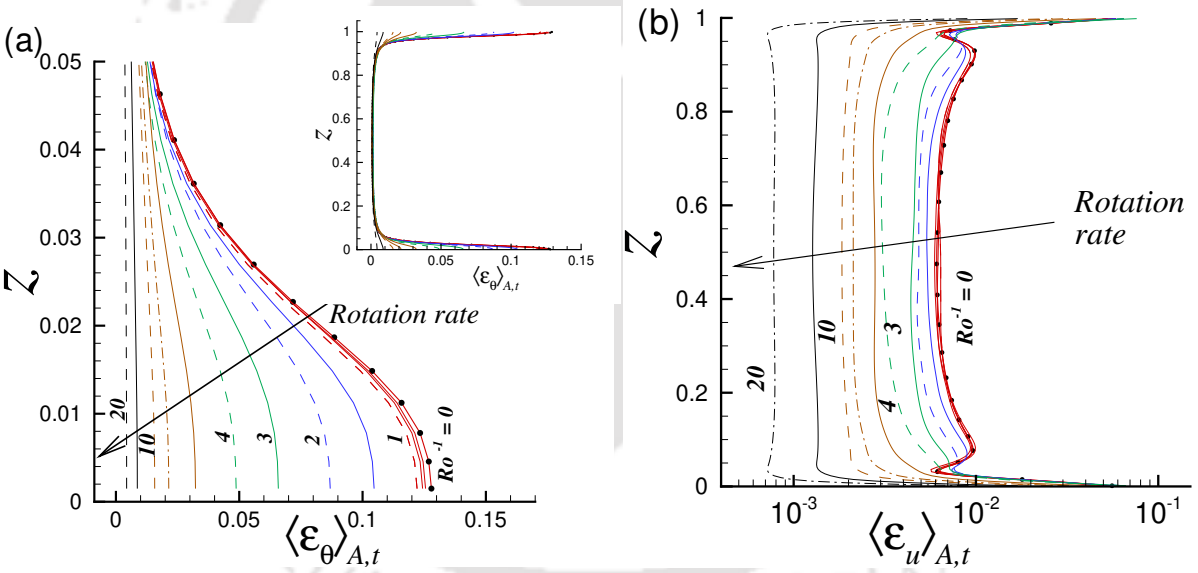

Figure 3.19: (a) Enlarged view (near bottom plate) of the variation of thermal dissipation along the vertical direction at $Ra = 2 \times 10^6$ for different Ro^{-1}. The inset shows the complete profile. (b) Variation of viscous dissipation rate along the vertical direction for different rotation rates in semi-log scale. Arrows indicate the direction of increase in rotation rate.

the thermal energy is dissipated near the thermal boundary layers. As rotation rate increases (regime III), the magnitude of thermal dissipation decreases near the top and bottom surfaces. The straight vertical lines in regime III suggest that the energy is dissipated more uniformly throughout the domain. On a similar note, the viscous dissipation also follows a different profile in the LSC regime compared to that at high rotation rates. In the LSC regime, two local

peaks are identified in the $\langle \epsilon_u \rangle_{A,t}$ profile before it becomes stable near the bulk region. However, at regime III, only a single peak is identified. These peculiar features of the dissipation rates at the interface of bulk and boundary layer may be associated with the interplay between different forces at different flow regimes. At low rotation rates (regime I), due to the competition between the viscous and buoyant forces, the viscous dissipation rate changes abruptly across the boundary layer. However, at higher rotation rates (regime III), the strong Coriolis force overshadows the buoyant force, and flow stabilization occurs. All the fluctuations in the system are damped out and as a result, the dissipation rates show a uniform trend along the vertical direction. The stabilizing effect of rotation on RBC is evident from these profiles.

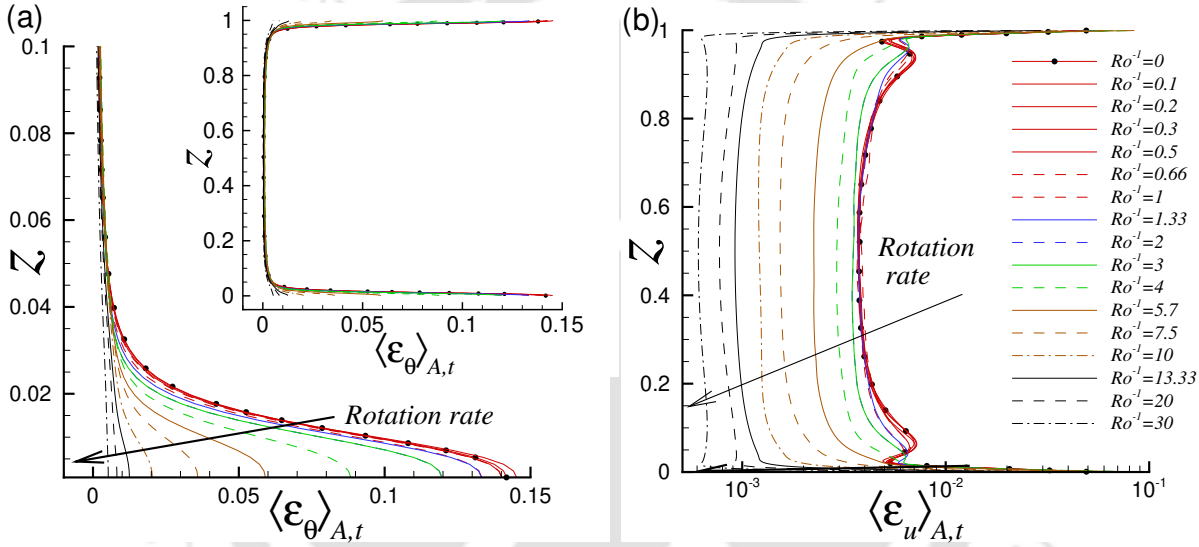

Figure 3.20: (a) Enlarged view (near bottom plate) of the variation of thermal dissipation along the vertical direction at $Ra = 2 \times 10^7$ for different Ro^{-1}. The inset shows the complete profile. (b) Variation of viscous dissipation rate along the vertical direction for different rotation rates in semi-log scale. Arrows indicate the direction of increase in rotation rate.

3.7 Planar statistics

To identify the flow characteristics in different regions of the flow, planar statistics of velocity and temperature are computed. Rotation primarily has a tendency to suppress the vertical motion, which leads to stratification of the flow along the rotation axis. Figure 3.21 shows the root mean square (rms) of vertical velocity (w or u_z) along the vertical direction for different rotation rates. We calculate $w_{rms} = \sqrt{\langle (w - \langle w \rangle_{A,t})^2 \rangle_{A,t}}$, where $\langle w \rangle_{A,t} = 0$. Recall that $\langle .. \rangle_{A,t}$

indicates horizontal plane (z planes) and time averaging. The magnitude of w_{rms} increases near the bulk and decreases near the no-slip walls. Note that in regime I, the w_{rms} profiles follow an almost similar trend, while apparent differences are seen across the higher rotation rate regimes II and III. The suppression of w_{rms} with increase in rotation is evident from Fig. 3.21, especially for $Ra = 2 \times 10^6$. As rotation rate increases, the rms of vertical velocity is considerably reduced, accompanied by flow stabilization along the vertical axis. At very high rotation rates, all the vertical velocity fluctuations are damped out and the magnitude of w approaches zero, which is theoretically explained by the Taylor-Proudman theorem [101, 102]. The theorem is generally used in the context of geostrophic flows, where the Coriolis force overshadows the other forces. The theorem states that in a homogeneous, inviscid flow dominated by Coriolis force, there is no variation of flow parameters along the flow axis, i.e., the flow behaves as 2-D in a plane orthogonal to the flow axis, in short

$$\frac{\partial \boldsymbol{u}}{\partial z} = 0 \tag{3.4}$$

Thus, there is no velocity variation along the vertical direction.

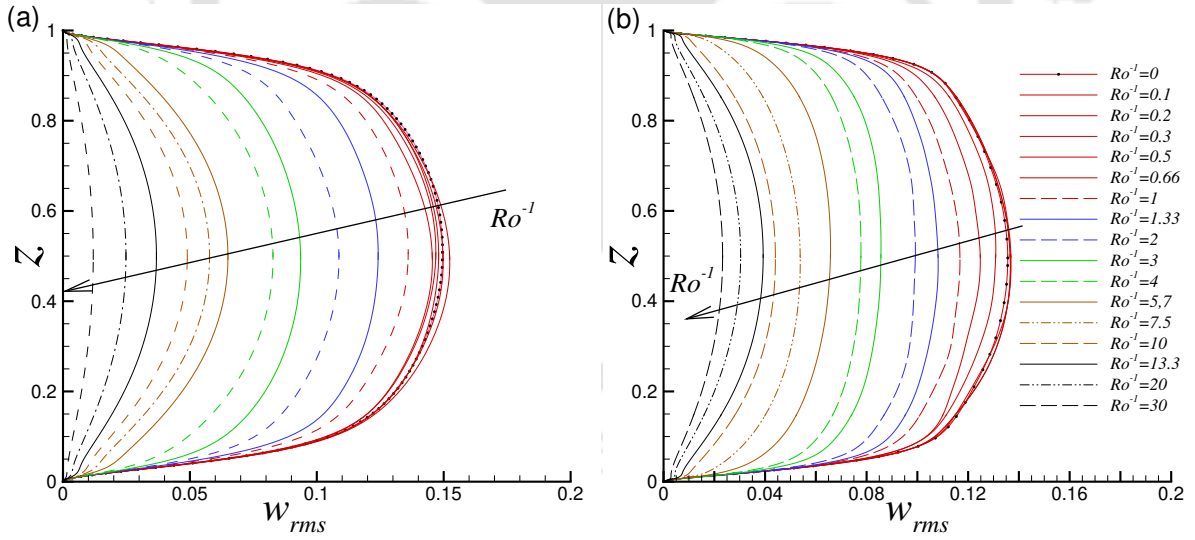

Figure 3.21: Variation of root mean square of vertical velocity along the vertical direction for (a) $Ra = 2 \times 10^6$ and (b) $Ra = 2 \times 10^7$ at different rotation rates. The arrows indicate the direction of increasing rotation rate.

The variation of rms of vertical velocity at the mid-plane ($z = 0.5H$) with rotation rate is shown in Fig. 3.22, where the dashed lines demarcate different flow regimes. It is apparent that w^m_{rms} remains almost constant at low rotation rate (regime I) and drops at higher rotation

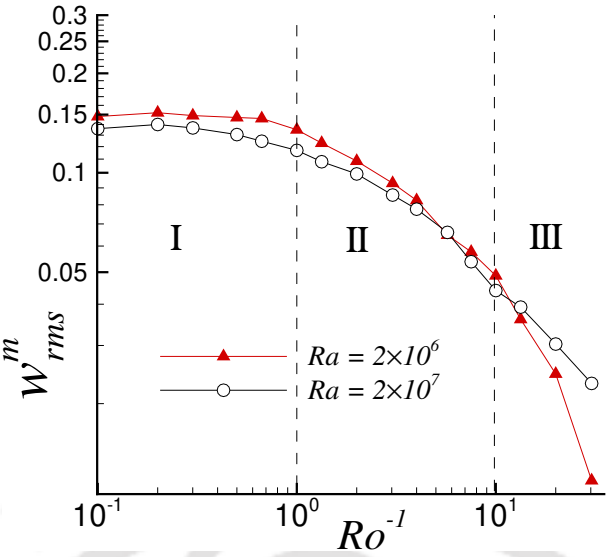

Figure 3.22: The root mean square of vertical velocity at the mid-plane as a function of rotation rate for $Ra = 2 \times 10^6$ and 2×10^7. The dashed lines indicate the different flow regimes.

rates. In regime III, we observe a power-law behaviour with respect to rotation rate as $w^m_{rms} = a(1/Ro)^b$, for both the Rayleigh numbers, as shown in Table 3.2. Note that as Ra increases, the scaling exponent reduces by half. This indicates that the stabilizing effect of rotation is reflected more at lower Ra.

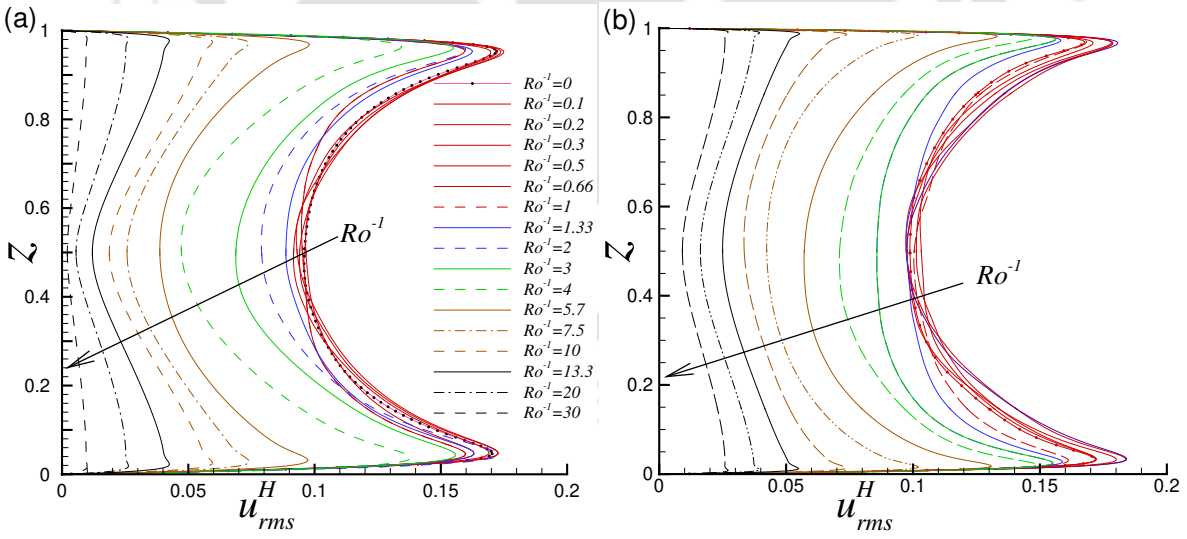

Figure 3.23: Variation of root mean square of horizontal velocity along the vertical direction for (a) $Ra = 2 \times 10^6$ and (b) $Ra = 2 \times 10^7$ at different rotation rates. The arrows indicate the direction of increasing rotation rate.

Next, we evaluate the fluctuations in the horizontal velocities. Following the formulations by Kerr [173] and Kunnen *et al.* [126], rms of net horizontal velocity is computed as $u^H_{rms} =$

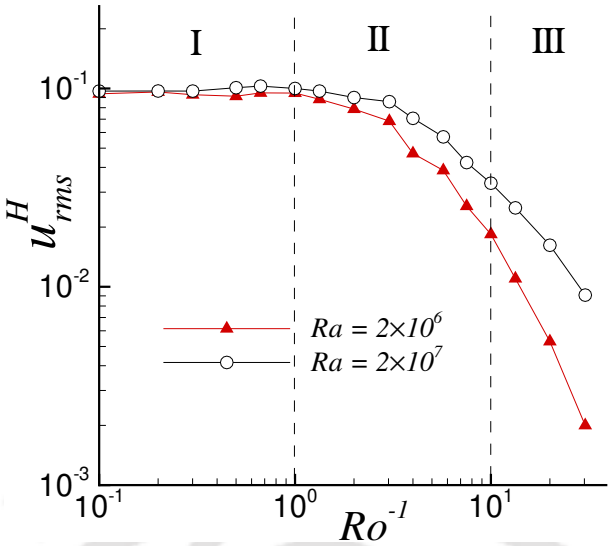

Figure 3.24: The root mean square of horizontal velocity at the mid-plane as a function of rotation rate for $Ra = 2 \times 10^6$ and 2×10^7. The dashed lines indicate the different flow regimes.

$\sqrt{u_r^2 + u_\phi^2}$, whose variation along the vertical direction is shown in Fig. 3.23. We observe that u^H_{rms} is zero at the walls, increases within the boundary layer to reach its peak value, and subsequently drops towards the central region. The vertical distance of the peak rms from the horizontal wall gives an estimate of viscous boundary layer thickness [173]. Overall, the horizontal velocity reduces with increase in rotation rate, both near the isothermal plates and in the bulk region, as shown in Fig. 3.23. However, in the low rotation rate regime I, the bulk region shows higher fluctuations than the non-rotating case. Due to rotation, the thermal plumes are spun up as they move away from the top and bottom plates, resulting in increase of horizontal velocities. This effect is noticed only at regime I, as even higher rotation rates result in damping of convective motion. Similar effect was observed by Kunnen *et al.* [126] in RRBC at low rotation rates.

The variation of rms of horizontal velocity at the mid-plane ($z = 0.5H$) with rotation rate is shown in Fig. 3.24. Similar to w_{rms}, the rms of horizontal velocity also remains almost constant in regime I, and drops considerably in regimes II and III, as the rotation rate increases. In regime III, we observe a power-law dependence with rotation rate, $u^H_{rms} = a(1/Ro)^b$, for both the Rayleigh numbers, as shown in Table 3.2. Similar trend was observed by Kunnen *et al.* [126] in their numerical study of rotating convection inside a rectangular domain for $Pr = 1$. Note that as Ra increases, the scaling exponent reduces by half as observed for the vertical

Table 3.2: The power-law fits for the rms of vertical and horizontal velocities at the mid-plane in regime III, $w_{rms} = a(1/Ro)^b$ and $u^H_{rms} = a(1/Ro)^b$, for $Ra = 2 \times 10^6$ and 2×10^7.

rms at mid-plane	Ra	a	b
w_{rms}	2×10^6	0.936	-1.26
w_{rms}	2×10^7	0.178	-0.59
u^H_{rms}	2×10^6	1.87	-1.99
u^H_{rms}	2×10^7	0.505	-1.17

velocity rms, indicating that the stabilizing effect of rotation is less apparent at higher Ra.

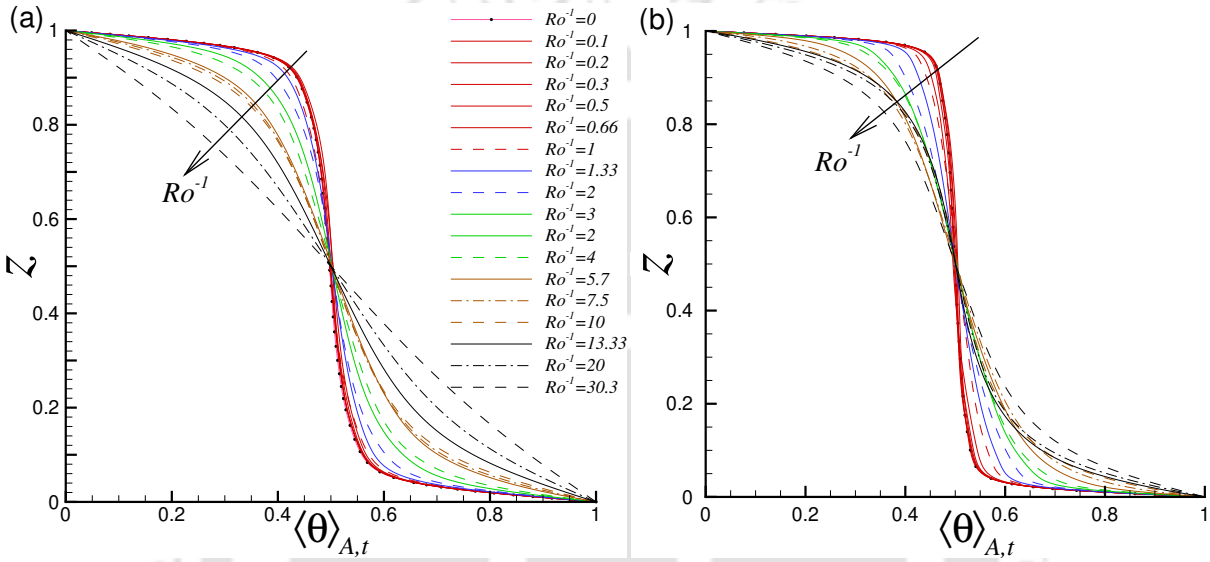

Figure 3.25: Variation of mean of temperature along the vertical direction for (a) $Ra = 2 \times 10^6$ and (b) $Ra = 2 \times 10^7$ at different rotation rates. The arrows indicate the direction of increasing rotation rate.

In Fig. 3.25, vertical profiles of mean of temperature $\langle\theta\rangle_{A,t}$ are shown for $Ra = 2 \times 10^6$ and 2×10^7, which clearly indicate different characteristic regions in the flow domain. The mean temperature shows a sharp gradient in the boundary layer region, which decreases gradually towards the bulk region ($z = 0.5H$). Note that at low rotation rates (regime I), there is hardly any temperature difference over the central region [173] and the imposed temperature difference across the top and bottom plates is accomplished almost entirely within the thermal boundary layer [140]. However, with increasing rotation rates, the temperature gradient becomes pronounced over the bulk. At higher rotation rates (regimes II and III), the temperature gradient stabilizes along the vertical direction and the mean temperature profile approaches the linear one. At extremely high rotation rates $Ro^{-1} = 30$, an almost linear profile is obtained for $Ra = 2 \times 10^6$, accompanied by Nu approaching unity. This is a clear indication of suppres-

sion of the convective motion. As explained previously, at extremely high rotation rates, the strong Coriolis force ceases the vertical motion and heat transfer occurs purely by conduction. However, for $Ra = 2 \times 10^7$, shown in frame (b), the profile is far from a linear one even at the highest rotation rate ($Ro^{-1} = 30$), due to higher buoyancy force.

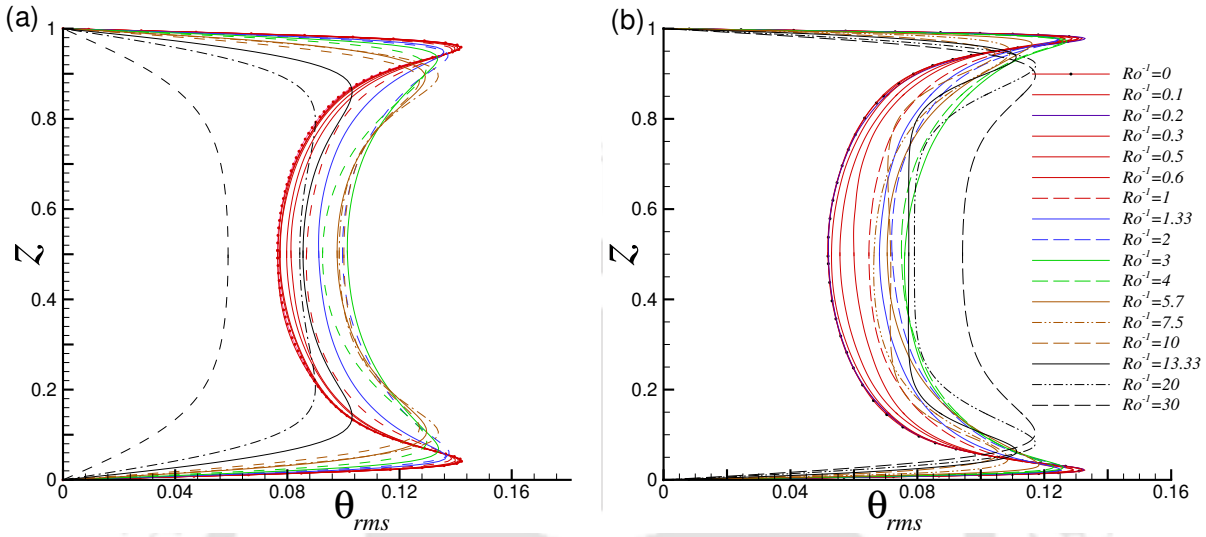

Figure 3.26: Variation of root mean square of temperature along the vertical direction for (a) $Ra = 2 \times 10^6$ and (b) $Ra = 2 \times 10^7$ at different rotation rates.

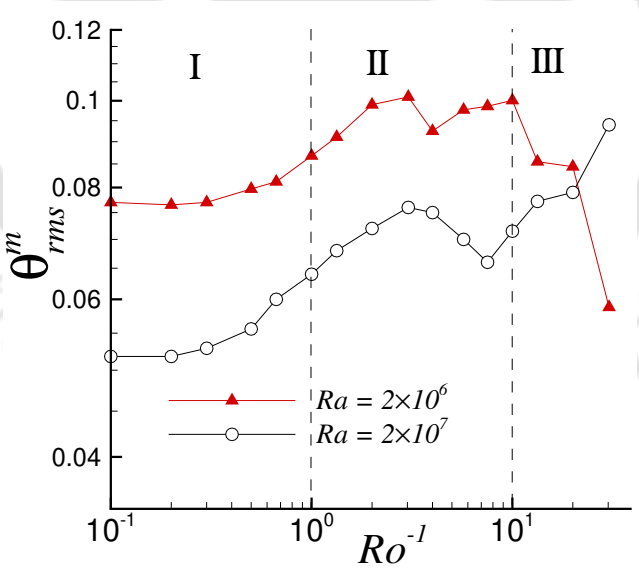

Figure 3.27: The root mean square of temperature at the mid-plane as a function of rotation rate for $Ra = 2 \times 10^6$ and 2×10^7. The dashed lines indicate the different flow regimes.

The rms of temperature increases as we move away from the isothermal plates and peaks near the edge of the boundary layer, where it shows a sharp gradient, as shown in Fig. 3.26. Subsequently, it drops gradually to attain an almost constant value near the center of the flow

domain. The vertical distance of the peak rms from the horizontal wall gives an estimate of the thermal boundary layer thickness [173]. The nearly constant value of θ_{rms} indicates homogeneity in the bulk region. Overall the temperature fluctuations in the bulk region increase with rotation rate. Due to the suppression of the vertical motions (see Fig. 3.22) by rotation, the thermal plumes moving across the flow domain requires a higher thermal contrast [124]. This was experimentally observed by Fernando *et al.* [174]. The variation of rms of temperature at the horizontal mid-plane ($z = 0.5H$) with rotation rate is shown in Fig. 3.27. For both the Rayleigh numbers, overall θ^m_{rms} increases in regimes I and II, although a slight dip in regime II is noticed. At low rotation rates, due to better mixing, the plumes are less likely to approach the central region, resulting in a homogeneous flow in the bulk, and hence shows lower θ_{rms}. However, as the rotation rate increases, the vortical columns of plumes appear even in the bulk region, and as a result, the rms of temperature increases. These observations are in line with the flow structures discussed in the previous section. It is important to note that this behaviour of increase in temperature rms does not appear at very high rotation rates. Here we observe a rapid decrease in the fluctuations, as shown in Fig. 3.26(a) for $Ra = 2 \times 10^6$. In regime III, the temperature fluctuations in the bulk reduce considerably, as shown in Fig. 3.27. This confirms the laminarization (or approaching towards the conduction stage) at strong rotation rates [126]. However, at $Ra = 2 \times 10^7$ this effect is not apparent, and θ^m_{rms} increases even in regime III (see Fig. 3.27). This is due to the higher buoyancy force in $Ra = 2 \times 10^7$ and hence requires even higher rotation rates to counter it.

3.8 Boundary layer

Boundary layer plays a key role in convective turbulence [76, 175–177]. For instance, the Nusselt number is directly related to the thermal boundary layer at the top and bottom of the flow domain, within which essentially all the temperature difference across the flow occurs. Shraiman and Siggia [75] reported that for large and moderate Prandtl numbers, the thermal boundary layer remains buried within the viscous layer, while for lower Pr the trend reverses. Interestingly, almost all the scaling theories for Nu, Ra and Pr are based on the characteristics of boundary layers, such as the marginal stability theory by Malkus [73], the turbulent

boundary layer assumption by Shraiman and Siggia [75], the laminar boundary layer assumption in Grossmann-Lohse theory [76, 77, 167], and multiple scaling introduced in the so-called ultimate regimes [178].

In order to characterize the boundary layer, we compute thickness of the thermal boundary layer using three techniques. Firstly, δ_θ^{Nu} which indicates the analytical thermal boundary layer thickness obtained from the relation $\delta_\theta^{Nu} \approx 1/2Nu$ [179, 180]. Secondly, δ_θ^{σ} which corresponds to the thickness computed as the vertical distance of the peak of the root-mean-square (rms) of temperature from the bottom plate [52]. Finally, δ_θ^{sl} which is the boundary layer thickness calculated as the vertical distance of the point from the bottom plate where the linear fit of the time-averaged temperature profile meets the bulk temperature [69, 181]. A sample temperature profile is shown in Fig. 3.28, where the geometric construction of the thermal boundary layer thickness is shown in the inset. Similar technique is adopted at all spatial locations (r, ϕ).

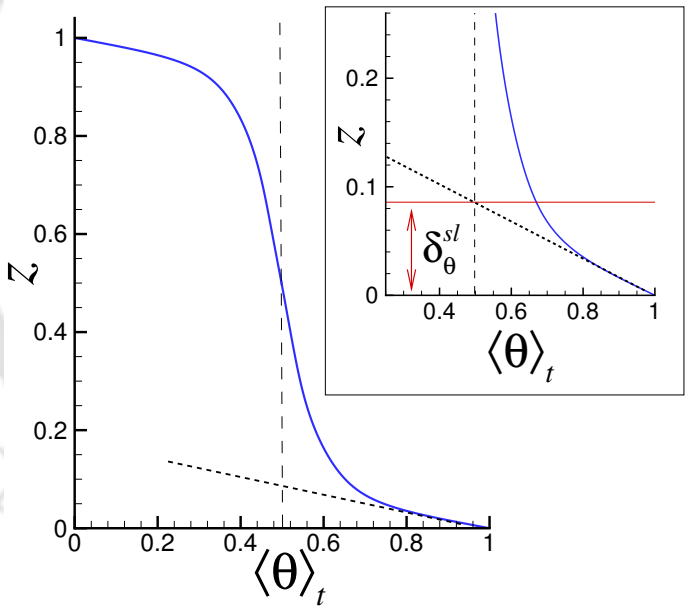

Figure 3.28: Schematic representation of the time averaged temperature profile showing the intersection of linear fit near the bottom plate with the bulk temperature. Inset shows the geometric construction of the thermal boundary layer thickness.

Figures 3.29(a) and 3.29(b) show the comparison between the thermal boundary layer thickness computed by different methods for $Ra = 2 \times 10^6$ and $Ra = 2 \times 10^7$, respectively. All the measures show while δ_θ remains constant at low rotation rate, it sharply increases at higher rotation rates. We observe that in regime I, boundary layer thickness obtained from all three methods are consistent, while at high rotation rates ($Ro^{-1} \gtrsim 10$) the one computed from the

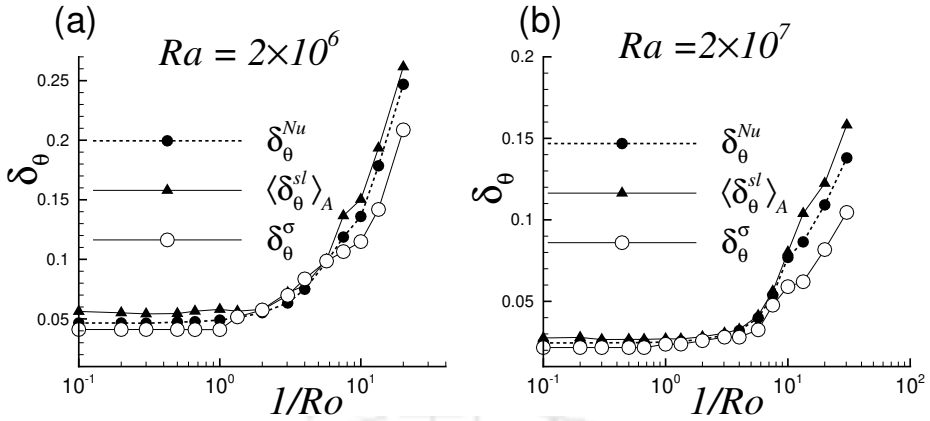

Figure 3.29: Thermal boundary layer thickness computed by different methods, as a function of inverse Ro.

rms profile under predicts the other two. Similar observation was made by Zhou *et al.* [181] in two-dimensional RBC, where the thickness from the rms method was found about 20% below that obtained from the slope method.

The variation of the thermal and viscous boundary layer thickness (obtained from the rms method) with rotation rate is shown in Fig. 3.30, where the dashed lines demarcate different flow regimes. For better visualization, the profiles are normalized by δ_θ corresponding to the non-rotating case, as $\delta^*_\theta = \delta^\sigma_\theta/\delta^{\sigma o}_\theta$ and $\delta^*_u = \delta^\sigma_u/\delta^{\sigma o}_u$. In regime I, the boundary layer thicknesses remain same as that of the stationary case. However, as rotation rate increases, i.e., in regimes II and III, the δ^*_θ increases while δ^*_u reduces. These observations are in good agreement with the numerical study by King *et al.* [140] in a Cartesian box with periodic sidewalls. They identified different flow regimes in turbulent convection based on the Ekmann number [$Ek = \nu/(2\Omega H^2)$] and Rayleigh number, such as $Ek \approx \infty$ the non-rotating case, $RaEk^{3/2} > 10$ the weakly rotating regime, and $RaEk^{3/2} > 10$ the geostrophic regime. For the rotation dominated regime, they reported a power-law behaviour for the viscous boundary layer as $\delta_v \propto Ek^{1/2}$. Generally, the viscous boundary layer in rotating flows is called as Ekman boundary layer [140] (named after V. W. Ekman [182]). In the present study, we obtain similar scaling with exponents 0.57 and 0.41 for Rayleigh numbers $Ra = 2 \times 10^6$ and $Ra = 2 \times 10^7$, respectively. For the thermal boundary layer thickness, King *et al.* [140] observed the scaling $\delta_\theta \propto Nu^{-1}$ at low rotation rates, while significant deviations were noted in the geostrophic regime. Interestingly, our present results show that δ_θ follows the scaling $\delta_\theta \propto Nu^{-1}$, for all the regimes.

In most of the previous studies, the boundary layer measurements are generally taken along

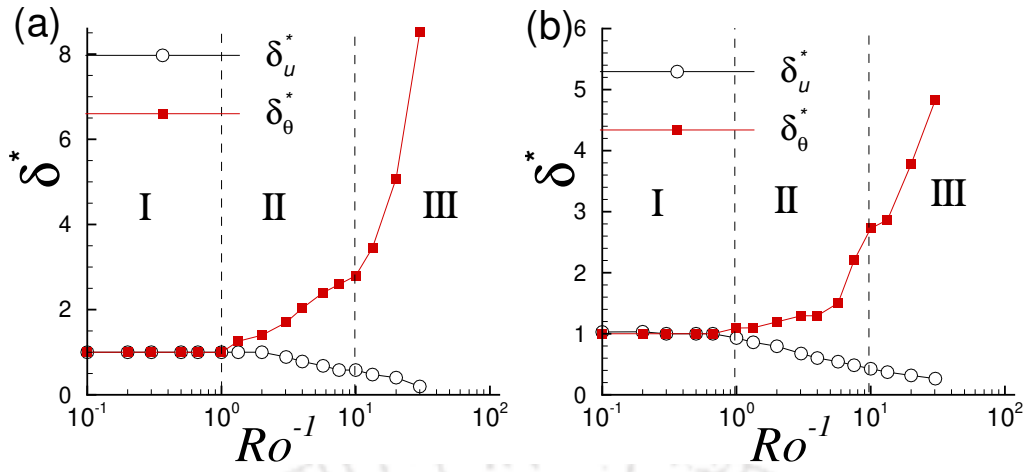

Figure 3.30: Variation of normalized viscous and thermal boundary layer thickness (obtained from the rms profiles) with rotation rate for (a) $Ra = 2 \times 10^6$ and (b) $Ra = 2 \times 10^7$.

the center of the convecting cell [183, 184]. An important question that arises here is whether the boundary layers appear uniformly across the horizontal surfaces. The numerical study by Werne [68] showed that boundary layers are distributed non-uniformly in space. The boundary layer computations along the cell's central region cannot reveal all of its properties, especially in a closed system due to the interactions between the flow and the solid walls [181]. Belmonte *et al.* [179] showed that the horizontal variation of the viscous and thermal boundary layers play a crucial role in the shear produced by LSC and boundary layers and the heat transfer dynamics. Hence the evaluation of spatial distribution of boundary layers is important in turbulent convection.

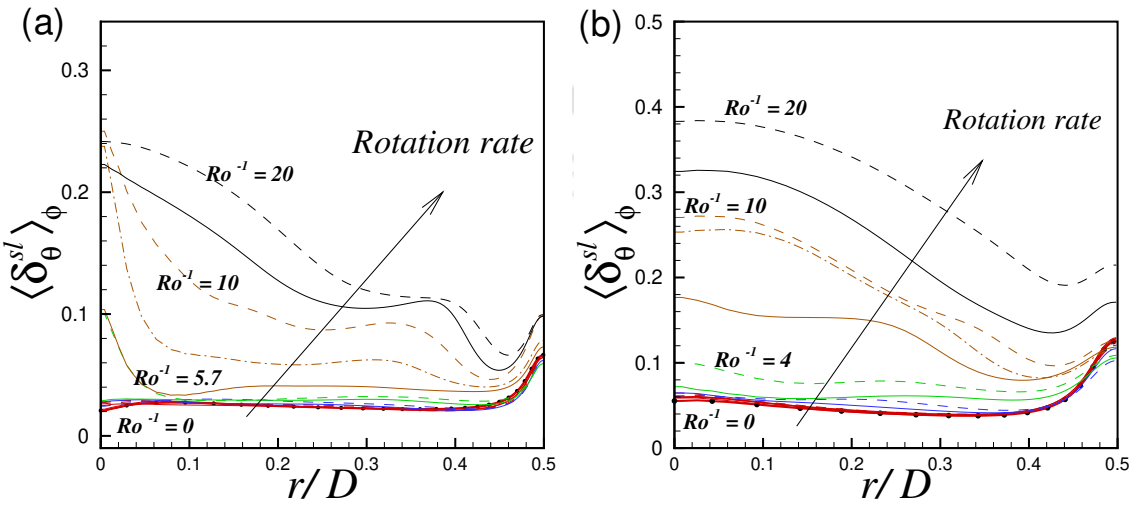

Figure 3.31: Variation of azimuthal averaged thermal boundary layer thickness along the radial direction for (a) $Ra = 2 \times 10^7$ and (b) 2×10^6, respectively, at different rotation rates.

The variation of azimuthal averaged boundary layer thickness $\langle \delta_\theta^{sl} \rangle_\phi$ along the radial direction is shown in Figs. 3.31(a) and 3.31(b). We find that the boundary layer is thinner and almost same as the non-rotating case at low rotation rates and increases considerably at higher rotation rates. The effect of rotation is evident near the core region of the cylindrical domain. However, it is less apparent near the lateral wall due to the near-wall viscous effects. Further, we observe that for low rotation rates, particularly in the LSC regime [red lines in Figs. 3.31(a) and 3.31(b)], the boundary layer is thicker near the wall and thinner near the core region, while at high rotation rates the trend is reversed. As rotation rate increases, the flow stabilizes as per Taylor-Proudman theorem [101, 102] and the temperature field approaches a conduction-like profile. Here we identify that flow stabilization is reflected noticeably near the core region as $\langle \delta_\theta^{sl} \rangle_\phi$ is much thicker along the core compared to that near the lateral wall.

3.9 Summary

In this chapter, we have presented a detailed three-dimensional numerical investigation on the effect of rotation in turbulent Rayleigh-Bénard convection. Direct numerical simulations were carried out in a cylindrical cell with $Pr = 0.7$ and two different Rayleigh numbers, $Ra = 2 \times 10^6$ and 2×10^7, for a wide range of rotation rate ($0 \leq Ro^{-1} \leq 30$). Based on the flow structure and Fourier modes, different flow regimes have been identified with respect to the rotation rates. We find LSC dominated flow at the low rotation rate ($Ro^{-1} \lesssim 1$), which is identified as the regime I. As the rotation rate increases, the fluctuations in the flow are damped out, and the coherence at a large scale is lost. At intermediate rotation rates, regime II ($1 \lesssim Ro^{-1} \lesssim 10$) is identified, where random chaotic plumes are observed without any specific organization of the flow. However, at even higher rotation rates, wall-bounded multiple roll structures such as quadrupole and sextupole have been observed, which is marked as the regime III ($Ro^{-1} \gtrsim 10$). Here the fluctuations in the bulk are completely absent, and the convection rolls are primarily concentrated near the lateral walls. This may be attributed to the strong Coriolis force that overshadows the buoyancy force at the rotation dominated flow regimes. Further, we observe that the addition of rotation severely affects the characteristics of the flow such as heat transport, dissipation rates and boundary layer thickness. The results show that rotation primarily has an inhibiting effect on the heat transfer rate. For both the Ra, Nusselt

number drops with increase in rotation rate. The decline is meagre at lower rotation rates and becomes significant at higher rotation rates. In regimes I and II, the PDF of thermal dissipation rate follows a stretched exponential behaviour, while significant deviations with shortened tail are observed at regime III, indicating the reduction in high amplitude dissipation events due to flow stabilization. As the rotation rate increases, the fluctuations in vertical velocity are considerably reduced, accompanied by flow stabilization along the vertical axis. At extremely high rotation rates, the strong Coriolis force ceases the vertical motion, and heat transfer occurs purely by conduction, which is identified by an almost linear mean temperature profile.

4

Dynamics and statistics of reorientations of large-scale circulation in weakly rotating turbulent Rayleigh-Bénard convection

In this chapter, we present the dynamics and statistics of reorientations of large-scale circulation in turbulent rotating Rayleigh-Bénard convection in a cylindrical cell with unit aspect ratio. Using the Fourier mode analysis of time series data obtained from different probes placed in the azimuthal direction of the container at the mid-plane, the orientation and associated dynamics of LSC are characterized. Further, the viscous and thermal dissipation rates along with the thermal boundary layer thickness are analyzed, and their association with the azimuthal orientation of LSC is studied. The amplitude of the first Fourier mode quantifies the strength of LSC and its phase Φ_1 gives the information of the azimuthal orientation of LSC. Based on their nature of occurrence, the reorientations are quantified as rotation-led and cessation-led. Further, depending on the degree of phase change, they are identified as partial and complete reversals. Finally, the statistics of reorientations of LSC are also investigated in this chapter. We observe that on an average, cessations account for about 4 to 7% of the total number of reorientations. Similar to the non-rotating counterpart, the reorientations in RRBC occur with a monotonically decreasing probability distribution.

4.1 Introduction

In turbulent state of RBC above a threshold Rayleigh number, statistical coherence of the flow is restored with the appearance of large-scale circulation with turbulent background which is a self-organized structure having length scale of order of size of the container and time-scale of the order of eddy turn-over time[40, 47, 74, 185–191]. During the course of time, the plane containing LSC exhibits changes in its orientation which is known as reorientations of LSC. This can occur in two ways in cylindrical domains: (a) by an azimuthal rotation of the plane containing LSC without considerable change in the circulation strength [43, 54], called as rotation-led reorientation and (b) by a momentary vanishing of the circulation strength accompanied by an arbitrary change in the orientation of flow, termed as cessation-led reorientation [54, 55]. Reorientations in which the large-scale flow completely changes its direction of circulation are termed as flow reversals [43]. Azimuthal changes in the orientation of LSC has been previously observed in a number of studies [45, 56, 60, 192–195]. Sudden changes in the orientation of LSC are not only interesting phenomenon but are extremely relevant in many of the geophysical and astrophysical flows. For example, field reversals are common in the natural convection of Earth's atmosphere [196] and magnetic field reversals in geodynamo [197]. Understanding the genesis of LSC and the nature of the instabilities that lead to the reorientations of LSC is one of the classical problems in RBC [57].

Experiments have played a key role in understanding the characteristics and dynamics of LSC in turbulent RBC. Cioni *et al* [43] identified LSC from dipolar temperature distribution obtained from probes placed along the azimuth of the container. Reversals in the flow were also obtained as the fluctuations in temperature switched sign randomly. Niemela *et al.* [44] and Sreenivasan *et al.* [45] also performed experiments in turbulent RBC with helium and reported reversals of LSC. Similar experiments were carried out by Brown *et al.* [54] and Brown and Ahlers [56] with water as the working fluid. The probes were placed at three different horizontal planes ($z = 1/4H$, $1/2H$ and $3/4H$) to get a better idea on the dynamics of LSC. They identified reorientations of LSC using the phase of the first Fourier mode Φ_1 and quantified them as rotation-led and cessation-led based on the amplitude of the modes. Brown and Ahlers [56] observed that rotation-led reorientations were more frequent than cessation-led reorientations. The rotation-led reorientations exhibited power-law distribution, while cessation-led reorien-

tations followed uniform distribution. Further, both rotations and cessations showed Poisson distribution in time. They observed that the probability density function (PDF) of the time interval between successive reorientations follows an exponential function. Similar observations were made by Xi and Xia [60]. However, Sreenivasan *et al.* [45] showed that although the PDF of time interval between successive reorientations shows exponential nature, for lower time intervals, it could be well fitted with power-law distribution. Xi and Xia [60] experimentally studied the aspect ratio dependency of reorientations in turbulent RBC. They observed that in contrast to the power-law distribution in unit aspect ratio container, reorientations in $\Gamma = 0.5$ geometry follows an exponential distribution. In another study [59], they found that the reorientations occur more frequently in $\Gamma = 0.5$ than these happen in $\Gamma = 1$. Funfschilling and Ahlers [58] observed that in addition to the azimuthal meandering of the direction of circulation, the upper and lower halves of LSC undergo twisting oscillations.

The numerical studies on the reorientations or reversals of LSC in RBC are rare compared to the experimental ones. Verzicco and Camussi [180] performed a detailed numerical study on the effect of Prandtl number on the dynamics of convective flow inside a cylindrical cell. They noticed that there is a significant drop in Nusselt number when the strength of LSC decreases for lower Pr compared to higher Pr. Later Stringano and Verzicco [198] studied the mean flow structure in RBC in a slender cylindrical cell and observed a single convection roll breaking into two counter-rotating rolls stacked vertically one above the other. Benzi and Verzicco [199] numerically investigated the statistical properties of the large scale flow in RBC at $Pr = 0.7$ and $Ra = 6 \times 10^5$, by using an external random perturbation on the temperature field. A detailed numerical study on the dynamics of reorientations of LSC in RBC was carried out by Mishra *et al.* [51], where they reproduced the experimentally observed rotation-led reorientations, cessation-led reorientations and double-cessations for a Rayleigh number range $6 \times 10^5 \leq Ra \leq 3 \times 10^7$, which is considerably lower than its experimental counterparts.

Although, there are many existing studies on the reorientation dynamics of LSC in turbulent RBC, the effect of rotation on these dynamics is less explored. Kunnen *et al.* [128] investigated RRBC both numerically and experimentally at $Ra = 2 \times 10^9$ and $Pr = 6.4$. At low rotation rates ($Ro^{-1} \lesssim 0.83$), a domain-filling LSC was observed, while it breaks down at higher rotation rates. At higher rotation rates, the Ekman-vortex structures diminish the strength of the LSC, and as a result, for Ro^{-1} significantly above unity, the LSC structure breaks down

[134, 200]. They observed a retrograde precession of the LSC structure, which depends on the rotation rate. However, prograde precession of the LSC at modest rotation rates ($Ro^{-1} \lesssim 1$) was observed by Weiss and Ahlers [201] in their experimental investigations on RRBC in a cylinder with aspect ratio $\Gamma = 0.5$ for Rayleigh number range $2.3 \times 10^9 \lesssim Ra \lesssim 7.2 \times 10^{10}$. Further, they observed that for large aspect ratio containers, LSC could manifest in the form of single or double-roll structures. The rotation has a stabilizing effect on the single-roll, while it destabilizes the double roll. This was later numerically substantiated by Stevens *et al.* [202] for the same parameter range.

Some of the critical questions that revolve around the analysis of LSC and its dynamics are: (i) How the coherent structure appears amidst the turbulent background? (ii) How the heat transfer and boundary layer dynamics get affected due to its presence? (iii) What are the different characteristics of the reorientations and the corresponding distributions of occurrence of these events? As discussed above, there are many experimental works that have taken the lead in these directions, but still comprehensive numerical and theoretical studies which may give some quantitative picture to them are lacking.

In the previous chapter, we identified different flow regimes in turbulent rotating RBC. At low rotation rates, LSC dominated flow was obtained, while at higher rotation rates, such coherence in large scale is lost, and at even higher rotation rates, quadrupolar and sextupolar flow behaviours were observed. In this chapter, we focus mainly on the LSC dominated flow regime. Three-dimensional direct numerical simulations are performed at Rayleigh numbers 2×10^6 and 2×10^7, for a wide range of rotation rate ($0 \leq Ro^{-1} \leq 30$) with air ($Pr = 0.7$) as the working fluid. To begin with, we identify the LSC using instantaneous flow structures and time signature of vertical velocity at the mid-height of the cylinder. Then we study the characteristics of LSC and its relation with heat transfer, boundary layer dynamics, and the thermal and viscous dissipation rates. Further, the dynamics of LSC are discussed in detail, where different types of reorientations, such as rotation-led and cessation-led, and partial and complete reversals are examined. Finally, the statistics of reorientation are presented.

4.2 Identification and characteristics of LSC

Large-scale circulation is a coherent structure in RBC where the thermal plumes organize to form a 'large-scale' convection roll with hot and cold fluid rising and dipping, respectively, along opposite sides of the lateral wall. Over the years a number of experimental [40, 56, 58, 89, 188] and numerical [51, 180, 198] studies have reported existence, reversal and a few statistical measure of LSC in stationary RBC. However, such attempts on the dynamics of LSC for flows modulated by rotation are less. Here, we focus on the identification of LSC in rotating and nonrotating RBC using flow structures and time signals of vertical velocity.

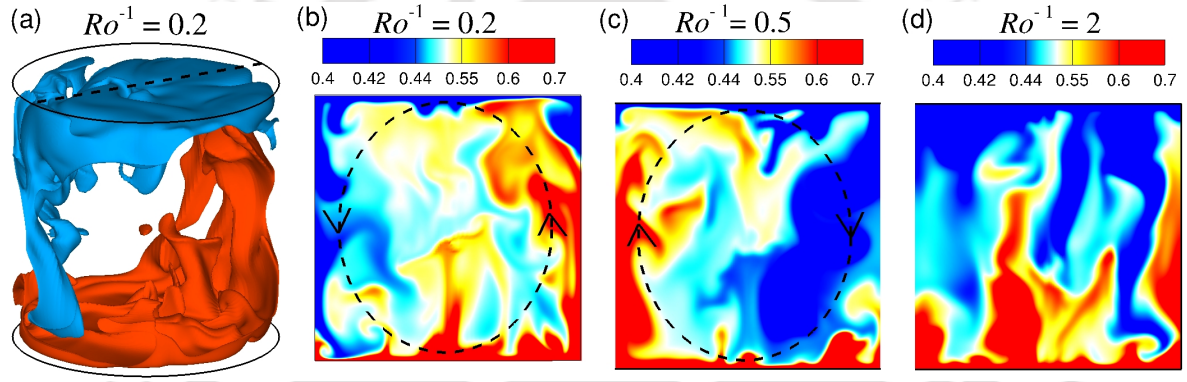

Figure 4.1: (a) Temperature iso-surfaces at $\theta = 0.4$ (blue) and $\theta = 0.6$ (red) indicating LSC for $Ra = 2 \times 10^7$ and $Ro^{-1} = 0.2$. The dashed line indicates the azimuthal orientation of LSC. (b) Temperature contour at the vertical plane where the LSC is oriented. The dashed line indicates the direction of circulation. (c) Temperature contour at LSC plane for $Ro^{-1} = 0.5$. (d) Temperature contour at $\phi = 0$ plane for $Ro^{-1} = 2$.

A sample view of the LSC is presented through temperature iso-surfaces in Fig. 4.1(a) for $Ra = 2 \times 10^7$ and $Ro^{-1} = 0.2$. The temperature contours at the vertical mid-plane along which LSC is aligned [indicated in frame (a)] is shown in Fig. 4.1(b) where the motion of the plume is shown by dashed line. Hot plumes are observed to erupt from the bottom boundary layer and plunge into the top plate and during its course of motion, it leaves structures along the lateral wall that are visually close to a wall jet. A similar flow structure is observed for $Ro^{-1} = 0.5$, shown in Fig. 4.1(c), although the sense of circulation is reversed. As discussed in the previous chapter, we observe LSC behaviour at lower rotation rates of $Ro^{-1} \lesssim 1$, while at higher rotation rates, the plumes are declustered as shown in Fig. 4.1(d), and resultantly the LSC structure is lost.

In order to analyze the dynamical characteristics of LSC, time-histories of vertical velocity are recorded at 36 equispaced azimuthal stations $(0, \pi/18, \pi/9, \pi/6, \cdots 35\pi/18)$ that are located at the mid-vertical plane ($z = 0.5$) near the lateral wall ($r = 0.4R$). Figure 4.2 shows the time signals of vertical velocity at either ends of two diametrical planes separated by an angle $\pi/2$. Recall that LSC is primarily identified by occurrence of non-zero mean vertical velocities that are anti-correlated, shown in rectangular windows (red). Note, while the LSC persists along a diameter, high-variance fluctuations are observed on the other and they switch between each other. This feature is popularly termed as reversal/reorientation of LSC. The time over which an LSC persists along a diameter depends strongly on the rotation rate. Figure 4.3(a) shows that as rotation rate is increased, the switching frequency of the signals increases.

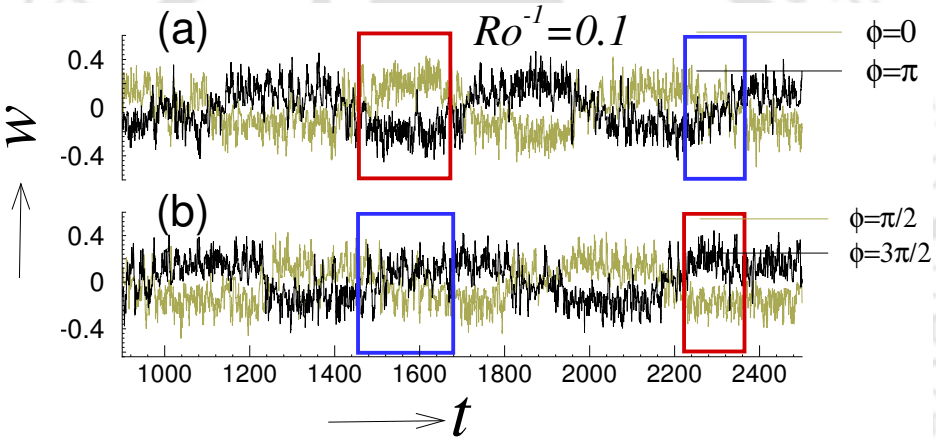

Figure 4.2: Time traces of vertical velocity from numerical probes at locations $\phi = 0, \pi/2, 3\pi/2$, and π for $Ra = 2 \times 10^7$ and $Ro^{-1} = 0.1$. The red and blue boxed regions indicate the anti-correlated signals and high-variance data, respectively, at diameters which are $\pi/2$ apart.

Recall that in the previous chapter, we identified the LSC regime based on the dominance of the energy fraction of the first Fourier mode. Another formalism that can be used to quantify the mean wind is the strength of LSC, S_{LSC} [202], defined as

$$S_{LSC} = Max\Big[\Big(\frac{E_1}{E_{tot}} - \frac{1}{N}\Big)/\Big(1 - \frac{1}{N}\Big), 0\Big]. \tag{4.1}$$

where E_1 and E_{tot} indicate the energy contained in the first Fourier mode and total energy, respectively, as discussed in the previous chapter. The value of S_{LSC} lies between 0 and 1. The strength close to unity indicates that most of the energy is contained in the first Fourier mode, i.e., $E_1/E_{tot} \approx 1$ and the azimuthal vertical velocity profile is close to a cosine fit, thus

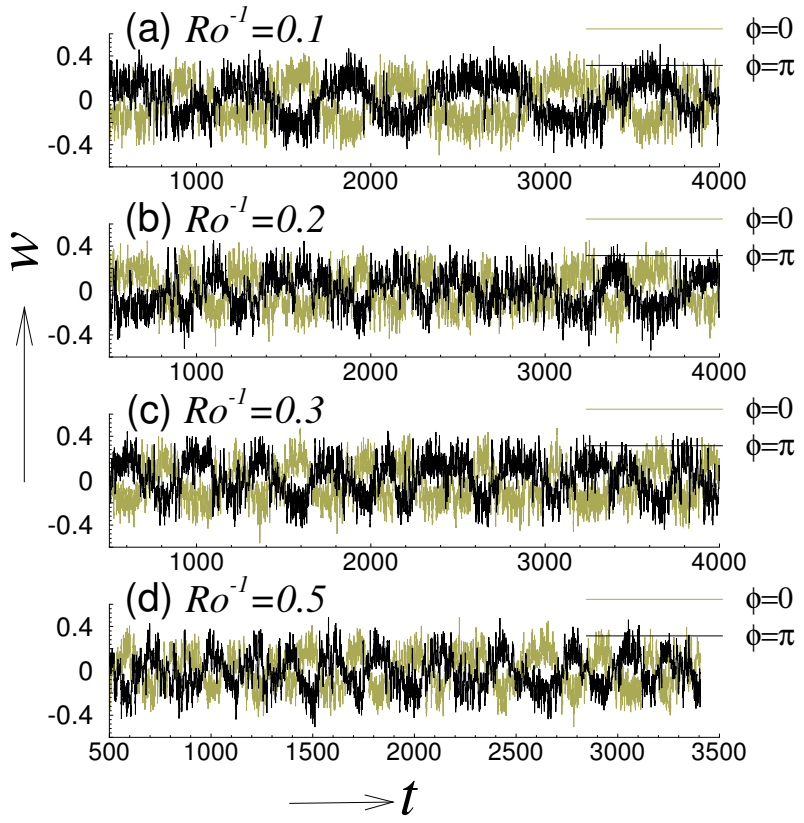

Figure 4.3: Time traces of vertical velocity from numerical probes at locations $\phi = 0$ and π for $Ra = 2 \times 10^7$ at (a) $Ro^{-1} = 0.1$, (b) $Ro^{-1} = 0.2$, (c) $Ro^{-1} = 0.3$, and (d) $Ro^{-1} = 0.5$.

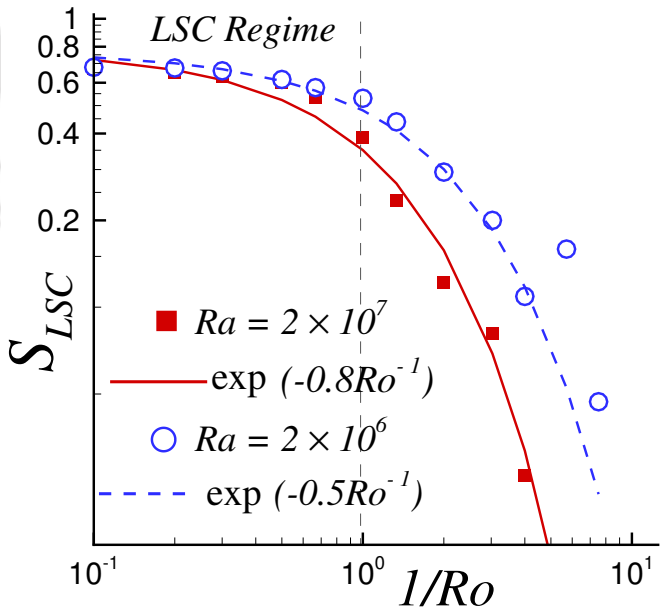

Figure 4.4: Exponential decay of the strength of the first Fourier mode with the increase in rotation rate for $Ra = 2 \times 10^6$ and 2×10^7.

indicating LSC. On the other hand, its value near to zero implies that the energy fraction of first Fourier mode is smaller ($E_1/E_{tot} << 1$), in effect, most of the energy is contained in the higher modes and hence, the flow behaviour is far from LSC. Thus, S_{LSC} is an indication of the circulation strength of LSC. In Fig. 4.4, we plot the circulation strength against the rotation rate. At low rotation rates, the strength is as high as 0.7; however, it drops exponentially with the increase in rotation rate. We observe a perfect exponential fit as $S_{LSC} \propto \exp(-0.5Ro^{-1})$ and $S_{LSC} \propto \exp(-0.8Ro^{-1})$ for $Ra = 2 \times 10^6$ and 2×10^7, respectively. The decay of S_{LSC} is at a higher rate for the higher Rayleigh number. We identify the LSC regime (or regime I) as $Ro^{-1} \lesssim 1$ where the circulation strength is greater than 0.5. This is consistent with the observations made by Kunnen *et al.* [128] and Stevens *et al.*[202], where they reported the break-down of LSC for $Ro^{-1} \gtrsim 0.86$.

4.2.1 Effect of LSC on the boundary layers

As the LSC appears in the system, the flow near the boundary layers gets severely affected [69, 203]. At this point, we are interested to see how the boundary layer thickness varies along and perpendicular to the plane containing LSC. The boundary layer thickness (δ_θ^{sl}) is calculated as the vertical distance of the point from the bottom plate where the linear fit of the time-averaged temperature profile approaches the bulk temperature [69, 181]. Similar technique is adopted to compute the boundary layer thickness for all the spatial locations (r, ϕ). Details of computation of the boundary layer thickness can be followed from the previous chapter.

Figure 4.5(a) shows the instantaneous temperature iso-surfaces indicating LSC structure. The time-averaged flow structure for the same is shown in Fig. 4.5(b), which is used to compute the thermal boundary layer thickness. Here averaging is performed within a time-span at which LSC persists in a particular plane. The planar contours thus obtained near the top and bottom plates are shown in Fig. 4.5(c), where the orientation of LSC is shown by dashed lines. Close to the bottom plate, thermal boundary layer is thicker near the region where hot plumes rise and is thinner near the opposite side of the lateral wall where the cold plumes plunge into the boundary layer. Similar observation is made near the top plate. Further, we plot δ_θ^{sl} along and perpendicular to the direction of LSC in Fig. 4.5(d). Note that perpendicular to LSC, the boundary layer thickness varies almost symmetrically. However, along the plane containing

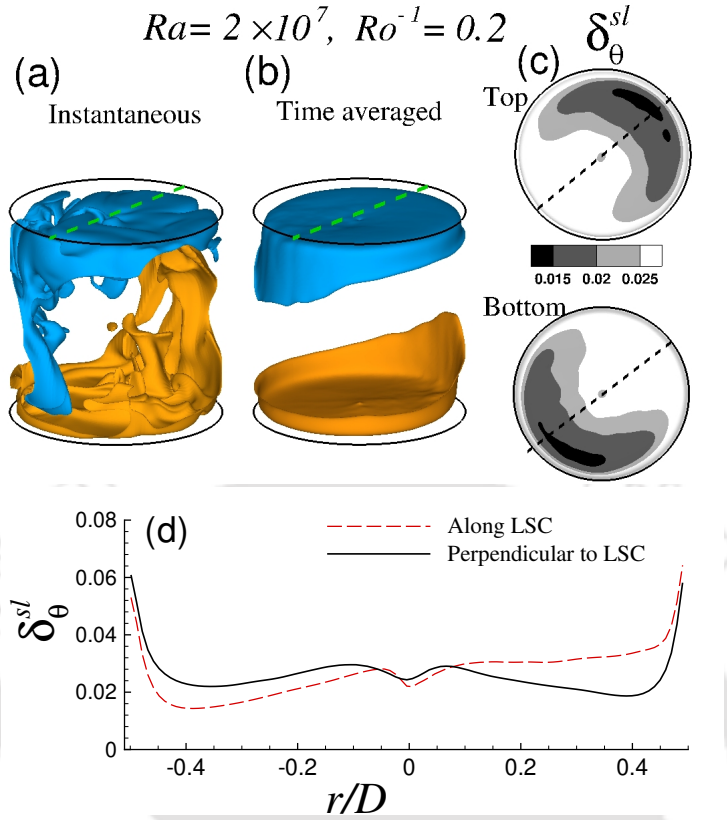

Figure 4.5: (a) Instantaneous temperature iso-surfaces at $\theta = 0.4$ (blue) and $\theta = 0.6$ (orange) indicating LSC. The dashed line represents the azimuthal orientation of LSC. (b) Time averaged temperature iso-surfaces at $\theta = 0.4$ and $\theta = 0.6$, obtained from a time span at which LSC persists. (c) Spatial distribution of thermal boundary layer thickness near the top and bottom plate. (d) Variation of boundary layer thickness along and perpendicular to the direction of LSC at the bottom.

LSC, δ_θ^{sl} shows an asymmetric trend, as it is thicker at one side and thinner near the opposite side of the lateral wall. These observations are consistent with the time traces of the vertical velocity discussed in the previous subsection (refer Fig. 4.2), wherein, the signal shows high variance fluctuation along the transverse direction of LSC with zero-mean value, and fluctuation about finite mean value along the LSC direction. The fluctuation about the finite-mean along LSC direction can clearly be associated with asymmetric behaviour of boundary layer width near the lateral wall.

4.2.2 Effect of LSC on heat transfer and dissipation rates

Some of the key issues that generally come up in RBC are: How heat transport occurs from the hot to the cold plate? And what is the role of thermal plumes in the heat transport and

subsequent dissipation near the boundary layers? Here we analyze how the heat transfer rate and dissipation rates are associated with the orientation of LSC. As discussed in the previous chapter, the local heat transfer rate, which is quantified by the Nusselt number at each spatial location is computed as $Nu(\boldsymbol{r}) = \sqrt{RaPr}w\theta - \dfrac{\partial\theta}{\partial z}$, where $\boldsymbol{r}$ is the position vector [166]. In chapter 3, we observed that the average Nusselt number across the flow domain remains almost uniform. Here, we evaluate how the heat transfer rate varies along horizontal planes close to the isothermal plates. Similarly, the distribution of the viscous ($\epsilon_u = \sqrt{Pr/Ra}|\nabla \boldsymbol{u}|^2$) and thermal dissipation ($\epsilon_\theta = 1/\sqrt{RaPr}|\nabla\theta|^2$) rates are also analyzed in connection with the thermal plumes which constitute the LSC.

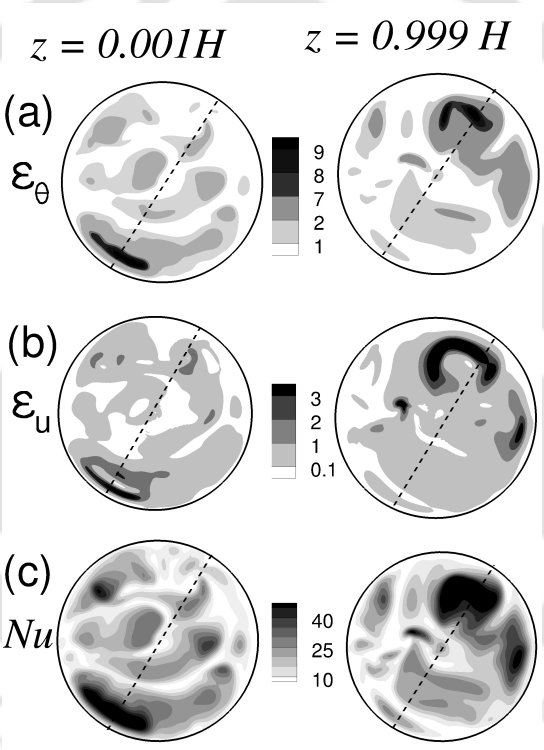

Figure 4.6: Spatial distribution of (a) thermal dissipation rate and (b) viscous dissipation rate near the bottom (left panel) and top (right panel) plate. The maximum dissipation is observed in the region where the plumes splash into boundary layers near the isothermal plates. (c) Spatial distribution of Nusselt number at the bottom (left panel) and top (right panel) plate. The dotted line indicates the azimuthal orientation of LSC.

The contours of thermal and viscous dissipation rates near the top and bottom plates [at the same instant as in Fig. 4.5(a)] are shown in Figs. 4.6(a) and 4.6(b), where the azimuthal orientation of LSC is represented by the dashed line. We observe that the dissipation rates vary significantly along the direction of LSC. The thermal and viscous dissipations are maximum in

the regions where the plumes collide with the boundary layer. Similar high-amplitude dissipation events associated with the collision of thermal plumes were observed by Schumacher and Scheel [204]. Further, the contours of Nusselt number at the top and bottom plates are shown in Fig. 4.6(c), which also suggests maximum heat transfer occurs at locations where the plumes collide with the boundary layer.

After characterizing the heat transfer and dissipation rates in the LSC regime, we now turn our focus to the dynamics of the LSC. In the following section, we discuss different kinds of azimuthal reorientations of the LSC, which is followed by the detailed statistical analysis of the reorientations.

4.3 Dynamics of reorientations

The vertical plane containing LSC is known to show spontaneous and erratic drifts or directional changes with time [55, 192–195, 205]. These sudden and significant changes in the orientation of LSC are referred to as reorientations of LSC [56]. During some reorientations, the amplitude of the first Fourier mode almost drops to zero and such events are termed as cessation-led reorientations. While in others, the LSC rotates azimuthally without considerable change in the amplitude of the first Fourier mode [43, 54]. These are referred as rotation-led reorientations. Although these events are reported experimentally by Brown *et al.* [54], Brown and Ahlers [56] and Xi *et al.* [206], confirmation by numerical studies is rare. Here we probe the dynamics and statistics of reorientations of LSC in rotating convection using direct numerical simulations.

Reorientations are generally quantified using the amplitude $A_k = |\hat{u}(k)|$ and phase $\Phi_k = \tan^{-1}[\mathbf{Im}\ \hat{u}(k)/\mathbf{Re}\ \hat{u}(k)]$ of the Fourier modes. Note that $\hat{u}_k$ denotes the k^{th} Fourier mode obtained from the Fourier transform of the velocity signal (u_j) from N ($= 36$) data points along the cylinder azimuth as $\hat{u}_k = \sum_{j=1}^{N} u_j e^{-i2\pi kj/N}$. The characterization of reorientations of LSC is not a well established concept, but in literature we find a few works in this direction. For example, Brown *et al.* [54] and Brown and Ahlers [56] identified the reorientations based on the phase of the first Fourier mode Φ_1 using two criteria: (a) The net angular change $|\Delta\Phi_1|$ has

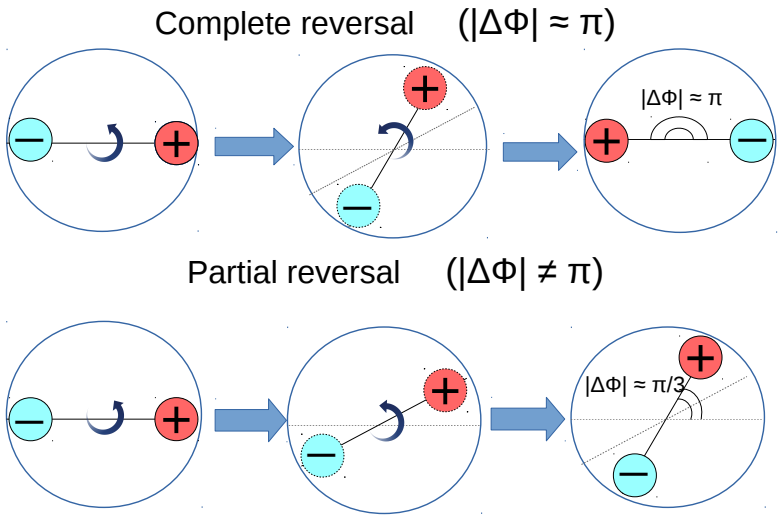

Figure 4.7: Schematic diagram showing the partial and complete reversals. The solid line indicates the azimuthal orientation of LSC with up-flow (+) and down-flow (−) on either side of the lateral wall.

to be greater than $\pi/4$, and (b) magnitude of the net azimuthal rotation rate $|\Delta\Phi_1/\Delta t|$ has to be greater than $\pi/5T_{eddy}$, where T_{eddy} is the eddy turn over time. The above procedure results in multiple overlapping subsets of reorientations and thus requires further conditioning using quality factors to pick the appropriate reorientation. To avoid this complexity, in the present study we ensure that the azimuthal rotation rate between any two adjacent points is greater than the specified cutoff ($\pi/5T_{eddy}$). Here $T_{eddy} = 2H/w^{rms}$ and w^{rms} is the average of the rms of vertical velocity time signals from the previously mentioned 36 numerical probes placed at the mid-vertical plane. Further, we identify these reorientations as complete reversal if the phase change $|\Delta\Phi_1| \approx \pi$ and as partial reversal if $|\Delta\Phi_1| \neq \pi$, as proposed by Mishra *et al.* [51]. Figure 4.7 shows the schematic representation of a partial and complete reversal at the horizontal mid-plane $z = 0.5$. The orientation of the plane containing LSC is shown by the solid line, while dashed lines indicate the intermediate stages during the reorientation. The up-flow and down-flow of the hot and cold fluid on opposite sides of the lateral wall are denoted by the $+$ and $-$ signs, respectively. Note that after a complete reversal, the direction of flow is interchanged as the up-flow and down-flow switches their corresponding sides.

The time evolution of the phase of the first Fourier mode along with the vertical velocity signals from different numerical probes are shown in Fig. 4.8. Here we identify reversals by

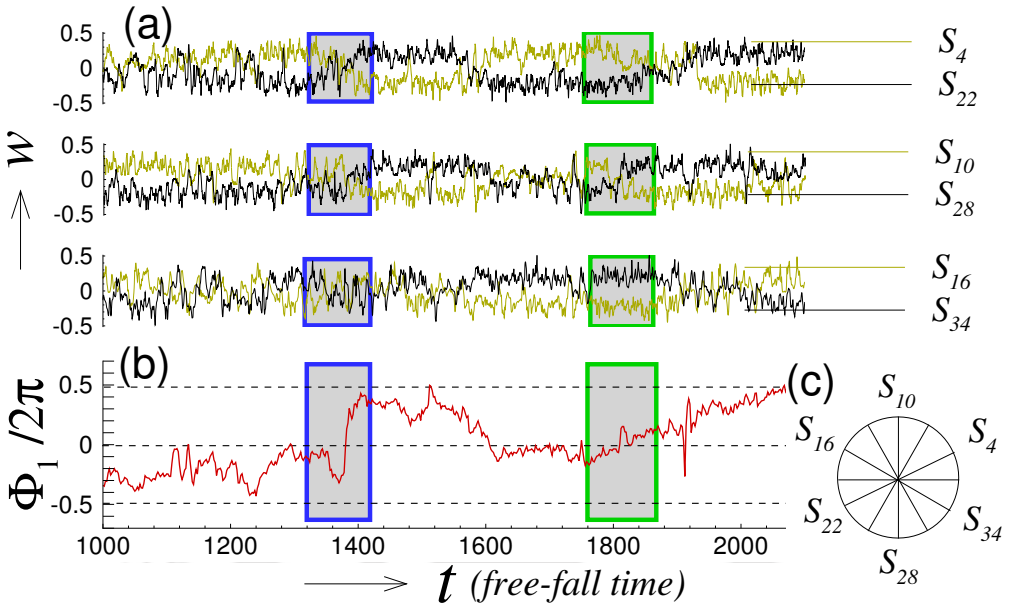

Figure 4.8: (a) Time signals of vertical velocity from different numerical probes at mid-plane of the cylinder and (b) the phase of first Fourier mode showing complete (blue box) and partial reversals (green box) for non-rotating RBC at $Ra = 2 \times 10^6$. (c) Schematic representation of the location of the numerical probes.

the sudden and considerable change in the phase Φ_1, along with the switching of mean vertical velocity. At $t \approx 1380$, a complete reversal is observed, where the phase change $|\Delta\Phi_1| \approx \pi$. This is accompanied by the switching of mean flow across all the probes. However, for the reversal at $t \approx 1810$, the mean value of w does not switch at all probes. Clearly, at probes S_4 ($\phi = \pi/6$), S_{22} ($\phi = 7\pi/6$), S_{16} ($\phi = 5\pi/6$) and S_{34} ($\phi = 11\pi/6$) the mean vertical velocity remains unaltered, while it switches sign at S_{10} ($\phi = \pi/2$) and S_{28} ($\phi = 3\pi/2$). This is a partial reversal where the phase change is less than π. We observe several partial reversals in our simulations while the number of complete reversals is very less.

To get better insights into the nature of these reversals, we analyze the time evolution of the first two Fourier modes. For both RBC and RRBC at low rotation rates (where LSC persists), the first Fourier mode dominates over the other modes. In Fig. 4.9, we observe that during the reorientations amplitude of the first Fourier mode $A_1 = |\hat{u}_1|$ drops below its mean value. On closer inspection, we observe that although A_1 shows a small dip in magnitude near $t \approx 1380$, the rise in amplitude of the second mode $A_2 = |\hat{u}_2|$ is marginal and thus the amplitude fraction A_2/A_1 remains negligibly small. Thus we identify these as rotation-led reorientation, where the LSC structure rotates azimuthally to reorient itself to a new direction without much change

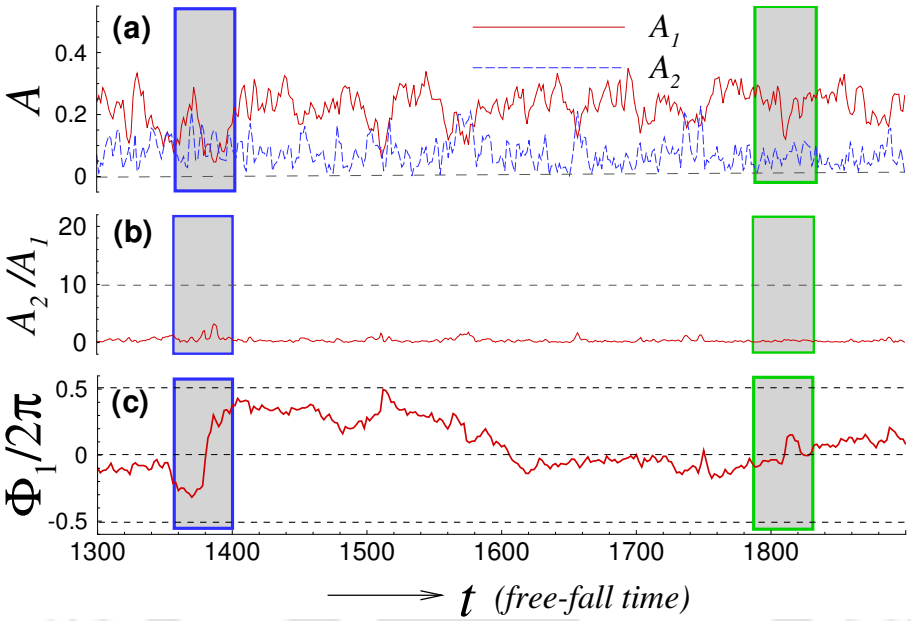

Figure 4.9: (a) The time series of first and second Fourier modes, (b) their corresponding amplitude ratio A_2/A_1 and (c) phase of the first Fourier mode during complete (blue box) and partial (green box) reversals for non-rotating RBC at $Ra = 2 \times 10^6$.

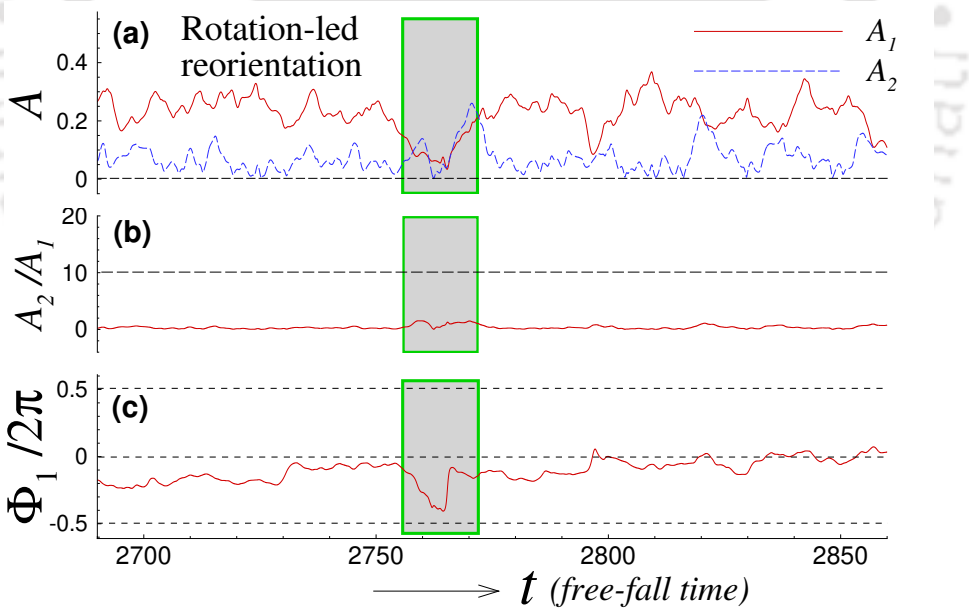

Figure 4.10: (a) The time series of first and second Fourier modes, (b) their corresponding amplitude ratio A_2/A_1, and (c) phase of the first Fourier mode during a rotation-led reorientation obtained for $Ra = 2 \times 10^6$ and $Ro^{-1} = 0.1$. The boxed region identifies the reorientation.

in the circulation strength.

Rotation-led reorientation observed for $Ra = 2 \times 10^6$ and $Ro^{-1} = 0.1$ is shown in Fig. 4.10. At $t \approx 2765$, the phase of the first Fourier mode shows an angular change $|\Delta\Phi_1| \approx 2\pi/3$.

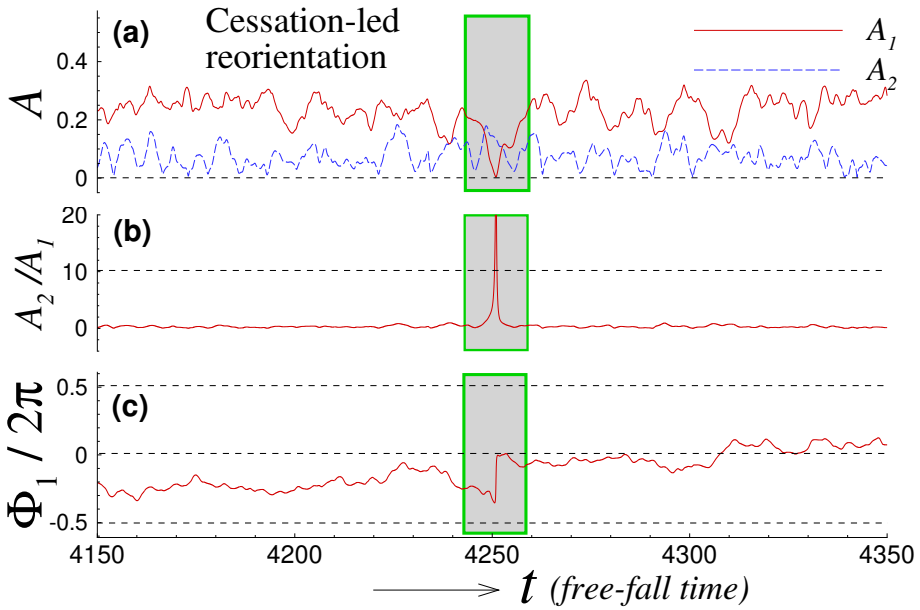

Figure 4.11: (a) The time series of first and second Fourier modes, (b) their corresponding amplitude ratio A_2/A_1, and (c) phase of the first Fourier mode during a cessation-led reorientation obtained for $Ra = 2 \times 10^6$ and $Ro^{-1} = 0.2$. The dotted line in the amplitude fraction plot indicates the cutoff value $A_2/A_1 = 10$, used to identify cessations.

Although A_1 shows a local minimum at this instant, A_2 is also minimal, and resultantly the amplitude fraction is close to zero, as shown in frame (b). However, during a different reorientation shown in Fig. 4.11, the amplitude of the first Fourier mode drops considerably ($A_1 \to 0$) and that of the second rises. These are identified as cessation-led reorientations. Here the strength of LSC diminishes at the cessation point (peak of A_2/A_1) and the flow reorients itself at any arbitrarily chosen direction. Due to the fluctuations in the A_1 and A_2 time signals, we use the amplitude fraction A_2/A_1 to clearly recognize the cessations. In the present study, cessations are identified as sharp peaks in the amplitude fraction such that $A_2/A_1 \gtrsim 10$, which is in line with the criteria used by Mishra *et al.*[51] to recognize these events in non-rotating RBC. The cutoff value is chosen such that it allows the identification of cessations most appropriately. Here we observe a partial cessation-led reorientation near $t \approx 4250$ with an angular change $|\Delta\Phi_1| \approx 3\pi/4$. The experimental studies by Brown *et al.* [54], Brown and Ahlers [56] and Xi *et al.* [206] have also reported cessation-led reorientations.

The reorientations observed for non-rotating and rotating RBC at $Ra = 2 \times 10^7$ are shown in Fig. 4.12. Although the amplitude ratio indicates cessation events, on close inspection of the phase Φ_1, two successive angular changes are observed here, i.e., one before the cessation

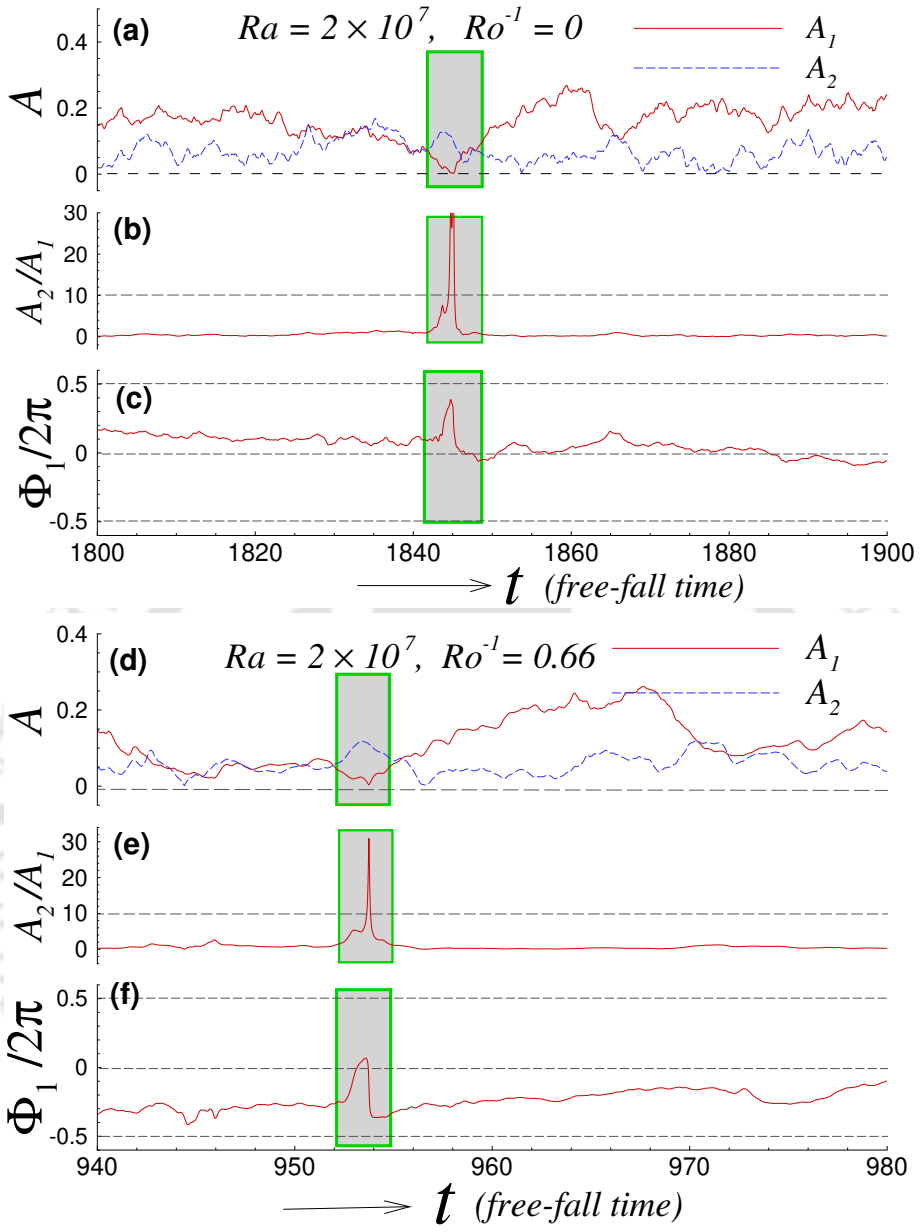

Figure 4.12: The time series of (a,d) first and second Fourier modes, (b,e) their corresponding amplitude ratio A_2/A_1 and (c,f) phase of the first Fourier mode during cessation-led reorientation for $Ra = 2 \times 10^7$ at $Ro^{-1} = 0$ (top panel) and $Ro^{-1} = 0.66$ (bottom panel). The dotted line in the amplitude fraction plot indicates the cutoff value $A_2/A_1 = 10$, used to identify cessations.

point (spike in A_2/A_1) and another after it. For $Ro^{-1} = 0.66$, at $t \approx 952$ the flow reorients with an angular change $|\Delta\Phi| \approx 2\pi/3$, the amplitude fraction spikes up instantly and reaches a local maximum (cessation point). Instantly, the flow reorients in the opposite direction with an angular change $|\Delta\Phi| \approx 3\pi/4$ and A_2/A_1 drops steeply. Note that the rate of angular change $|\Delta\Phi/\Delta t|$ is smaller for the first reorientation (gradual slope), while it is steeper for the second.

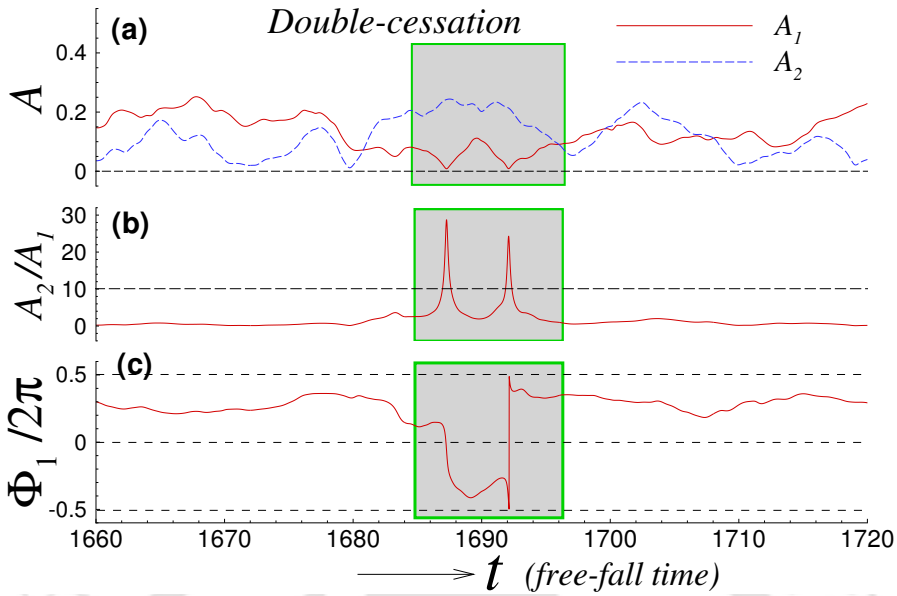

Figure 4.13: (a) The time series of first and second Fourier modes, (b) their corresponding amplitude ratio A_2/A_1 and (c) phase of the first Fourier mode during double cessation observed for $Ra = 2 \times 10^6$ at $Ro^{-1} = 0.3$. The dotted line in the amplitude fraction plot indicates the cutoff value $A_2/A_1 = 10$, used to identify cessations. The boxed region bounds an eddy turnover time within which the double-cessation prevails.

This means that the LSC gradually slowed down its reorientation in a particular azimuthal direction, reached a point corresponding to the peak in A_2/A_1, and then sped up to reorient in the opposite direction. We quantify these as two reorientations, of which the second one is identified as cessation-led.

Occasionally, two cessations occur in quick succession, i.e., within a eddy turnover time. These are referred as double-cessations. Figure 4.13 shows a double-cessation observed for $Ra = 2 \times 10^6$ and $Ro^{-1} = 0.3$. The boxed region bounds an eddy turnover time ($T_{eddy} \approx 11$ free-fall time units), within which the double-cessation occurs. The amplitude of the first Fourier mode drops ($A_1 \to 0$) at $t \approx 1687$ and $t \approx 1692$, accompanied by a sharp rise in the amplitude fraction A_2/A_1. Here we observe that the phase of first Fourier mode Φ_1 changes successively, first by $|\Delta\Phi_1| \approx \pi$ and second by $|\Delta\Phi_1| \approx \pi/2$. The angular change as a result of the double-cessation is the sum of these two successive events. Double-cessations were first reported by Xi *et al.* [206] in their experimental work. They proposed that these are caused by the situation that whatever event that triggered the first cessation had insufficient energy to overturn the flow, and as a result, the mean wind stopped and then started again in the previous direction. Note that in the double-cessations observed by Xi *et al.* [206] the effective angular

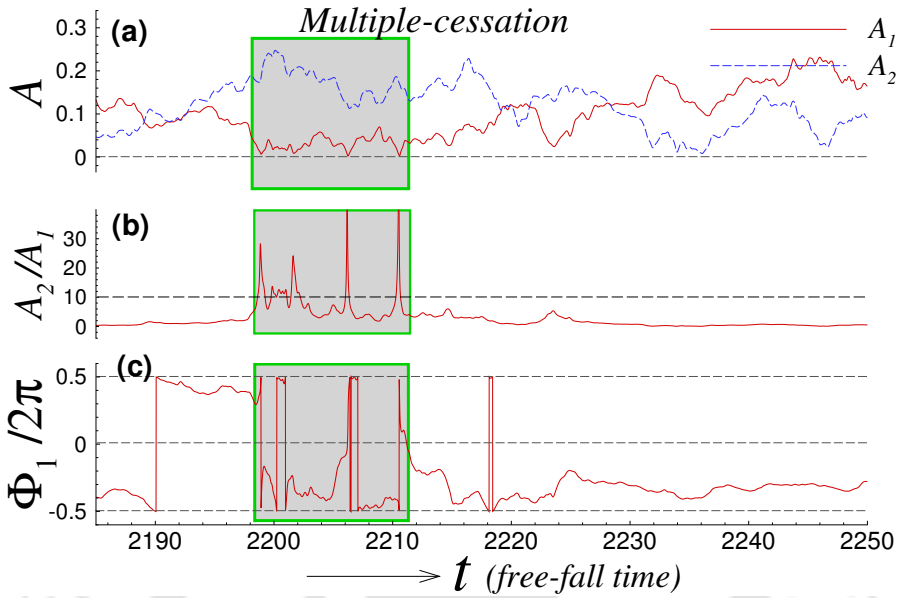

Figure 4.14: (a) The time series of first and second Fourier modes, (b) their corresponding amplitude ratio A_2/A_1 and (c) phase of the first Fourier mode during multiple cessations observed for $Ra = 2 \times 10^7$ at $Ro^{-1} = 0.2$. The dotted line in the amplitude fraction plot indicates the cutoff value $A_2/A_1 = 10$, used to identify cessations. The boxed region bounds an eddy turnover time within which the multiple-cessation prevails.

change was zero, i.e., no change in the final orientation of LSC. Similar events are observed in our simulations also. In addition, we observe double cessations where the angular change is non-zero, i.e., the LSC reorients by a finite angle after the event. Similar events were reported in the numerical study by Mishra *et al.* [51]. Note that reorientations are random and erratic events and the exact reasons for which are still not properly understood. The number of double-cessations observed is much fewer compared to regular (or single) cessations.

Interestingly, in our simulations, we observe more than two cessations occur within an eddy turnover time. This has not been reported before, and we term this phenomenon as multiple-cessation. Figure 4.14 shows the multiple-cessation observed for $Ra = 2 \times 10^7$ at $Ro^{-1} = 0.2$. The boxed region bounds an eddy turnover time within which the multiple-cessation occurs. We notice that A_1 drops close to zero successively at $t \approx 2199, 2201, 2205$ and 2210, and the amplitude fraction A_2/A_1 shows sharp peaks at these locations. The discontinuities (sudden fluctuations) in the phase are due to the spikes near $-\pi$ and π, which represent the same point. We observe only a single instance of multiple-cessation in our entire set of simulations.

A schematic representation of different cessation events is shown in Fig. 4.15. Here the horizontal mid-plane of the cylindrical domain is shown with $+$ and $-$ signs representing the

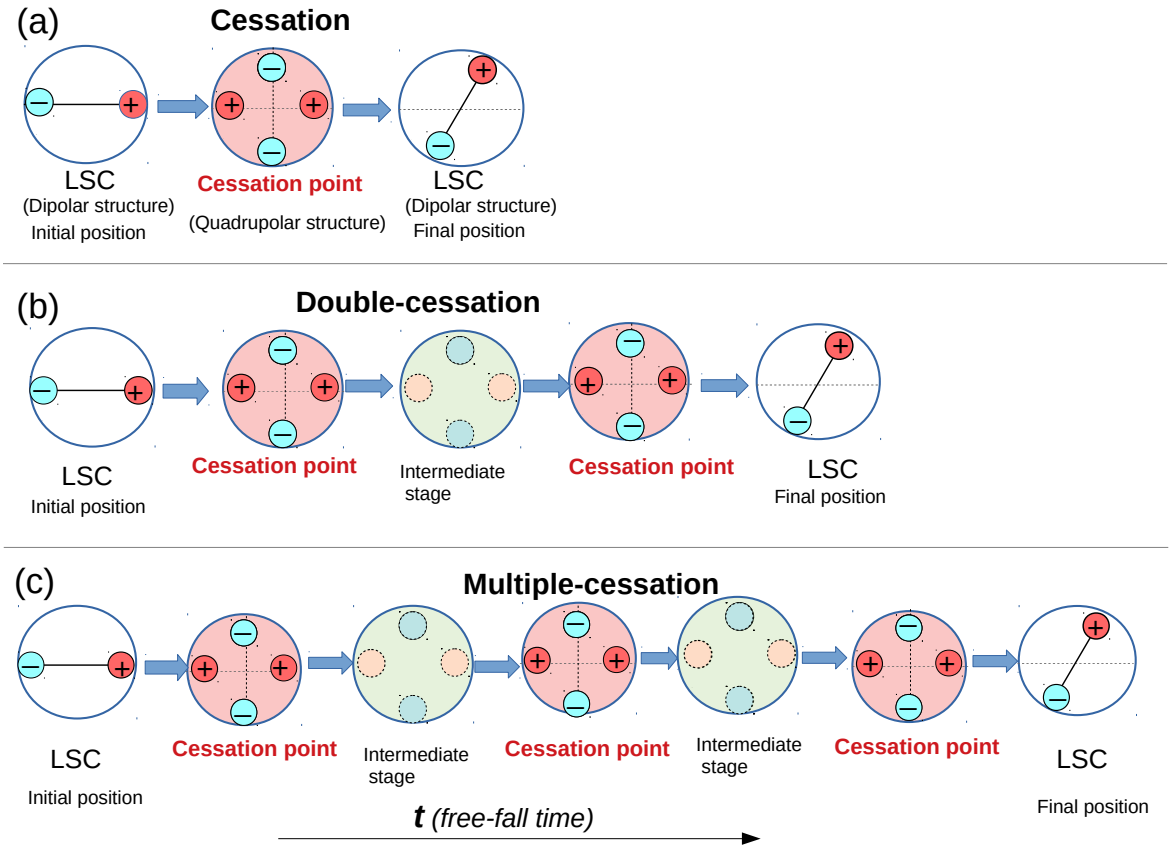

Figure 4.15: Schematic diagram showing (a) cessation, (b) double-cessation, and (c) multiple-cessation. The solid line indicates the azimuthal orientation of LSC with up-flow (+) and down-flow (-) on either side of the lateral wall.

upflow and downflow, respectively. In Fig. 4.15(a), a regular cessation-led reorientation is shown, where the LSC vanishes at the cessation point and then resumes at a different position. Note that during the cessation, a dipolar nature of the flow is lost (as $A_1 \rightarrow 0$) and a quadrupolar structure appears. In Fig. 4.15(b) a double-cessation event is shown. In this case, after the first cessation, the first Fourier mode (dipolar mode) regains its strength and thus an intermediate state is observed with a chaotic flow behaviour. Here, the flow structure is neither dipolar nor quadrupolar. After this intermediate state, the first Fourier mode again approaches zero and thus a second cessation is observed. Figure 4.15(c) represents a multiple-cessation where more than two cessations occur within an eddy turn over time. Note that here three cessation points occur in quick succession.

Next, we study the relation between cessations and the dynamics of flow structure. We observe that during cessations, as the amplitude of first Fourier mode diminishes, the flow

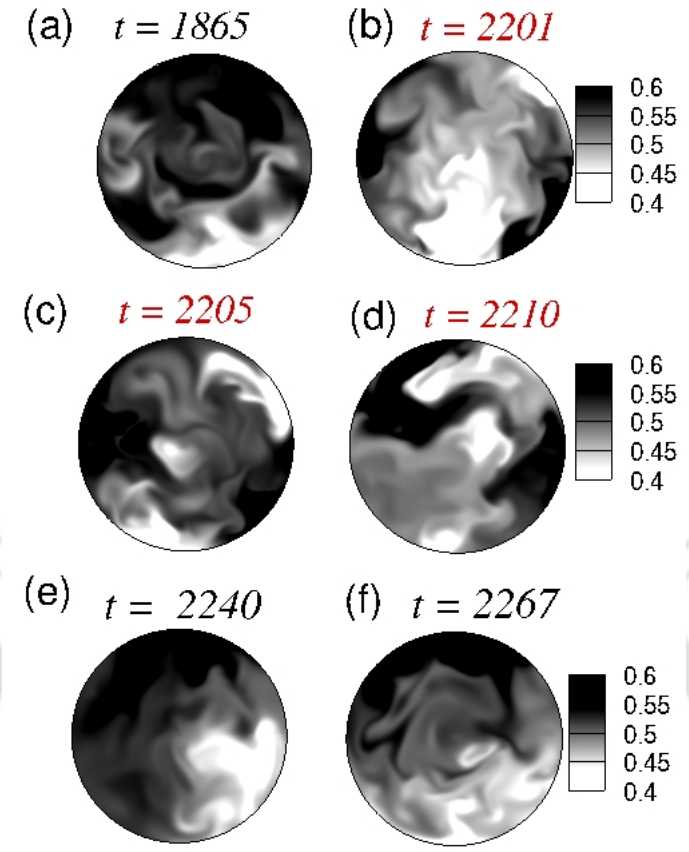

Figure 4.16: Snapshots of temperature at the horizontal mid-plane showing quadrupolar and dipolar structures observed (a) before, (b-d) during, and (e-f) after cessation, for $Ra = 2 \times 10^7$ at $Ro^{-1} = 0.2$.

structure corresponding to the first mode (dipolar structure) becomes weak, and the quadrupolar structure corresponding to the second Fourier mode becomes dominant. However, after the cessation, the dipolar structure reappears accompanied by a change in the azimuthal orientation of LSC. This is consistent with the observations made by Mishra *et al.*[51] for non-rotating RBC. Here we substantiate this by illustrating the instantaneous spatial distribution of temperature at mid-plane ($z = 0.5$) before, during, and after the cessation, as shown in Fig. 4.16. Before the cessation, the temperature distribution at $t \approx 1865$ follows an almost dipolar structure, where hot and cold fluid appear at opposite sides (π apart) of the lateral wall, as shown in frame (a). However, during cessations, i.e., at $t \approx 2201$, 2205 and 2210 (refer Fig. 4.14 also) the temperature snapshots indicate a quadrupolar behaviour [see frames (b), (c), and (d)]. Here the hot and cold fluids are observed alternately and separated azimuthally by about $\pi/2$. After the cessations, the flow goes back to the dipolar structure, as shown in frames (e) and (f). Thus, we infer that cessations are associated with a paradigm shift in the flow structure, where

it changes from dipolar to quadrupolar and then back to dipolar state.

4.4 Statistics of reorientations

After investigating the dynamics of reorientations of LSC, we turn our focus on its statistics. The number of reorientations (N_{Tot}) and cessations (N_{Cess}) per eddy turnover time at different rotation rates are shown in Fig. 4.17 for the two Rayleigh numbers. On an average we consider about 550 and 300 eddy turnover times (T_{eddy}) for $Ra = 2 \times 10^6$ and 2×10^7, respectively. With the increase in rotation rate, we observe a considerable increase in the number of reorientations. As the rotation rate increases, the strength of the LSC structure weakens and other modified structures, such as the quadrupolar, sextupolar, slowly start to appear in the system. Thus, the increase in the reorientation of LSC can be attributed to the transfer of energy from the LSC to these higher modes. This is in agreement with observations made in the previous chapter, where it was shown that with increase in rotation rate the fraction of energy contained in the first Fourier mode decreases while that in the higher modes (second and third) increases. Further, the number of reorientations are higher for lower Ra for both rotating and non-rotating RBC. Although we observe comparatively more cessations at lower Ra, the number of cessations are quite low to arrive at any conclusion.

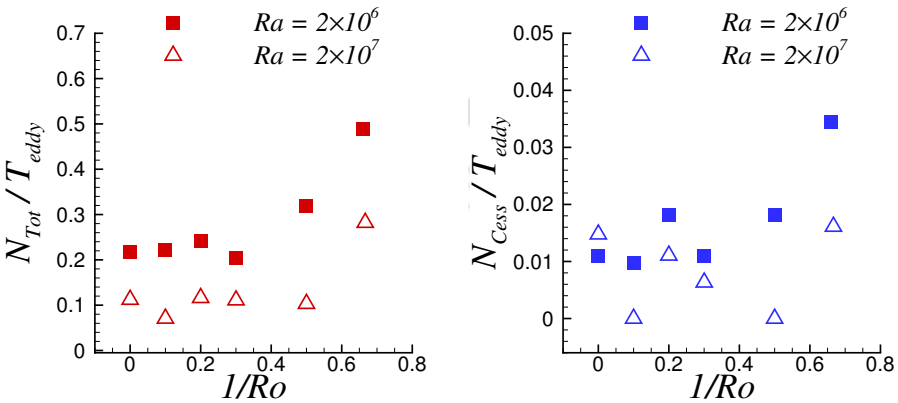

Figure 4.17: Number of reorientations and cessations per eddy turnover time observed for $Ra = 2 \times 10^6$ and 2×10^7.

As reported by previous studies, cessations are rare phenomena and double-cessations are even rarer. Brown and Ahlers [56] observed that cessations account for about 5% of the total

reorientations. In our simulations, we observe that for $Ra = 2 \times 10^6$ nearly 4-7% reorientations are cessation-led. Likewise, for $Ra = 2 \times 10^7$ the percentage of cessations is about 4%. However, for the non-rotation case at $Ra = 2 \times 10^7$ cessations account for about 13% for the total reorientations. Since our criterion for identification of cessations depends on the amplitude fraction of the Fourier modes (A_2/A_1), and that of reorientations depends on the angular change $|\Delta\Phi_1|$ and angular rotation rate $|\Delta\Phi_1/\Delta t|$, which are independent of each other, some events appear in both the categories while some are exclusive to either cessations or reorientations. In the entire set of simulations, we observe only two cessations ($A_2/A_1 \gtrsim 10$) where the phase change $|\Delta\Phi_1|$ is less than $\pi/4$ and thus do not qualify to be accounted as reorientations. However, while calculating the percentage of cessations, these two cases are considered as reorientations, as we classify cessations as a subset of total reorientations. Note that the number of reorientations observed in the present study is much lesser compared to the experimental observations [54, 56, 206] due to the limitations in the recorded length of time histories.

Next, we quantify the possibility of occurrence of the reorientations based on the angular change $|\Delta\Phi_1|$. Figure 4.18 shows the probability distribution $P(|\Delta\Phi_1|)$ for different rotation rates. We observe that the statistics of reorientation follow a power-law distribution as $P(|\Delta\Phi_1|) \propto |\Delta\Phi_1|^{-m}$, where $m = 3.7 \pm 0.5$. The power-law fit is carried out by maximum likelihood estimation (MLE) [207, 208], to prevent the errors arising due to the binning of data. MLE is preferred over least squares method, which can produce substantially inaccurate estimates of parameters for the distribution due to smaller size of the data sample [208]. In MLE, the parameter values of the distribution are calculated such that they maximize the likelihood function, which is the product of probability densities of the individual events. The exponent of the power-law distribution is calculated as

$$m = 1 + n \left[\sum_{i=1}^{n} \ln \frac{|\Delta\Phi_1^i|}{|\Delta\Phi_1^{min}|} \right]^{-1} \tag{4.2}$$

where $|\Delta\Phi_1^i|, i = 1, ...n$ are the angular changes from n number of observations and $|\Delta\Phi_1^{min}|$ is the minimum angular change. Similar power-law fits with negative exponents are observed for all cases (rotating and non-rotating RBC), indicating a monotonically decreasing distribution of $|\Delta\Phi_1|$. This suggests that smaller reorientations are more frequent events, while the larger ones are rare occurrences. Note that the exponent is well within the range of -3.25 to -4.45

experimentally observed for different Ra by Brown and Ahlers [56] and Brown *et al.* [54]. The works of Xi and Xia [60] also found the slope of the power-law fit to be of the order of -3.3 for unit aspect ratio container. However, all these experiments were on non-rotating RBC. In the present study, we infer that even for rotating RBC, the reorientations follow a power-law distribution.

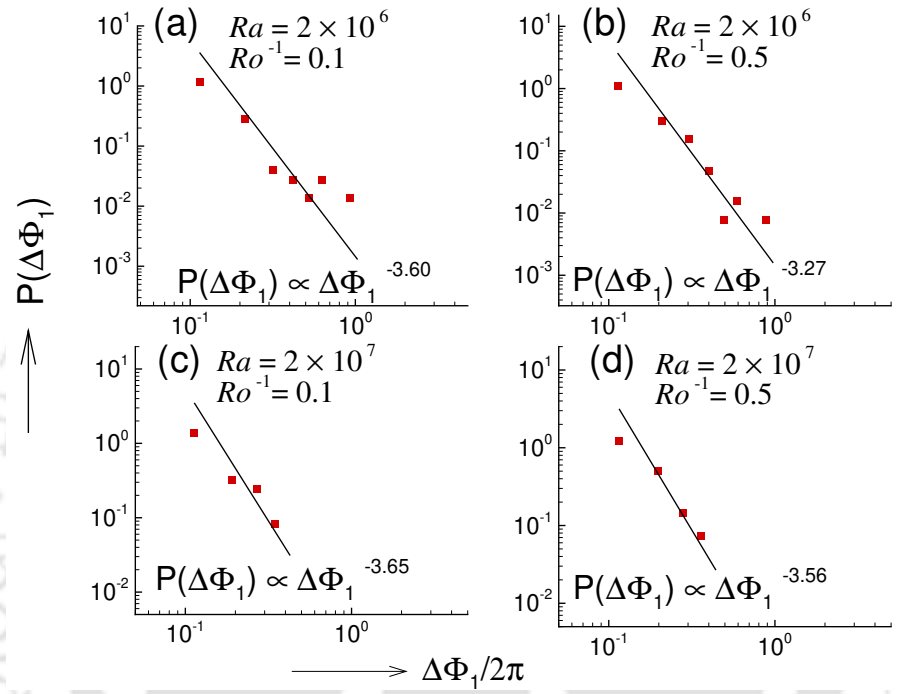

Figure 4.18: PDF of the angular change $\Delta\Phi_1$ for $Ra = 2\times10^6$ and $Ra = 2\times10^7$ at $Ro^{-1} = 0.1$ and 0.5. Solid line indicates the power law fit by MLE.

We now evaluate the occurrence of reorientations with time. Here τ indicates the time interval between two successive reorientations, with μ_τ its mean value. Experimental studies by Xi and Xia [60], Brown and Ahlers [56] and Brown *et al.* [54] have reported that the PDF of time interval of reorientations can be well fitted with an exponential function, which suggests that the occurrence of reorientations follows a Poisson process. Figure 4.19 shows the probability distribution $P(\tau/\mu_\tau)$ for different rotation rates ($Ro^{-1} = 0.2$ and 0.5), where the solid line shows the exponential function $P(\tau/\mu_\tau)$=$\exp(\tau/\mu_\tau)$. Note that for $Ra = 2\times10^6$ the time interval is in good agreement with the exponential function, while deviations are observed in $Ra = 2\times10^7$, which might be due to the lesser number of observations for the latter. Poisson distribution of the time interval suggests that reorientations are independent of each other and they do not have any memory of the previous event [60].

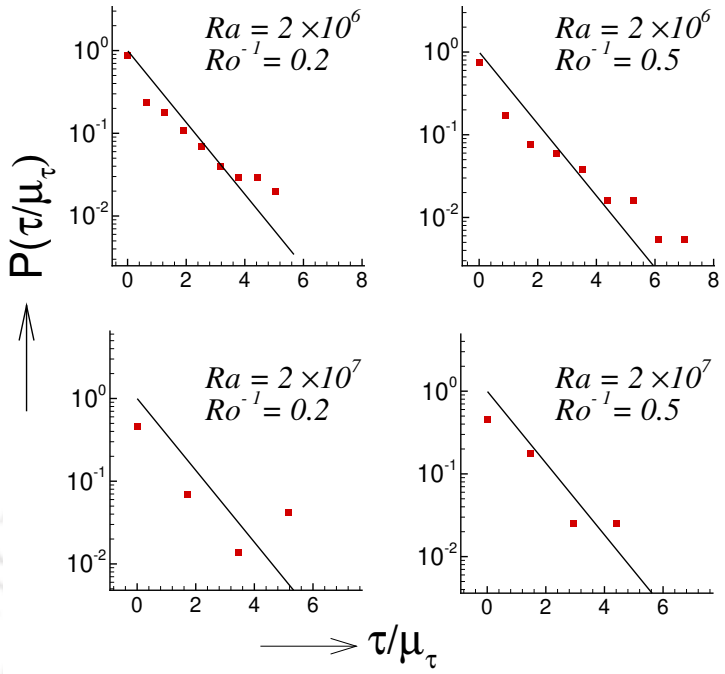

Figure 4.19: PDF of time interval between successive reorientations τ for $Ra = 2 \times 10^6$ and $Ra = 2 \times 10^7$ at $Ro^{-1} = 0.2$ and 0.5. The solid line indicates the exponential function P(τ/μ_τ)=exp(τ/μ_τ).

Note that numerical studies on the reorientations of LSC in turbulent convection are rare compared to the experimental ones, especially on the statistics. Further, all the reported works on reorientations of LSC are on non-rotating RBC. However, in the present study, we discuss these features in detail for rotating RBC. At the outset, we identify the reversals as partial and complete using the vertical velocity time signals and connect them with the reorientations by evaluating the phase of the first Fourier mode. Then we discuss the rotation-led and cessation-led reorientations, which were earlier reported by Brown and Ahlers [56], Brown *et al.* [54], Xi and Xia [60] and Mishra *et al.*[51] etc. In addition, we report double cessation, previously reported by Xi *et al.* [206] and Mishra *et al.*[51]. A new phenomenon in our simulations is multiple- cessation, which has not been reported before. Finally, we have evaluated the statistics of reorientations. We observe that similar to non-rotating RBC [54, 56], the reorientations in RRBC occur with a power-law probability distribution. Additionally, as reported by previous experimental studies [56, 60], the time interval between successive reorientations follows a Poisson distribution, which suggests that reorientations are independent of each other.

4.5 Summary

In this chapter, we have presented a detailed three-dimensional numerical investigation on the dynamics and statistics of reorientations of LSC in turbulent RRBC in a unit aspect ratio cylindrical cell with $Pr = 0.7$ and two different Rayleigh numbers $Ra = 2 \times 10^6$ and 2×10^7, for a wide range of rotation rate ($0 \leq Ro^{-1} \leq 30$). LSC and its reorientations have been identified using Fourier mode analysis of vertical velocity signals near the lateral wall at the mid-horizontal plane. The orientation of LSC significantly affects the heat transfer, dissipation rates, and the boundary layer thickness (δ_θ). Along the direction of LSC, δ_θ shows an asymmetric trend, as it is thicker at one side and thinner near the opposite side of the lateral wall. However, perpendicular to LSC, the boundary layer thickness varies almost symmetrically. Further, the reorientations of LSC have been characterized as rotation-led and cessation-led based on their nature of occurrence, and as partial and complete reversal depending on the azimuthal drift. In addition to the previously reported rare events like cessations and double-cessation, an interesting event of multiple-cessation has been observed, where more than two cessations occur in quick succession. Cessation-led reorientations are rare events, which account for about 4-7% of the total number of reorientations. Double-cessations are even rarer, and multiple-cessations are the rarest of all reorientations. As the rotation rate increases ($Ro^{-1} \approx 0.66$), a significant increase in the number of reorientations is observed. Note that due to the lesser number of cessation-led events in our study, it is quite difficult to claim any specific trend for the effect of rotation on the cessation-led events. Similar to non-rotating RBC, we find that the probability distribution of the reorientations exhibits a power-law distribution with the exponent nearly equal to -3.7. In addition, the PDF of time interval between two successive reorientations follows a Poisson distribution, which indicates that reorientations are independent of each other.

5

Significance of Prandtl number on the heat transport and flow structure in rotating convection

Direct numerical simulations of rotating Rayleigh-Bénard convection for different fluids ($Pr = 0.015, 0.7, 1, 7, 20$ and 100) in a cylindrical cell of aspect ratio $\Gamma = 0.5$ are carried out in this chapter. The Rayleigh number is fixed at $Ra = 10^6$ and the rotation rates are varied for a wide range, starting from no-rotation ($Ro^{-1} = 0$) to high rotation rates ($Ro^{-1} \approx 100$). The significance of Prandtl number on the heat transfer rate, flow structures, their associated dynamics, and influence on the boundary layers are investigated. For all the Prandtl numbers, a reduction in heat transfer with increase in rotation rate is observed. However, for $Pr = 7$ and 20, a marginal increase of the Nusselt number for low rotation rates is obtained, which is attributed to the change in the flow structure from quadrupolar to dipolar state. The change in flow structure is associated with the statistical behaviour of the boundary layers. As the flow makes a transition from quadrupolar to dipolar state, a reduction in the thermal boundary layer thickness is observed. At higher rotation rates, the thermal boundary layer thickness shows a power-law variation with the rotation rate. The power-law exponent is close to unity for moderate Pr, while it reduces for both lower and higher Pr. At extremely high rotation rates, the flow makes a transition to the conduction state. The critical rotation rate ($1/Ro_c$) for which the transition to the conduction state is observed depends on the Prandtl number according to $1/Ro_c \propto Pr^{0.5}$.

5.1 Introduction

In previous chapters, we studied the effect of rotation in turbulent Rayleigh-Bénard convection. Different flow regimes were identified, and characteristics of the flow, such as heat transfer, boundary layer, and dissipation rates, were evaluated in these regimes. Apart from the rotation rate, Prandtl number is also expected to alter the flow behaviour. Prandtl number is a fluid property and varies widely across different fluids. Table 5.1 shows the Prandtl number for some fluids. Generally, the fluids with $Pr < 1$ are considered as low-Prandtl number fluids, while those with $Pr > 1$ are considered as high-Prandtl number fluids. It has been observed that the flow dynamics in thermal convection is largely affected by the Pr. For rotating convection, Chandrasekhar [25, 99] observed that for $Pr > 1$, the critical Rayleigh number (Ra_c) for the onset of convection depends only on the rotation rate (Ro^{-1}). However, for lower Prandtl number, Ra_c depends on both Pr and the rotation rate. Convective flows with very low Prandtl number ($Pr \ll 1$) are present in flows inside the Earth's outer core, metal melting processes, to name a few. The magnetic fields, atmospheric jets, and emitted heat flux patterns of planets are controlled by the turbulent rotating convective movements of molten metals within the planets [17, 18]. Air (and other gases) and water, which constitute most of the natural systems (atmospheric and oceanic), mostly fall under the Prandtl number range $0.1 \leq Pr \leq 10$. Industrial and technological applications also involve flows with a wide range of Pr (coolants, lubricants, oils, etc.). Thus, modelling of these flows is extremely important from astronomical, geological, and technological point of view.

Table 5.1: Typical range of value of Prandtl number for different fluids.

Fluid	Pr
Sun's interior	$\approx 10^{-8}$
Liquid metals	$0.001 - 0.03$
Mercury	≈ 0.015
Air	≈ 0.7
Water	≈ 7
Oils	$100 - 40000$
Earth's mantle	$\approx 10^{23}$

Weiss *et al.* [209] experimentally investigated the heat transport enhancement in slowly rotating turbulent thermal convection in a cylinder of unit aspect ratio for different Prandtl

numbers ($0.74 \leq Pr \leq 35.5$). They observed that the average Nusselt number increases with rotation rate up to a threshold, while above it Nu exhibits a decreasing behaviour. The threshold rotation rate increases with Pr at a fixed Ra, and drops with increase in Ra at a constant Pr. A maximum heat transfer enhancement of 40% from the non-rotating case was recorded for higher Pr, while the lowest Prandtl number ($Pr = 0.74$) showed only 2% increment. King and Aurnou [17] investigated the effects of rotation on the turbulent convection in liquid metal gallium ($Pr = 0.025$) in a cylindrical cell with unity aspect ratio. It was observed that the behaviour of liquid metal convection with and without rotation was completely different from those obtained at moderate Pr ($Pr \approx 7$). A difference in Nu scaling was observed ($Nu \sim Ra^{0.25}$) as compared to the moderate Pr cases ($Nu \sim Ra^{0.33}$), which was due to the dominant role of turbulent fluctuations at small scales in liquid metal convection.

Verzicco and Camussi [180] numerically studied the influence of Pr on the heat transfer in RBC in a cylindrical cell with unit aspect ratio at $Ra = 6 \times 10^5$. They investigated a wide range of Pr ($0.022 \leq Pr \leq 15$) and identified two distinct flow regimes depending on the Pr. For $Pr \leq 0.35$ flow was seen dominated by large scale structures (also responsible for the heat transfer), while for $Pr \geq 0.35$ the flow dynamics were thermal plumes dominated. Effect of Ra, Pr, and Ro on heat transfer in turbulent RRBC was studied by Zhong *et al.* [135] in a cylindrical container with unit aspect ratio at $Ra \geq 10^8$ and $0.07 \leq Pr \leq 20$. An increase in heat transfer rate from the non-rotating case was observed in all the Prandtl numbers except $Pr = 0.7$. The study was carried out in a plume dominated regime and the increase in Nu at moderate Pr was explained by Ekman pumping [125, 127]. At moderate rotation rates, the converging radial fluid in the Ekman layer swirls cyclonically resulting in the formation of vertical vortex tubes. These vertical vortices suck the fluid out of the Ekman layers and create a vertical heat flux. This occurs near the top and bottom isothermal plates and depends strongly on Ra, Pr, Ro, and the boundary conditions. For $Pr \leq 0.7$ no increment in Nu was observed, due to the larger thermal diffusion, which negates the effect of heat transfer increment by Ekman pumping.

Stevens *et al.* [138] numerically showed that at a fixed Ro, there exists a Pr for maximum heat transfer enhancement. The simulations were performed in a cylindrical domain at $Ra = 10^8$ and a wide range of Prandtl numbers ($0.7 \leq Pr \leq 55$). The results showed that for $Pr > 1$, heat transfer rate increases (compared to the non-rotating case) due to Ekman pumping

at moderate rotation rates. It was also found that the critical rotation rate for maximum heat transfer enhancement increases with the increase in Pr. On the similar line Poel *et al.* [210] studied the connection between flow structures and heat flux in turbulent RBC and observed that Nu is more sensitive to the flow organization at low Prandtl number ($Pr = 0.7$) as compared to moderate Prandtl number ($Pr = 4.38$). They associated this feature to the dynamics of viscous and thermal boundary layers. Pharasi *et al.* [211] studied the Nusselt number scaling with Rayleigh number for low Prandtl number fluid ($Pr = 0.1$) for Rayleigh numbers $10^4 \leq Ra \leq 10^8$ and Taylor numbers $0 \leq Ta \leq 10^8$. The Nu scales with Ra as $Nu \propto Ra^{2/3}$ for Nu greater than a critical Nusselt number Nu_c corresponding to $Ta/Ra \approx 1$. Beyond this critical value, Nu becomes a function of Ta also. The critical Nusselt number scales with Ta as $Nu_c \propto Ta^{0.277}$. In their DNS study, Guzman *et al.* [212] investigated the transition to geostrophic regime [124] in RRBC at low Prandtl number, $Pr = 0.1$ and $Ra = 1 \times 10^{10}$. In the geostrophic regime, the Coriolis force dominates over the other forces. They observed that different statistical quantities, such as Nu scaling and thermal boundary layer thickness, show transition to the geostrophic regime at different rotation rates. In this chapter, we focus on the significance of Prandtl number in RRBC at $Ra = 10^6$, which is expected to be dominated by large-scale flow structures. In particular, we investigate the effect of Pr and Ro on heat transfer rates and its association with the flow structure dynamics. Most works on RRBC are focused on the enhancement of heat transfer rates at moderate rotation rates and followed by its suppression at higher rotation rates for high Rayleigh number regime. In this chapter, we mainly examine the effect of rotation in different Prandtl numbers at a rotation dominated regime and the transition to conduction stage.

The organization of the chapter is as follows. The next section discusses the overall problem setup and the details of the computational grid. This is followed by principal findings of the present study. At the outset, we identify different flow states by evaluating the time signals and flow structures. Then we study the heat transport dynamics and connect it with the flow structures, Fourier modes, and boundary layers. Finally, we conclude the chapter by summarizing the principal findings.

5.2 Numerical details

We consider a cylindrical domain of aspect ratio $\Gamma(= D/H) = 0.5$ with bottom heated (T_H) and top cooled (T_C). Rotation is applied about the vertical axis of the cylinder. A schematic diagram of the flow domain with boundary conditions used is shown in Fig. 5.1(a). For temperature isothermal condition on the horizontal walls and adiabatic conditions on the lateral walls are implemented, while for velocity no-slip conditions are implemented on all the surfaces. Figure 5.1(b) shows a geometric construction of the locations of the numerical probes that are used to record the field time signals. The signals are recored from eight equidistant ($\phi = \pi/4$ apart) locations at the horizontal mid-plane ($z = 0.5H$) close to the lateral wall ($r = 0.24H$).

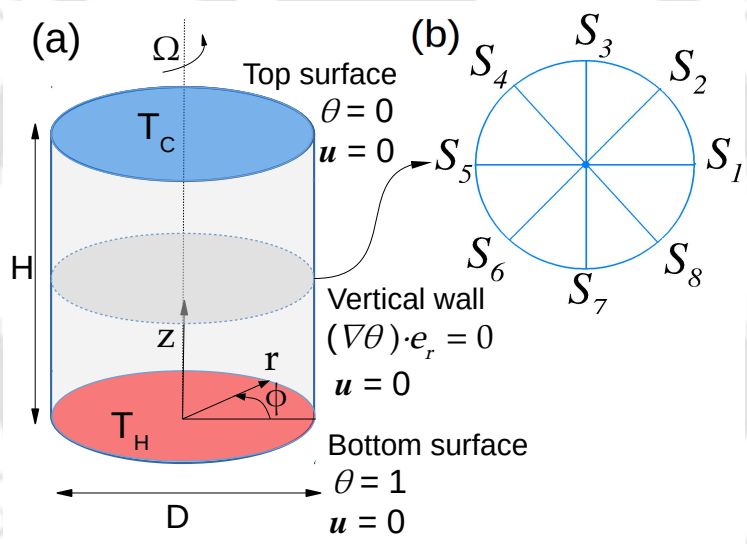

Figure 5.1: (a) Schematic diagram of the flow domain with relevant boundary conditions. (b) Schematic representation of the location of numerical probes at mid-vertical cross section of the cylindrical domain used for signal analysis.

The mesh size is chosen such that it is refined adequately to capture the flow dynamics correctly, and at the same time, it takes less computational resources. For all the simulations, the boundary layers are resolved by placing more than 10 grid points within the thermal boundary layer. A structured and non-uniform grid with refinement near the top and bottom surfaces and the lateral wall is chosen for the simulations. Three different mesh sizes are used in all the cases with 10% increase in the number of grid points along the radial, azimuthal, and axial directions. In addition, a highly refined mesh that is double the size in each direction compared to the coarsest mesh size is also evaluated to check for grid independence. As dis-

cussed in chapter 3, we evaluate the Nusselt number and dissipation rates at different mesh sizes to test for grid convergence. Table 5.2 shows the average Nusselt number and ratio of the numerically computed values of thermal and viscous dissipation rates to their analytical counterparts for different Pr at various grid sizes, with the corresponding minimum grid size in the radial (Δr_{min}) and the axial direction (Δz_{min}). Only selected cases, which are expected to be most sensitive, are presented here. Nusselt number at the walls (top and bottom) is computed as $Nu_S = \langle \partial\theta/\partial z \rangle_{A,t}$, where $\langle .. \rangle_{A,t}$ indicates averaging over horizontal plane and time. The volume-averaged Nusselt number over the entire domain $Nu_{vol} = 1 + \sqrt{RaPr}\langle w\theta \rangle$ is also calculated, where $\langle .. \rangle$ denotes averaging over volume and time. Nu is sensitive to the grid resolution near the walls and Nu_{vol} to that near the bulk. Both the values agree after time averaging (refer Table 5.2), which provides an additional check on the spatial resolutions of the numerical simulations [166, 213]. The difference between the Nu (or Nu_{vol}) values computed at the finest and coarsest mesh for all cases is less than 5%, which suggests a reasonable grid convergence. Further, the ratio of the numerical to the theoretical estimate of the viscous ($\langle \epsilon_u^r = \langle \epsilon_u^{num} \rangle / \langle \epsilon_u^{th} \rangle$) and thermal dissipation rates ($\epsilon_\theta^r = \langle \epsilon_\theta^{num} \rangle / \langle \epsilon_\theta^{th} \rangle$) are also calculated. Recall that $\epsilon_u^{num}\rangle = \nu V^2 H^{-2} \langle |\nabla \boldsymbol{u}|^2 \rangle$ and $\langle \epsilon_\theta^{num} \rangle = \alpha (\Delta T)^2 H^{-2} \langle |\nabla \theta|^2 \rangle$ are respectively the numerically calculated values of viscous and thermal dissipation rates, while $\langle \epsilon_u^{th} \rangle = \nu^3 (Nu - 1) RaPr^{-2} H^{-4}$ and $\langle \epsilon_\theta^{th} \rangle = \alpha (\Delta T)^2 NuH^{-2}$ are their corresponding analytical values [75]. The ratios are always close to unity, indicating that the spatial resolution is good enough to perform the proposed numerical calculations [51, 153]. Considering the computational cost and accuracy of the parameters shown in Table 5.2, the grid $33 \times 49 \times 129$ has been chosen for $Pr = 100, 20, 7, 1, 0.7$. For $Pr = 0.015$ a mesh size of $41 \times 61 \times 161$ is used. For unsteady periodic flows, the temporal averaged quantities are calculated after reaching a statistically stationary state. Time increment of $\Delta t = 10^{-3}$ is used for all $Pr \geq 0.7$, while for $Pr = 0.015$ a time-step of 5×10^{-4} is used. Note that the time step in each case is well below the Kolmogorov time-scale $\eta_t = \sqrt{Pr/(Nu - 1)}$. The ratio $\Delta t/\eta_t$ for all cases is below 0.005, which suggests that the flow is well resolved temporally. Further, we make sure that the Courant-Friedrichs-Lewy (CFL) condition is satisfied, and the maximum Courant number for all cases is below 0.2.

Table 5.2: Nusselt number at the bottom wall (Nu_S), volume averaged Nusselt number (Nu_{vol}) and ratio of numerical to analytical dissipation rates (ϵ_u^r and ϵ_θ^r) at different mesh sizes, with the corresponding minimum grid size in radial (Δr_{min}) and vertical direction (Δz_{min}) for different Pr at $Ra = 10^6$.

$N_r \times N_\phi \times N_z$	$\Delta r_{min}(\times 10^{-3})$	$\Delta z_{min}(\times 10^{-3})$	Pr	Nu_S	Nu_{vol}	ϵ_u^r	ϵ_θ^r
$29 \times 45 \times 117$	2.72	2.56	7	7.99	8.01	0.971	0.993
$33 \times 49 \times 129$	2.37	2.32	7	7.99	8.00	0.971	0.994
$37 \times 55 \times 141$	2.09	2.11	7	7.98	7.99	0.973	0.996
$59 \times 91 \times 235$	1.28	1.27	7	7.98	7.98	0.974	0.997
$29 \times 45 \times 117$	2.72	2.56	0.7	9.83	9.84	1.01	0.996
$33 \times 49 \times 129$	2.37	2.32	0.7	9.81	9.84	1.00	0.997
$37 \times 55 \times 141$	2.09	2.11	0.7	9.80	9.80	1.00	0.998
$59 \times 91 \times 235$	1.28	1.27	0.7	9.80	9.80	1.01	0.998
$37 \times 55 \times 145$	2.09	2.05	0.015	3.72	3.70	0.93	0.970
$41 \times 61 \times 161$	1.88	1.85	0.015	3.68	3.67	0.965	0.981
$45 \times 67 \times 177$	1.70	1.67	0.015	3.60	3.62	0.973	0.980
$75 \times 111 \times 291$	1.00	1.06	0.015	3.77	3.76	0.964	0.998

5.3 Identification of flow regimes

In Rayleigh-Bénard convection, the flow state changes from steady to periodic, then to quasi-periodic and finally to chaotic with the increase in Ra [41, 131]. A similar trend is observed here with decrease in Pr at $Ra = 10^6$ and with no rotation. The flow remains steady for $Pr \geq 7$, becomes periodic at $Pr = 1$, then quasi-periodic at $Pr = 0.7$, and finally becomes chaotic at $Pr = 0.015$. For rotating convection, we identify different flow states and their dynamics with the increase in rotation rate for different Pr at a fixed Ra by evaluating the time signals and the flow structures. A general trend of flow stabilization is observed at higher rotation rates for all Pr, where the time signals become periodic, followed by a considerable reduction in the magnitude.

5.3.1 Time evolution of the flow

In order to analyze the characteristics of the unsteady flows, time signals are taken from eight equidistant locations $\pi/4$ apart along the azimuthal direction in the horizontal mid-plane ($z = 0.5H$) at a radial distance of $r = 0.24R$ [refer Fig. 5.1(b)]. Temperature signals at probe points which are π apart are shown in Fig. 5.2, for low Prandtl numbers. For $Pr = 0.015$ the signals obtained for all cases (non-rotating and rotating) are chaotic. Figures 5.2(a) and 5.2(b) show

that the signals at S_1 $(r = 0.24, \phi = 0, z = 0.5)$ and S_5 $(r = 0.24, \phi = \pi, z = 0.5)$ are out of phase and switch between high temperature ($\theta > 0.5$) and low temperature ($\theta < 0.5$) in a random way. The anti-correlated signals from azimuthal locations that are π apart is a sign of dipolar flow behaviour, as discussed in chapter 3. Note that with increase in rotation the switching becomes more frequent, accompanied by a reduction of the peak-to-peak amplitude of the signals, which is an indication of flow stabilization at high rotation rates. The peak-to-peak amplitude reduces from ≈ 0.6 for $Ro^{-1} \lesssim 1$ to ≈ 0.4 at $Ro^{-1} = 3$ [see Figs. 5.2(a)-5.2(e)]. At even higher rotation rates ($Ro^{-1} = 10$), all the temperature fluctuations are damped out and steady signals are obtained indicating a conduction-like state.

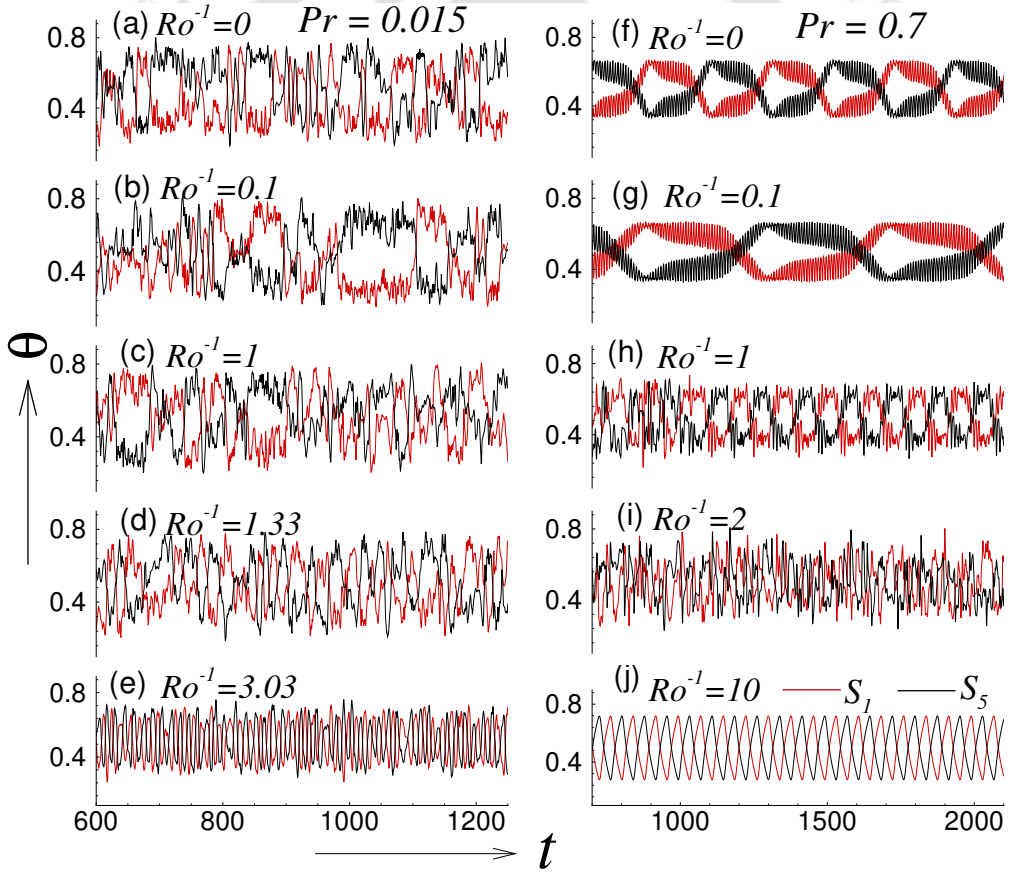

Figure 5.2: Time traces of temperature from numerical probes S_1 and S_5 for $Pr = 0.015$ (left panel) and $Pr = 0.7$ (right panel) at different rotation rates.

At $Pr = 0.7$ for non-rotating case, the signals at S_1 and S_5 indicate a quasi-periodic flow. Figures 5.2(f) and 5.2(g) show that two bands of frequencies are present in the signals. One corresponds to the large-scale flow and the other represents the fluctuations around it. The signals at S_1 and S_5 switch between high and low temperatures after specific time interval

($t \approx 210$ for $Ro^{-1} = 0$). However, for low rotation rate of $Ro^{-1} = 0.1$, the time period of such switching increases considerably ($t \approx 400$). With the increase in rotation rate ($Ro^{-1} = 1$), the time period of the flow decreases. Interestingly, the flow characteristic changes to chaotic at $Ro^{-1} \approx 2$. Similar chaotic flow behaviour at intermediate rotation rates is observed for $Pr = 1$ and 7 [see Figs. 5.3(c), 5.3(d), and 5.3(i)]. However, with further increase in the rotation rate, flow stabilization becomes evident and regular periodic signals are obtained at $Ro^{-1} \approx 10$.

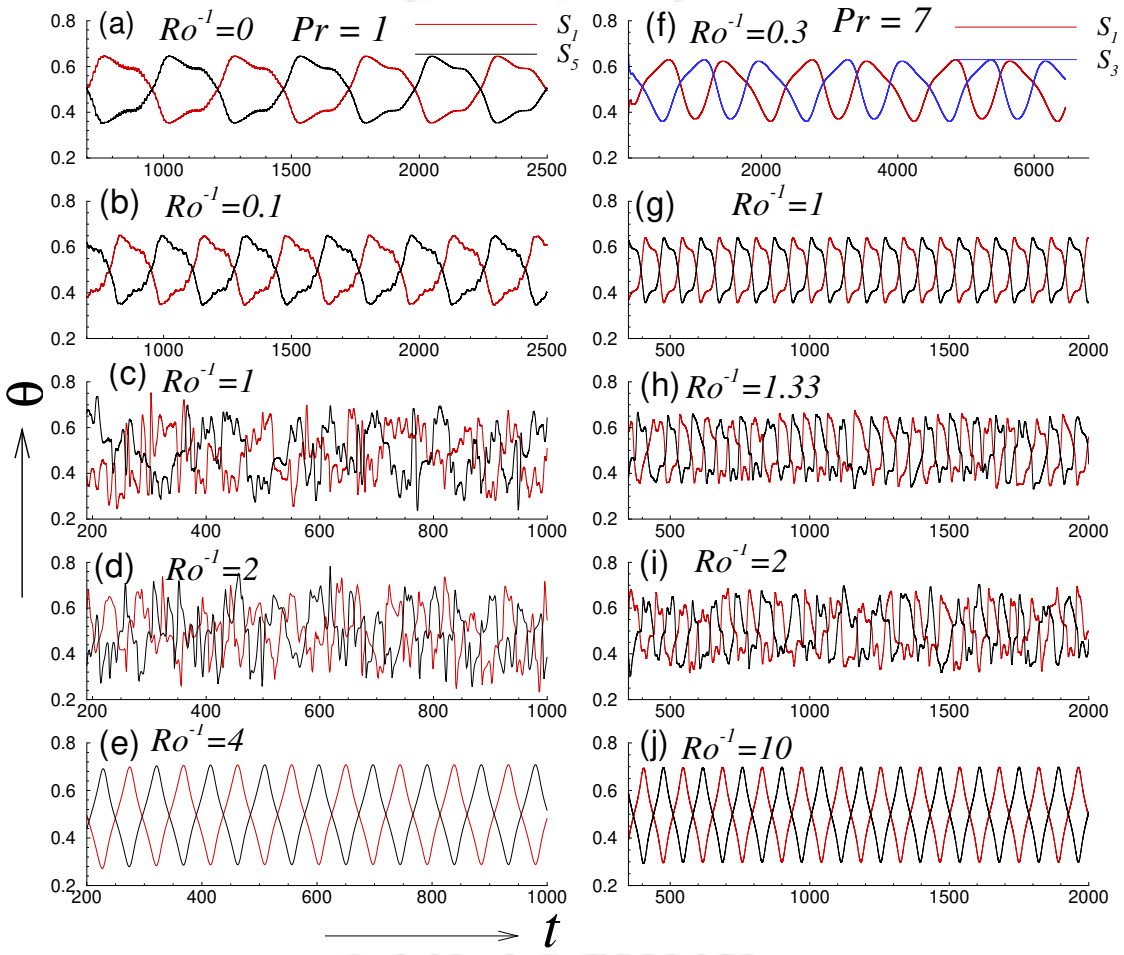

Figure 5.3: Time traces of temperature from numerical probes S_1, S_3 and S_5 for $Pr = 1$ (left panel) and $Pr = 7$ (right panel) at different rotation rates.

For $Pr \geq 7$, steady state flow is obtained for the non-rotating case. However, for low rotation rates, although the flow structures remain similar to the non-rotating case, the temperature and vertical velocity signals exhibit periodic nature. Figure 5.3(f) shows that for $Pr = 7$ at $Ro^{-1} = 0.3$, flow is periodic and the time signals at S_1 and S_3, which are $\pi/2$ apart in the azimuthal direction, are nearly out of phase. This suggests that the flow behaviour is far from dipolar nature, but close to a quadrupolar (or higher) one. However, for moderate rotation rates

($0.4 \leq Ro^{-1} \leq 1$), the dipolar behaviour of the flow is restored, as the time traces at probe points S_1 and S_5, which are π apart, are out of phase [see Fig. 5.3(g)]. Note that the time signals from localized probes do not provide a complete picture of the flow; hence we evaluate the flow structures in the next subsection.

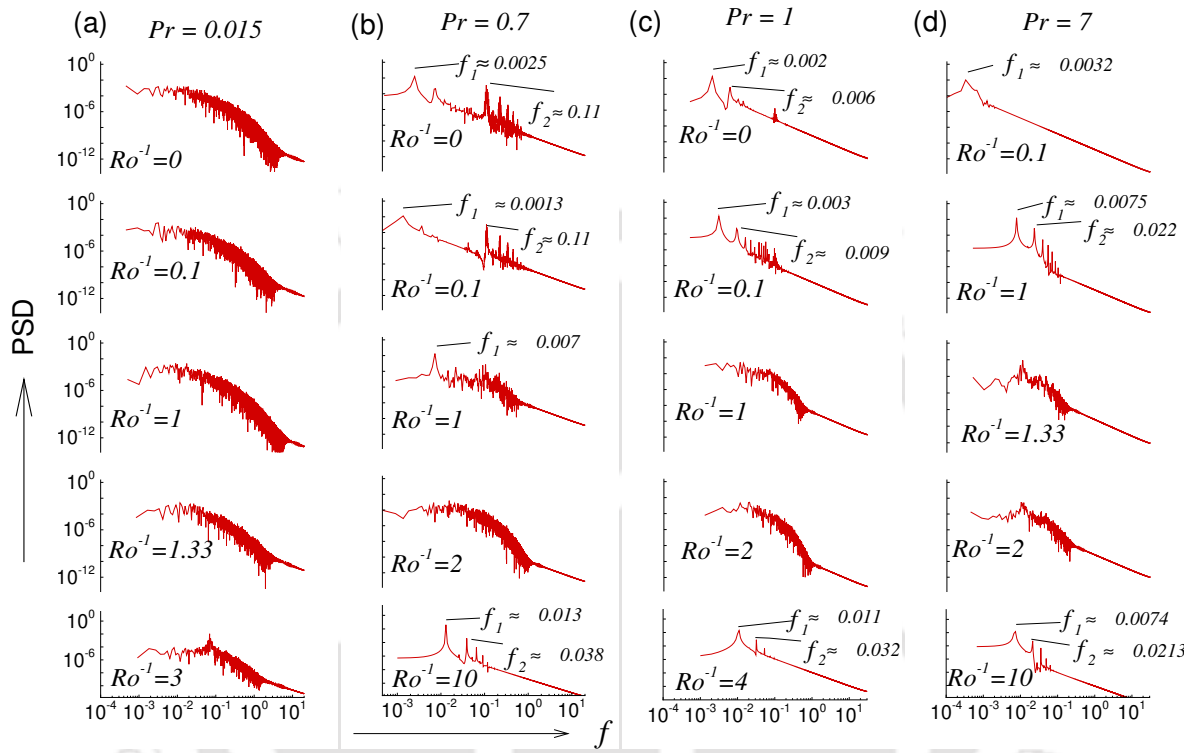

Figure 5.4: Power spectral density of temperature signals from numerical probe S_1 for (a) $Pr = 0.015$, (b) $Pr = 0.7$, (c) $Pr = 1$, (d) $Pr = 7$ at different rotation rates.

In order to characterize the unsteady flows, we compute the power spectrum of the above time signals as $P_x(f) = N^{-2}|\sum_{j=1}^{N} x_j e^{-i2\pi j f \Delta t}|^2$. Here x_j is the discrete value of the variable at time $t_j = j\Delta t$, with Δt the sampling time, f the frequency of the fluctuation and T $(= \Delta t N)$ the total time interval for which data is considered. A sampling time of $\Delta t = 0.01$ and $T \approx 1000$ time units is used for all cases. Figure 5.4 shows the power spectral density (PSD) for different fluids at various rotation rates. For $Pr = 0.015$, a continuous spectrum is observed for all cases, clearly indicating chaotic flows. For $Pr = 0.7$ at low rotation rates ($Ro^{-1} \leq 0.1$), two bands of frequencies are observed in the power spectrum. For the non-rotating case $f_1 \approx 0.0025$ is the dominant frequency and $f_2 \approx 0.1$ the second dominant frequency. Note that numerous smaller frequencies are present near f_2. f_1 corresponds to the frequency of the large-scale flow, while f_2 and smaller frequencies indicate the fluctuations around it. At $Ro^{-1} = 0.1$, the first

dominant frequency is reduced to $f_1 \approx 0.0013$, which explains the larger switching time scale observed in Fig. 5.2(g). At higher rotation rates ($Ro^{-1} \approx 2$), a near continuous power spectrum is obtained. However, as rotation is increased further to $Ro^{-1} = 10$, frequency content in the signals reduces due to flow stabilization by strong Coriolis force. For $Pr = 7$ and 1, the power spectrum shows fewer peaks at low rotation rates, indicating quasi-periodic flows (ratio f_1/f_2 is an irrational number). However, as rotation rate increases, the frequency content in the signals increases and a near-continuous power spectrum is obtained at $1 \lesssim Ro^{-1} \lesssim 2$. This justifies the chaotic flow regime observed at these intermediate rotation rates (see Fig. 5.3). With further increase in the rotation rate, the frequency content reduces and the power spectrum shows fewer peaks.

The change in flow states with the increase in Pr at low rotation rates ($Ro^{-1} \leq 0.1$) is also evident from Fig. 5.4. The PSD at $Pr = 0.015$ shows a continuous spectrum indicating chaotic flows, while at $Pr = 0.7$ multiple peaks are observed suggesting quasi-periodic flow behaviour. The increase in Pr is accompanied by a considerable reduction in frequency content. For $Pr = 7$, the power spectrum shows a single peak at $f_1 \approx 0.003$ for $Ro^{-1} = 0.1$ indicating periodic flow.

5.3.2 Flow structures

In order to obtain better insights into the flow states, we analyze the flow structures for different Prandtl numbers at various rotation rates. Figure 5.5 shows the instantaneous temperature iso-surfaces along with the vertical velocity contours at the horizontal mid-plane for different Pr and Ro^{-1}. The iso-surfaces are drawn at $\theta = 0.4$ (blue) and 0.6 (red). For $Pr = 100$ at $Ro^{-1} = 0$ (and lower rotation rates $Ro^{-1} \leq 1$), the temperature iso-surfaces show a rising hot plume at one side of the lateral wall accompanied by a falling cold plume at the opposite side, as shown in Fig. 5.5(a). This represents a dipolar flow structure [156]. Supporting this, the vertical velocity contours show positive values on one side and negative on the opposite side. Note that the up-flow ($+w$) and down-flow ($-w$) are clearly distinguished by the solid and dashed lines, respectively. Similar dipolar behaviour was reported by Silano *et al.* [214] for non-rotating RBC at higher Prandtl numbers. As the rotation rate is increased ($Ro^{-1} = 10$

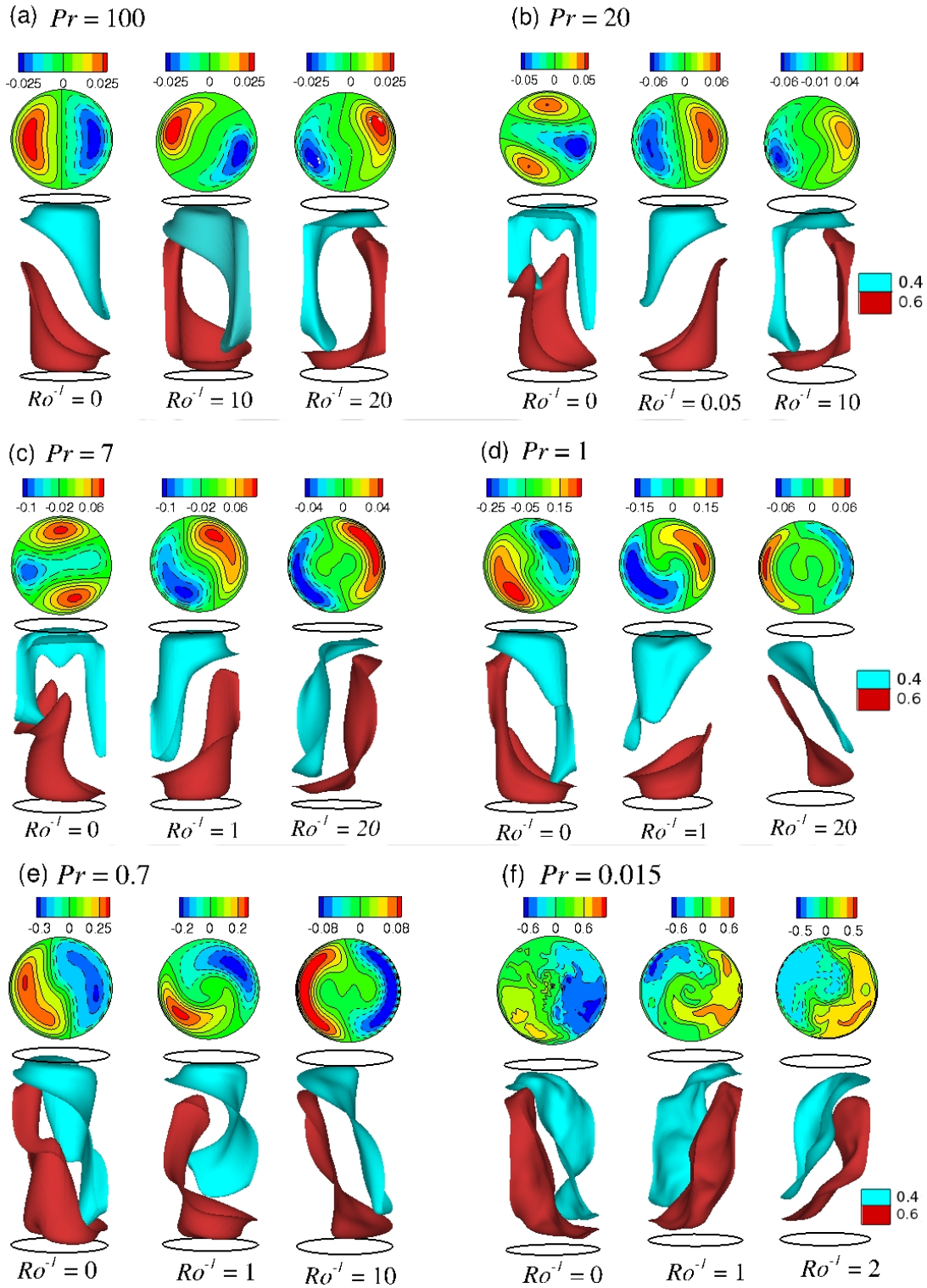

Figure 5.5: Instantaneous flow structures obtained for (a) $Pr = 100$, (b) $Pr = 20$, (c) $Pr = 7$, (d) $Pr = 1$, (e) $Pr = 0.7$, and (f) $Pr = 0.015$ at different rotation rates. Upper panel shows the contours of vertical velocity at mid-vertical plane with dotted (solid) lines indicating $w < 0$ ($w > 0$). Lower panel shows the temperature iso-surfaces at $\theta = 0.4$ and 0.6.

and 20), a significant increase in the vertical length of the temperature iso-surfaces is observed. Note that the flow maintains the dipolar behaviour even at high rotation rates.

The flow structures obtained for $Pr = 7$ and $Pr = 20$ are shown in Figs. 5.5(b) and 5.5(c). For non-rotating case (and low rotation rates), the hot fluid rises as a single plume near the bottom wall and bifurcates into two on reaching the mid-height. As a result, at the mid-vertical plane, two regions of hot up-flow and two cold down-flow exist intermittently along the azimuthal direction, which suggests a quadrupole mode dominated flow structure [156]. For $Pr = 20$, as rotation is increased ($Ro^{-1} \approx 0.05$), the flow structure changes to a dipolar state. However, for $Pr = 7$, flow maintains the quadrupolar structure up to $Ro^{-1} \leq 0.33$. At higher rotation rates [see $Ro^{-1} = 1$ in Fig. 5.5(c)] it shifts to dipolar structure. As rotation is increased further ($Ro^{-1} \approx 20$), the plumes become wall-bounded, and the bulk region shows a reduction in the vertical velocity fluctuations. Recall that in chapter 3 we observed that strong rotation force stabilizes the fluctuations in the bulk region which results in the so-called wall mode convection [215], where pairs of wall-bounded hot and cold plumes appear alternatively in the azimuthal direction. Further, we observed that wall modes are characterized by a significant drop in the Nusselt number. Here, we observe wall mode convection for all Prandtl numbers at very high rotation rates. In later sections, the analysis on the association between flow structure and heat transport for different Pr and Ro^{-1} will be taken up.

For low Prandtl numbers ($Pr = 1$ and 0.7), dipolar flow behaviour is noticed for all rotation rates, as shown in Figs. 5.5(d) and 5.5(e). Similar to $Pr = 7$, at higher rotation rates ($Ro^{-1} = 10$ and 20), the fluctuations in the bulk are suppressed, and the flow becomes wall-bounded. The flow structures observed for $Pr = 0.015$ at different rotation rates are shown in Fig. 5.5(f). Although, the vertical velocity contours at mid-plane suggests a chaotic flow behaviour, the dipolar nature of the flow is apparent. The temperature iso-surfaces scale almost the entire cylinder even at low rotation rates. A static conduction stage is obtained at $Ro^{-1} = 10$. In general, we observe a dipolar flow structure for all Pr except for $Pr = 7$ and 20, where a quadrupole dominated flow structure is obtained for low rotation rates (and $Ro^{-1} = 0$) followed by dipolar behaviour at moderate rotation rates. After characterizing the flow, now we discuss the statistics of the mean flow in the next section.

5.4 Statistics of the mean flow

In order to identify how rotation and change in Pr affect the mean flow behaviour, we evaluate the root mean square (rms) and mean of temperature and vertical velocity. The mean temperature profile ($\langle\theta\rangle_{A,t}$) along the axial direction for $Pr = 0.7$ at different rotation rates are shown in Fig. 5.6(a). As the rotation rate is increased, the temperature gradient stabilizes along the vertical direction and the mean temperature profile approaches a linear one. At $Ro^{-1} = 20$, temperature profile is nearly linear. Similar inference can be made from the rms of vertical velocity profiles shown in Fig. 5.6(b). We calculate the rms of vertical velocity as $w_{rms} = \sqrt{\langle(w - \langle w\rangle_{A,t})^2\rangle_{A,t}}$ where $\langle w\rangle_{A,t} \approx 0$. As rotation is increased, the vertical velocity rms decreases, accompanied by the reduction in magnitude of w. This is an indication of flow stabilization, which is theoretically explained by Taylor-Proudman theorem [101, 102]. The theorem states that in a homogeneous, inviscid flow dominated by Coriolis force, there is no variation of flow parameters along the rotation axis. Further details on the flow stabilization by Taylor-Proudman theorem in RRBC is discussed in chapter 3. Similar trend in the $\langle\theta\rangle_{A,t}$ and w_{rms} profiles with the increase in rotation rates was observed by Kunnen *et al.* [124, 126] in their numerical simulations of RRBC in a rectangular domain with periodic side walls.

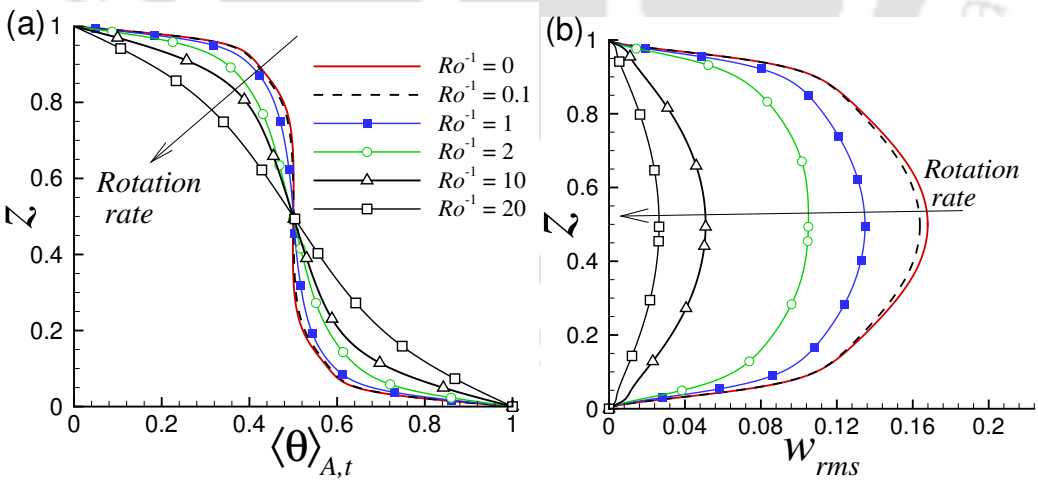

Figure 5.6: Variation of (a) mean temperature and (b) root-mean-square of vertical velocity along the vertical direction for $Pr = 0.7$ at different rotation rates.

As the main aim of our present study is to analyze the effect of Pr on the overall dynamics of the flow, we vary the Prandtl number and identify its effects on the statistics of the mean flow. The variation of the horizontal plane and time-averaged temperature ($\langle\theta\rangle_{A,t}$) along the axial

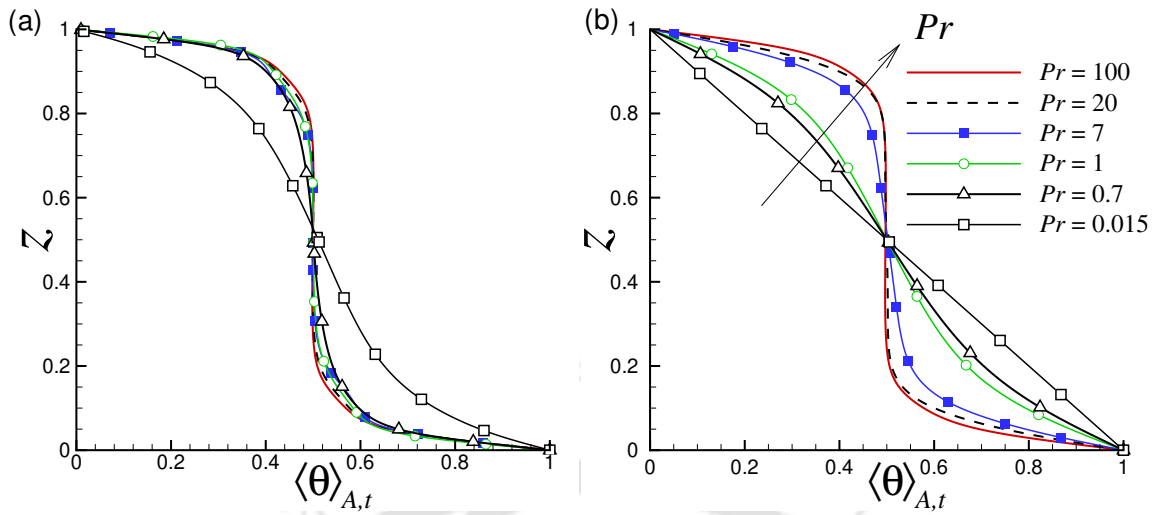

Figure 5.7: Variation of mean temperature along the vertical direction for (a) $Ro^{-1} = 1$ and (b) $Ro^{-1} = 20$ at different Pr.

direction for different Pr at $Ro^{-1} = 1$ and 20 are shown in Fig. 5.7. At $Ro^{-1} = 1$, the mean temperature profiles are almost similar for different Prandtl numbers except for $Pr = 0.015$ [see Fig. 5.7(a)]. For higher Prandtl numbers, a steep temperature gradient exists near the top and bottom walls, and it reduces near the bulk. However, for $Pr = 0.015$ a much stable temperature gradient along the vertical direction is observed. At $Ro^{-1} = 20$, the effect of rotation with the change in Prandtl number is clearly reflected in the mean profiles shown in Fig. 5.7(b). As Pr is reduced, the mean temperature profile approaches a linear one along the vertical direction. For $Pr = 100$ and 20 the profiles are similar to that obtained at $Ro^{-1} = 1$. This is due to the stronger viscous force at higher Pr. For $Pr = 0.015$, the flow reaches the conduction stage at $Ro^{-1} = 0.05$, and as a result, the mean temperature profile approaches a linear one.

The variation of rms of vertical velocity and temperature along the vertical direction for different Pr is shown in Fig. 5.8, for high rotation rate $Ro^{-1} = 20$. For higher Prandtl numbers, w_{rms} increases near the bulk and decreases near the no-slip walls. With decrease in Prandtl number, w_{rms} increases in the bulk for $Pr \geq 1$. However, for lower Prandtl numbers, $Pr = 0.7$ and 0.015, the rms of vertical velocity drops considerably. This is due to the significantly strong Coriolis force that dominates both the viscous and inertial forces. Similar observation is made from the rms of temperature shown in Fig. 5.8(b). The rms of temperature is calculated as $\theta_{rms} = \sqrt{\langle(\theta - \langle\theta\rangle_{A,t})^2\rangle_{A,t}}$. For high Pr, θ_{rms} increases as we move away from the isothermal plates and peaks near the edge of the boundary layer, where it shows a sharp gradient. With

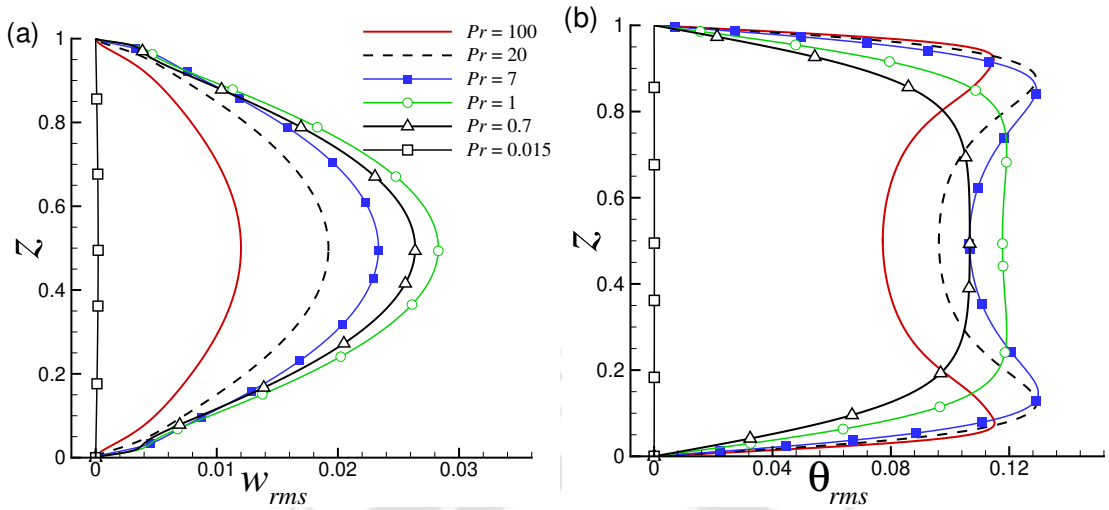

Figure 5.8: Variation of root mean square of (a) vertical velocity and (b) temperature at high rotation rate $Ro^{-1} = 20$ for different Pr.

decrease in Pr, both θ_{rms} in the bulk and boundary layer region increases, while for $Pr \leq 0.7$ they apparently reduce. For $Pr = 0.015$, all the velocity and temperature fluctuations are damped out, and w_{rms} and θ_{rms} approach zero, indicating a conduction stage. After characterizing the flow structures and investigating the effect of Ro^{-1} and Pr on the mean flow, we next study their impact on the heat transport.

5.5 Effect of rotation and Prandtl number on heat transport

In RRBC, dynamics of heat transport strongly depends on the rotation rate. It is well known that at strong enough rotation rates, heat transfer reduces due to the suppression of vertical velocity fluctuations [115, 120]. However, at moderate rotation rates the Nusselt number increases considerably, depending on Ra and Pr [135, 138]. Horn and Shishkina [139] studied the Nusselt number trend with increasing rotation rate for $10^5 \leq Ra \leq 6.7 \times 10^9$, $Pr = 0.7$ and $\Gamma = 0.5$, and observed a general behaviour for all the Rayleigh numbers, i.e., heat transfer rate remained almost constant for slow rotation and then dropped rapidly at a higher rotation rate. Here we identify the effect of rotation on heat transfer rate and how these dynamics change with Pr. A similar study in this direction was performed by Stevens *et al.* [138] where they identified the optimal Pr for maximum heat transfer enhancement at $Ra = 10^8$ and for $0.7 \leq Pr \leq 55$. They observed heat transfer enhancement for all Pr except $\mathrm{Pr} = 0.7$. Here, in addition to the

moderate Pr regime, we consider two extreme Prandtl numbers, i.e., $Pr = 0.015$ and 100, and investigate the associated heat transfer dynamics with rotation.

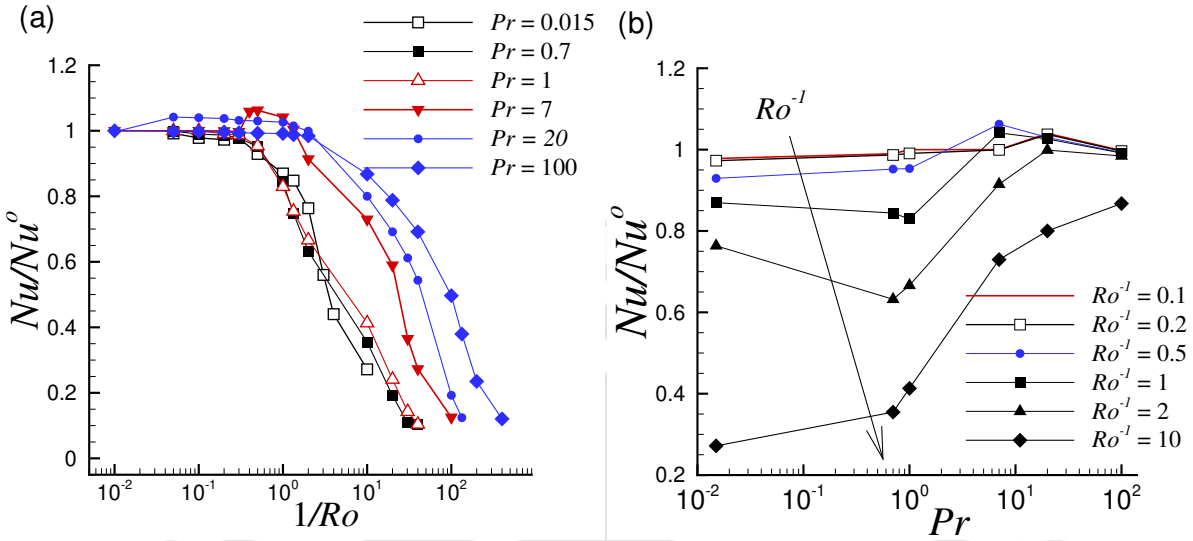

Figure 5.9: (a) The average Nusselt number Nu normalized by Nu^o as a function of inverse Ro for different Pr. (b) The variation of Nu/Nu^o with Pr for different rotation rates. The arrow indicates the direction of increasing rotation rate.

The horizontal plane averaged Nusselt number at the bottom plate, Nu (note that the subscript S is dropped for simplicity) is evaluated for heat transfer analysis. For unsteady flows, Nu computed is time-averaged ($t \approx 300$ to 500 convective time units) after reaching a statistically stationary state. A general trend of suppression of heat transfer due to rotation is evident from Fig. 5.9(a), where the ratio of the average Nusselt number for rotating case to that of its stationary counterpart Nu/Nu^o is plotted against rotation rate $(1/Ro)$. At lower rotation rates, the ratio remains almost constant and decreases significantly at higher rotation rates. For moderate Prandtl numbers $Pr = 7$ and 20, we obtain an increase in Nusselt number of about 6% and 4%, respectively, from the stationary value, at low rotation rates. A similar increment in heat transfer rate at moderate Prandtl numbers was found by Zhong *et al.* [135] and Stevens *et al.* [138] at plume dominated flow regimes ($Ra \geq 10^8$). However, in the present study at $Ra = 10^6$, flow is mainly dominated by large-scale flow structures. We identify that the increment in the heat transfer rate is obtained in the region where the flow structure changes from quadrupolar to dipolar behaviour. A similar connection between heat transfer rate and the flow structures has been observed by Xi *et al.* [156] in their experiments with water. Additionally, we observe that the increment in Nusselt number occurs at a lower rotation rate for $Pr = 20$

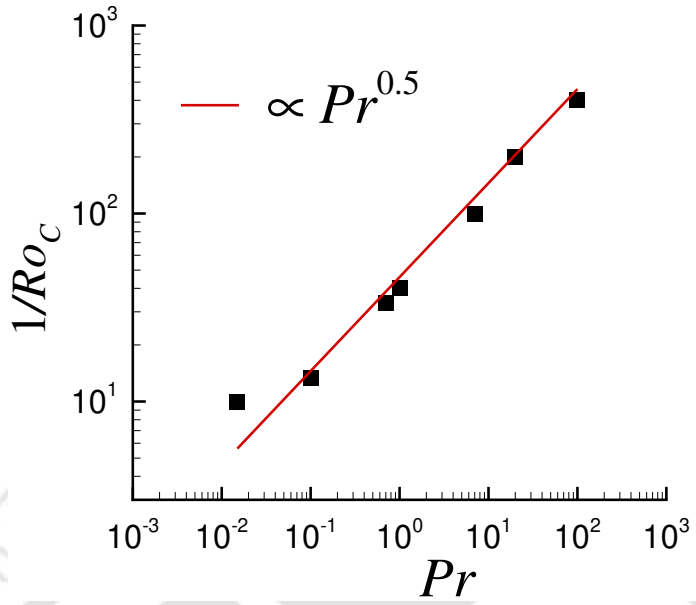

Figure 5.10: Critical rotation rate (expressed as $1/Ro_c$) for conduction stage versus Pr, showing power law variation.

than for $Pr = 7$. It is to be noted that heat transfer enhancement is limited to this moderate Pr regime as no increase in Nu/Nu^o is observed for the two extreme Prandtl numbers, i.e., $Pr = 0.015$ and 100.

The critical rotation rate which corresponds to the onset of decreasing trend in Nusselt number regime is attributed to the change in Pr. It is apparent from Fig. 5.9(a) that the departure of Nu from its stationary value is delayed with the increase in Pr. This suggests the stabilizing effect of Pr on RRBC. The effect of Prandtl number on heat transfer rate at different Ro is evident from Fig. 5.9(b). At higher rotation rates, Nu/Nu^o increases with the increase in Pr, while at lower rotation rates, it remains almost constant for all Pr. However, for moderate Prandtl numbers ($Pr = 7$ and 20), Nu/Nu^o rises above unity for low rotation rates.

At extremely high rotation rates, flow essentially becomes two-dimensional. The heat transfer occurs solely by conduction and Nusselt number approaches unity. The critical rotation rate ($1/Ro_c$) at which flow attains a conduction stage is shown as a function of Pr in Fig. 5.10. The plot indicates that as Pr increases, a higher rotation rate is required to accomplish the conduction stage. We observe a power-law behaviour of $1/Ro_c \propto Pr^{0.5}$. As Ro approaches Ro_c, the flow becomes geostrophic, i.e., the inertial and viscous forces become negligible as compared to the Coriolis force [124]. However, with the increase in Pr, the viscous force increases. As

a result, higher rotation rate (Coriolis force) is required to counter this larger viscous force at higher Pr.

5.6 Heat transport and associated flow structures

Heat transport and flow dynamics are strongly connected in Rayleigh-Bénard convection. The relation between the mean flow structure and heat transfer rate in RBC was investigated in the works of Roche *et al.* [216], Chilla *et al.* [217], Nikolaenko *et al.* [218], and Stringano and Verzicco [198]. In their experimental study, Weiss and Ahlers [219] reported an increase in Nusselt number for single-roll convection state compared to double-roll state. Verzicco and Camussi [180] carried out a detailed numerical study on the dependency of flow structure on heat transport and observed that as the LSC structure is suppressed, Nu drops substantially for lower Pr than for moderate Pr.

Here, we turn our focus on the quantification of the flow structures and their temporal evolution. Note that in chapter 3, we identified and quantified different flow regimes based on the Fourier decomposition of vertical velocity along the cylinder azimuth. Following the same idea, here, we identify the dominant Fourier modes and connect these with the associated heat transfer dynamics. For this, Fourier mode analysis of vertical velocity signals is carried out along the mid-height of the cylindrical cell. If u_j is the velocity signal from $N = 8$ uniformly sampled data points ($\pi/4$ apart) along the azimuthal direction, which can be seen from Fig. 5.1(b), then the Fourier transform of u_j can be written as

$$\hat{u}_k = \sum_{j=1}^{N} u_j e^{-i2\pi kj/N}, \tag{5.1}$$

where $\hat{u}_k$ represents the k^{th} Fourier mode. The energy of each mode is evaluated as the square of the amplitude ($E_k = |\hat{u}_k|^2$) and the total energy E_{tot} is computed as the sum of energy in all modes. The ratio of the energy of each mode to the total energy (E_k/E_{tot}) is calculated to estimate the energy fraction.

Table 5.3 shows the time-averaged energy fraction $\langle E_k/E_{tot}\rangle_t$ for different fluids at various rotation rates. For $Pr = 0.015$ first Fourier mode is active in all cases and contains almost 80%

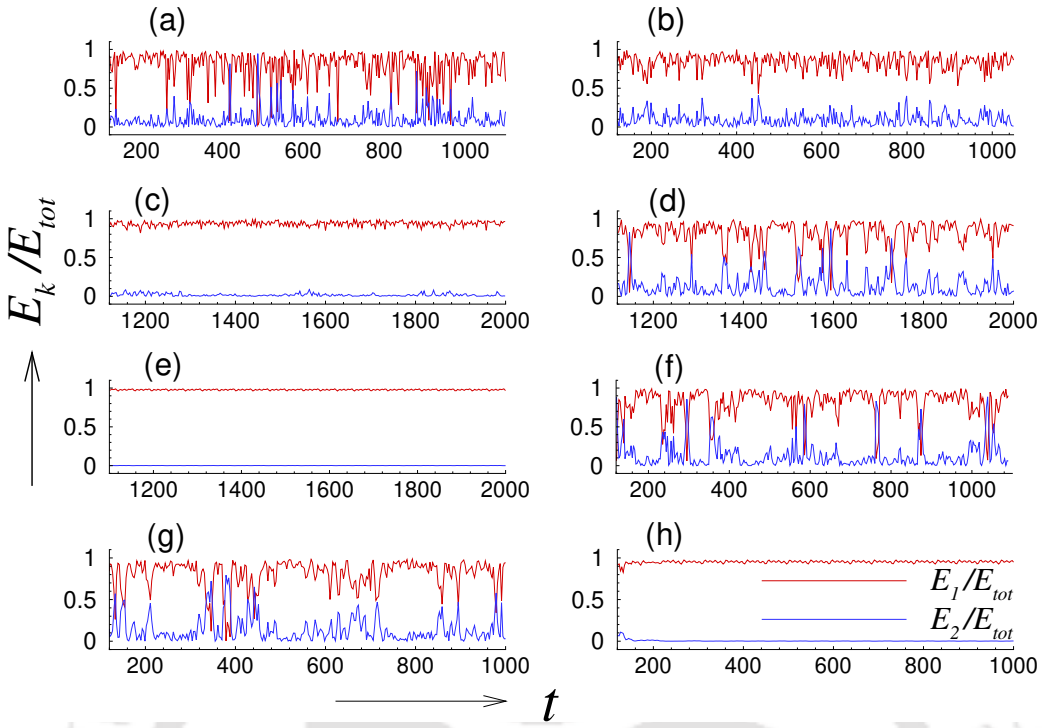

Figure 5.11: The temporal evolution of energy fraction E_k/E_{tot} of the first and second Fourier modes for (a) $Pr = 0.015$ and $Ro^{-1} = 0$, (b) $Pr = 0.015$ and $Ro^{-1} = 1.33$, (c) $Pr = 0.7$ and $Ro^{-1} = 1$, (d) $Pr = 0.7$ and $Ro^{-1} = 2$, (e) $Pr = 0.7$ and $Ro^{-1} = 10$, (f) $Pr = 1$ and $Ro^{-1} = 1$, (g) $Pr = 1$ and $Ro^{-1} = 2$, and (h) $Pr = 1$ and $Ro^{-1} = 4$.

of the total energy. The time evolution of the energy of the first two Fourier modes for $Pr = 0.015$ at $Ro^{-1} = 0$ and 1.33 is shown in Figs. 5.11(a) and 5.11(b). It can be clearly seen that at $Ro^{-1} = 0$, the energy fraction of the first mode E_1/E_{tot} is dominant, with frequent exchange of energy between the first and second mode. However, as the rotation rate is increased ($Ro^{-1} = 1.33$), the magnitude of the exchange of energy between the Fourier modes reduces.

For $Pr = 0.7$ and 1, first mode dominated flow is obtained even at the non-rotating case. Table 5.3 shows that for $Ro^{-1} \leq 0.5$, more than 90% of the energy is contained in the first Fourier mode, and there is negligible exchange of energy between the modes [see Fig. 5.11(c)]. At higher rotation rates, a minor reduction in the energy fraction of first mode followed by an increment in that of second mode is observed, where the flow becomes chaotic ($1.33 \leq Ro \leq 2$ for $Pr = 0.7$ and $1 \leq Ro^{-1} \leq 2$ for $Pr = 1$). Here, we observe frequent exchange of energy between the first and second modes, as shown in Figs. 5.11(d), 5.11(f), and 5.11(g). However, at even higher rotation rates, more than 97% of the energy is contained in the first Fourier mode, and the magnitude of the exchange of energy between the Fourier modes reduces [see

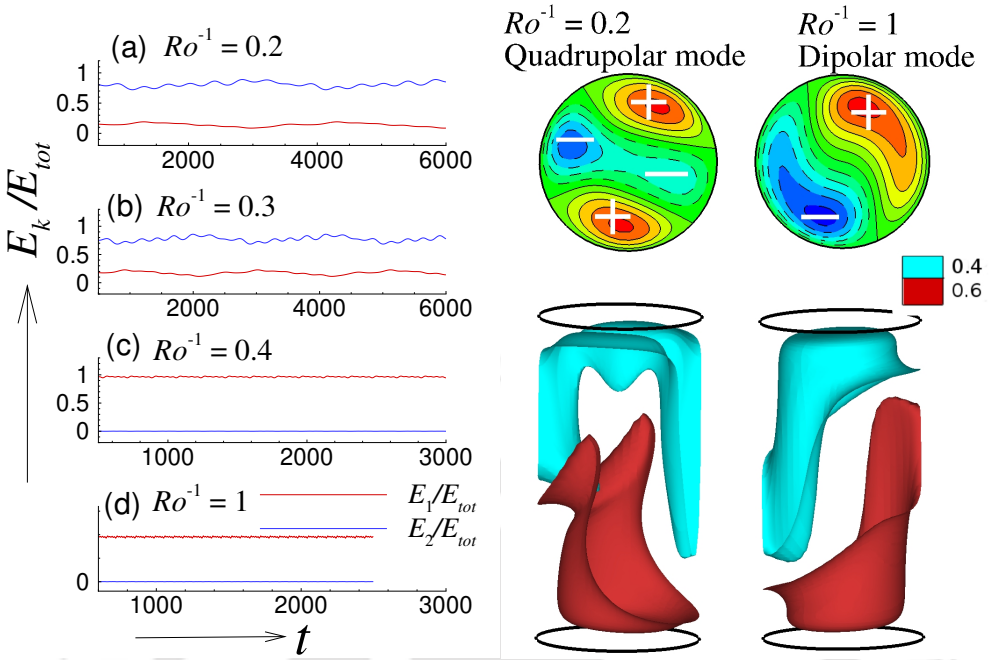

Figure 5.12: The left panel shows the temporal evolution of energy fraction E_k/E_{tot} of the first and second Fourier modes for $Pr = 7$ at (a) $Ro^{-1} = 0.2$, (b) $Ro^{-1} = 0.3$, (c) $Ro^{-1} = 0.4$, and (d) $Ro^{-1} = 1$. The right panel shows the quadrupolar and dipolar mode dominated flow structures obtained for $Ro^{-1} = 0.2$ and $Ro^{-1} = 1$, respectively. Here upper plot shows the contours of vertical velocity at mid-vertical plane with $+$ $(-)$ sign indicating the poles with $w > 0$ $(w < 0)$ and lower plot shows the temperature iso-surfaces at $\theta = 0.4$ (blue) and 0.6 (red).

Figs. 5.11(e) and 5.11(h)].

Table 5.3: Fraction of energy of the dominant Fourier modes for different Pr at various rotation rates.

Pr	Ro^{-1}	$\langle E_1/E_{tot}\rangle_t$	$\langle E_2/E_{tot}\rangle_t$
0.015	$0 \le Ro^{-1} \le 0.5$	≈ 0.80	≈ 0.1
0.015	$1 \le Ro^{-1} \le 2$	≈ 0.83	≈ 0.095
0.7	$0 \le Ro^{-1} \le 1$	≈ 0.92	≈ 0.001
0.7	$1.33 \le Ro^{-1} \le 2$	≈ 0.81	≈ 0.12
0.7	$10 \le Ro^{-1} \le 20$	≈ 0.98	≈ 0.002
1	$0 \le Ro^{-1} \le 0.5$	≈ 0.95	≈ 0.002
1	$1 \le Ro^{-1} \le 2$	≈ 0.82	≈ 0.12
1	$10 \le Ro^{-1} \le 20$	≈ 0.99	≈ 0.001
7	$Ro^{-1} = 0$	0.13	0.82
7	$0.1 \le Ro^{-1} \le 0.33$	≈ 0.06	≈ 0.87
7	$0.4 \le Ro^{-1} \le 1$	≈ 0.95	≈ 0.001
7	$1.33 \le Ro^{-1} \le 2$	≈ 0.90	≈ 0.05
7	$Ro^{-1} = 10$	0.97	0.001
20	$Ro^{-1} = 0$	0.210	0.71
20	$0.05 \le Ro^{-1} \le 10$	≈ 0.96	≈ 0.001
100	$0 \le Ro^{-1} \le 10$	≈ 0.97	≈ 0.001

For $Pr = 7$ at low rotation rates, second Fourier mode is dominant and contains more than 80% of the total energy (refer Table 5.3). Figure 5.12 shows the energy fraction of first Fourier mode at $Ro^{-1} = 0.2, 0.3, 0.4$ and 1. The flow remains second mode dominated at lower rotation rates ($Ro^{-1} \leq 0.3$). However, at moderate rotation rates ($Ro^{-1} \approx 0.4$), first mode reappears and contains 97% of the total energy. We observe an increment in heat transfer rates as the flow makes the transition from second Fourier mode dominated to first mode dominated state. The flow structures obtained for these cases are shown in Fig. 5.12, where the vertical velocity contours clearly indicate a quadrupole mode dominated flow for $Ro^{-1} = 0.2$ and dipole mode dominated flow at $Ro^{-1} = 1$. The temperature iso-surfaces at $Ro^{-1} = 0.2$ show that hot plume rises near the bottom plate and bifurcates on reaching the mid-plane. As a result, two pairs of hot up-flow and cold down-flow regions exist intermittently and separated azimuthally by approximately $\pi/2$ near the mid-planar region. However, at $Ro^{-1} = 1$, a single pair of hot and cold plumes is seen. Similar observation is made for $Pr = 20$, where a second mode dominated flow is observed for the non-rotating case (and $Ro^{-1} = 0.01$). It can be established that the increment in heat transfer rate in the case of $Pr = 7$ and 20 is an outcome of the change in flow modes from quadrupolar to dipolar. This is consistent with the experimental observations made by Xi *et al.* [156], where they reported the first Fourier mode to be associated with higher heat transfer rate. For $Pr = 100$ first Fourier mode dominated flow is obtained for all cases, with more than 90% of the energy contained in the first mode.

Note that the quadrupolar structures show no symmetry about the centre, while the dipolar structures are symmetric [see Fig. 5.12(b)]. This can be associated with the interplay between the Fourier modes at different rotation rates. For the non-rotating case at $\mathrm{Pr} = 7$, about 80% of the total energy is contained in the second Fourier mode and nearly 10% in the first Fourier mode (Table 5.3). As a result, the flow structure is more close to a quadrupolar state. But it does not exhibit a symmetric behaviour due to the presence of other modes (which are less dominant). However, at $Ro^{-1} = 1$, about 95% energy is contained in the first Fourier mode, while that in the second mode is less than 1%. This clearly shows that it is a near-perfect first Fourier mode dominated flow structure (dipolar) and thus displays symmetry about the centre. After establishing the connection of heat transfer with the flow structure, we now turn our focus to investigate the dynamics of boundary layer, which is presented in the next section.

5.7 Boundary layer and heat transport

Heat transport and global features of Rayleigh-Bénard system are strongly related to the boundary layers. In fact almost all the theories of heat transport in turbulent RBC [75–78], are essentially based on the boundary layer dynamics. Here we analyze the thermal boundary layer thickness and identify its relation with rotation rate and change in Pr. Further, we connect the spatial structure of the thermal boundary layer with the heat transfer rate. Strong radial dependence of boundary layer structure in RBC was observed by Stevens *et al.* [153]. In their numerical simulations, Verzicco and Camussi [52] reported single roll and two-roll convective patterns in a cylindrical cell and found that the transition between these states has an appreciable impact on the boundary layer structure and global heat transfer properties. Here we try to connect the heat transfer enhancement observed for moderate Pr (at low rotation rates) with the thermal boundary layer dynamics.

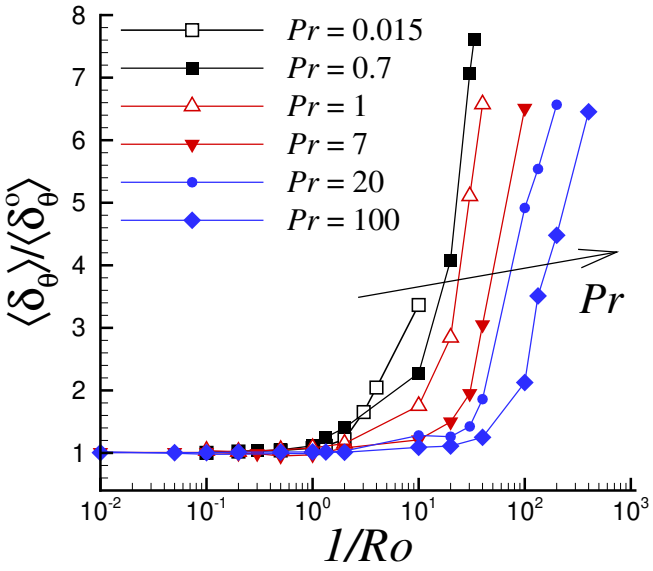

Figure 5.13: The variation of the ratio of average thermal boundary layer thickness for rotating case to that of the stationary case, $\langle\delta_\theta\rangle/\langle\delta_\theta^o\rangle$, with rotation rate $(1/Ro)$ for different Pr. The departure of $\langle\delta_\theta\rangle/\langle\delta_\theta^o\rangle$ from unity is delayed with the increase in Pr.

Here, the thermal boundary layer thickness is evaluated near the bottom plate. The vertical distance of the point from the bottom plate where the linear fit of the time-averaged temperature profile approaches the bulk temperature ($\theta = 0.5$) is taken as the local boundary layer thickness (δ_θ). More details on the computation of δ_θ using the so-called slope method is discussed in

chapter 3. Same method is adopted to compute the boundary layer thickness for all the spatial locations (r, ϕ). The ratio of the spatial averaged thermal boundary layer thickness for rotating case to that of the non-rotating case ($\langle\delta_\theta\rangle/\langle\delta_\theta^o\rangle$) is computed and plotted against $1/Ro$ for different Prandtl numbers in Fig. 5.13. We observe that $\langle\delta_\theta\rangle/\langle\delta_\theta^o\rangle$ remains almost constant at lower rotation rates and rises at higher rotation rates. As rotation is increased, the temperature profile stabilizes along the vertical direction, and boundary layer thickness increases. Further, the departure of $\langle\delta_\theta\rangle$ from its stationary value is delayed as Pr increases, which shows the stabilizing effect of Pr from the boundary layer aspect. At higher rotation rates we observe a power law behaviour $\langle\delta_\theta\rangle/\langle\delta_\theta^o\rangle = a(1/Ro)^b$. The values of a and b for different Pr is shown in Table 5.4. The exponent b is smallest for $Pr = 0.015$. At moderate Pr we observe an exponent close to unity. Thus, the increase in boundary layer thickness with the increase in rotation rate is reflected more at moderate Prandtl number regime.

Table 5.4: Values of a and b for different Prandtl numbers corresponding to the power law $\langle\delta_\theta\rangle/\langle\delta_\theta^o\rangle = a(1/Ro)^b$.

Pr	a	b
0.015	0.82	0.63
0.7	0.41	0.81
1	0.18	0.96
7	0.09	0.94
20	0.08	0.85
100	0.08	0.74

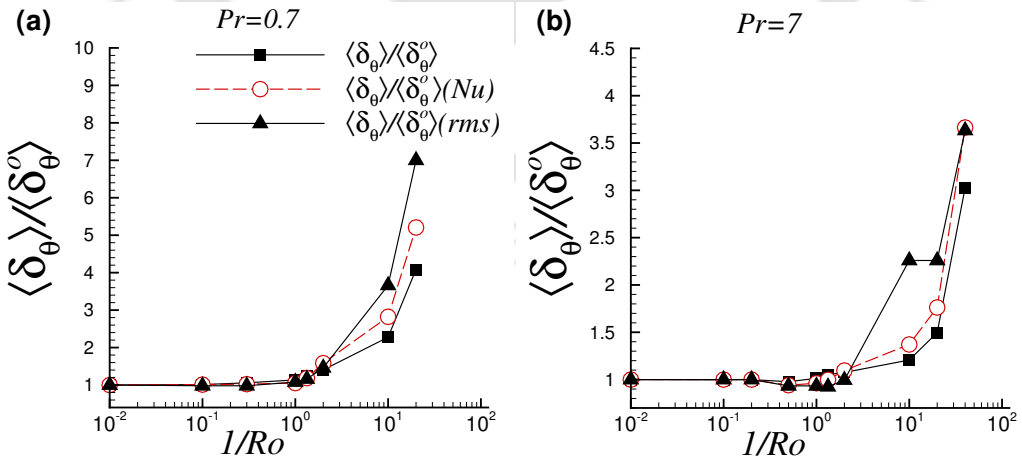

Figure 5.14: Comparison of $\langle\delta_\theta\rangle/\langle\delta_\theta^o\rangle$ obtained from mean temperature, rms of temperature, and analytical method for $Pr = 0.7$ and 7.

Figure 5.14 shows the comparison between the thermal boundary layer thickness computed by different methods for $Pr = 7$ and 0.7. Here $\langle\delta_\theta\rangle(Nu)$ indicates the analytical thermal bound-

ary layer thickness obtained from the relation $\delta_\theta \approx 1/2Nu$, while $\langle\delta_\theta\rangle(rms)$ corresponds to the boundary layer thickness calculated from the rms of temperature profile along the axial direction. It is computed as the vertical distance of the peak rms from the bottom wall [52]. $\langle\delta_\theta\rangle$ is the thickness from mean temperature profile, as discussed previously. It is evident that for both the Prandtl numbers, boundary layer thickness computed from mean temperature profile agrees with the analytical thermal boundary layer thickness. This substantiate our boundary layer calculations ($\langle\delta_\theta\rangle/\langle\delta_\theta^o\rangle$) discussed previously. We observe that the boundary layer thickness computed from the rms method agrees with the other two at low rotation rates, while it over-predicts at higher rotation rates.

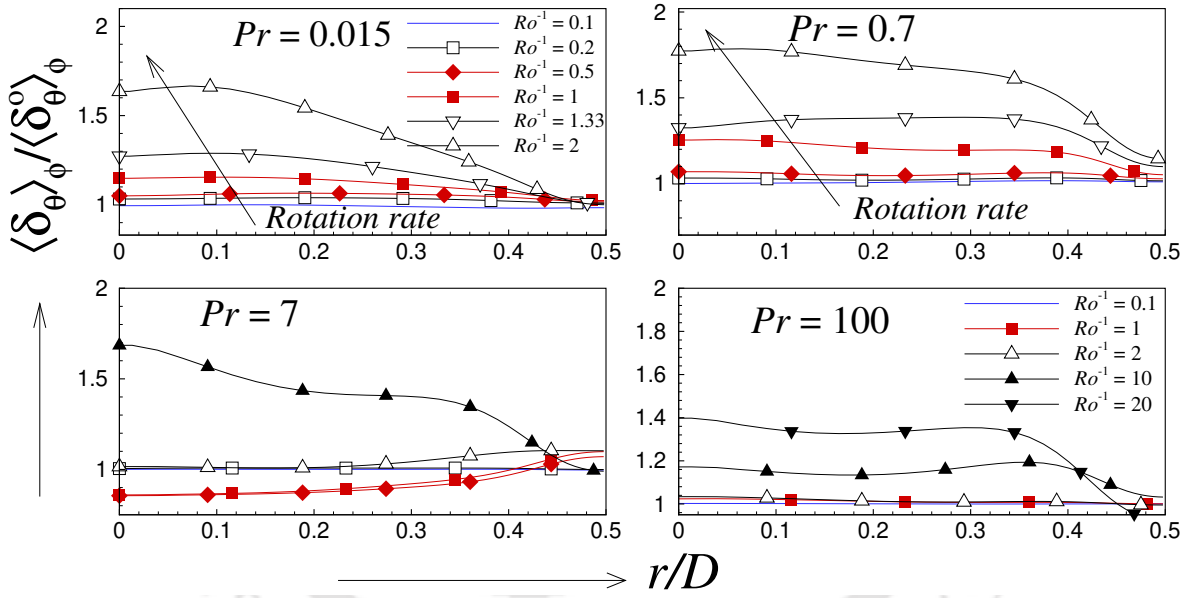

Figure 5.15: Variation of $\langle\delta_\theta\rangle_\phi/\langle\delta_\theta^o\rangle_\phi$ along the radial direction for (a) $Pr = 0.015$, (b) $Pr = 0.7$, (c) $Pr = 7$, and (d) $Pr = 100$ at different rotation rates. The arrows indicate the direction of increase in rotation rate.

The variation of azimuthal averaged boundary layer thickness with respect to the non-rotating case $\langle\delta_\theta\rangle_\phi/\langle\delta_\theta^o\rangle_\phi$ along the radial direction for different fluids at various rotation rates is shown in Fig. 5.15. Here $\langle..\rangle_\phi$ denotes averaging along the azimuthal direction. For low Pr, the effect of rotation is more evident near the core region ($r/D \leq 0.2$) of the cylindrical domain, where $\langle\delta_\theta\rangle_\phi/\langle\delta_\theta^o\rangle_\phi$ increases with the increase in rotation rate, while it remains almost constant near the lateral wall ($r/D \geq 0.4$). The effect of rotation is less apparent along lateral wall due to the near wall viscous effects. Similar trend is observed at higher Prandtl number $Pr = 100$, where $\langle\delta_\theta\rangle_\phi/\langle\delta_\theta^o\rangle_\phi$ remains close to unity at lower rotation rates and becomes

thicker ($\langle\delta_\theta\rangle_\phi/\langle\delta_\theta^o\rangle_\phi \approx 1.3$) near the core at stronger rotation rates. For $Pr = 7$, a considerable reduction in thermal boundary layer thickness is evident at $Ro^{-1} = 1$ and 0.5, where $\langle\delta_\theta\rangle_\phi/\langle\delta_\theta^o\rangle_\phi \approx 0.85$ near the core region. This corresponds to the rotation rates where the increment in heat transfer rate is observed for $Pr = 7$ [see Figs. 5.9(a) and 5.9(b)]. Here the thermal boundary layer is thicker near the lateral wall and thinner near the core region compared to the non-rotating case.

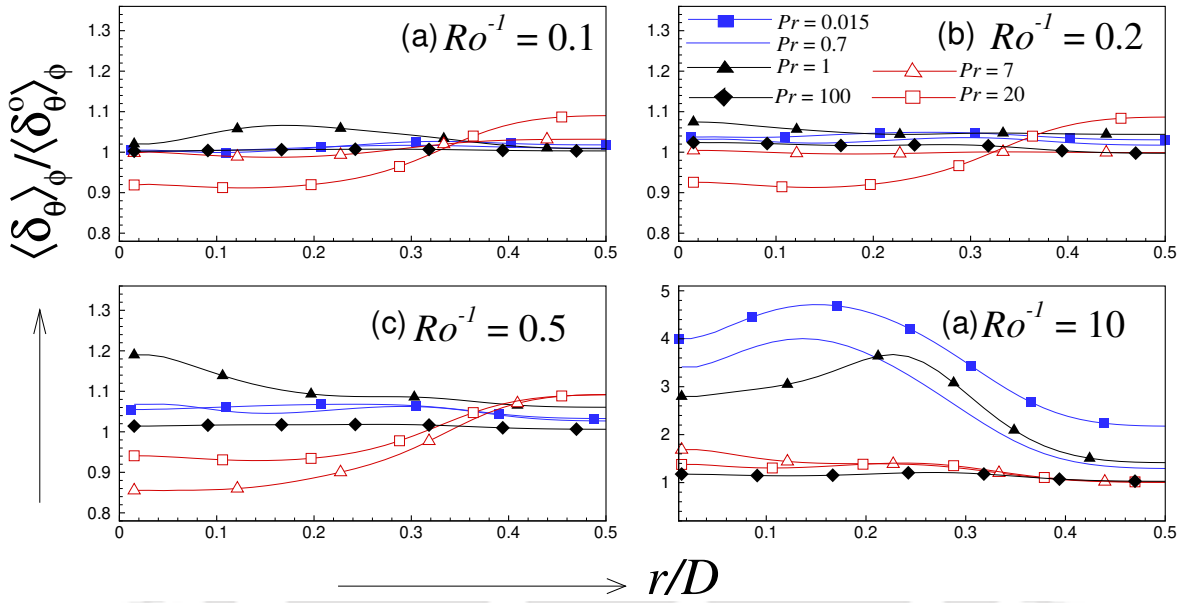

Figure 5.16: Variation of $\langle\delta_\theta\rangle_\phi/\langle\delta_\theta^o\rangle_\phi$ along the radial direction for different fluids at (a) $Ro^{-1} = 0.1$, (b) $Ro^{-1} = 0.2$, (c) $Ro^{-1} = 0.5$, and (d) $Ro^{-1} = 10$.

The variation of $\langle\delta_\theta\rangle_\phi/\langle\delta_\theta^o\rangle_\phi$ along the radial direction for different fluids at specific rotation rates is shown in Fig. 5.16. At low rotation rates $Ro^{-1} = 0.1$ and 0.2, all Prandtl numbers except $Pr = 20$ shows negligible variation from the non-rotating boundary layer thickness. However, for $Pr = 20$ the thermal boundary layer becomes thinner near the core region and thicker near the lateral wall ($Ro^{-1} = 0.1, 0.2$ and 0.5). This is the region where heat transfer enhancement is observed for $Pr = 20$. Similar reduction in $\langle\delta_\theta\rangle_\phi/\langle\delta_\theta^o\rangle_\phi$ near the core region is observed for $Pr = 7$ at $Ro^{-1} = 0.5$. However, for all other Prandtl numbers the thermal boundary layer thickness remains almost close to its stationary counterpart throughout the radial direction. Further, at $Ro^{-1} = 0.5$, the effect of Pr on the thermal boundary layer thickness is reflected more in the core region than near the lateral wall. At higher rotation rate, $Ro^{-1} = 10$, a trend of increasing $\langle\delta_\theta\rangle_\phi/\langle\delta_\theta^o\rangle_\phi$ with the decrease in Pr is observed in the core region, while it is less evident near the lateral wall. With increase in rotation, flow stabilization occurs due

to the dominance of Coriolis force over the viscous force, and the boundary layer thickness increases. However, with increase in Pr the viscous force increases and thus larger rotation rate is required to counter it. This explains the flatter profile of $\langle\delta_\theta\rangle_\phi/\langle\delta_\theta^o\rangle_\phi$ close to unity obtained for $Pr = 100$.

We observe that the heat transport in RRBC is strongly connected with the flow structures and boundary layer dynamics. For moderate Prandtl numbers ($Pr = 7$ and 20), we observe a heat transfer enhancement at low rotation rates where the flow makes a transition from quadrupolar to dipolar behaviour. Further, we identify that transition in flow states is accompanied by the reduction in thermal boundary layer thickness.

5.8 Summary

A detailed numerical investigation on the effect of Prandtl number on the flow structure and heat transfer rate in rotating Rayleigh-Bénard convection at $Ra = 10^6$ has been carried out in this chapter. For all Pr, a reduction in heat transfer rate is observed with the increase in rotation rate. However, for $Pr = 7$ and 20, an increase in Nusselt number of about 6% and 4%, respectively, from the non-rotating case is observed at low rotation rates. This is followed by a steep reduction in Nu at higher rotation rates. The present study reveals that the rise in heat transfer rate is observed in the region where the flow structure changes from quadrupolar to dipolar state. Further, as the flow transforms to the dipolar state, the thermal boundary layer thickness reduces, which in turn results in efficient heat transfer rate. At higher rotation rates, a power-law behaviour is observed for the boundary layer thickness as $\langle\delta_\theta\rangle/\langle\delta_\theta^o\rangle \propto (1/Ro)^b$, with the exponent b close to unity for moderate Pr. However, it reduces for both lower and higher Pr. The present work infers that there is an intermediate Pr regime where the increase in heat transfer occurs at low rotation rates. For lower Prandtl numbers ($Pr \leq 1$) and higher Prandtl number ($Pr = 100$), no increase in Nusselt number is observed where the flow remains dipole mode dominated even at low rotation rates and continues to remain so at moderate and high rotation rates. The critical rotation rate ($1/Ro_c$) for which transition to the conduction state occurs exhibits a power-law dependence on Prandtl number as $1/Ro_c \propto Pr^{0.5}$.

6

Statistics of thermal plumes in turbulent convection in a cubic cell

In this chapter, the statistics of thermal plumes in turbulent Rayleigh-Bénard convection inside a cubic cell filled with air ($Pr = 0.7$) is studied for the Rayleigh number range $2 \times 10^6 \leq Ra \leq 10^9$. Based upon the product of the vertical velocity and temperature fluctuation ($v'\theta'$), the entire cell volume is decomposed into plume and background dominated regions. Different cutoff values ($C_t = 0$-10% of the global maximum of $v'\theta'$) are used to demarcate these regions, and for all C_t, the volume fraction of the plume dominated region ($v'\theta' > C_t$) decreases with the increase in Ra, while that of the background ($v'\theta' \leq C_t$) increases. The thermal dissipation rate contribution from the plume and background regions show decaying power-law behaviour with Rayleigh. Further, at $C_t = 0$, the average thermal dissipation rate from the plume and background approach the global scaling for higher Rayleigh numbers ($Ra \geq 10^8$). At lower cutoffs, the plume contributions scale with Reynolds number as predicted by the Grossmann-Lohse theory, while deviations are observed in the background counterpart. The PDFs of thermal and viscous dissipation rates are well described by a stretched exponential function, and their tails become more extended with increase in Ra. In addition, statistical measures like variance, skewness and flatness of velocity and temperature are also evaluated to study different characteristics of the flow.

6.1 Introduction

The recurring themes in both theoretical descriptions and phenomenological pictures of Rayleigh-Bénard convection are how heat transport occurs in the system and what are the roles of thermal plumes in the heat transport and dissipation rates [57, 220]. Flow visualizations of turbulent RBC using various methods revealed coherent structures with mushroom-like appearance [89, 221]. These coherent structures are called thermal plumes. Over the years, researchers have used different techniques to identify plumes. The plumes are created near the top and bottom plates in the boundary layers and driven to the opposite plate as a result of buoyancy [222]. The morphology and dynamics of thermal plumes in turbulent RBC have become a subject of interest recently. Flow visualizations have shown that the plumes have a mushroom-like cap with sharp temperature gradient and a stem that is relatively diffuse (when observed from the sides) [87, 89, 94, 186, 222–224]. These are generally referred to as "mushroom-like" plumes. However, while observed from the top (or bottom) the morphology of the plumes is completely different, i.e., the thermal plume appears to be extended in one horizontal direction but concentrated in the opposite (orthogonal) direction [46, 62, 117, 225–229]. Such structures are often assumed to have considerable vertical extent and thus are referred as "sheet-like plumes". Zhou *et al.* [228] observed that the sheet-like plumes transform into mushroom-like ones as they move away from the boundary layer to the bulk region. Moreover, they observed that the area and heat content of the sheet-like plumes follow a log-normal distribution. In a different study, Zhou and Xia [224] characterized the geometrical and statistical properties of thermal plumes. They noticed that as Ra increases, the plume geometry changes from more-elongated to less-elongated. Further, the plume number followed a power-law dependency with Ra, which ultimately affects the $Ra - Nu$ scaling behaviour. Bosbash *et al.* [230] observed that below the top plate, the plumes undergo fragmentation due to interactions with the fluctuations in the bulk.

Thermal plumes play an important role in dictating the overall heat transport in turbulent RBC. Grossmann and Lohse [76, 167, 231] analyzed the viscous and thermal dissipation rates in turbulent RBC and split their volume averaged contributions from the bulk and boundary layers separately. As per Grossmann-Lohse theory (GL theory), the contribution of viscous and thermal dissipation from the background part dominates over that from boundary layers

for higher Rayleigh numbers. As the bulk and boundary layer decomposition does not account for the effect of thermal plumes (which can be considered as detached boundary layers), Grossmann-Lohse [167] divided the thermal dissipation rate into two subsets. One is the thermal dissipation rate in the plumes along with boundary layers and other the contribution from the turbulent background. The plumes and thermal boundary layers are assumed to have the same characteristic length δ_θ, which is the thermal boundary layer thickness [167]. He *et al.* [232] experimentally measured the local thermal dissipation using thermistors inside a cylinder of unit aspect ratio filled with water and decomposed the thermal dissipation rates into the mean and the fluctuating part. They observed that the mean part remains significant in the boundary layers, while the fluctuating part dominates in the bulk of the container.

Verzicco and Camussi [52] found that the contribution from the boundary layers (excluding the plumes) to the volume-averaged dissipation rate increases with Ra, which suggests that the role of plumes decreases for high Ra in thermally driven convection. Emran and Schumacher [95] investigated the statistics of thermal dissipation rate for a fluid of $Pr = 0.7$ contained in a unit aspect ratio cylindrical cell and concluded that the contribution due to the plume in the dissipation rate decreases with increase in Rayleigh number. From their statistical analysis, they concluded that the largest thermal dissipation events are always found in the plume dominated regions. Shishkina and Wagner [222] classified plume and background regions based on the combined analysis of local heat flux, thermal dissipation rates, and selected components of the velocity and vorticity fields. Further, they investigated the geometrical (plume area, diameter, curvature, thickness, etc.) and the physical properties (temperature, heat flux, dissipation, etc.) of the sheet-like plumes. In a different study, Shishkina and Wagner [94] performed a detailed analysis of thermal dissipation rates in turbulent RBC in a wide aspect ratio cylinder ($\Gamma = 10$). The simulations were performed at Rayleigh numbers 10^5, 10^6 and 10^7 and Prandtl number 0.7. They found that the turbulent background and its contribution to the volume-averaged thermal dissipation rate increases with Ra. Further, the ratio of the area-averaged (over the top or bottom plates) to the volume-averaged thermal dissipation rate was always greater than or equal to the Nusselt number irrespective of Ra, Pr and Γ. They observed that the plumes have a tendency to be arranged in a regular manner for low Rayleigh number ($Ra = 10^5$), while for higher Ra, they appear to form a large-scale circulation. On a similar note, the experimental study by Xi *et al.* [89] showed that plumes drive the onset of LSC in thermal convection.

Emran and Schumacher [170] analyzed the fine-scale statistics of temperature and its derivatives in convective turbulence. They observed that the PDFs of temperature or its fluctuations are always non-Gaussian. The PDFs of thermal dissipation rate deviated significantly from the log-normal distribution, and the PDF tails were well fitted with a stretched exponential function. Further, the tails became more extended with the increase in Ra, indicating the increase in the degree of small-scale intermittency of the dissipation field. Similar observations were made by Zhang *et al.* [169] in 2-D turbulent RBC in the Rayleigh number range $10^6 \leq Ra \leq 10^{10}$ for $Pr = 0.7$ and 5.3. They also reported that the tails of PDFs become more extended with decrease in Pr. Further, the thermal dissipation contribution from the plume and background regions were computed, and these quantities were compared with the Grossmann-Lohse theory [76]. The plume contributions scaled as predicted by GL theory, while the background contributions showed significant deviation from it. Bhattacharya *et al.* [233] carried out the DNS of turbulent RBC inside a cubic cell at $Ra = 10^6$ and 10^8, and derived the scaling relations for viscous dissipation rate in the bulk and boundary layers. They observed that the viscous dissipation rate in the bulk follows a log-normal distribution, while it follows a stretched exponential distribution inside the boundary layer.

Generally, in turbulent convection, the thermal dissipation rate is divided into two parts: contribution from the bulk and the boundary layers. It is assumed that the plume contribution in the thermal dissipation rate mainly comes from the boundary layer and the background contribution from the bulk. In the present work, depending on the positive correlations between the vertical velocity and the temperature we have divided the box volume into two subregions: plume and background dominated, and their corresponding contributions in the global thermal dissipation rate are evaluated. The threshold for separating these regions is varied and scaling relations with respect to Rayleigh number are established. The simulations are carried out in a cubic box in a large Rayleigh number range (up to $Ra = 10^9$) and highlight the statistics of contribution from the plume and background regions in dictating the overall scaling of dissipation rates. Further, different statistical quantities, such as variance, skewness, flatness and turbulent kinetic energy budget are evaluated in order to identify the flow characteristics in different regions of the flow.

6.2 Problem description

We investigate thermo-convective instability of an incompressible Newtonian fluid confined in a cubic cell with bottom-heated and top-cooled configuration. Figure 6.1 shows the schematic representation of the flow domain with appropriate boundary conditions. No-slip conditions are implemented on all the surfaces. For temperature, horizontal surfaces are iso-thermal, while the lateral walls are adiabatic. Direct numerical simulations are carried out for the Rayleigh number range $2\times10^6 \leq Ra \leq 10^9$ with air ($Pr = 0.7$) as the working fluid. Time advancement of $\Delta t = 5 \times 10^{-4}$ is used for $Ra \geq 5 \times 10^7$, while for lower Ra, $\Delta t = 10^{-3}$ is used. The time step for the time advancement is chosen such that the Courant number always remains less than 0.2.

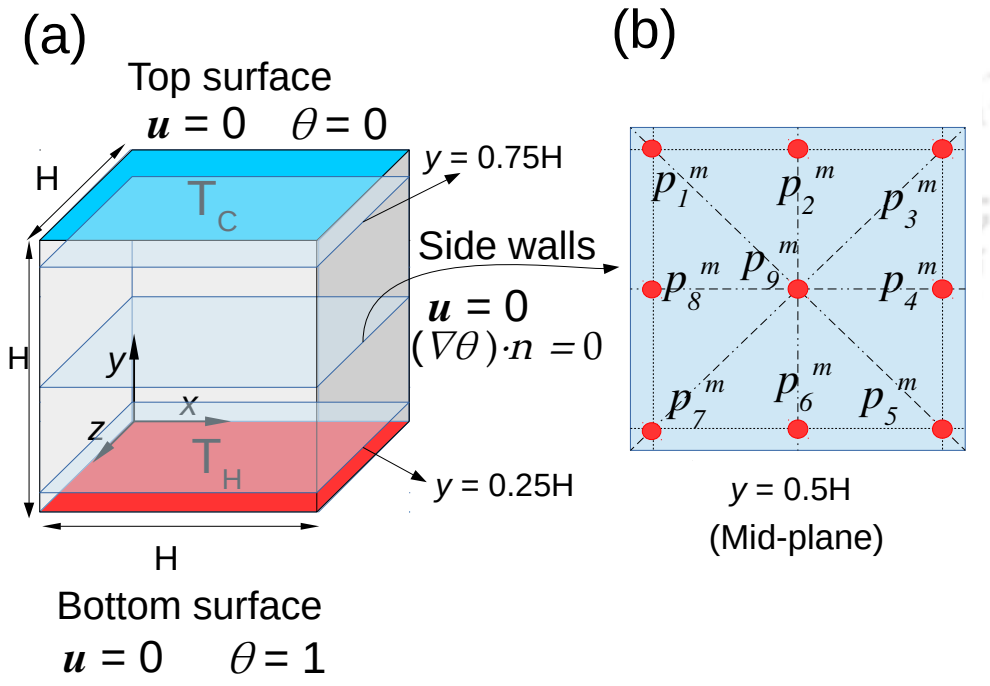

Figure 6.1: (a) Schematic diagram of the flow domain with boundary conditions. (b) The location of the numerical probes at the mid-plane ($y = 0.5H$) that are used to record the time signals.

Structured, non-uniform grids with refinement near the walls are used in the present study. Since the flow dynamics are greatly affected by the boundary layers, it is necessary to resolve the regions near the top plate, the bottom plate, and the lateral walls. The grid resolution for a given Rayleigh number is chosen in such a way that the maximum grid spacing (Δ_{max})

Table 6.1: Columns from left to right indicate, Ra, total number of grid points ($N_x \times N_y \times N_z$), number of grid points in the thermal boundary layer (N_{BL}), Nusselt number computed by different methods (Nu_S, Nu_{ϵ_θ}, and Nu_{ϵ_u}), Nusselt number reported by Kaczorowski and Xia [151] (Nu_{ref}), the convective time over which averaging is performed (t_{av}), and the maximum grid spacing normalized by the Kolmogorov length scale (η_k).

Ra	$N_x \times N_y \times N_z$	N_{BL}	Nu_S	Nu_{ϵ_θ}	Nu_{ϵ_u}	Nu_{ref}	t_{av}	Δ_{max}/η_k
2×10^6	$100 \times 100 \times 100$	10	10.1	10.1	10.2	10.0	1000	0.954
3×10^6	$100 \times 100 \times 100$	7	11.5	11.3	11.4	11.4	800	0.963
5×10^6	$168 \times 168 \times 168$	13	13.2	13.2	13.4	13.4	800	0.927
1×10^7	$168 \times 168 \times 168$	11	16.0	16.0	16.2	16.2	500	0.962
2×10^7	$200 \times 200 \times 200$	8	19.9	19.6	19.8	19.6	250	0.990
3×10^7	$200 \times 200 \times 200$	7	22.3	21.3	22.0	22.0	225	0.985
5×10^7	$264 \times 264 \times 264$	8	25.7	25.3	25.4	$--$	225	0.964
1×10^8	$300 \times 300 \times 300$	8	31.1	30.8	30.8	31.4	250	0.964
2×10^8	$372 \times 372 \times 372$	7	38.2	37.6	37.8	$--$	200	0.989
5×10^8	$420 \times 420 \times 420$	6	50.7	49.3	49.3	$--$	50	1.157
1×10^9	$512 \times 512 \times 512$	6	62.1	60.6	60.6	$--$	50	1.188

remains mostly lower than the global Kolmogorov length scale η_k. Here Δ_{max} indicates the maximum of mean grid size calculated as $\max(\Delta x \Delta y \Delta z)^{1/3}$ and η_k is estimated using the analytical prediction $\eta_k \approx (Pr^2/(RaNu))^{1/4}$ given by Grotzbach [152]. Table 6.1 shows that the ratio Δ_{max}/η_k is almost less than or equal to unity. The thermal boundary layer width (δ_θ) is computed using the theoretical estimate $\delta_\theta \sim 1/(2Nu)$ and we ensure that the number of grid points inside the thermal boundary layer (N_{BL}) is at least 6-10 [51]. For details refer to Table 6.1. To validate the numerical code, the Nusselt number is computed by three different methods: (a) using the mean heat flux at the horizontal surfaces ($Nu_S = \langle \partial\theta/\partial y \rangle_{A,t}$), (b) from the thermal dissipation rate ($Nu_{\epsilon_\theta} = (RaPr)^{1/2}\langle \epsilon_\theta \rangle$), and (c) from the viscous dissipation rate ($Nu_{\epsilon_u} = (RaPr)^{1/2}\langle \epsilon_u \rangle + 1$). Note that $\langle .. \rangle$ denotes volume and time averaging, while $\langle .. \rangle_{A,t}$ represents horizontal surface and time averaging. Table 6.1 shows that for all Ra, the Nusselt numbers computed using different methods are almost equal suggesting that the simulations are well resolved. Further, the present computed Nusselt numbers are in good agreement with those reported by Kaczorowski and Xia [151] for similar configuration. Turbulent statistics are computed for a sufficient sampling time after reaching a statistically stationary state. The time span (t_{av}) used for computing the temporal statistics for different Rayleigh numbers are also shown in Table 6.1. As Ra increases, the turbulent intensity increases and hence lesser sampling time is required.

To study the flow dynamics, time signals of velocity and temperature are recorded at different locations of the cell. Nine probes each are placed at three different vertical heights given by, $y = 0.25H$, $0.5H$, and $0.75H$. Figure 6.1(b) shows the location of the probes at the mid-plane $y = 0.5H$, where the superscript m indicates mid-plane. Similarly, the notations t and b are used to identify the probes at top and bottom planes, respectively. The time signals extracted from the locations are used to evaluate the temporal flow behaviour, compute the PDFs, and to identify flow regimes. Further, the azimuthally equispaced probes (separated by $\phi = \pi/4$), which are close to the lateral wall ($0.1H$ apart) at the mid-plane, i.e., P_1^m to P_8^m are used for Fourier analysis to be taken up in the next chapter in connection with large-scale circulation.

In the following sections, the turbulent structures in RBC are discussed in detail using a number of visualization methods, i.e., instantaneous contours, temperature iso-surfaces, and Q structures. This is followed by a comprehensive analysis of heat transport, dissipation rates, and thermal plumes. Scaling relations with Rayleigh number are established and are compared with existing results. Further, a number of turbulent statistics are calculated to describe the flow characteristics aptly.

6.3 Flow structures and heat transport

Flow visualizations provide a deeper understanding of the characteristics of a turbulent flow, such as the presence of multiple scales, plumes, homogeneity, and turbulent mixing. In turbulent RBC, thermal plumes erupt from the top and bottom plates/boundary layers and traverse towards the opposite plate. As discussed in previous chapters, under specific parameter range, these plumes organize to form a large-scale coherent structure with hot and cold fluid rising and dipping, respectively, along opposite sides of the lateral wall, i.e., the large-scale circulation (LSC) [40, 61]. The instantaneous temperature iso-surfaces for different Rayleigh numbers are shown in Fig. 6.2, which indicates the presence of LSC (especially at higher Ra). The hot plumes erupt from the boundary layer and rise along a diagonal corner, while the cold plumes sink along the opposite corner. Generally, in box configurations, the LSC shows a tendency to align along one of the diagonals of the box [65]. A detailed discussion on LSC and its dynamics are carried out in the next chapter. Note that the organization of the plumes to form

a coherent LSC is more pronounced at higher Ra, as their appearance changes from domain filling and disorganized structures to organized wall-bounded circulation. In Fig. 6.2, apparent differences are seen across different Ra, as smooth and broad structures give way to sharp and smaller structures with the increase in Rayleigh number. This is an indication that the range of Ra considered in the present study spans both the so-called "soft" and "hard" turbulent regimes.

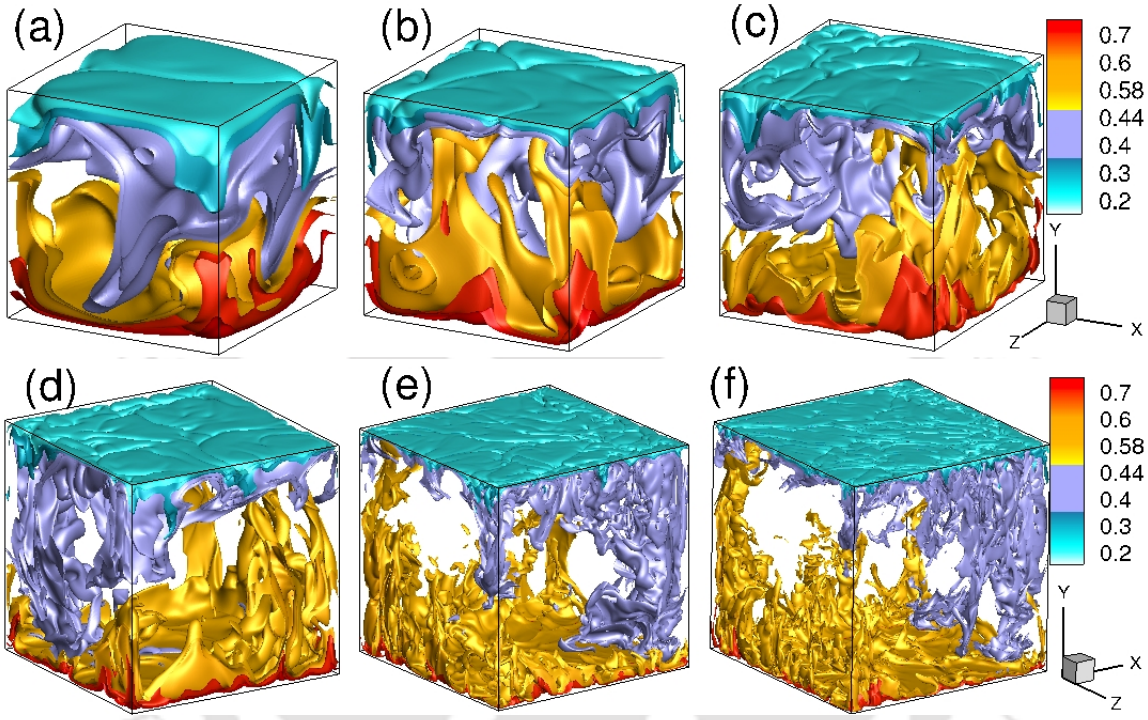

Figure 6.2: Temperature iso-surfaces for (a) $Ra = 2 \times 10^6$, (b) $Ra = 10^7$, (c) $Ra = 5 \times 10^7$, (d) $Ra = 10^8$, (e) $Ra = 5 \times 10^8$, and (f) $Ra = 10^9$. The structures become finer with the increase in Rayleigh number.

Plumes are generally referred to as columns of fluid that rise or descend through a comparatively quieter ambient fluid. The characteristics of a plume are determined by its momentum and density difference. In the case of thermal plumes, it is the temperature difference (buoyancy) that primarily characterizes it. In bottom-heated and top-cooled configurations like RBC, hot and cold plumes originate from the bottom and top plates, respectively. Usually, as a plume moves away from its source, it widens because of entrainment of the surrounding fluid at its edges. The hot plume being lighter than the surrounding fluid, rises, and the cold plume being heavier, falls. To get a better understanding of the plume behaviour, the contours of instantaneous temperature are analyzed at different planes. Figure 6.3 shows the snapshots of the temperature at planes $x = 0.5H$, $y = 0.5H$ and $z = 0.5H$ for different Rayleigh numbers. It is

evident that the flow becomes homogeneous in the bulk as the Rayleigh number is increased. At higher Ra, the plumes appear mainly near the walls, and a well-mixed fluid occupies a significant portion near the central region. This is due to the enhanced turbulent mixing at higher Ra, which also results in increased heat transport. The appearance of large scale structures with the finer structures in the background is also noticed at higher Ra. The apparent similarity of the temperature contours in the three different planes ($x = 0.5H$, $y = 0.5H$, and $z = 0.5H$) shows the isotropic behaviour of the flow [see Fig. 6.3(d)]. Further, the reduction in the thermal boundary layer thickness with the increase in Ra is evident from the temperature contours in the vertical planes. In the following sections, these aspects are investigated in detail using turbulent statistics.

From the above observations, a possible mechanism of plume dynamics emerge. The hot plumes erupt from the boundary layer at the bottom due to thermo-convective instabilities and move upwards due to the buoyancy force. During the course of their motion, the plumes cluster towards the side walls. In the bulk region, they lose their strength due to the interaction with the adjacent fluid. This results in a well-mixed homogeneous region. The plumes near the side walls reach the top plate and spread horizontally, thereby creating horizontal motions, which results in instabilities in the top boundary layer that trigger the formation of cold plumes at the top plate. Note that the formation and dynamics of the cold plumes are similar to that of the hot plumes. However, their locations of formation are always on opposite sides of the horizontal plates. For instance, in the case of $Ra = 10^9$, shown in Fig. 6.2(f), the hot plumes are seen primarily near the left corner of the bottom plate, while the cold plumes originate from the right corner of the top plate. It is evident from Figs. 6.2(d)-6.2(f) that hot (cold) plumes emerge from the bottom (top) plate, impinges on the opposite plate, and thereby inhibit the formation of a cold (hot) plume near those locations. A comprehensive discussion on the quantification of thermal plumes and their statistics is performed in the following section.

Turbulent flows are purely random phenomena that are characterized by multi-scale vorticity fluctuations and chaotic motions. However, it appears to contain an element of clearly organized structures, referred to as coherent structures [160, 234]. The main characteristic of coherent structures is their consistency (for example, a consistent pattern in the velocity, temperature, or vorticity field), and their primary influence is to instil some degree of organization [235]. Fiedler[160] defined coherent structure as a flow structure with discernible correla-

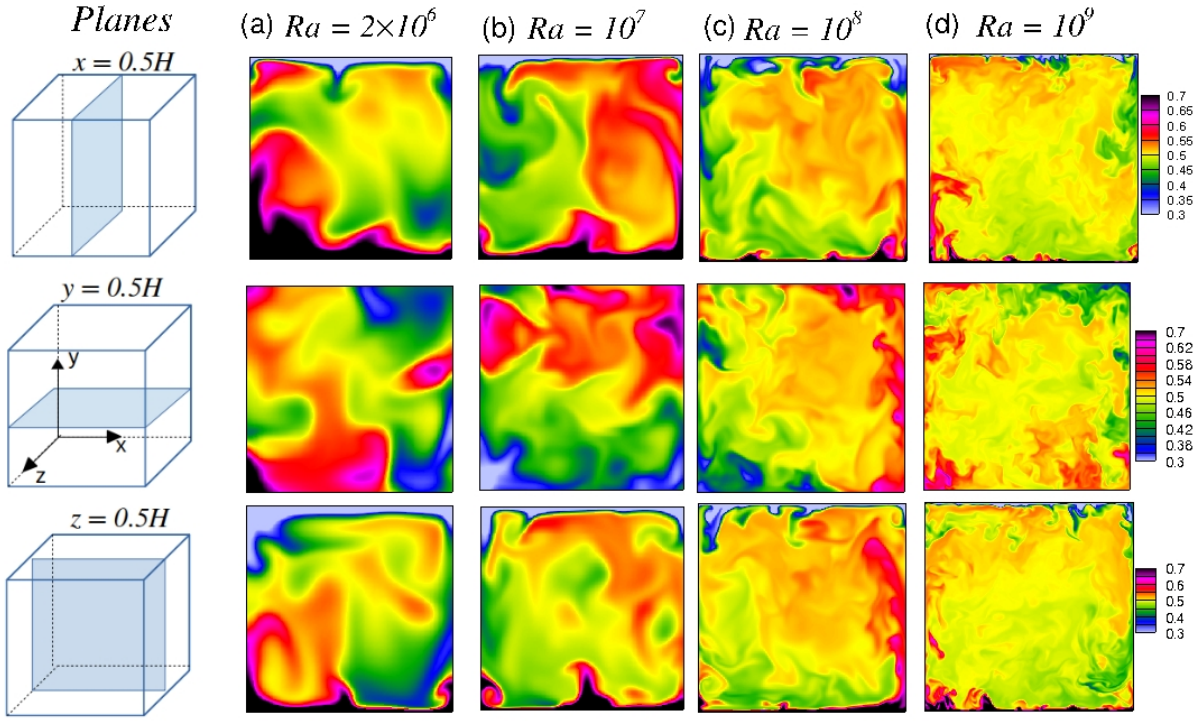

Figure 6.3: Contours of instantaneous temperature field at $x = 0.5H$, $y = 0.5H$ and $z = 0.5H$ mid-planes for (a) $Ra = 2 \times 10^6$, (b) $Ra = 10^7$, (c) $Ra = 10^8$, and (d) $Ra = 10^9$.

tion, i.e., an element of turbulent motion which is set off against the stochastic background and which by its repetitive specific properties characterizes a specific flow. Thermal plumes, eddies, vortex-rings, hairpins, and even large-scale circulation are loosely understood as coherent structures [159]. Identifying these vortical structures, their orientations, and distributions provide a deeper understanding of the flow dynamics. One of the key identifiers of a coherent structure is the coherent vorticity [159]. Several methods have been used to identify vortical coherent structures, such as minimum pressure regions, closed-loop streamlines, and pathlines, and absolute magnitude of vorticity. It has been observed that the minimum pressure regions do not necessarily identify the vortex filaments. Though the streamlines and path lines provide the locus of the fluid particles, they do not truly identify vortex cores as the particles may not realize a complete revolution around the vortex core, thus making these methods less reliable. Several studies [236–238] suggest that the second invariant of the velocity gradient tensor and the negative part of the second-largest eigenvalue of the same tensor are reliable indicators of coherent structures in a variety of flow situations. The second invariant is given by

$$Q = \frac{1}{2}(R_{ij}R_{ij} - S_{ij}S_{ij}). \tag{6.1}$$

Recall that S_{ij} and R_{ij} are the strain rate and rotational rate tensors, respectively, as discussed in chapter 3. As the shearing motion is excluded, Q only takes into account the contribution by vortical motions and essentially represents a strong local rotation in regions with $Q > 0$. In Fig. 6.4, the second invariant of the velocity gradient tensor for different Rayleigh numbers is shown. The appearance of large-scale structures with finer structures in the background is observed across three decades of Ra. Note that a wide range of values of Q are possible, and thus, an appropriate choice of Q is necessary to extract the relevant information [161]. The appropriate threshold value is based on the global maximum of Q over the entire flow field. Here the levels are shown at about 1% of the corresponding global maximum of Q.

Heat transport and plume dynamics are interlinked in turbulent RBC [222]. The thermal plumes carry heat from the boundary layers at the top and bottom towards the bulk region. The Nusselt number provides a globally integrated description of the heat transport in thermal systems. To characterize the heat transport for different Ra, we present the Nusselt number scaling with Rayleigh number ($Nu \sim Ra^n$) in Fig. 6.5. Scaling laws facilitate an excellent

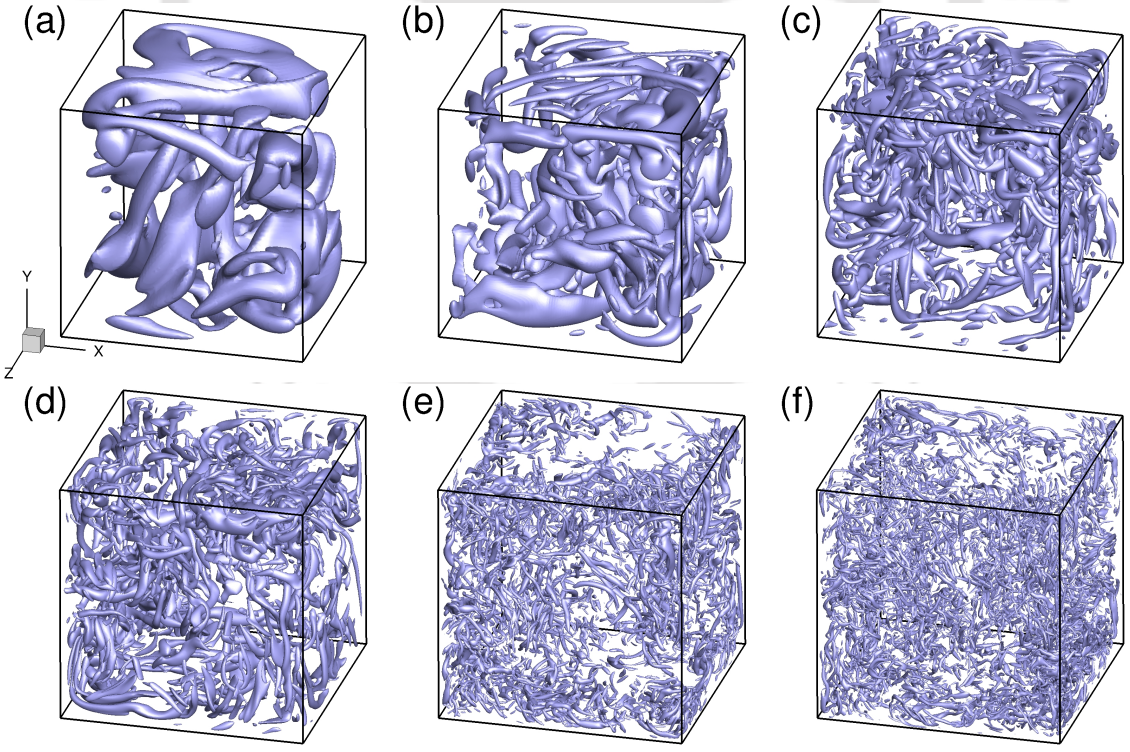

Figure 6.4: Coherent structures characterized by the second invariant of the velocity gradient tensor (Q) for (a) $Ra = 2 \times 10^6$, (b) $Ra = 10^7$, (c) $Ra = 5 \times 10^7$, (d) $Ra = 10^8$, (e) $Ra = 5 \times 10^8$, and (f) $Ra = 10^9$. The structures become finer with the increase in Rayleigh number.

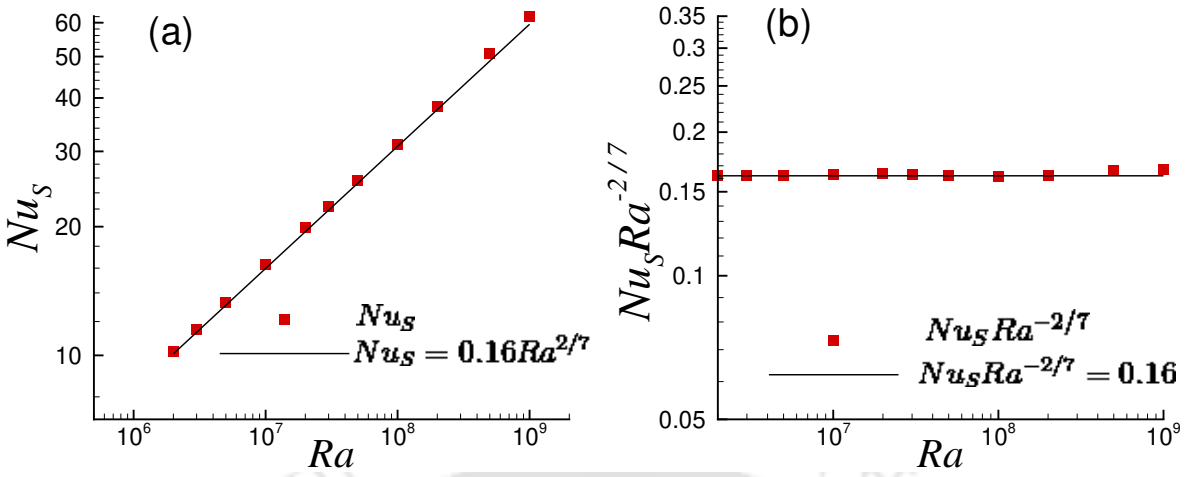

Figure 6.5: (a) Scaling of Nusselt number with Rayleigh number, where the solid line represents the best fit by least-squares method. (b) The compensated plot ($NuRa^{-2/7}$ Vs Ra) for the same data.

way of studying physical systems, especially in geophysical and astrophysical flows, as they provide a basis for extrapolation to extreme parameter regimes that are inaccessible to current computational and experimental efforts. In turbulent RBC the scaling relation between Nusselt number and Rayleigh number has been a matter of extensive study over the years [73–75]. The unifying theory of scaling in thermal convection proposed by Grossmann and Lohse [76] (GL theory) suggests that there are no pure power laws for the Nusselt and Reynolds numbers as a function of the Rayleigh and Prandtl numbers in the experimentally accessible parameter regime. By decomposing the viscous and thermal dissipation rates into the bulk and boundary layer contributions, Grossmann and Lohse [76, 77] identified different flow regimes in the parameter space (Ra, Pr), and established the Nusselt number scalings ($Nu \sim Ra^n Pr^m$) at these regimes. Later Stevens *et al.* [239] updated the theory by determining the prefactors for the scaling relations using newer experimental and numerical data, and based on the modern understanding of the physics of RBC.

The experimental study by Chu and Goldstein [240] showed deviation from the classical theory ($Nu \sim Ra^{1/3}$) in the Rayleigh number range $2.76 \times 10^5 < Ra < 1.05 \times 10^8$. At moderate Rayleigh numbers, the flow organizes to form an LSC, which is comparable to the size of the flow domain. The presence of this circulation results in communication between the boundary layers. By including the effects of shear flow across the thermal boundary layers, Shraiman and Siggia [75] deduced the scaling exponent $n = 2/7$ in turbulent RBC. Since

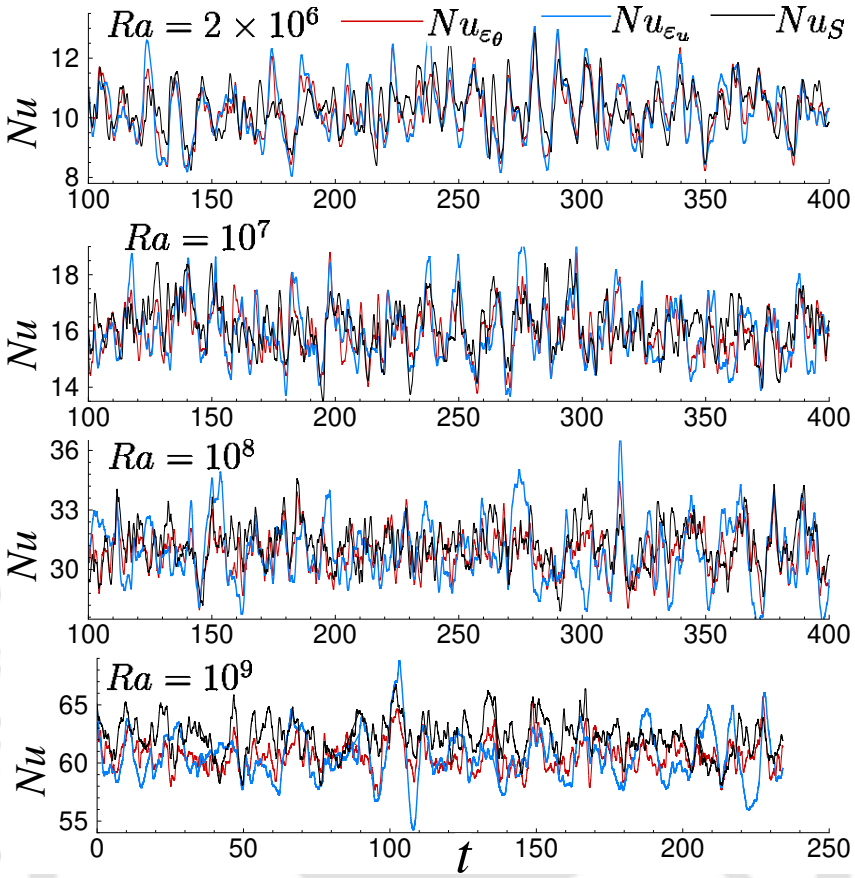

Figure 6.6: The time signals of Nusselt number computed by different methods for $Ra = 2 \times 10^6$, 10^7, 10^8 and 10^9.

then a number of experimental [241, 242] and numerical studies [57, 166, 243] have reported the scaling exponent as $2/7$, for moderate Rayleigh number regime, $Ra \lesssim 10^{10}$ [164]. The recent LES study by Foroozani *et al.* [71] reported a scaling of $Nu = 0.15Ra^{0.29}$ for $10^6 \leq Ra \leq 10^{10}$ inside a cubic cell. In the present study, we observe a scaling behaviour $Nu = 0.16Ra^{2/7}$ [refer Fig. 6.5(a)], which is in good agreement with previous results [71, 151]. Further, a compensated Nusselt number versus Rayleigh number plot is shown in Fig. 6.5(b). Here the flat line (zero slope) or the plateau demonstrates the robustness of the scaling relation. As discussed previously, we compute the Nusselt number using different methods. The time variation of Nusselt number computed by the three different methods (Nu_S, Nu_{ϵ_θ} and Nu_{ϵ_u}) are shown in Fig. 6.6. Although the mean values of all the signals are in excellent agreement, the Nusselt number computed using the viscous dissipation shows maximum fluctuations, while those computed from the thermal dissipation and wall normal gradient follow a similar trend. Table 6.1 shows that for all Ra, average Nusselt numbers computed using different methods

are almost equal, suggesting the simulations are well resolved. The volume averaged Nusselt numbers are sensitive to the resolution in the bulk, and the Nusselt number computed at the isothermal walls (Nu_S) to the resolution in the near-wall regions. The agreement of these quantities provides an additional confirmation on the spatial resolution used in the numerical simulations [153, 166, 244]. Further, the values of the scaling exponent ($Nu \sim Ra^n$) calculated from all these methods are found identical up to two decimal places.

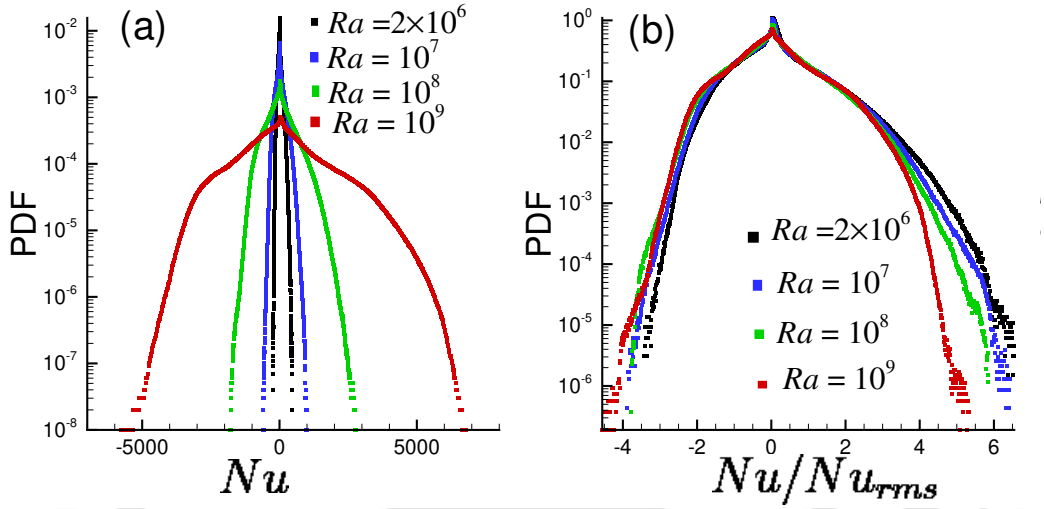

Figure 6.7: (a) The spatial PDF of Nusselt number at different Ra. (b) The PDF of Nusselt number normalized by standard deviation for different Ra.

To get better insights into the distribution of heat transfer in different parts of the flow domain, probability density function of Nusselt number at different Ra is evaluated. In their experimental study, Shang *et al.* [245] computed the histogram of vertical heat flux at the center of the convecting cell and observed a non-symmetric distribution. The histograms were skewed towards the right, indicating more fluctuations in positive heat flux, which results in a small positive mean value. Recently, Kaczorowski and Xia [151] also obtained a skewed PDF for vertical heat flux in the bulk region. They observed that for higher Pr, the Nusselt number fluctuations are stronger, and thus the PDFs become more skewed. The spatio-temporal PDF of Nusselt number for different Ra is shown in Fig. 6.7(a). The Nusselt number at each spatial location is computed as $Nu = \sqrt{RaPr}(v\theta) - \partial\theta/\partial y$. The PDFs are computed by taking at least 20 samples of instantaneous volume data. As observed in the previous studies, the PDFs are asymmetric, and they become more skewed with the increase in Ra. Note that the PDFs are skewed towards the right and hence results in a positive mean for the net heat transfer rate. Similar skewed distribution of Nusselt number was observed by Lulff [246] for turbulent RBC

inside a cylindrical domain. Plumes are the major carriers of heat in turbulent RBC. As the hot plumes move upwards (in the buoyancy direction), they induce positive fluctuations in local heat transfer. However, when a cold plume descends, the convective motion is in opposite direction of buoyancy, which is indicated by the negative values of Nusselt number. Note that the net effective heat transfer is always in the buoyancy direction, as suggested by the positive global value of Nusselt number. The PDFs are non-Gaussian and spread with the increase in Rayleigh number, which indicates the increase in high amplitude temperature fluctuations at high Ra. Note that the volume and time average of Nu also agrees well with the Nusselt number computed using the previously mentioned methods (Nu_{ϵ_θ}, Nu_{ϵ_u} and Nu_S), which also suggests that the simulations are locally well resolved. In Fig. 6.7(b), the PDF of normailzed Nusselt number is shown. Here the Nusselt number is divided by the respective standard deviation (Nu_{rms}) for different Ra. After normalization, we observe that the core of the PDFs collapse to each other, while the tails do not.

6.4 Statistics of dissipation rates

Statistical description of viscous and thermal dissipation rates and their possible connection to the global heat transport is constructed here. These quantities signify the dissipation of kinetic and thermal energy due to the effects of fluid viscosity and thermal diffusivity [169]. They are quantified by the norm of the gradients of velocity and temperature fields. As discussed in chapter 3, the non-dimensional viscous and thermal dissipation rates are computed as

$$\epsilon_u = \sqrt{\frac{Pr}{Ra}}\,|\nabla \boldsymbol{u}|^2, \tag{6.2}$$

$$\epsilon_\theta = \sqrt{\frac{1}{RaPr}}\,|\nabla \theta|^2. \tag{6.3}$$

Dissipation rates are often used to identify different flow regimes [167], establish scaling laws, and quantify different flow characteristics. These quantities form the backbone of the GL theory [76], where they are decomposed into their bulk and boundary layer contributions to identify different subsets in the parameter space defined by Ra and Pr, leading to predictions of scaling behaviour of Nusselt and Reynolds (associated with the large-scale flow) numbers in these

regimes. Shishkina and Wagner [94, 222] investigated the formation and interactions of thermal plumes by evaluating the dissipation rates. They identified boundary layers and thermal plumes as regions associated with large values of the thermal dissipation rate. Recall that the global average of dissipation rates are connected to the global heat transport through the analytical relations [75]

$$\langle \epsilon_u^{th} \rangle = \nu^3 H^{-4} (Nu - 1) RaPr^{-2}, \tag{6.4}$$

$$\langle \epsilon_\theta^{th} \rangle = \alpha (\Delta T)^2 Nu H^{-2}. \tag{6.5}$$

Note that here $\langle .. \rangle$ indicates volume and time averaging, as defined earlier. The above equations are normalized to obtain the relations

$$\langle \epsilon_u^{th} \rangle = \frac{Nu - 1}{\sqrt{RaPr}}, \tag{6.6}$$

$$\langle \epsilon_\theta^{th} \rangle = \frac{Nu}{\sqrt{RaPr}}. \tag{6.7}$$

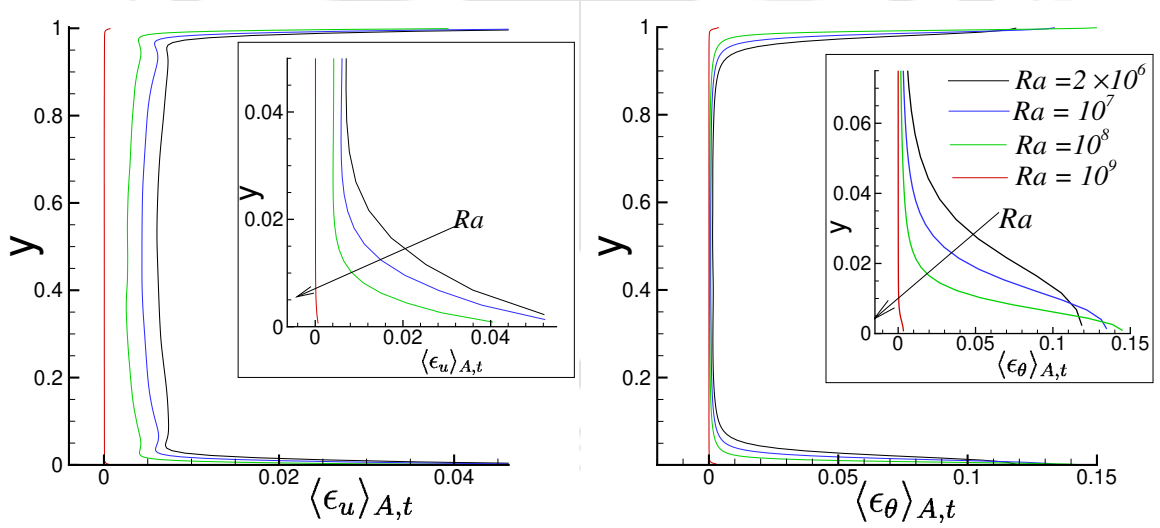

Figure 6.8: Area and time averaged vertical profiles of viscous and thermal dissipation rate for different Ra.

First, the spatial distribution of dissipation rates is taken up. The variation of the horizontal plane and time averaged dissipation rates along the vertical direction are shown in Fig. 6.8, where the insets show zoomed view near the bottom plate. Note that the maximum value of the dissipation rates occur at the top and bottom plates, which is consistent with the observations made by Zhang *et al.* [169] and Emran and Schumacher [95]. In the bulk region, both

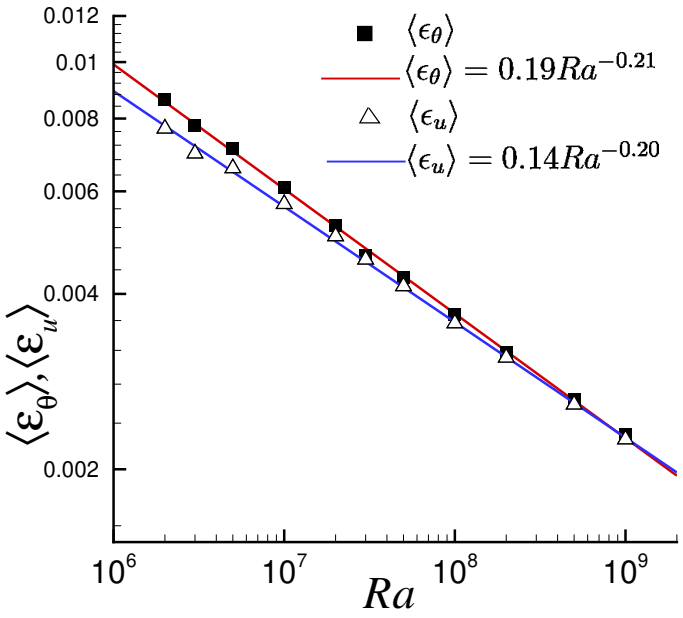

Figure 6.9: Scaling of viscous and thermal dissipation rates with Rayleigh number.

$\langle\epsilon_u\rangle_{A,t}$ and $\langle\epsilon_\theta\rangle_{A,t}$ remain nearly constant which indicates a well-mixed homogeneous region. However, near the top and bottom boundary layers, the dissipation rates increase sharply to attain maximum values on the isothermal plates. This suggests that the thermal and viscous dissipations occur mainly in the vicinity of the horizontal plates. Note that with the increase in Ra, the homogeneity in the bulk increases, and the dissipation rates become more concentrated near the isothermal plates.

Next, we examine the Rayleigh number scaling of the dissipation rates. The variation of the ensemble averaged non-dimensional dissipation rates, $\langle\epsilon_u\rangle = \sqrt{Pr/Ra}\langle|\nabla \boldsymbol{u}|^2\rangle$ and $\langle\epsilon_\theta\rangle = \sqrt{1/RaPr}\langle|\nabla\theta|^2\rangle$ with Ra are shown in Fig. 6.9. The solid lines indicate the least-square fit to the corresponding data, which gives the scaling relations $\langle\epsilon_u\rangle = 0.14Ra^{-0.20}$ and $\langle\epsilon_\theta\rangle = 0.19Ra^{-0.21}$. Note that the scaling behaviours are in excellent agreement with the theoretical predictions, which are obtained by plugging the relation $Nu \sim Ra^{2/7}$ into the global estimates of the dissipation rates, given by Eqs. 6.6 and 6.7, resulting in $\langle\epsilon_\theta^{th}\rangle \sim Ra^{-0.21}$ and $\langle\epsilon_u^{th}\rangle \sim Ra^{-0.21}$.

The spatio-temporal PDF of the thermal and viscous dissipation rates normalized by their respective root mean square (rms) values ($\epsilon_\theta^{rms} = \sqrt{\langle\epsilon_\theta^2\rangle}$ and $\epsilon_u^{rms} = \sqrt{\langle\epsilon_u^2\rangle}$) are shown in Fig. 6.10 for different Ra. For both thermal and viscous dissipation rates, the tails of the PDF become more extended with increase in Ra, suggesting an increased level of small-scale

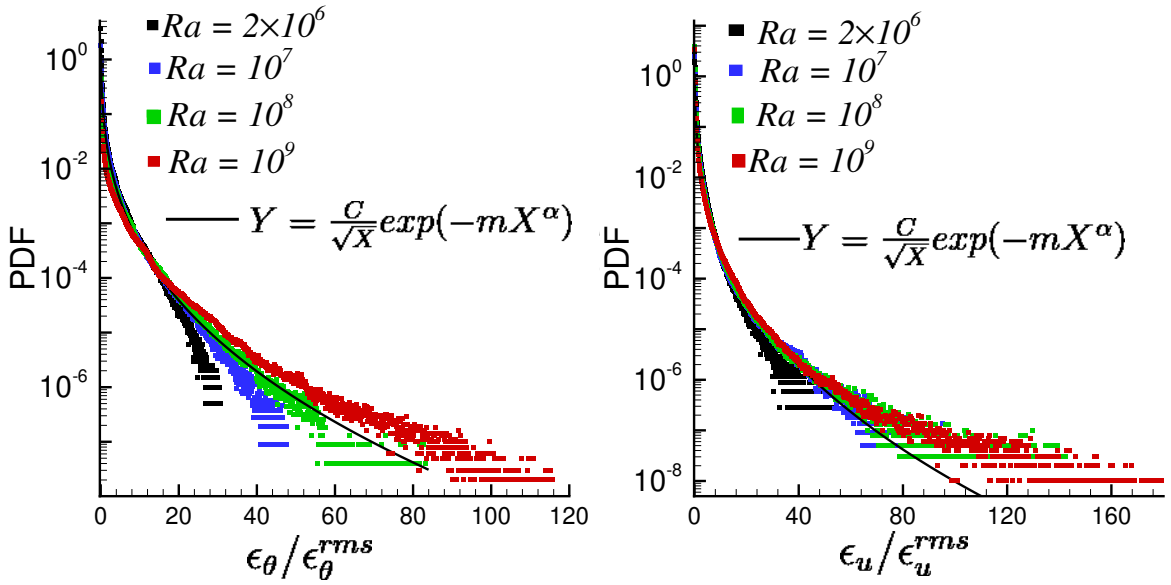

Figure 6.10: Spatio-temporal PDF of the thermal and viscous dissipation rates at different Ra fitted with a stretched exponential function.

intermittency of the dissipation fields. This is consistent with the observations made by Zhang *et al.* [169] and Emran and Schumacher [95]. Intermittency is one of the key issues in turbulent flows. In an intermittent flow field, turbulent activity is characterized by intervals of low intensity turbulence interrupted irregular bursts of strong turbulence [247]. PDFs and structure functions are generally used in turbulent flow analysis to quantify the intermittency effects [247–249]. PDFs of intermittent fields are usually observed to show strong tails of extreme fluctuations and a pointed peak, which indicates the frequent low amplitude events. Figure. 6.10 shows that low amplitude dissipation events are more probable, while the high amplitude events are rare. However, with increase in Ra, the magnitude of these extreme events increases, which is shown by the extended tails at higher Ra. To quantify the dissipation rates, the tails of the PDF are fitted with a stretched exponential function as

$$P(X) = C/\sqrt{X}exp(-mX^{\alpha}). \tag{6.8}$$

Here, C, m and α are fitting parameters, and X corresponds to $\epsilon(r)/\epsilon^{rms}$. The fitting is carried out for the values which are greater than $X = 1$. For all the cases, we obtain a scaling exponent $\alpha = 0.3$ - 0.4, which is in good agreement with earlier results [169, 170, 233]. The stretched exponential function (Eq. 6.8) was used by Overholt and Pope [250] and Schumacher and

Sreenivasan [171] to quantify passive scalar dissipation in homogeneous isotropic turbulent flow, where in the limit of large Peclet numbers, $\alpha = 1/3$ was obtained. This was later adopted for active scalar dissipation in various studies [170, 172].

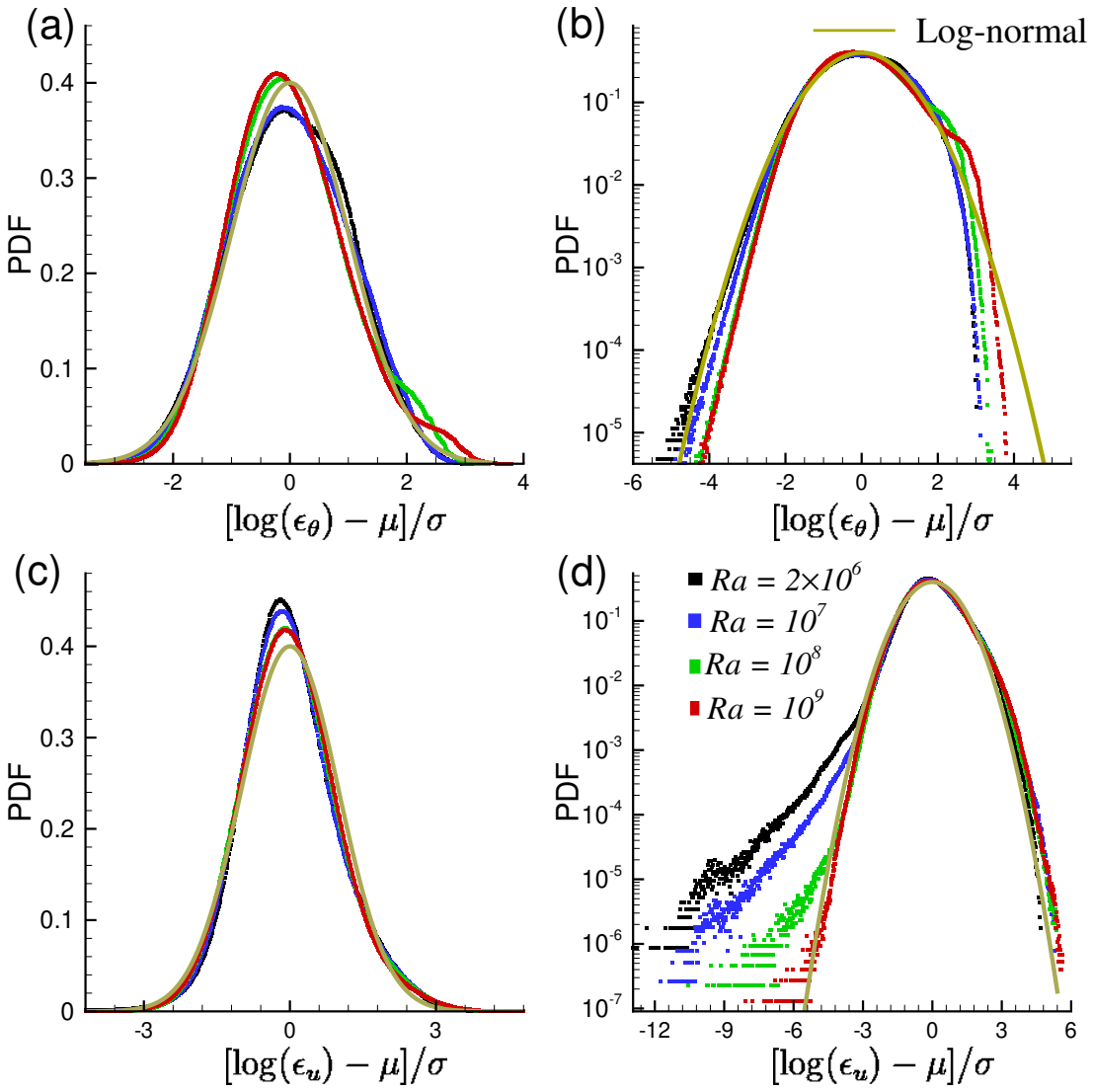

Figure 6.11: Spatio-temporal PDF of (a,b) log ϵ_θ and (c,d) log ϵ_u at different Ra in log-normal coordinates. The solid line represents the standard normal distribution. The data is represented in (a,c) linear plots and (b,d) linear-logarithmic plots.

In RBC, dissipation rates are often expected to follow a log-normal distribution [168]. However, considerable deviations due to the highly intermittent nature of local dissipation have also been reported [169–172]. Emran and Schumacher [170] investigated the spatial distribution of thermal dissipation rate in two different sub-volumes of the domain, i.e., the bulk and near-wall region, and observed that dissipation rate in both the regions deviate significantly from log-normality. Zhang *et al.* [169] also observed deviations of dissipation rate from log-normal

behaviour. Bhattacharya *et al.* [233] observed that the viscous dissipation in bulk follows a log-normal distribution while it follows a stretched exponential distribution inside the boundary layer.

To examine such deviations in the present study, the PDFs of thermal and viscous dissipation rates are represented in log-normal coordinates in Fig. 6.11, where μ and σ indicate the corresponding mean and standard deviation of the logarithmic dissipation rates. The solid line represents the normal distribution curve for reference. In order to distinguish the differences in the PDFs, the data is shown in both linear [Figs. 6.11(a) and 6.11(c)] and linear-logarithmic [Figs. 6.11(b) and 6.11(d)] axes. It is evident that for both ϵ_θ and ϵ_u, the cores, as well as the tails of the PDFs, deviate considerably from log-normality. Figure 6.11(b) shows that for thermal dissipation rate, both the small and large amplitude tails are more scattered than the log-normal curve. The right tails depart with a bump and then drop steeply. A similar feature has been reported by Kaczorowski and Wagner [243]. Emran and Schumacher [170] also reported such bumps in the PDFs of ϵ_θ and associated it with the boundary layer dynamics. They analyzed the PDFs of ϵ_θ in bulk and boundary layers separately and observed that both the regions show a significant departure from the log-normal curve, although the bumps were identified only in the boundary layer region. Figures 6.11(c) and 6.11(d) show that the PDFs of viscous dissipation rate appear to converge towards log-normality with increase in Ra. Here the right tails almost follow the log-normal behaviour while the core region and left tails deviate from it. With the increase in Ra, the left tail and core also approach towards log-normality. It has been shown in previous studies [233] that the viscous dissipation in the bulk follows a log-normal behaviour, similar to the predictions by Obukhov [251] for hydrodynamic turbulence. The deviations in the present study are primarily due to the presence of solid walls and boundary layers. As Rayleigh number increases, bulk homogeneity also increases, leading to thinner boundary layers. This is reflected in Fig. 6.11(d), as the distribution functions approach the log-normal behaviour.

6.5 Plume and turbulent background decomposition

In the past few decades, a number of methods have been explored for identifying thermal plumes. Belmonte and Libchaber [90] identified plumes by analyzing the skewness of the

temperature derivative. A threshold value of the vertical velocity and temperature was used by Julien *et al.* [91] for recognizing plumes, while Zhou and Xia [92] used a cutoff on the temperature difference for the same. Ching *et al.* [252] quantified plumes by decomposing the local velocity into two parts and analyzing its correlation with the local temperature fluctuations. Recently, Alexandre *et al.* [93] characterized plumes based on positive temperature fluctuations and on a threshold value of the turbulent heat flux, which is the product of temperature and vertical velocity fluctuations. The central theme of these methods is that plumes are generated by buoyancy, and their velocity is expected to be related to the temperature fluctuations in one way or the other. Shishkina and Wagner [94] used an approach based on the local thermal dissipation rates. They considered the thermal boundary layers and plumes as regions associated with larger thermal dissipation rates. In the present study, we identify plumes based on the product of the vertical velocity and temperature fluctuations ($v'\theta'$), a proposition made by Emran and Schumacher [95].

In the present technique, the cell volume is decomposed into two disjoint subsets, such as, the plume-dominated regions and the remaining turbulent background. The decomposition is achieved based on the amplitude and sign of the correlation between vertical velocity and temperature, $v'\theta'$. Here v' and θ' are the fluctuations about the mean, given by, $\theta' = \theta - \langle\theta\rangle_{A,t}$ and $v' = v$ as $\langle v\rangle_{A,t} = 0$. A plume can be considered as a local phenomenon of fluctuation of vertical velocity and temperature about the mean. Thus, the regions are identified as

$$v'\theta' > C_t \quad : \quad \text{plume}, \tag{6.9}$$

$$v'\theta' \leq C_t \quad : \quad \text{background}, \tag{6.10}$$

where C_t indicates the cutoff value that demarcates the plume and background. Five different values of C_t are considered in the present study, which are $0,\ 0.1\%,\ 1\%,\ 5\%$ and 10% of the instantaneous global maximum of $v'\theta'$. For each cutoff, the volume of the plume and turbulent background regions are calculated, which are denoted by V_{pl} and V_{bg}, respectively, where

$$V_{cell} \quad = \quad V_{pl} + V_{bg}. \tag{6.11}$$

Here V_{cell} represents the total volume of the cell, while the subscripts pl and bg correspond to the plume and background regions, respectively. The volume fractions of each regions are

calculated as $V'_{pl} = V_{pl}/V_{cell}$ and $V'_{bg} = V_{bg}/V_{cell}$.

Table 6.2: Volume fraction of the plume and background at $Ra = 10^7$, $Pr = 0.7$ and $\Gamma = 1$, for different cutoffs compared with those obtained by Emran and Schumacher [95].

$C_t\%$	V'_{pl}	V'_{bg}	V'_{pl} [95]	V'_{bg} [95]
0	0.76	0.24	0.74	0.26
0.1	0.71	0.29	0.69	0.31
1	0.58	0.42	0.56	0.44
5	0.30	0.70	0.28	0.72
10	0.20	0.80	0.19	0.81

For validating the plume and background decompositions, simulations are carried out at $Ra = 10^7$ and $Pr = 0.7$ in a cylindrical container with aspect ratio $\Gamma = 1$, and the results are compared with the numerical study by Emran and Schumacher [95]. Table 6.2 shows the volume fractions of plume and background regions for different cutoffs, which are in good agreement with those obtained by Emran and Schumacher [95]. With the increase in cutoff, the volume fraction of plume decreases, while that of the background increases.

Figures 6.12 and 6.13 show 3-D perspective of the thermal plumes obtained for $Ra = 10^8$ and 10^9 corresponding to the threshold value $C_t = 10\%$. The plumes are further identified as hot or cold based on whether the instantaneous temperature is greater or less than the mean temperature ($\theta = 0.5$). As discussed previously, using the temperature iso-surfaces (refer Fig. 6.2), the organization of hot and cold plumes to form a coherent LSC is quite evident. Here red and blue colours indicate hot and cold plumes, respectively. The plumes become finer with the increase in Ra. Further, the planar view of the plumes in the diagonal plane containing LSC is shown in 6.14(a), which clearly shows the organized motion of the hot and cold plumes to form an LSC in the clockwise direction. However, in the other diagonal, a four-roll structure is observed [refer Fig. 6.14(b)]. Here the hot and cold plumes coming from opposite planes collide near the mid-plane $y = 0.5H$, which results in disconnected fragments of plumes in the bulk region. Detailed discussion on the flow structure and dynamics in the LSC and non-LSC diagonals are carried out in the next chapter.

Planar view of the plume and background regions at different mid-planes, i.e., $x = 0.5H$, $y = 0.5H$ and $z = 0.5H$ are shown in Figs. 6.15 and 6.16 at $C_t = 0$ and $C_t = 1\%$, respectively, for $Ra = 10^9$. It is evident that plume regions are identified mainly near the boundary layers

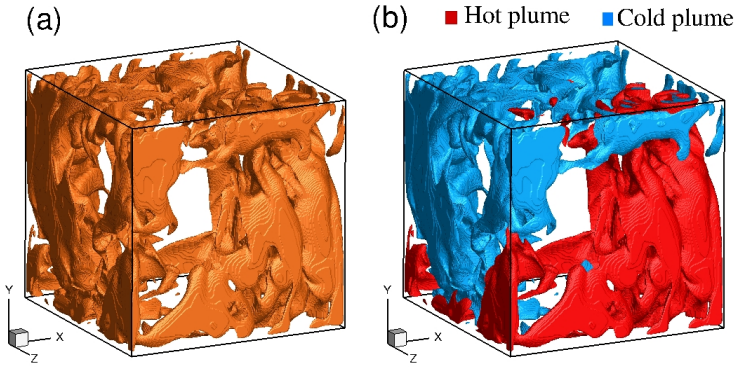

Figure 6.12: (a) Thermal plumes identified using the correlation between vertical velocity and temperature fluctuations for cutoff $C_t = 10\%$ at $Ra = 10^8$. (b) Hot and cold plumes for the same cutoff and Ra.

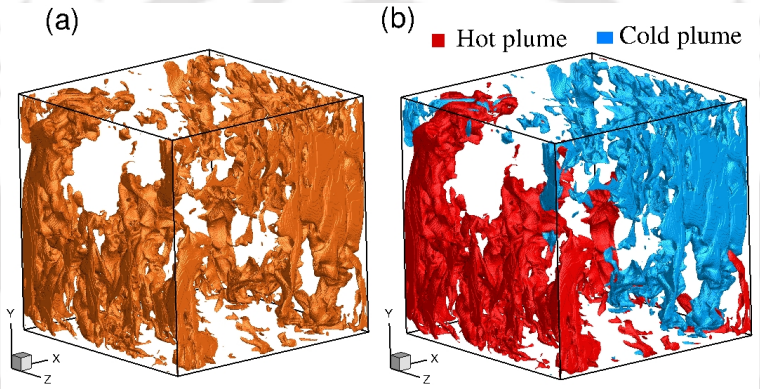

Figure 6.13: (a) Thermal plumes identified using the correlation between vertical velocity and temperature fluctuations for cutoff $C_t = 10\%$ at $Ra = 10^9$. (b) Hot and cold plumes for the same cutoff and Ra.

and close to the side walls. However, at $C_t = 0$, disconnected, finer fragments of plumes are observed in the bulk region, which are absent for $C_t = 1\%$. The apparent similarity in the appearance of plume and background regions in different planes (especially Fig. 6.15) signifies the isotropic nature of the flow. The observed plume behaviour and its structure are in good agreement with earlier studies [95]. However, the present study does not identify any so-called "mushroom" shaped plumes.

Next, the plume morphology near the boundary layers and their evolution as they travel towards the bulk are evaluated. Near the top and bottom boundary layers, the so-called "sheet-like" or "line-like" [222, 229] structures are observed, which are evenly distributed throughout the horizontal plane, as shown in Figs. 6.17(a) and 6.17(c). However, on reaching the mid-plane, the plumes get clustered and thus loose their line-like behaviour and segregate near the lateral walls [see Fig. 6.17(b)]. Note that although the formation of the plumes takes place

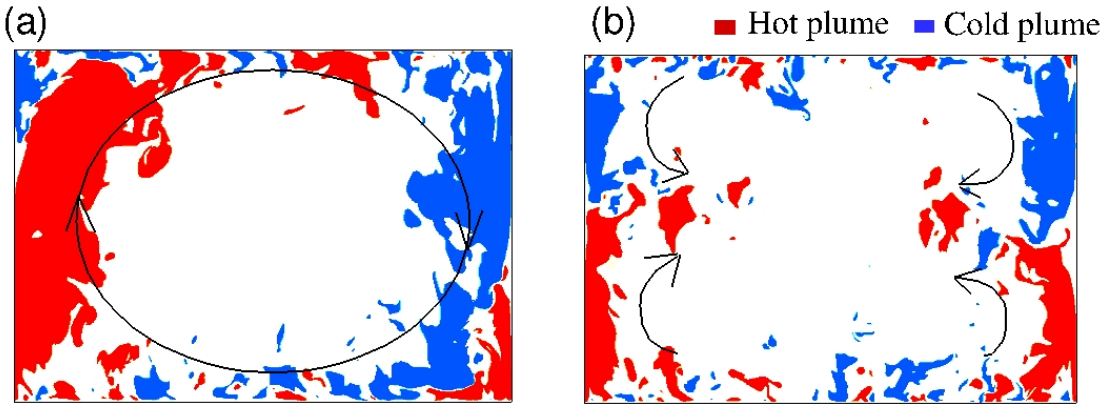

Figure 6.14: Hot and cold plumes for $Ra = 10^9$ and cutoff $C_t = 1\%$ at (a) diagonal plane containing LSC and (b) four-roll structure. The arrows indicate the direction of plume motion.

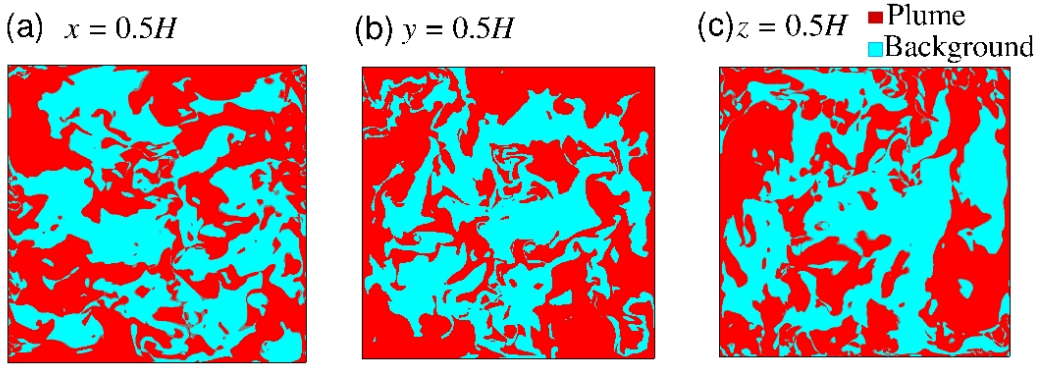

Figure 6.15: Plume and turbulent background regions identified using the correlation between the vertical velocity and temperature fluctuations for $Ra = 10^9$ and cutoff $C_t = 0$ at (a) $x = 0.5H$, (b) $y = 0.5H$, and (c) $z = 0.5H$. Red and blue colours indicate plume and background regions, respectively.

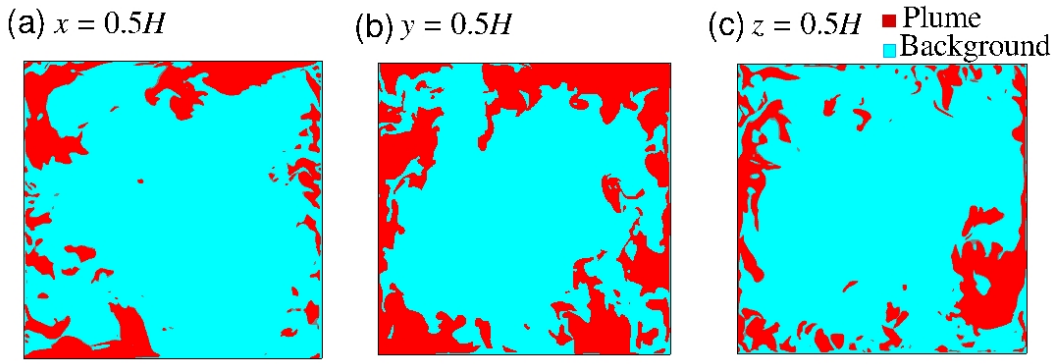

Figure 6.16: Plume and turbulent background regions identified using the correlation between the vertical velocity and temperature fluctuations for $Ra = 10^9$ and cutoff $C_t = 1\%$ at (a) $x = 0.5H$, (b) $y = 0.5H$, and (c) $z = 0.5H$. Red and blue colours indicate plume and background regions, respectively.

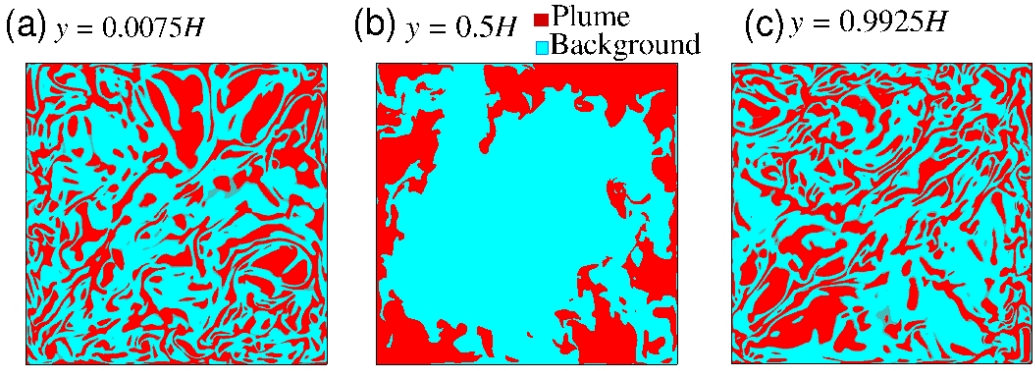

Figure 6.17: Plume and turbulent background regions identified using the correlation between the vertical velocity and temperature fluctuations for cutoff $C_t = 1\%$ at $Ra = 10^9$ at different planes; (a) $y = 0.0075H$, (b) $y = 0.5H$, and (c) $y = 0.9925H$. Red and blue colours indicate plume and background regions, respectively.

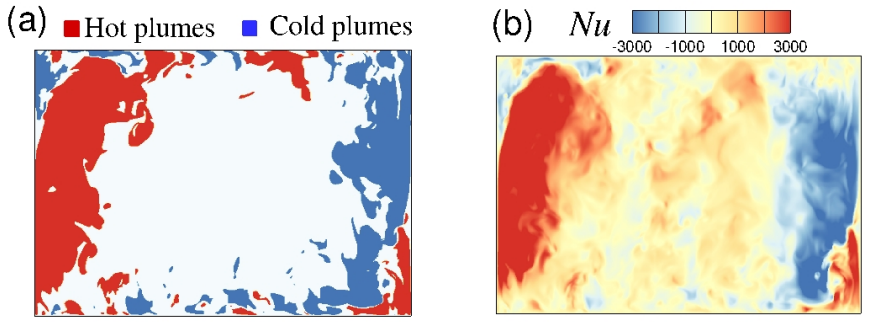

Figure 6.18: (a) Hot and cold plumes identified using the correlation between the vertical velocity and temperature fluctuations for cutoff $C_t = 1\%$ at $Ra = 10^9$ in the diagonal plane containing the large-scale flow. (b) The contours of Nusselt number in the same plane.

uniformly across the boundary layers (near the top and bottom plates), they are swept away in the direction of the large-scale flow. As a result, away from the boundary layers, the plumes appear clustered near the lateral walls.

Plumes are primarily responsible for a significant share of heat transport in turbulent convection. Here, we investigate how the thermal plumes are associated with the local heat transfer rate, $Nu(\boldsymbol{r})$. The hot and cold thermal plumes, along with the contours of Nusselt number, are shown in Fig. 6.18, in the LSC diagonal plane of the box. It is evident that plumes are strongly associated with higher magnitudes of local Nusselt number. Note that positive values of Nu are associated with the hot plumes due to positive vertical velocity (upward motion), suggesting its movements in the buoyancy direction. On the other hand, the negative values of Nusselt number are connected to the cold plumes.

The variation of volume fraction of the plume and background with Ra for different threshold values (C_t) is shown in Fig. 6.19. It is evident that for all values of C_t, volume fraction of the plume drops, and that of the background increases with the increase in Ra. Thus, at very high Ra, the plume dominated regions are negligible and the background region dominates. Further, power-law behaviour, $V'_{pl} = a_{pl}Ra^{b_{pl}}$ and $V'_{bg} = a_{bg}Ra^{b_{bg}}$, are observed with respect to Ra. The values of the fitting parameters are listed in Table 6.3. The power-law exponent b_{pl} shows a decreasing trend with the increase in threshold value, while the exponent for background fraction does not show any particular trend. The volume fractions show a clear dependence on the threshold value C_t, i.e., larger the C_t is greater the probability of identifying a local region as turbulent background. These trends are consistent with the numerical study of Emran and Schumacher [95].

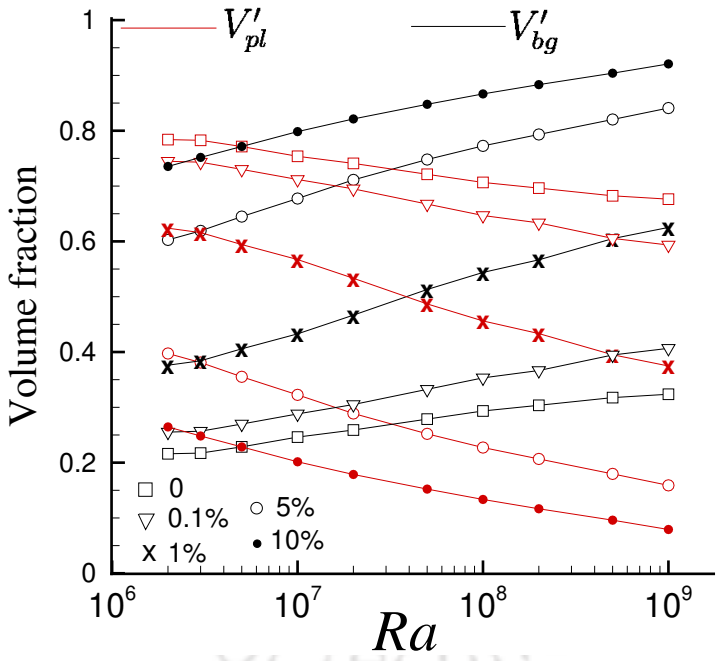

Figure 6.19: Variation of volume fraction of the plume and the background regions with Ra for different threshold values. The volume fractions exhibit a power-law behaviour with Ra.

Next we turn our focus to the contribution of plume and background to the thermal dissipation rate, computed as

$$\langle \epsilon_\theta \rangle_{pl} = \langle \frac{1}{V_{pl}} \int_{V_{pl}} \epsilon_\theta dv \rangle, \tag{6.12}$$

$$\langle \epsilon_\theta \rangle_{bg} = \langle \frac{1}{V_{bg}} \int_{V_{bg}} \epsilon_\theta dv \rangle. \tag{6.13}$$

Table 6.3: The power-law fits for volume fraction of the plume and turbulent background region, $V'_{pl} = a_{pl}Ra^{b_{pl}}$ and $V'_{bg} = a_{bg}Ra^{b_{bg}}$, at different cutoffs C_t.

$C_t\%$	a_{pl}	b_{pl}	a_{bg}	b_{bg}
0	1.14	−0.025	0.078	0.070
0.1	1.31	−0.038	0.079	0.080
1	2.20	−0.085	0.108	0.086
5	3.45	−0.147	0.280	0.054
10	4.34	−0.189	0.440	0.036

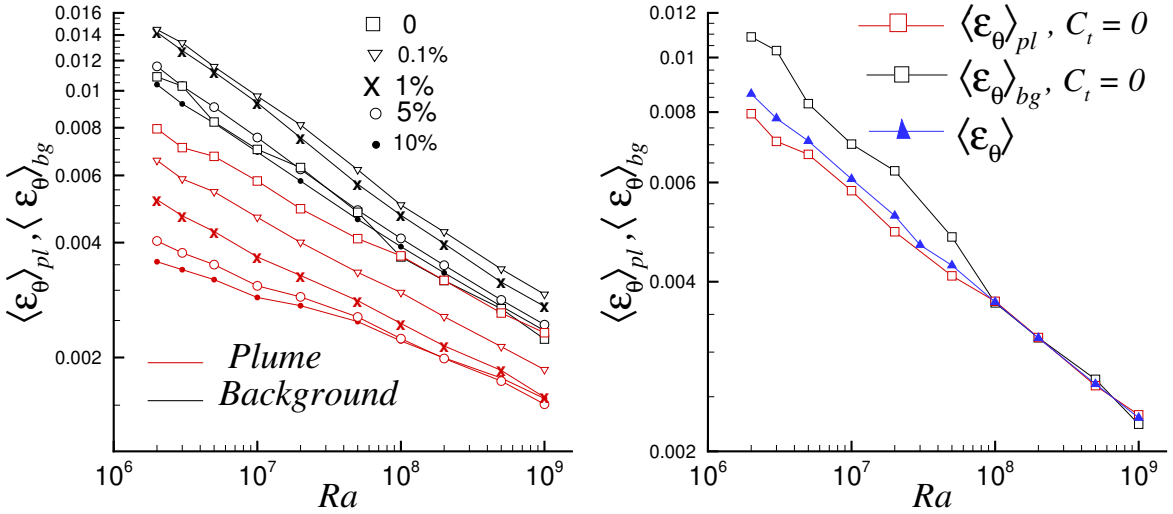

Figure 6.20: (a) Variations of the contribution of the plume and the background to the thermal dissipation rate with Rayleigh number at different cutoffs ($C_t = 0,\ 0.1\%,\ 1\%,\ 5\%$, and 10%). (b) For $C_t = 0$, the contributions of the plumes and background become equal and approach the global scaling at high Rayleigh numbers.

Here $\langle\epsilon_\theta\rangle_{pl}$ and $\langle\epsilon_\theta\rangle_{bg}$ are the average thermal dissipation contributions from the plume and background dominated regions, respectively, which follow the global balance $V_{cell}\langle\epsilon_\theta\rangle_V = V_{pl}\langle\epsilon_\theta\rangle_{pl} + V_{bg}\langle\epsilon_\theta\rangle_{bg}$. The variation of $\langle\epsilon_\theta\rangle_{pl}$ and $\langle\epsilon_\theta\rangle_{bg}$ with Ra for different threshold (C_t) is shown in Fig. 6.20. Similar to the global averaged dissipation, $\langle\epsilon_\theta\rangle_{pl}$ and $\langle\epsilon_\theta\rangle_{bg}$ also follow a power-law behaviour with Rayleigh number. The power-law fits to the data result in the scaling behaviour $\langle\epsilon_\theta\rangle_{pl} = a_{pl}Ra^{b_{pl}}$ and $\langle\epsilon_\theta\rangle_{bg} = a_{bg}Ra^{b_{bg}}$. The exponents and prefactors obtained from least-squares fit for different cutoffs are shown in Table 6.4. Note that the power-law exponent b_{pl} shows decreasing trend with the increase in threshold value. However, the exponent for the background dissipation shows only slight variations with C_t. Interestingly, for $C_t = 0$, the contribution from the plume and background to the thermal dissipation rates approach the global ($\langle\epsilon_\theta\rangle \sim Ra^{-0.21}$) scaling for higher Rayleigh numbers ($Ra \geq 10^8$).

Table 6.4: The power-law fits for thermal dissipation in the plume and turbulent background region, $\langle \epsilon_\theta \rangle_{pl} = a_{pl} Ra^{b_{pl}}$ and $\langle \epsilon_\theta \rangle_{bg} = a_{bg} Ra^{b_{bg}}$, at different cutoffs C_t.

$C_t\%$	a_{pl}	b_{pl}	a_{bg}	b_{bg}
0	0.138	−0.197	0.553	−0.269
0.1	0.115	−0.198	0.838	−0.279
1	0.072	−0.182	0.919	−0.287
5	0.033	−0.144	0.531	−0.265
10	0.02	−0.118	0.377	−0.248

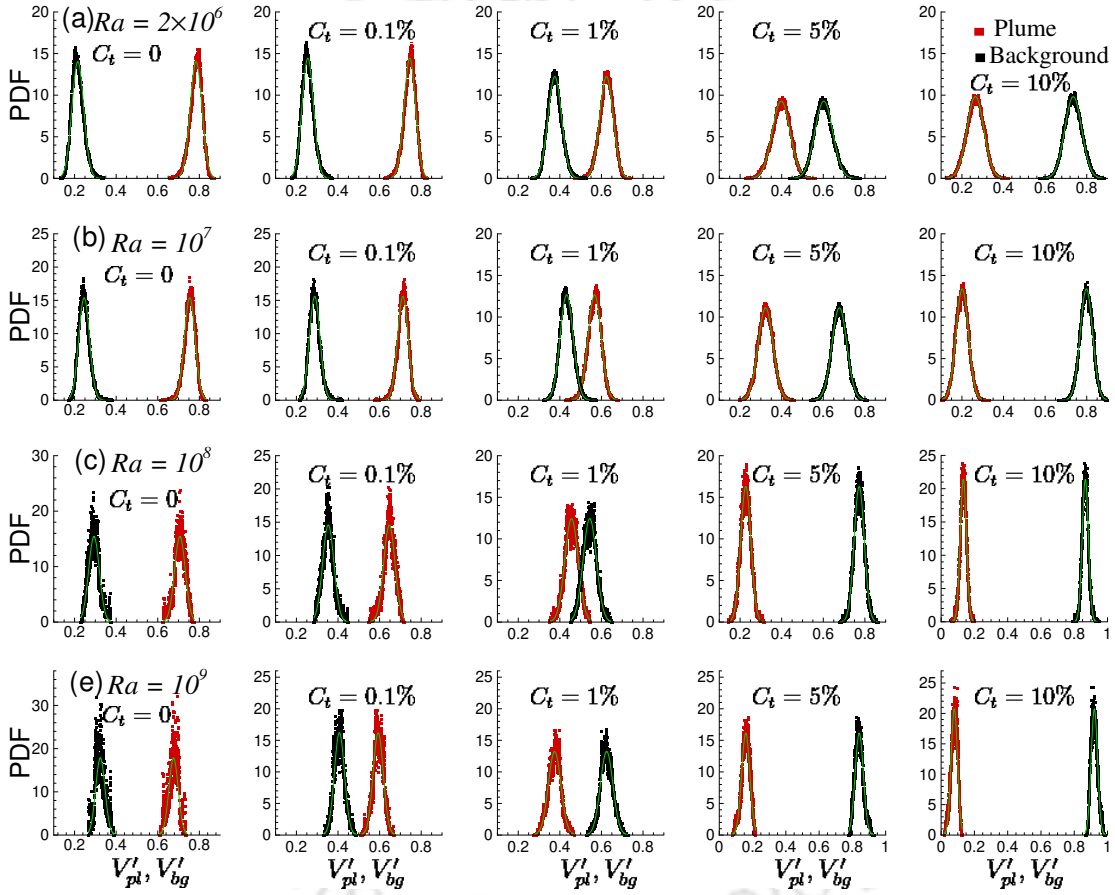

Figure 6.21: Temporal PDF of the volume fraction of the plume and background regions for different cutoffs at (a) $Ra = 2 \times 10^6$, (b) $Ra = 10^7$, (c) $Ra = 10^8$, and (d) $Ra = 10^9$. The solid lines represent the corresponding normal distribution.

The temporal PDFs of volume fraction of the plume and background regions are shown in Fig. 6.21. For all cutoffs, the PDFs follow a normal distribution, although small deviations are observed at $Ra = 10^9$. Dependence of the cutoff on the plume and background decomposition is evident from the frames shown. For $C_t < 1\%$, the volume fraction of the plume dominates for all Ra, as V'_{pl} is shifted towards high amplitude events (right side) while V'_{bg} to the low amplitude events. However, for higher values of C_t, the trend reverses and background fraction

dominates. Further, with the increase in Ra, the PDFs become thinner and more localized near the respective mean values.

Grossmann and Lohse [167] split the thermal dissipation rates into their contributions from the plume and background regions. The theoretical estimates are given as

$$\epsilon_{\theta,pl}^{th} \sim \alpha \frac{(\Delta T)^2}{H^2} Re^{1/2} Pr^{1/2} f^{1/2}, \tag{6.14}$$

$$\epsilon_{\theta,bg}^{th} \sim \alpha \frac{(\Delta T)^2}{H^2} RePrf, \tag{6.15}$$

where f is the shedding frequency of the plumes which has no dependence on the Reynolds number Re. The Reynolds number associated with the large-scale mean flow is computed as $Re = UH/\nu$, where $U = \sqrt{\langle u^2 + v^2 + w^2 \rangle}$ [169, 253]. The equations can be further cast into

$$\epsilon_{\theta,pl}^{th} \sim V \frac{(\Delta T)^2}{H} \frac{1}{\sqrt{RaPr}} Re^{1/2} Pr^{1/2} f^{1/2}, \tag{6.16}$$

$$\epsilon_{\theta,bg}^{th} \sim V \frac{(\Delta T)^2}{H} \frac{1}{\sqrt{RaPr}} RePrf. \tag{6.17}$$

Thus, the non-dimensional thermal dissipation rate contributions are written as

$$\epsilon_{\theta,pl} \sim \frac{1}{\sqrt{RaPr}} Re^{1/2} Pr^{1/2} f^{1/2}, \tag{6.18}$$

$$\epsilon_{\theta,bg} \sim \frac{1}{\sqrt{RaPr}} RePrf. \tag{6.19}$$

To check these scalings in the present study, the normalized thermal dissipation contribution from the plume and background regions are plotted against Re in Fig. 6.22, where solid lines show the exact scalings corresponding to $\sqrt{RaPr}\,\epsilon_{\theta,pl} \sim Re^{1/2}$ and $\sqrt{RaPr}\,\epsilon_{\theta,bg} \sim Re$. Note that here $\epsilon_{\theta,pl} = \langle \epsilon_\theta \rangle_{pl} V_{pl}$ and $\epsilon_{\theta,bg} = \langle \epsilon_\theta \rangle_{bg} V_{bg}$ are the effective dissipation from the plume and background regions, respectively. The power-law fits of the dissipation rates in the form $\sqrt{RaPr}\,\epsilon_{\theta,pl} \sim Re^{b_{pl}}$ and $\sqrt{RaPr}\,\epsilon_{\theta,bg} \sim Re^{b_{bg}}$ are attempted using the least-squares method, and the observed exponents are shown in Table 6.5. For lower values of cutoff ($C_t = 0,\ 0\%$ and 1%), the thermal dissipation from the plume region scales well with the GL theory [167] with an observed exponent (b_{pl}) between $0.46 - 0.55$, while for higher values of C_t deviations are observed. On the other hand, the background dissipation does not follow GL scaling for all values of C_t.

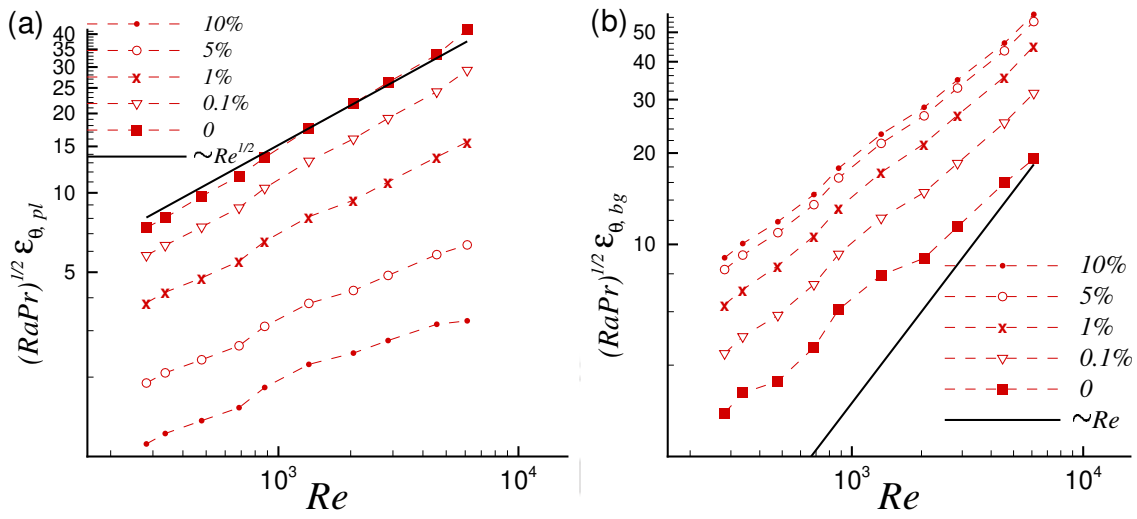

Figure 6.22: Variation of the normalized thermal dissipation contribution from the (a) plume and (b) background with Reynolds number at different cutoffs ($C_t = 0,\ 0.1\%,\ 1\%,\ 5\%$, and 10%). The solid lines represent the corresponding scaling obtained by GL theory.

Table 6.5: The power-law fits for the normalized thermal dissipation rate from the plume and background region, $\sqrt{RaPr}\ \epsilon_{\theta,pl} \sim Re^{b_{pl}}$ and $\sqrt{RaPr}\ \epsilon_{\theta,bg} \sim Re^{b_{bg}}$, at different cutoffs.

$C_t\%$	b_{pl}	b_{bg}
0	0.55	0.63
0.1	0.52	0.64
1	0.46	0.63
5	0.39	0.61
10	0.37	0.30

In their 2D simulations on turbulent RBC, Zhang *et al.*[169] also observed such deviations in the bulk scaling and they attributed it to inverse energy cascade[254]. Note that similar deviations for the bulk contributions have already been reported in many three-dimensional works also. Calzavarini *et al.*[83] reported that these deviations in the bulk are due to the presence of large vertical jets. These jets are associated with the formation of strong vertical temperature gradients on the surfaces at their boundaries. In their simulations in spherical shells, Gastine *et al.*[255, 256] also observed deviations from theoretical predictions. They proposed that the problem is due to the inherent difficulty in the separation of the bulk and boundary layer contributions. The dynamical plumes constantly departing from the boundary layers obviously complicate matters. Similarly, in the present work also we infer that the deviations from theoretical predictions might be due to the errors arising from the decomposition of plume and background regions. Note that different researchers use different methods for identifying the

plume and background regions and there exist no hard and fast rule for the same. Hence, deviations from the theoretical predictions are expected.

6.6 Temperature and velocity fluctuations

Kaczorowski and Wagner [172] analyzed the turbulent fluctuation of velocity and temperature in turbulent RBC, and observed that the velocity and temperature fields are correlated within the thermal boundary layers and tend to be uncorrelated in the core region of the flow. The decorrelation was also observed with increasing Ra, when the flow becomes fully turbulent. Generally, the transition from Gaussian to exponential distribution of velocity and temperature is used to characterize the soft and hard turbulence regimes [257, 258]. However, based on Ra, Pr, and aspect ratio (Γ) of the container, the nature of transition changes. For unit aspect ratio containers, Heslot *et al.* [257] and Sano *et al.* [185] reported that the distribution of temperature fluctuations at the center of the domain transforms from Gaussian in soft turbulent regime to exponential distribution in the hard turbulent regime, and the transition occurs approximately around $Ra \approx 10^7$. However, Deluca *et al.* [259], Solomon [258], and Solomon and Gollub [260] observed exponential distribution in the Rayleigh number range $10^6 \leq Ra \leq 2\times10^8$. On the other hand, Qui *et al.* [261] obtained a clean Gaussian distribution for velocity fluctuations at the center of the cell for $Ra = 3.7\times10^9$. Also, a mixed Gaussian and exponential distribution was observed by Christie and Domaradzki at $2.5 \times 10^5 \leq Ra \leq 6.3 \times 10^5$ for larger aspect ratio containers ($\Gamma \approx 5$). Here, we evaluate the distribution of temperature and vertical velocity to identify the flow behaviour in different regions of the flow domain. Firstly, the temporal behaviour of the flow at the center of the flow domain is examined. Following this, the spatial PDFs are analyzed at different horizontal sections of the cubic cell. Further, we examine how these statistics are connected with the flow structure and plume behaviour.

The normalized PDFs of velocity and temperature fluctuations at the center of the cubic cell (measured by the probe P_9^m) are shown in Fig. 6.23, where the abscissa is $(\theta - \mu_\theta)/\sigma_\theta$ or $(v - \mu_v)/\sigma_v$ and the ordinate is its corresponding PDF. Here μ and σ represent the mean and standard deviation of the respective variables. The solid lines represent the corresponding normal distribution. The velocity fluctuations approach a Gaussian profile with the increase in

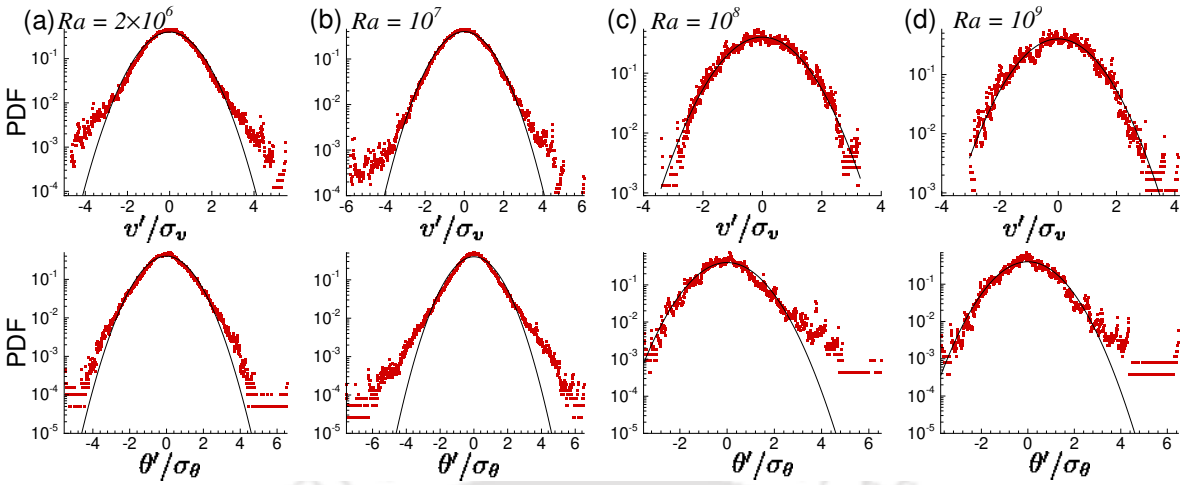

Figure 6.23: PDF of vertical velocity and temperature fluctuations at the center of the cell for different Ra. The solid lines represent the corresponding standard normal distribution.

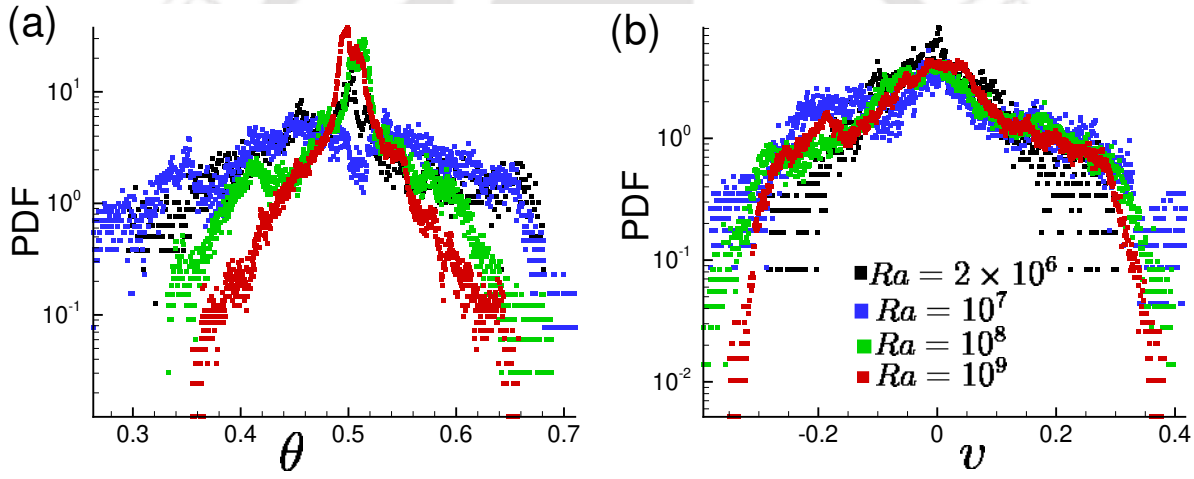

Figure 6.24: Spatial PDF of (a) temperature and (b) vertical velocity at mid-plane ($z = 0.5H$) for different Ra.

Ra, while the temperature fluctuations show a clear departure from it. The PDF of temperature at $Ra = 2 \times 10^6$ follows a near Gaussian distribution, while at higher Ra, it shows significant deviations. For higher Ra, an exponential distribution is observed, which is consistent with the observations made by Heslot *et al.* [257] and Sano *et al.* [185]. It is evident that as the Ra increases, the temperature PDFs become more skewed as the left tail becomes shorter, and the right tail extends beyond the standard normal curve. The stretched behavior of the high amplitude tail indicates the increased level of small-scale intermittency at high Rayleigh numbers.

The spatial PDFs of temperature and vertical velocity at the horizontal mid-plane ($y =$

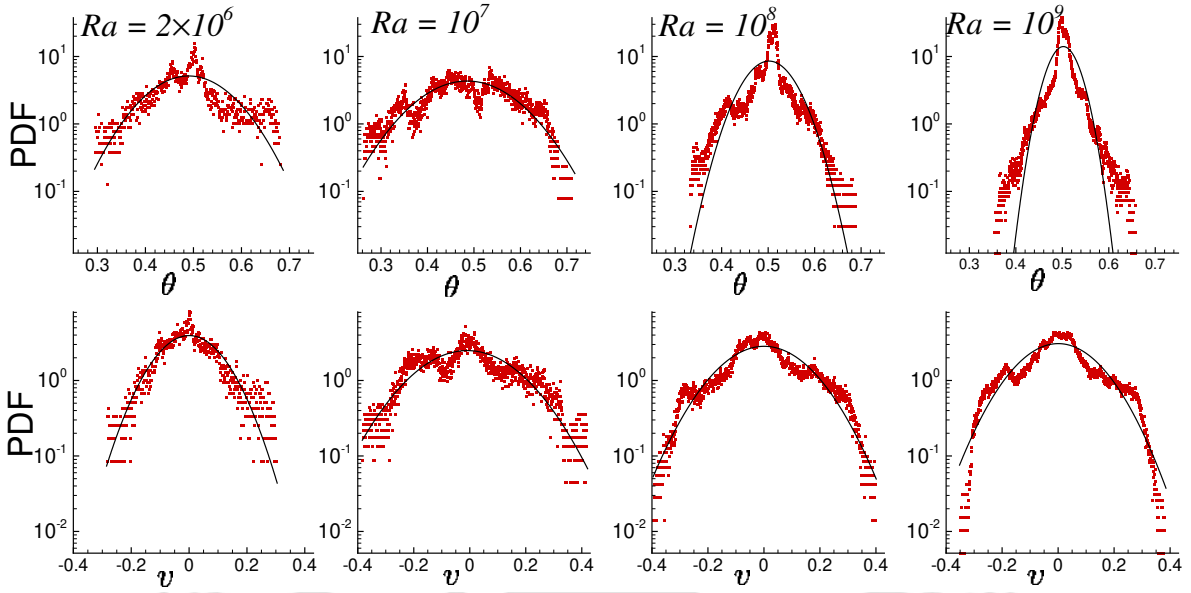

Figure 6.25: Spatial PDF of temperature (top row) and vertical velocity (bottom row) at mid-plane ($z = 0.5H$) for (a) $Ra = 2 \times 10^6$, (b) $Ra = 10^7$, (c) $Ra = 10^8$, and (d) $Ra = 10^9$. Solid line shows the Gaussian distribution curve.

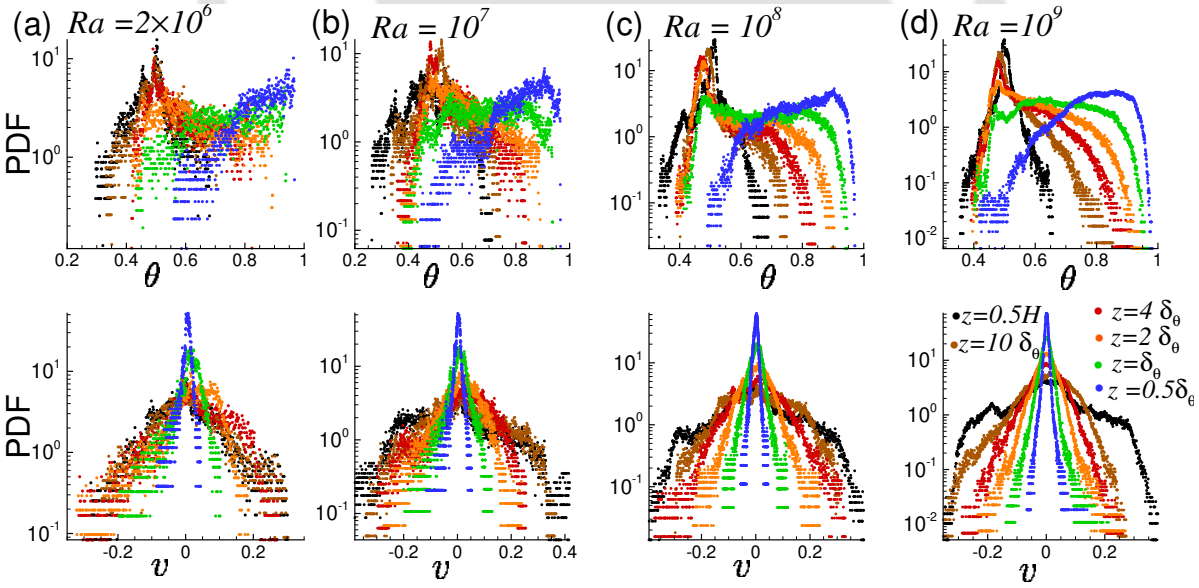

Figure 6.26: Spatial PDF of temperature (top row) and vertical velocity (bottom row) at various heights ($z = \delta_\theta/2$, δ_θ, $2\delta_\theta$, $4\delta_\theta$, $10\delta_\theta$, and $0.5H$) for (a) $Ra = 2 \times 10^6$, (b) $Ra = 10^7$, (c) $Ra = 10^8$, and (d) $Ra = 10^9$.

$0.5H$) of the cell for different Rayleigh numbers are shown in Fig. 6.24. The PDFs of temperature become narrower with the increase in Ra as shown in Fig. 6.24(a), which was also observed by Emran and Schumacher [170]. Recall that in the previous sections, we observed that with the increase in Ra bulk homogeneity increases, and the turbulent background dom-

inates the plume region. The plumes are high amplitude events, i.e., they are associated with high or low temperatures. Hence, the decrease in plume dominated regions reduces the spread of the PDFs of temperature. Thus at higher Ra, the PDFs become thinner and more localized near the mean temperature [see Fig. 6.24(a)]. The PDF of vertical velocity does not follow any particular trend with Ra. To check the deviations from Gaussian distribution, the same data set is shown in Fig. 6.25, where the solid lines represent the corresponding Gaussian distribution. It is apparent that the profiles are non-Gaussian at all Ra for temperature. Moreover, the departure from Gaussian becomes pronounced as the Rayleigh number is increased. For vertical velocity, though at low Ra the PDFs show a near-Gaussian distribution, significant deviations are observed at high Rayleigh numbers.

To evaluate the variation of the temperature and velocity field with vertical height, PDFs are computed at different heights from the bottom plate, such as, $y = \delta_\theta/2$, δ_θ, $2\delta_\theta$, $4\delta_\theta$, $10\delta_\theta$ and $0.5H$, as shown in Fig. 6.26, with δ_θ being the thermal boundary layer thickness. The disparity in the PDFs of temperature and vertical velocity is apparent. Note that the PDFs of temperature become more symmetric with the increase in height. At the center of the cell, symmetric profiles are obtained for all Ra. On the other hand, the PDFs of vertical velocity are always symmetric, and they appear to become narrow with the increase in height. At any horizontal plane, the upward and downward flow cancels out, and hence the effective vertical velocity becomes zero. Thus, the distributions of vertical velocity are always symmetric and centered around $v = 0$. However, for temperature distribution, other than the turbulent bulk region (near the horizontal midplane $y = 0.5H$), the horizontal plane averaged temperature is either higher or lower than the bulk mean temperature. At mid-height the mean temperature is 0.5, and hence the PDFs are seen to center around $\theta = 0.5$. However, away from the bulk, they get skewed towards either higher or lower temperatures. It is apparent in Fig. 6.26 that the PDFs of temperature near the bottom plate are skewed towards higher temperatures ($\theta > 0.5$). Similarly, the PDFs near the top plate will appear shifted to lower temperatures ($\theta < 0.5$). This is also reflected in the vertical profiles of the horizontal plane and time averaged temperature ($\langle\theta\rangle_{A,t}$) discussed in later section. These observations are in line with previous studies [170, 173]. The height dependent symmetry of the temperature and velocity fields is quantified by evaluating the skewness (of v and θ), which is carried out in the next section (Fig. 6.34).

6.7 Planar statistics

To identify the flow characteristics in different regions of the flow, planar statistics of temperature and velocity are computed. Four different measures of temperature fluctuations, namely, the average temperature $\langle\theta\rangle_{A,t}$, variance σ_θ, skewness S_θ, and flatness F_θ are evaluated as

$$\sigma_\theta = \langle\theta'^2\rangle_{A,t},\ S_\theta = \frac{\langle\theta'^3\rangle_{A,t}}{\langle\theta'^2\rangle^{3/2}_{A,t}},\ \text{and}\ F_\theta = \frac{\langle\theta'^4\rangle_{A,t}}{\langle\theta'^2\rangle^{2}_{A,t}}. \tag{6.20}$$

Here the averages $\langle..\rangle_{A,t}$ are obtained by time averaging the horizontal plane (y planes) averaged quantities. Similarly, the variance (σ_v), skewness (S_v), and flatness (F_v) of vertical velocity are also calculated. Statistical convergence of the flow is ensured by the symmetric profiles of the mean and variance about the mid-plane ($y = 0.5H$).

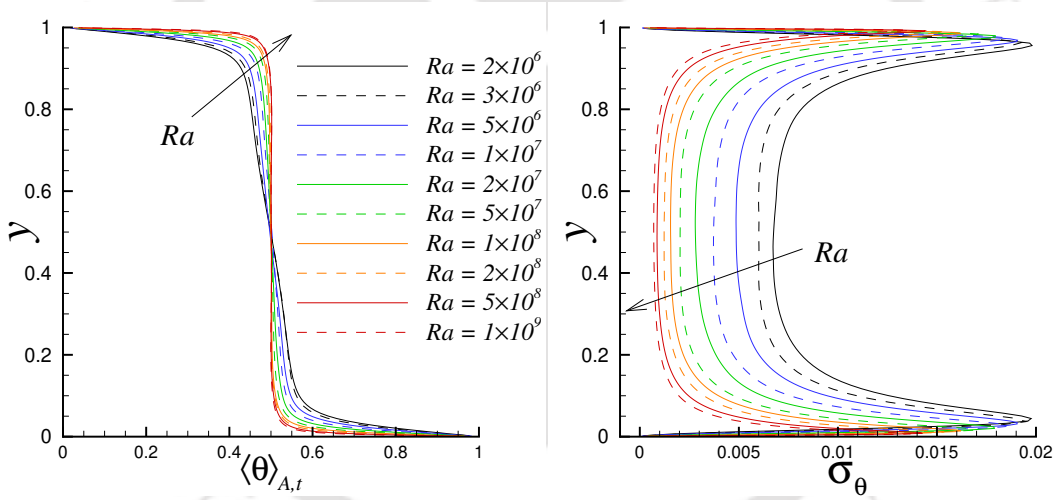

Figure 6.27: Area and time averaged vertical profiles of mean temperature $\langle\theta\rangle_{A,t}$ and variance of temperature σ_θ at different Ra.

In Fig. 6.27, vertical profiles of mean and variance of temperature are shown, which clearly indicate different characteristic regions in the flow domain. The mean temperature shows a sharp gradient in the boundary layer region, which decreases gradually towards the bulk region ($y = 0.5H$). With increase in Ra, the temperature in the bulk becomes almost constant. Hence, at high Rayleigh numbers, the imposed temperature difference across the top and bottom plates is accomplished almost entirely within the thermal boundary layer [140]. Note, Nusselt number is defined as the ratio of total heat transport to that of the conductive (only) heat transport ($Nu \approx q_{total}/q_{cond}$). The conductive heat transport across the fluid layer is given

by $q_{cond} = K\Delta T/H$, where K is the thermal conductivity of the fluid. In an idealized case, where the entire imposed temperature gradient is lost in the thermal boundary layers, the total heat transport can be written as $q_{total} \approx K\Delta T/2\delta_\theta$. Thus, we obtain the relation between Nusselt number and thermal boundary layer thickness as

$$Nu \approx \frac{q_{total}}{q_{cond}} \approx \frac{H}{2\delta_\theta} \tag{6.21}$$

The variance of temperature increases as we move away from the isothermal plates and peaks near the edge of the boundary layer where it shows a sharp gradient, as shown in Fig. 6.27. Subsequently, it drops gradually to attain an almost constant value near the center of the flow domain. This nearly constant value of σ_θ indicates homogeneity in the bulk region. Note that the homogeneous region widens with the increase in Ra, as the peaks shift towards the top and bottom plates. As discussed in the previous sections, at low Ra, thermal plumes extend over the entire cell domain, and they are more likely to travel across the bulk region. Thus, the magnitude of variance of temperature (and velocity) becomes larger in the bulk. However, with the increase in Ra, due to better mixing, the plumes are less likely to approach the central region, resulting in a homogeneous turbulent flow in the bulk. Hence, the variance reduces in the bulk with increase in Ra.

For both mean and variance of temperature, the high gradient region represents the thermal boundary layers. The thermal boundary layer thickness δ_θ is computed as the distance of the local maxima in variance profile from the plates [173], as shown schematically in Fig. 6.28. Figure 6.29(a) shows thermal boundary layer thickness obtained from the peak variance of temperature for different Ra, which follows a power-law behaviour $\delta_\theta = 2.82Ra^{-0.289}$. Substituting the Nusselt number scaling ($Nu = 0.16\ Ra^{0.286}$) observed in the previous section in Eq. 6.21 yields the relation $\delta_\theta = 3.12Ra^{-0.286}$, which is in good agreement with the observed scaling relation. Further, the comparison with the numerical study by Verzicco and Camussi [52] (cylindrical cell) is shown in Fig. 6.29(a), which suggests adequate resolution of the present simulations. On a similar note, a scaling exponent of 0.285 was reported by Wagner *et al.* [50].

It has been observed in various experimental [74], numerical [173], and theoretical [75] studies that the maximum variance of temperature, σ_θ^{max} (at the edge of the boundary layer)

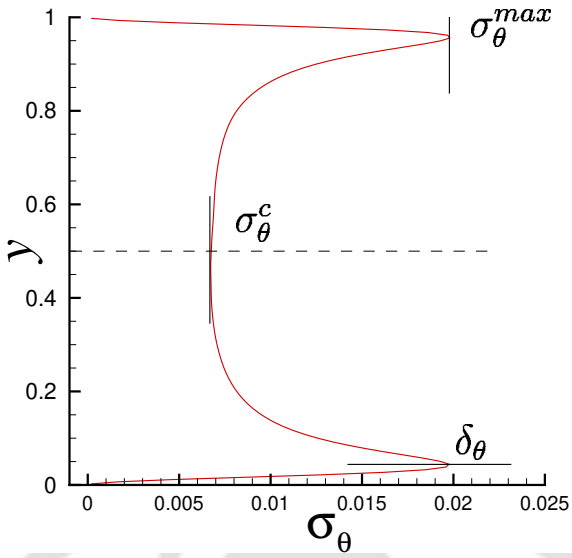

Figure 6.28: Sample profile of variance of temperature showing the locations of maximum variance σ_θ^{max}, variance at center σ_θ^c, and the thermal boundary layer thickness corresponding to maximum variance δ_θ.

and the variance at the bulk, σ_θ^c (at the center of the domain) follow different power law behaviour with Ra. Figure 6.28 schematically shows the locations of σ_θ^{max}, σ_θ^c, and the thermal boundary layer thickness corresponding to maximum variance. Here the superscripts c and max correspond to the domain center and maximum value, respectively, which are also followed in case of velocity profiles. Figure 6.29(b) shows the scaling behaviour observed for the variance of temperature where we observe a power-law behaviour as $\sigma_\theta^{max} = 0.048Ra^{-0.061}$ and $\sigma_\theta^c = 1.15Ra^{-0.37}$. The scaling exponent for maximum variance is in good agreement with the $-1/14$ scaling of Kerr [173]. However, the bulk scaling shows significant deviation from the theoretical prediction ($-1/7$ scaling) by Castaing *et al.* [74] and Shraiman and Siggia [75], and the DNS of Kerr [173].

Vertical profiles of rms ($u_{rms} = \sqrt{\sigma_u}$ and $w_{rms} = \sqrt{\sigma_w}$) of the horizontal velocities are shown in Fig. 6.30. Both the horizontal components show high fluctuations near the wall which eventually flattens to yield a homogeneous central region. With increase in Ra, the bulk homogeneity increases, and thus the rms values of the horizontal velocities reduce, as observed in case of σ_θ. The vertical distance of the peak rms from the horizontal wall gives an estimate of viscous boundary layer thickness. For better representation, total horizontal velocity is considered as $u_{rms}^H = \sqrt{u_{rms}^2 + w_{rms}^2}$, which is subsequently normalized to Peclet number, given by $Pe_u = u_{rms}^{H*} H/\alpha$, where $u_{rms}^{H*} = V\ u_{rms}^H$ is the dimensional rms (with V being the

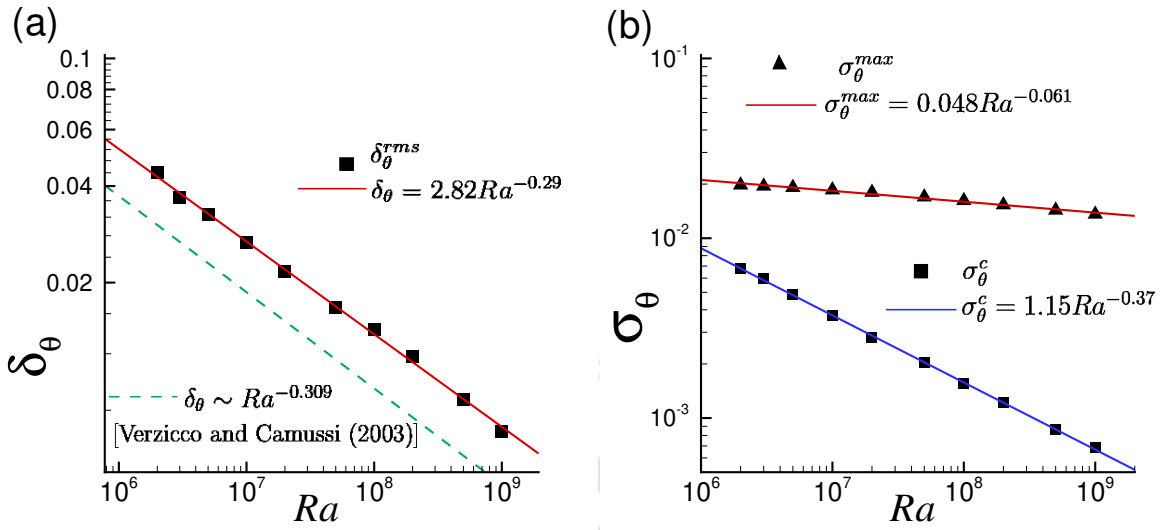

Figure 6.29: (a) Scaling of the thermal boundary layer thickness with Ra. (b) Scaling of maximum variance of temperature, σ_θ^{max} and the variance at the bulk, σ_θ^c with Ra. The solid lines represent the corresponding power-law obtained by least-squares approximation and dashed line represents the observations by previous study.

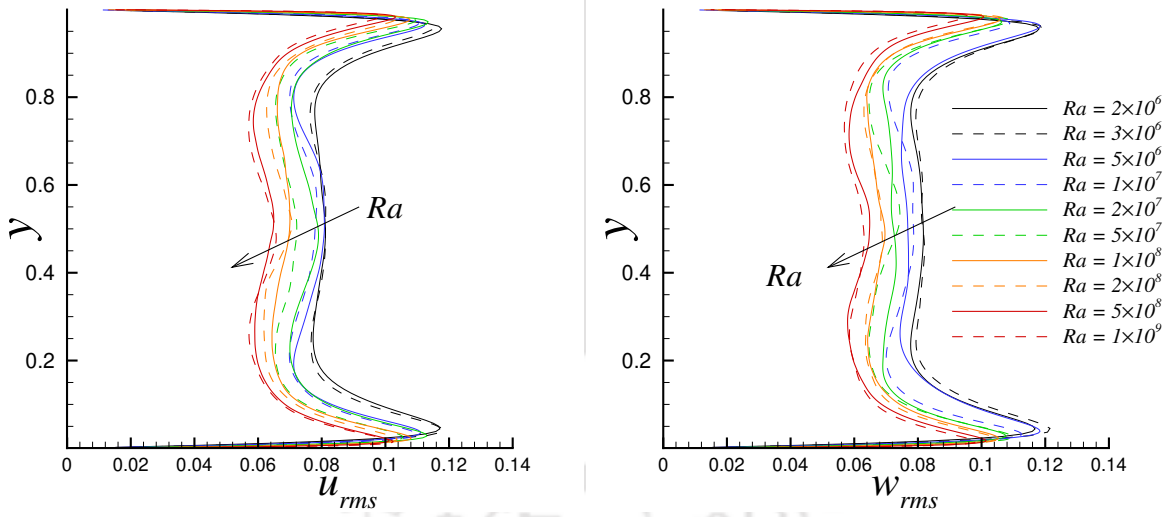

Figure 6.30: Vertical profiles of rms of horizontal velocities (u_{rms} and w_{rms}) at different Ra. The arrows indicate the direction of increasing Rayleigh number.

velocity scale). As in the present computation we use only non-dimensional quantities, Pe is calculated from the non-dimensional rms as $Pe_u = \sqrt{RaPr}\ u_{rms}^H$. Similarly, the normalized rms of vertical velocity, given by $Pe_v = v_{rms}^* H/\alpha = \sqrt{RaPr}\ v_{rms}$, is also calculated. The vertical variation of the normalized rms of the horizontal velocity and vertical velocity is shown in Fig. 6.31. Pe_u increases as we move away from the isothermal plates, peaks near the edge of the viscous boundary layer, where it shows a sharp gradient and subsequently reduces gradually

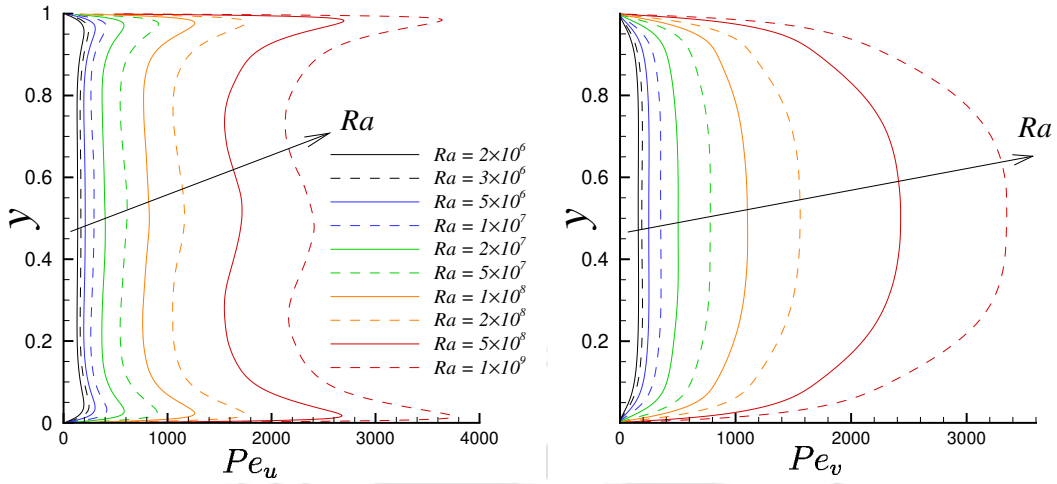

Figure 6.31: Vertical profiles of the normalized effective horizontal velocity and vertical velocity, in terms of Peclet number, at different Ra. The arrows indicate the direction of increasing Rayleigh number.

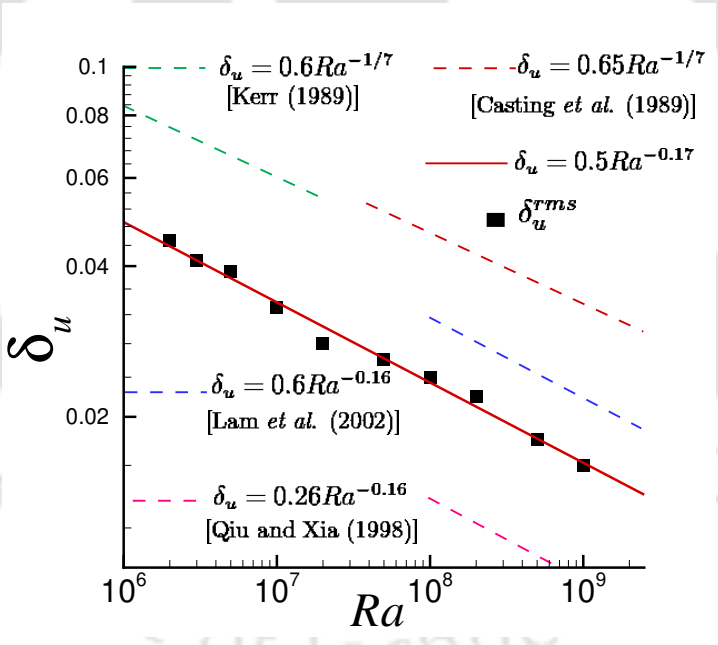

Figure 6.32: Scaling of the viscous boundary layer thickness with Ra constructed using the least-square approximation. The dashed lines represent the observations by previous studies.

in the bulk region. In contrast to the horizontal velocity, the variance of vertical velocity Pe_v increases all the way up to the center of the cell, as shown in Fig. 6.31. The large value of Pe_u near the top and bottom plates suggest that the flow is dominant in the horizontal direction (note that Pe_v is negligible near the isothermal plates). On the other hand, away from the horizontal plates, flow occurs predominantly along the vertical direction, and as a result, Pe_u reduces and Pe_v increases. The large-scale behaviour of the flow to form a coherent LSC mentioned in

the previous sections is apparent from these observations. Further, with increase in Rayleigh number, the magnitude of the normalized variances increase (see Fig. 6.31), indicating the dominance of the LSC at higher Ra.

Kerr [173] defined the viscous boundary layer thickness as the vertical distance of the peak value of $Pe_{u_{rms}}$ from the horizontal wall. Figure 6.32 shows the velocity boundary layer thickness for different Ra, which follows a power-law behaviour as $\delta_u = 0.5Ra^{-0.17}$. The exponent is in reasonable agreement with Qiu and Xia [63], Castaing *et al.* [74] (cylindrical cell), and Kerr [173]. The experimental study by Lam *et al.* [262] showed that the viscous boundary layer thickness depends on both Ra and Pr, and follows the relation $\delta_u = 0.65Ra^{-0.16}Pr^{0.24}$. For fixed Prandtl number of $Pr = 0.7$, the power law behaviour becomes $\delta_u = 0.6Ra^{-0.16}$, which agrees well with the present study as shown in Fig. 6.32. Previous studies [165, 173] have shown that the maximum rms of horizontal velocity, Pe_u^{max} (at the edge of the boundary layer) and the rms at the bulk, Pe_u^c follow a power-law behaviour with Ra. Figure 6.33(a) shows the scaling observed for the rms of velocities. The least-squares fits of the data show a power-law behaviour of $Pe_u^{max} = 0.21Ra^{0.47}$ and $Pe_u^c = 0.18Ra^{0.46}$. The rms of vertical velocity at the center also follows a power-law behaviour, $Pe_v^c = 0.12Ra^{0.5}$, as shown in Fig. 6.33. The scaling relations obtained in the present study are compared with those obtained by Kerr [173] in Fig. 6.33(b) which shows excellent agreement. In their experimental studies with water in cubic cell, Qiu and Xia [63, 70] also reported a scaling behaviour of $Pe_v \propto Ra^{0.5}$.

The mean and variance provide a qualitative description of thermal boundary layer and the bulk region, while skewness being the third-order moment, indicates a measure of the symmetry around the mean value. Positive skewness means that the tail on the right side of the distribution is longer or fatter, whereas negative skewness indicates a fatter left tail. If the distribution is symmetric, then the skewness becomes zero. Willis and Deardorff [263] showed that the skewness of vertical velocity and temperature are crucial for turbulent diffusion in atmospheric boundary layers. The vertical profiles of skewness of temperature S_θ and vertical velocity S_v are shown in Fig. 6.34. Both skewnesses show a skew-symmetric distribution about the center with significant negative fluctuations near the hot plate, which renders $S_\theta, S_v < 0$. While vertical velocity loses its intensity to saturate in the intermediate and bulk regions, temperature fluctuations follow a slow linear variation. This feature is different from free surface flows where only positive skewness is reported. A similar effect can be observed here if the

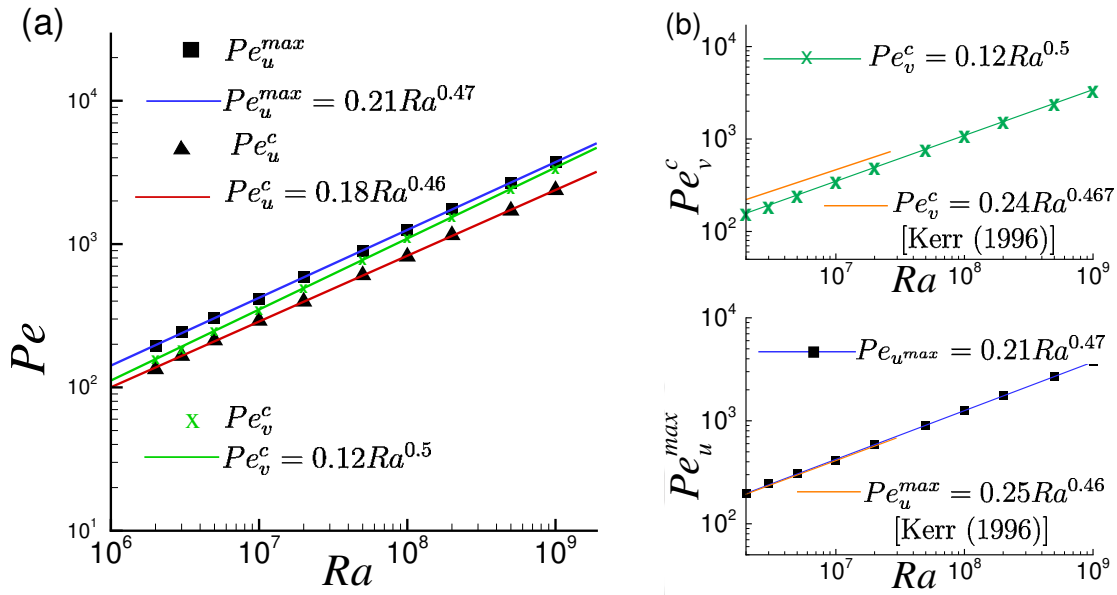

Figure 6.33: (a) Scaling of maximum variance and the variance at the bulk of normalized velocities with Ra, constructed using least-square approximation. (b) Comparison of the present results with those obtained by Kerr [173].

upper surface is insulated so that the effect of the cold plumes are negated. In RBC, hot and cold plumes extend into the flow domain and approach the opposite plate. In the boundary layer at the bottom, the cold plumes coming from the top plate dominates the background flow intermittently, and thus S_θ and S_v are negative near the hot plate [165, 173]. A similar effect is noticed at the top plate, where the intermittent presence of hot plumes results in positive values of skewness.

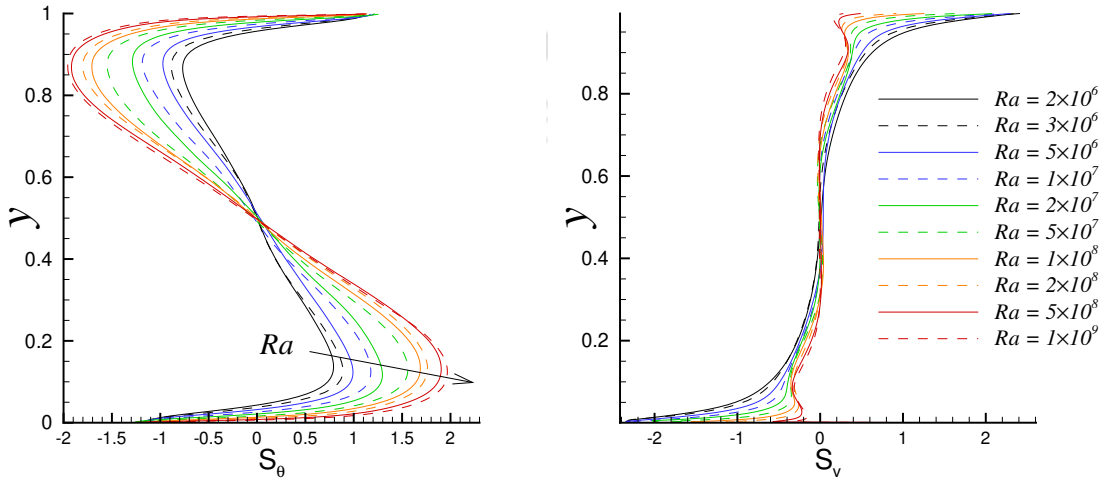

Figure 6.34: Vertical profiles of skewness of temperature and vertical velocity at different Ra. The arrow indicates the direction of increasing Rayleigh number.

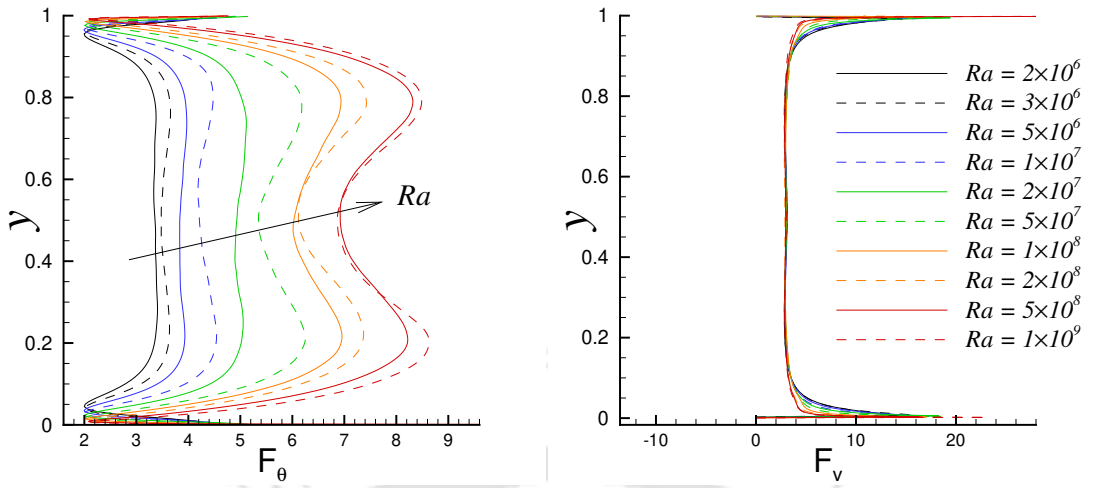

Figure 6.35: Vertical profiles of flatness of temperature and vertical velocity at different Ra. The arrow indicates the direction of increasing Rayleigh number.

The vertical variation of skewness of temperature is consistent with the corresponding PDFs at different heights of the cell shown in Fig. 6.26. The PDFs of temperature near the bottom plate are evidently skewed due to more high amplitude fluctuations in temperature. As a result, skewness of temperature shows significant deviation from zero. With the increase in height, the PDF of temperature becomes symmetric centered around the bulk mean temperature. This is reflected in the vertical profile of S_θ shown in Fig. 6.34, i.e., as $y \rightarrow 0.5H$, S_θ approaches zero. In contrast to S_θ, the skewness of vertical velocity is trivial all along the bulk region, which is due to the symmetric distribution of vertical velocity in both positive and negative directions (refer Fig. 6.26). Both the vertical velocity and temperature skewness switch sign across the center of the domain and thus exhibit a skew-symmetric profile. These observations are consistent with previous results [165, 173, 263]. With the increase in Ra, the skewness profiles show sharp gradients near the top and bottom plates, which also supports the reduction in boundary layer thickness with increase in Rayleigh number.

Figure 6.35 shows the flatness or kurtosis of temperature and vertical velocity for different Ra. Flatness is a fourth-order moment which measures the deviation of a distribution from Gaussian. Skewness indicates the degree of symmetry of distribution, whereas the kurtosis represents the degree of peakedness. Large values of flatness ($F_\theta >> 3$) indicate that the distribution is "heavily tailed", i.e., the tails extend much beyond the normal distribution. On the other hand, lower flatness represents a "light tailed" distribution, where the tails are generally shorter than that of the normal distribution. The flatness of any normal distribution is 3. It

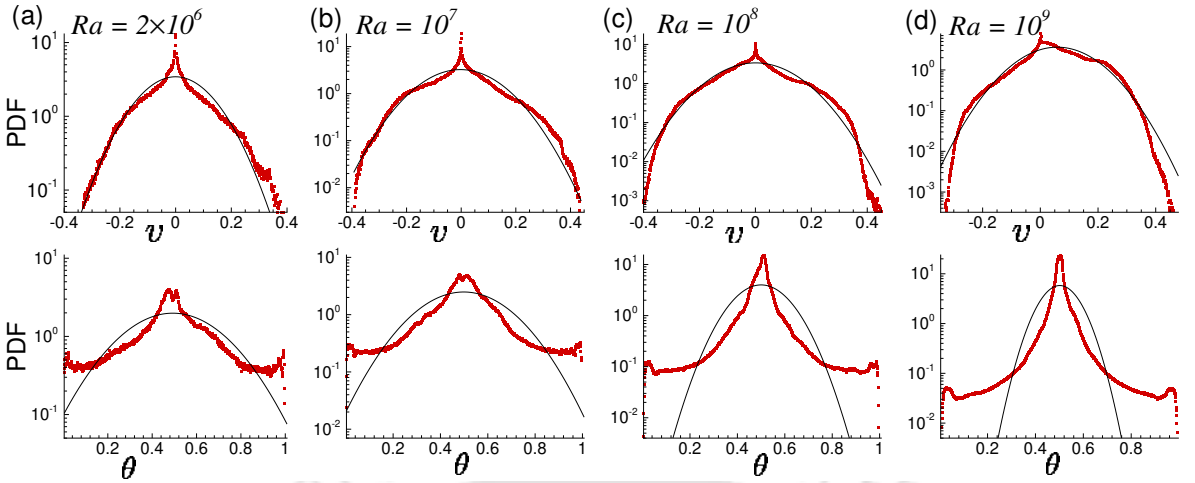

Figure 6.36: Spatial PDF of vertical velocity (top row) and temperature (bottom row) for (a) $Ra = 2 \times 10^6$, (b)$Ra = 10^7$, (c) $Ra = 10^8$, and (d) $Ra = 10^9$. The solid line represents the corresponding normal distribution.

is evident from Fig. 6.35 that the flatness of temperature increases with the increase in Ra. At low Ra, F_θ is close to 3 in the bulk, indicating a near Gaussian distribution, and it departs significantly at higher Rayleigh number. However, flatness of vertical velocity shows $F_v \approx 3$ at the bulk region, suggesting a Gaussian distribution even at a very high Ra. Near the boundary layers, F_v shows a significantly high value indicating a non-Gaussian distribution. To elucidate this, the spatial PDFs of temperature and vertical velocity fields for the entire cell are shown in Fig. 6.36. It is apparent that the vertical velocity follows a near Gaussian distribution, although slight deviations along with a bump in the core region are observed for all Ra. This is due to the effect of the boundary layer region (as the PDF is computed over the entire volume, i.e., including the boundary layers). On the other hand, the temperature fields show significant deviation from the Gaussian profile for all Ra, as indicated by F_θ. Note that the PDFs of temperature are heavily tailed, and as a result, F_θ shows large positive values (see Fig. 6.35).

6.8 Turbulent kinetic energy budget

Evaluation of turbulent kinetic energy (TKE) budget is crucial in understanding convective turbulence. It facilitates a deeper understanding of multiple layers based on the local flow dynamics which include boundary layers close to the wall, turbulent bulk region in the center [57, 76], and mixing zone embedded in between these two [74]. These layers are generally quantified

using the vertical profiles of velocity and temperature, which shows different behaviour across them [181, 183]. The relative strength of dissipation and production of TKE within these layers is understood to considerably affect the dynamics of convection, particularly the heat transport [76]. Petschel *et al.* [264] analysed the kinetic energy budget for a range of Prandtl numbers at a fixed Ra. They observed that the kinetic energy is mainly produced in the bulk region where the temperature field is well mixed, from where it is transported outwards and dissipated near the walls. Similar observations were made by Deardorff and Willis [265] and Kerr [266]. Here a global budgetary analysis of each term of the dynamical equation governing turbulent kinetic energy is carried out. The same is written in its most popular form as

$$\underbrace{\frac{\partial}{\partial t}(\frac{1}{2}\overline{u_i'u_i'}) + U_j\frac{\partial}{\partial x_j}(\frac{1}{2}\overline{u_i'u_i'})}_{A_k} = \underbrace{-\frac{\partial}{\partial x_j}\left(\overline{u_j'p'} - 2\sqrt{\frac{Pr}{Ra}}\overline{u_i's_{ij}'} + \frac{1}{2}\overline{u_i'u_i'u_j'}\right)}_{T_k} \\ \underbrace{-\overline{u_i'u_j'}S_{ij}}_{P_S} + \underbrace{\overline{u_i'\theta'}\delta_i y}_{P_B} - \underbrace{2\sqrt{\frac{Pr}{Ra}}\overline{s_{ij}'s_{ij}'}}_{\epsilon}, \tag{6.22}$$

where $u_i^{'}$ $(= u_i - U_i)$, $p^{'}$ $(= p - P)$, and $s_{ij}^{'}$ $(= s_{ij} - S_{ij}$) are the fluctuating components of velocity, pressure and strain rate tensor, respectively, while U_i, P_i, and S_{ij} represent their corresponding mean counterparts. The left-hand side of the above equation indicates the advection of turbulent kinetic energy A_k. The first term on the right-hand side is the transport (T_k) which is a conserved quantity (of the form $\nabla\cdot\,\phi$) that redistributes the kinetic energy in the domain. The second and third terms on the right-hand side are production due to buoyancy (P_B) and shear (P_S), while the fourth term is the dissipation (ϵ) of turbulent kinetic energy. The main difference between a shear flow and thermal convection is the presence of the production due to buoyancy (P_B) in Eq. 6.22. In the case of steady, homogeneous shear flow turbulence, an approximate balance between shear production and dissipation is observed. However, similar dynamics in case of buoyancy driven flows are less explored.

Figure 6.37 shows the vertical variation (horizontal plane and time averaged) of different terms of the above equation for different Rayleigh numbers. It is interesting to note that the contribution of shear production is negligible at all Ra. However, the buoyancy production, though trivial at the walls, increases with a steep gradient to attain a maximum outside the boundary layers. In the vicinity of the walls, high dissipation is observed while it decreases

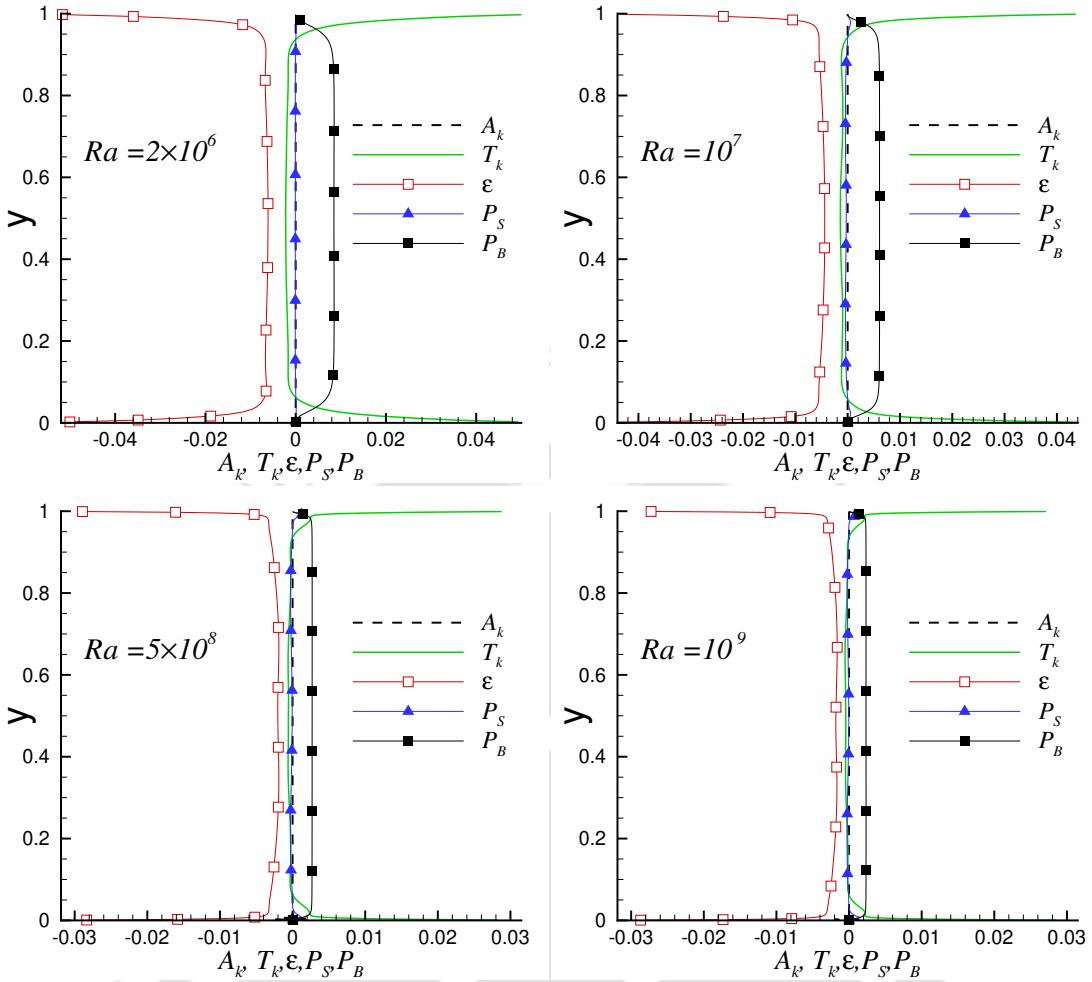

Figure 6.37: Vertical variation of different TKE budget constituents for different Rayleigh numbers.

across the boundary layers and becomes nearly constant near the bulk region. Note that high dissipation observed near the walls, the production being negligible, indicates the importance of the transport term, which shows a high positive value [267]. Dissipation acts as the sink for turbulent kinetic energy. Based on the distribution of TKE, Petschel *et al.* [264, 268] identified different regions of the flow, such as source layer which is characterized by enhanced kinetic energy production, flux layer with dominant transport, and dissipation layers close to the boundary with significantly enhanced dissipation. They defined the edge of the dissipation layers as the location at which the dissipation becomes equal to the volume-averaged dissipation. For $Ra = 5 \times 10^6$ and $Pr \approx 1$ the dissipation layers were found to be thicker than the classical boundary layers.

Figure 6.38 shows the zoomed view of the TKE budget near the boundary layer and the

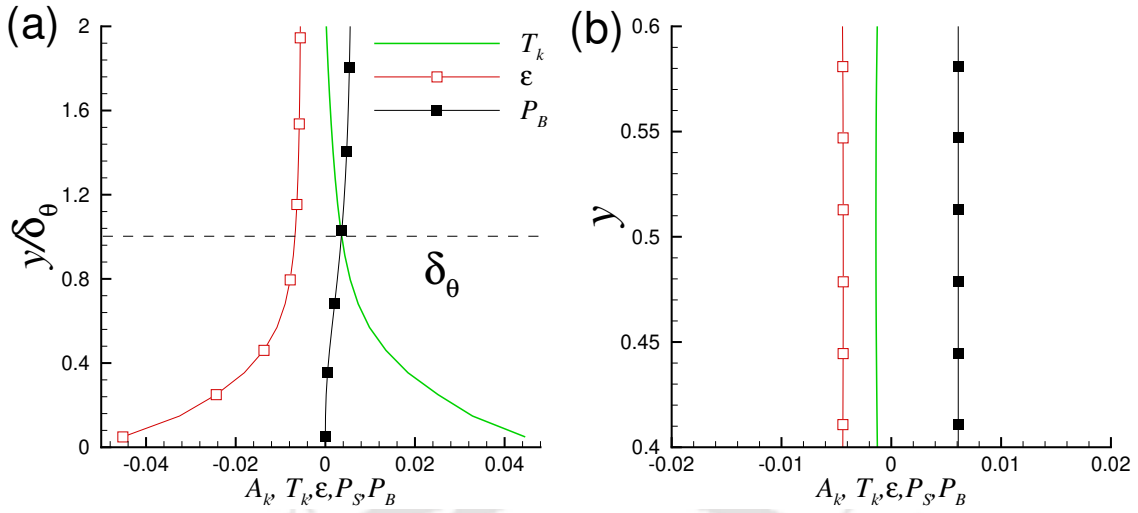

Figure 6.38: Zoomed vertical profiles of P_S, ϵ and T_k for $Ra = 10^7$ near (a) boundary layer region and (b) bulk. The dotted line represents the thermal boundary layer thickness.

bulk region for $Ra = 10^7$. As the advection and shear production terms are trivial, they are not shown in these frames. For better visualization, the vertical direction is scaled appropriately using the boundary layer thickness (δ_θ) in Fig. 6.38(a). Near the wall, owing to stronger viscous effects, velocity fluctuation is small, which results in a smaller buoyancy production, but viscous transport is significant, which leads to an approximate balance $T_k \approx \epsilon$. Note that the transport term indicates the divergences of energy fluxes, and consists of the transport by viscous stresses, turbulent velocity fluctuations and pressure gradient work [269]. Petschel *et al.* [264] analyzed the contribution of different flux terms near the horizontal walls and observed that all flux divergences vanish at the boundary, except for the viscous stresses. They hence concluded that the dissipation near the walls is balanced by the divergence of the shear-stress flux only. In the bulk region, although an approximate balance between buoyancy production and dissipation is observed, the transport term is also non-trivial. Note that the transport appears with a negative sign in bulk which implies the extraction of TKE. Thus, kinetic energy is mainly produced in the bulk region due to buoyancy effect, from where it is transported towards the walls, and dissipated in the boundary layers. The homogeneity of the bulk is also evident from the flatter profiles in Fig. 6.38(b).

The production of TKE due to buoyancy and its dissipation at different Ra are shown in Fig. 6.39. It is evident that P_B drops considerably with the increase in Ra. The peak production is observed in the bulk, and it scales with the Rayleigh number as $P_B^{max} = 0.19Ra^{-0.212}$. This

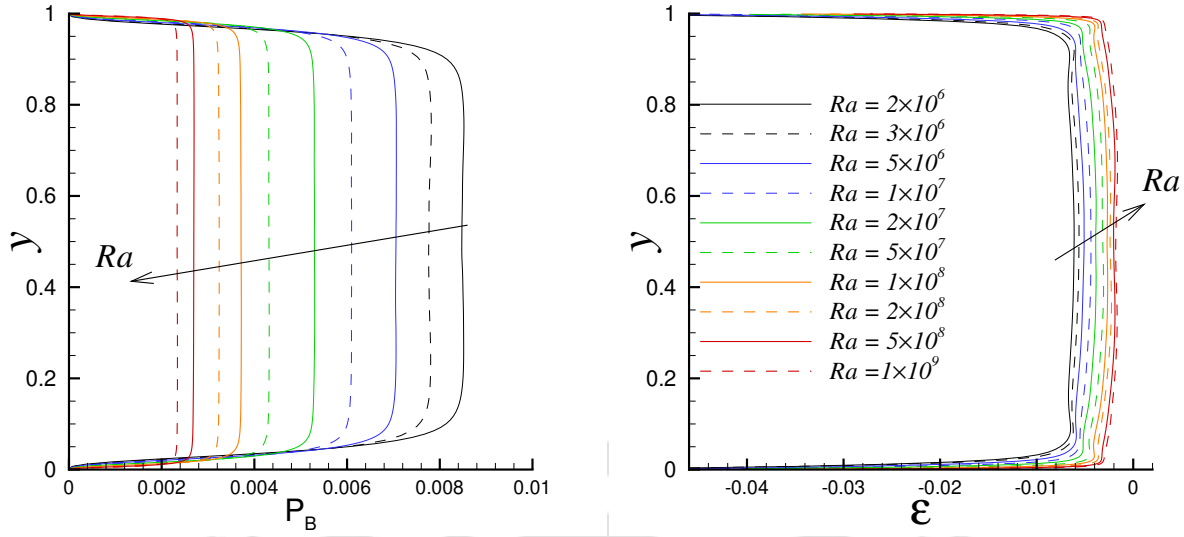

Figure 6.39: Vertical variation of buoyancy production and dissipation of TKE for different Ra. The arrows indicate the direction of increasing Rayleigh number.

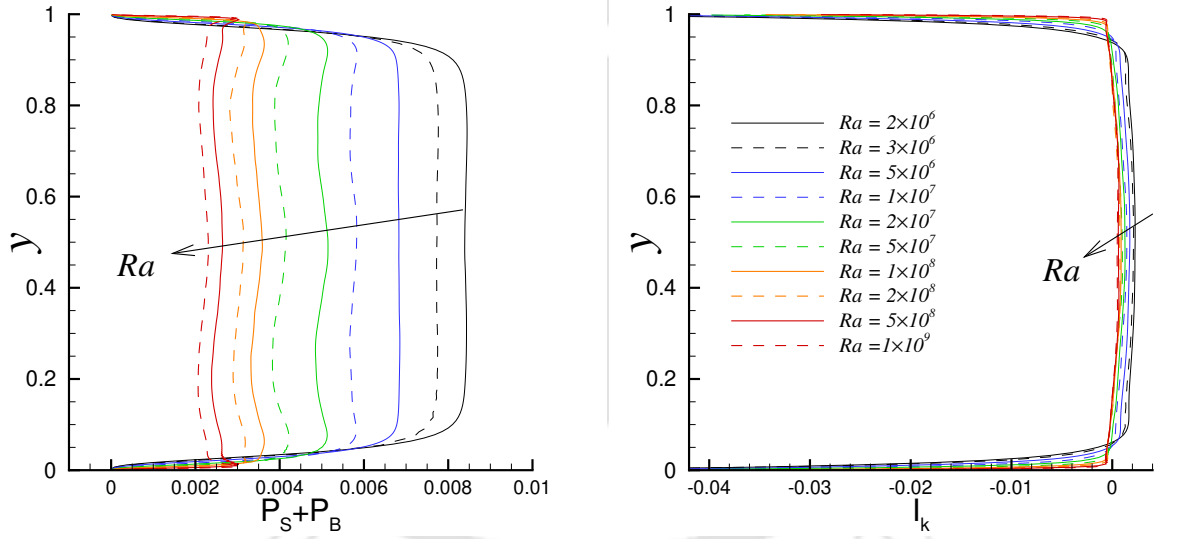

Figure 6.40: Vertical variation of total production and imbalance ($I_k = P_S + P_B + \epsilon$) of TKE for different Ra. The arrows indicate the direction of increasing Rayleigh number.

power-law behaviour is in good agreement with the recent observation by Chand *et al.* [270] in 2-D RBC. With increase in Ra, the dissipation drops in the bulk region and becomes concentrated near the isothermal plates. We observe that the dissipation in the bulk (at $y = 0.5H$) scales with Rayleigh number as $|\epsilon| = 0.11Ra^{-0.2}$. Both buoyancy production and dissipation assume nearly constant values outside the boundary layer which becomes thinner with the increase in Ra, as shown in Fig. 6.39.

The total production of TKE and the imbalance ($I_k = P_S + P_B + \epsilon$) are shown in Fig. 6.40.

Table 6.6: Columns from left to right represent Ra, volume averaged advection, transport, dissipation, shear production, buoyancy production, imbalance and production ratio for all the cases.

Ra	$< A_k >$	$< T_k >$	$< \epsilon >$	$< P_S >$	$< P_B >$	$< I_k >$	$< P_B/P_S >$
2×10^6	5.45×10^{-7}	-2.78×10^{-4}	-6.85×10^{-3}	-5.37×10^{-5}	7.78×10^{-3}	8.75×10^{-4}	1.45×10^{2}
3×10^6	8.67×10^{-7}	-6.14×10^{-5}	-6.81×10^{-3}	-3.35×10^{-5}	7.19×10^{-3}	3.51×10^{-4}	2.15×10^{2}
5×10^6	2.79×10^{-7}	-1.02×10^{-3}	-3.68×10^{-3}	-1.56×10^{-4}	6.57×10^{-3}	2.74×10^{-3}	4.23×10^{1}
1×10^7	3.80×10^{-7}	-1.47×10^{-3}	-1.55×10^{-3}	-2.70×10^{-4}	5.75×10^{-3}	3.92×10^{-3}	2.13×10^{1}
2×10^7	1.25×10^{-6}	-7.38×10^{-4}	-2.85×10^{-3}	-2.25×10^{-4}	5.04×10^{-3}	1.97×10^{-3}	2.24×10^{1}
5×10^7	6.64×10^{-7}	-7.11×10^{-4}	-2.07×10^{-3}	-2.49×10^{-4}	4.15×10^{-3}	1.83×10^{-3}	1.67×10^{1}
1×10^8	2.05×10^{-7}	-9.49×10^{-4}	-8.68×10^{-4}	-1.96×10^{-4}	3.59×10^{-3}	2.53×10^{-3}	1.84×10^{1}
2×10^8	3.48×10^{-7}	-6.93×10^{-4}	-1.13×10^{-3}	-1.83×10^{-4}	3.15×10^{-3}	1.84×10^{-3}	1.72×10^{1}
5×10^8	6.59×10^{-7}	-4.59×10^{-4}	-1.24×10^{-3}	-1.25×10^{-4}	2.64×10^{-3}	1.28×10^{-3}	2.11×10^{1}
1×10^9	3.85×10^{-7}	-4.53×10^{-4}	-9.41×10^{-4}	-1.12×10^{-4}	2.30×10^{-3}	1.25×10^{-3}	2.05×10^{1}

It is apparent that both production and imbalance of TKE decreases with increase in Ra. In the bulk region, an approximate balance between the total production and dissipation is observed as the imbalance is close to zero. The maximum imbalance is observed near the isothermal plates. Further, with increase in Ra, the imbalance in the bulk region reduces considerably as shown in Fig. 6.40. This suggests the lack of TKE transport in the bulk at higher Ra. It is apparent from Fig. 6.37 that as Rayleigh number increases, T_k approaches zero in the bulk region. The volume averaged contribution of different terms in the TKE equation, along with the imbalance and ratio of buoyancy to shear production are listed in Table 6.6. Note that the buoyancy production reduces, and the shear production increases with Ra. To quantify this, the ratio of buoyancy to shear production is calculated, which drops nearly ten manifolds across two extreme Ra, as seen in the last column. Hence, although the flow is conceivably driven by buoyancy, TKE production due to shear becomes increasingly important with the increase in Ra.

6.9 Summary

In this chapter, we have presented the statistics of thermal plumes in turbulent RBC inside a Cartesian box. The cell region is locally identified as plume or turbulent background based on the correlation between vertical velocity and temperature fluctuation ($v'\theta'$). We have shown that the volume fraction of the plume as well as background exhibit a power-law behaviour, where the plume fraction decreases, and the background fraction increases with Ra. Further, we have computed the dependence of the contribution of the plume and background regions

to the thermal dissipation rate and found that both contributions exhibit a decreasing trend with Ra. At cutoff $C_t = 0$, both the contributions become equal and approach the global scaling for higher Rayleigh numbers ($Ra \geq 10^8$). Comparisons with the theoretical predictions show that the dissipation from the plume region follows the GL scaling at lower cutoffs, while considerable deviations are observed in the background contribution. The PDFs of thermal dissipation rate deviate considerably from a log-normal distribution, while those of viscous dissipation approach log-normality at higher Ra. We observe that the PDFs of both viscous and thermal dissipation rates compare well with a stretched exponential function and their tails get more extended with the increase in Ra. The mean and variance of temperature clearly show the boundary layers and a near-homogeneous bulk region. With the increase in Ra, the boundary layer thickness decreases and bulk-homogeneity enhances. Turbulent kinetic energy budget unveils a transport-dissipation balance near the walls with buoyancy production nearly sustains turbulent fluctuations in the bulk region. Turbulent kinetic energy is mainly produced in the bulk region; from there it is transported towards the walls, and finally dissipated in the boundary layers.

7

Dynamics and statistics of large-scale circulation in turbulent Rayleigh-Bénard convection in a cubic cell

In this chapter, the characteristics and dynamics of large-scale circulation in turbulent Rayleigh-Bénard convection inside in a cubic cell is presented. The simulations are carried out for air ($Pr = 0.7$) with Rayleigh number ranging from $2 \times 10^6 \leq Ra \leq 10^9$. Using the Fourier mode analysis of time series data obtained from different probes placed at the mid vertical plane of the container, the strength, orientation, and associated dynamics of LSC are characterized. We observe that the plane containing LSC is generally aligned along one of the diagonals of the box accompanied by a four-roll structure in the other. In addition to the primary roll, two secondary corner-roll structures are also observed in the LSC plane which grow in size and destabilize the LSC resulting in partial ($\Delta\Phi_1 \approx \pi/2$) and complete ($\Delta\Phi_1 \approx \pi$) reversals. In addition to previously reported rotation-led reorientations, we also observe cessation events which are rare in cubic cells. We observe that at higher Ra, the strength of LSC increases and the corner-rolls reduce in size, which leads to the reduction in the occurrence of reorientations. By evaluating the kinetic energy budget, we discuss the energy transfer mechanism that connects the dynamics between the LSC and non-LSC planes. Further, the effect of LSC on the dissipation rates and the boundary layer thickness are also investigated.

7.1 Introduction

Large-scale circulation is a coherent structure of the flow in which the fluid particles ascend from one side of the wall and descend from the opposite side. As discussed in chapter 4, in cylindrical containers, the vertical plane containing LSC drifts in the azimuthal direction swiftly, called as the reorientations of LSC. Recall that such reorientations occur in two ways: (i) rotation-led, in which reorientation takes place without changing the amplitude of the LSC, and (ii) cessation-led, where the amplitude of LSC vanishes during the reorientation that typically leads to flow reversals [51, 56, 57].

Over the years, a number of works on LSC dynamics in 2D RBC have reported that corner-rolls play an important role in flow reversals. Here the LSC is confined to a single plane and the complex three-dimensional dynamics are absent [55, 271–273]. Sugiyama *et al.* [274] combined both numerical and experimental analysis to evaluate the LSC dynamics in 2D/quasi-2D systems for a range of Ra and Pr. They observed that the kinetic energy and size of the corner rolls grow with time as a result of plume detachment from the boundary layers, and finally they take over the main large-scale diagonal flow, thus resulting in reversal. Similar relevance of corner-rolls in flow reversals has been reported in many numerical and experimental studies in 2D/quasi-2D systems [72, 275–279]. However, in 3D, these phenomena are much more complex. It is now established that corner-rolls do exist in 3D systems also [65, 188], but unlike the 2D/quasi-2D counterparts, these rolls are not strictly confined to the LSC plane (for 3D systems). Resultantly, when fed with energy, the corner rolls need not essentially grow in diameter at the expense of shrinking the main LSC roll; rather, they can move or grow outside the LSC plane.

In box configuration, the plane containing LSC is generally known to align along one of the diagonals [63]. This is contrary to the cylindrical domain, where the LSC can settle in any diametrical plane owing to the azimuthal symmetry. A number of experimental studies have reported these dynamics of LSC in cylindrical geometry [45, 59]. However, the reorientation dynamics of LSC in cubic box configuration is a less explored area. Bai *at al.* [61] experimentally observed the switching of the plane containing LSC between the two diagonal directions of the cubic cell. The experiments were conducted with water ($Pr = 6.4$) at $Ra = 10^8$. They

demonstrated that the time intervals between switching of the orientation between the two corners of the box follow a Poisson distribution consistent with the low dimensional model for turbulence. The model consists of stochastic ordinary differential equations, which are derived as a function of boundary geometry from the Navier-Stokes equations [280]. The model considers the diagonal orientations of LSC as the two minimum states of a double-well potential and the switching between them as the stochastic crossing of a potential barrier. The switching was understood as a result of turbulent noise which assists the system in making the transition from one diagonal to another.

Foroozani *et al.* [65] used large eddy simulation to investigate the dynamics of the LSC for air inside a cubic box. They observed that while the plane of LSC is confined along one of the diagonals of the box, two counter-rotating vortices are developed consequently in the other diagonal plane. They reported that this flow structure is not static and the plane containing LSC reorients or switches between the two diagonal planes at non-periodic time intervals. The average switching rate between the diagonals was in good agreement with the experimental results of Bai *et al.* [61]. Further, they observed that these reorientations are a result of lateral rotation of the plane of LSC and some finite time is spent in a transition state between the two diagonals where the large-scale flow becomes parallel to the side walls (faces) of the container. They identified all reorientations as rotation-led [43, 54] and no such event of cessation-led reorientation [54–56] was observed. Further the observed reorientations were restricted to angular change of $\pi/4 \leq \Delta\phi \leq 3\pi/4$. Thus the so-called "complete reversals", where the LSC changes its azimuthal orientation by $\phi \approx \pi$ (mostly seen in cylindrical containers as discussed in chapter 4), were not observed in their LES study.

Although there are many experimental works that have investigated LSC and its dynamics over the years, comprehensive numerical studies in this direction are less, especially for turbulent flow inside a Cartesian box. In this chapter, using three-dimensional simulations, we aim to obtain more insights into the reorientation dynamics of LSC inside a cubic box. Some of the prime objectives are to probe for any possible event of complete reversals, to identify and characterize the reorientations as rotation-led or cessation-led using the same methodology adopted for cylindrical cells, and to evaluate and propose a mechanism of partial and complete flow reversals.

7.2 Identification of LSC and its dynamics

One of the striking features of turbulent RBC is the presence of LSC, which is a large-scale discernible convection pattern comprising thermal plumes sustained by its own dynamics, depending not only on the state of the turbulence but also on the geometric constraints. The instantaneous iso-surfaces of temperature for $Ra = 10^9$ are shown in Fig. 7.1(a), where hot plumes erupt from the boundary layer inducing cold plumes to sink along the opposite corner giving rise to a large-scale coherent structure, i.e., LSC. Previous numerical [65, 66] and experimental [61] studies have shown that in cubic enclosures, LSC has a tendency to align along the diagonal planes. Here the LSC is aligned along the diagonal plane labelled as d_1, shown in Fig. 7.1(b). On the other hand, owing to such a large spatial occupancy of the LSC, a four-roll structure [refer Fig. 7.1(c)] is seen confined along the other diagonal d_2. Note the apparent similarity in planar boundary layers and the stark difference in subsequent plume formation along the indicated diagonals. In the diagonal plane containing LSC, the hot and cold plumes primarily traverse along the opposite sides. However, in d_2, the hot plumes arise and cold plumes fall from both the sides, finally to intermix along the central region.

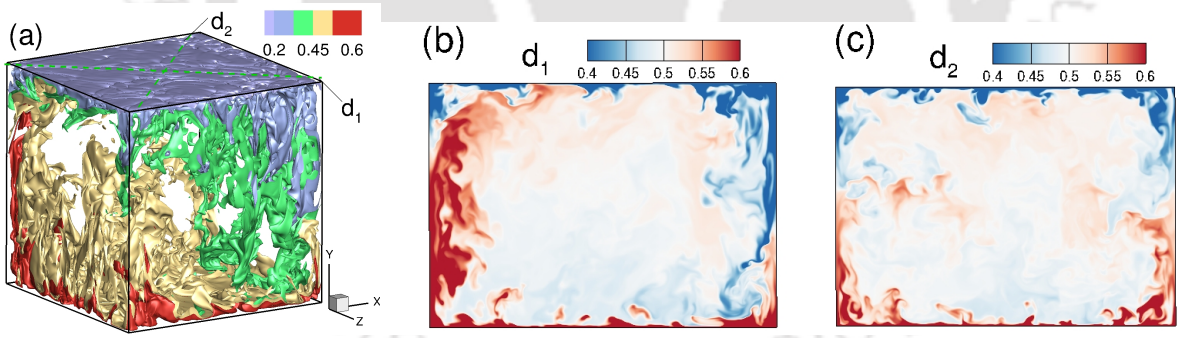

Figure 7.1: (a) Instantaneous temperature iso-surfaces indicating LSC oriented along the diagonal plane d_1 for $Ra = 10^9$. The contours of temperature in the diagonal planes (b) d_1 and (c) d_2.

In order to identify and characterize the LSC, time traces of vertical velocity are sampled at eight azimuthally equispaced stations, shown in Fig. 7.2(a), at horizontal mid-plane ($y = 0.5H$) located $0.1H$ distance from the lateral walls. The time signals from the probes located across the two diagonals are presented in frames (b) and (c), where red and blue windows indicate the alignment of LSC along the diagonal planes d_1 and d_2, respectively. The LSC identifies by opposite finite mean vertical velocity, i.e., anti-correlated signals along a diagonal. However,

in the other diagonal, the time signals show high variance fluctuations due to the intermixing of hot and cold plumes. Note that this finite mean of the signals switch sign intermittently as the anti-correlated and high-variance fluctuations swap between the diagonals, which indicates the reorientation of LSC. We observe that LSC remains confined in a particular diagonal plane for a longer duration for $Ra = 10^7$ than $Ra = 2 \times 10^6$ [see Figs. 7.2(b) and 7.2(c)], though it also becomes erratic. At even higher Rayleigh numbers reorientations are unlikely as it remains locked along a diagonal for a very long time. Further details on the reorientations of LSC are discussed in the subsequent sections.

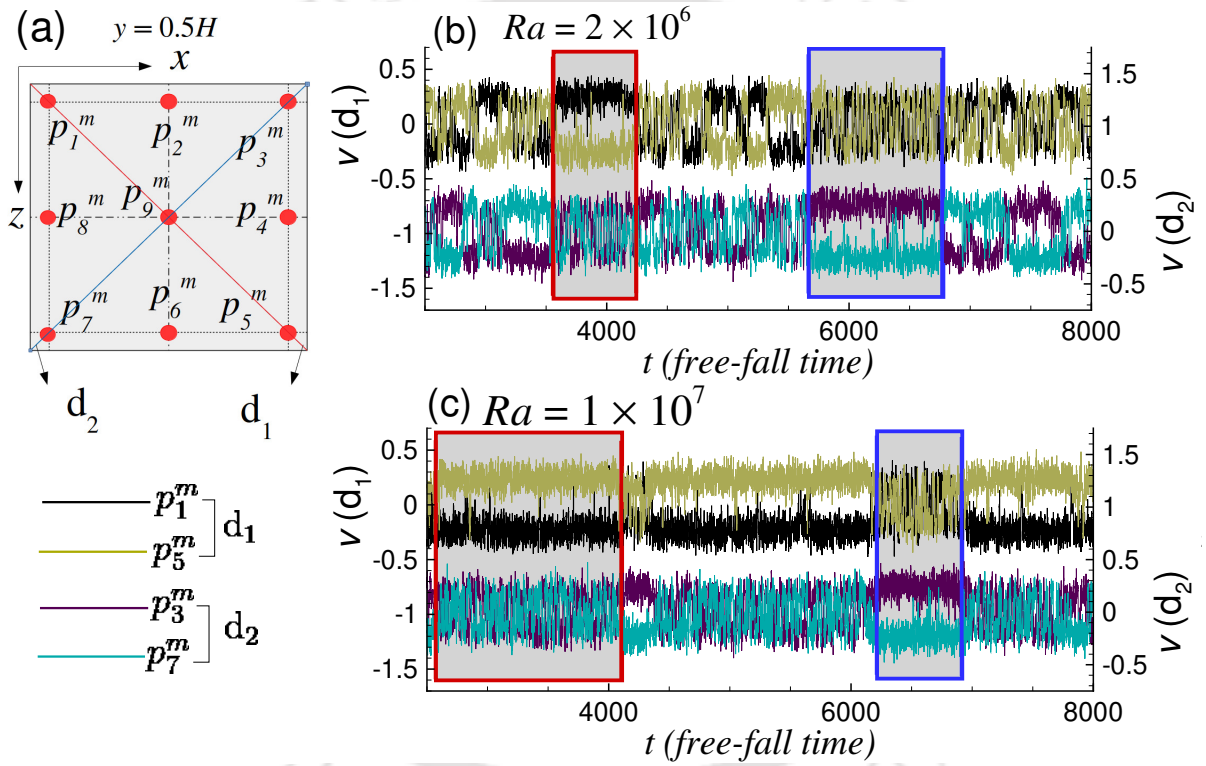

Figure 7.2: (a) Schematic diagram of the mid-plane ($y = 0.5H$) showing the location of numerical probes along with the diagonal planes. Time signals of vertical velocity at numerical probes placed across the two diagonals for (b) $Ra = 2 \times 10^6$ and (c) $Ra = 10^7$.

The time average vertical velocity and temperature along the above-mentioned azimuthally equispaced numerical probes are shown in Fig. 7.3, where the averaging is carried out within a time span over which LSC remains in a particular diagonal plane. The profile shows a cosine function with a single cycle spanning the entire (2π) domain, which confirms the presence of LSC, and is consistent with previous studies [43, 56, 162, 163]. This particular nature of the flow in the azimuthal direction can be associated with the dipolar structure and is generally identified as the signature of LSC. Recall that a similar dipolar nature of LSC was also observed

in the cylindrical domain, discussed in chapter 3. It is interesting to note that the domain shape does not affect the primary nature of the large-scale flow. We observe that with increase in Ra, magnitude of the temperature profile reduces considerably, which signifies the bulk stabilization at higher Ra. As the Rayleigh number increases, the imposed temperature difference across the top and bottom plates is accomplished almost entirely within the thermal boundary layer [140] (as discussed in the previous chapter). On the contrary, the velocity profile almost remains the same for all Ra. This points towards the loss in correlation between θ and v due to a better turbulent mixing at higher Ra.

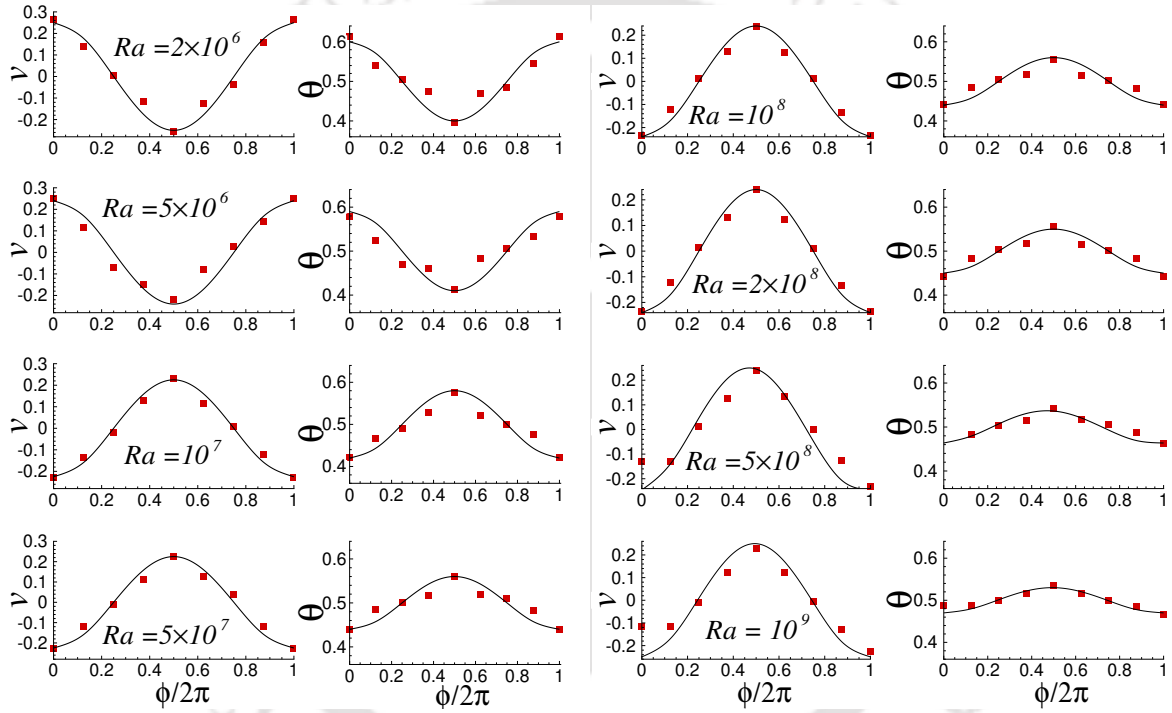

Figure 7.3: The temporal averaged vertical velocity and temperature profiles along the azimuthal direction for different Rayleigh numbers. The solid red line indicates a pure cosine fit.

To gain insight into the large-scale flow structure, the time-averaged velocity and temperature fields are evaluated. Here also the averaging is carried out within a time span during which LSC is aligned along a particular diagonal. Figure 7.4(a) shows a 3D perspective of the time-averaged streamlines colour coded with the magnitude of vertical velocity. The dotted line shows the diagonal plane d_1, along which the LSC is oriented, while the arrows indicate the direction of flow. The streamlines show that the hot fluid rises through the right side of the box and impinges on the top plate. The dark spot that appears on the top plate represents this collision of the hot plumes onto the top plate [see Fig. 7.4(b)]. Near the top plate, flow occurs

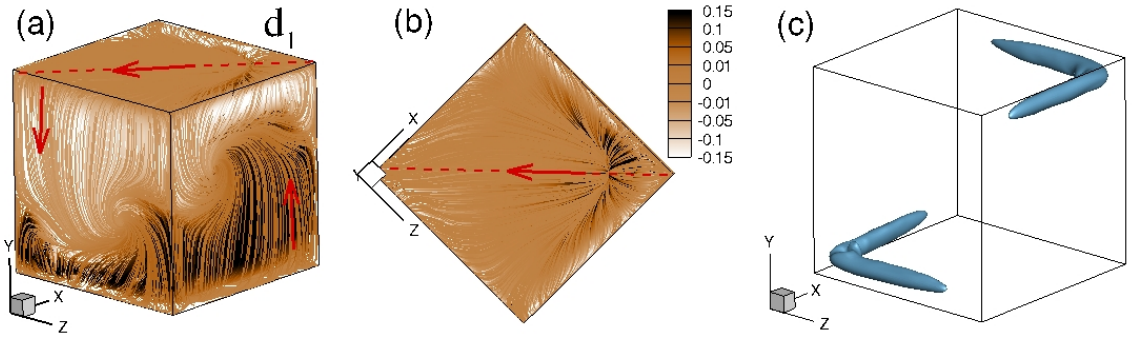

Figure 7.4: (a) Time-averaged velocity streamlines colour coded with the magnitude of vertical velocity for $Ra = 10^7$. (b) Top-view of the streamlines. (c) Q structures drawn at about 10% of the global maximum, showing the corner vortices that extend beyond the diagonal plane to form a "boomerang" shape.

horizontally (along the diagonal direction as indicated by the arrow). Similarly, the cold fluid descends along the left side and impinges on to the bottom plate. In the other diagonal plane, fluid rising and falling, respectively, from the bottom and top plates collide on to each other (converges) at mid-height (around $y = 0.5H$), and the flow occurs inwards from the corners to the interior part of the box.

Interestingly, as the hot fluid impinges on the top plate, a parcel of entrapped cold fluid is visible near the top-right corner of the cell, as shown in Fig. 7.4(a). This interaction between the ascending hot fluid and the cold plumes generated near the top plate results in a recirculating vortex. A similar phenomenon near the bottom plate gives rise to a corner vortex near the bottom left side of the box. It has been well established that these corner vortices play a crucial role in the stability and dynamics of LSC in 2D Rayleigh-Bénard flows [72, 274, 275]. However, in 3D RBC, such dynamics are less explored. To quantify these vortices, the second invariant of the velocity gradient tensor, Q (refer chapter 6), is shown in Fig. 7.4(c). Here $Q > 0$ represents regions of strong local rotation, i.e., high vortical motions. It is apparent from Fig. 7.4(c) that the corner vortices are not restricted to the LSC plane (as are destined in 2D RBC), but they extend along the adjacent faces sharing the diagonal plane to yield a "boomerang" shape. In Sec. 7.4, we provide a detailed discussion on the dynamics of these corner vortices and their role in the reorientations of LSC.

We observe that in cubic geometries LSC is generally aligned along a diagonal plane accompanied by a four-roll structure in the other. In the following analysis, we focus primarily on these planes. Time-averaged velocity vectors superimposed on the temperature contours at

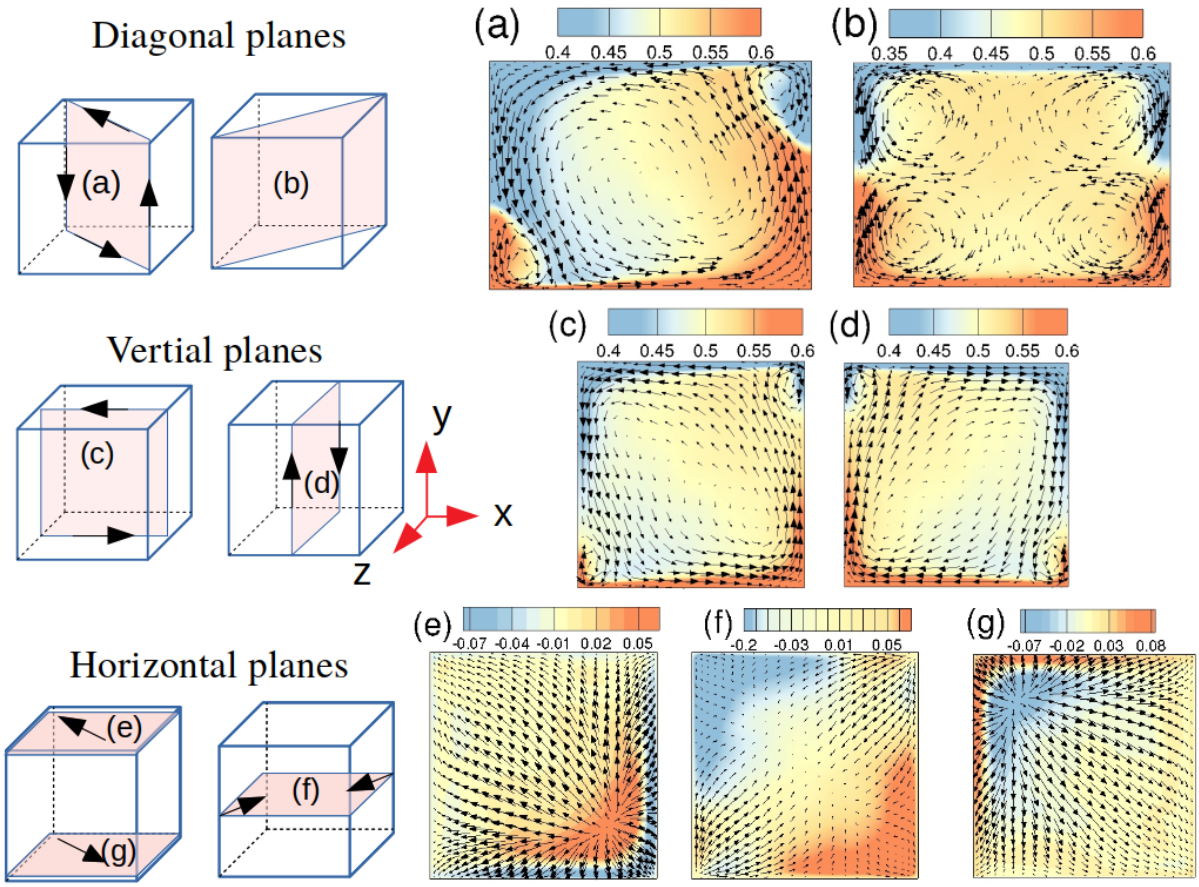

Figure 7.5: Velocity streamlines superimposed on the temperature contours at different planes of the box. (a) Diagonal plane containing LSC and (b) four-roll structure. The same at face-planes (c) $z = 0.5H$ and (d) $x = 0.5H$ and horizontal planes (e) $y = 0.97H$, (f) $y = 0.5H$, and (g) $y = 0.03H$ for $Ra = 10^7$. The left panel shows the schematic diagram of different planes and the arrows indicate the direction of flow in the corresponding planes.

different planes of the cube, for $Ra = 10^7$, are shown in Fig. 7.5, where the left panel shows the schematic location of these planes. In the diagonal plane containing LSC, a counter-clockwise (CCW) rotating primary roll (LSC) along with two corner rolls are observed [see Fig. 7.5(a)]. Note that the direction of circulation of the corner rolls is clockwise (CW), which is opposite to that of the LSC. In the opposite diagonal, two pairs of CW and CCW convective rolls are noticed, forming a four-roll structure, as shown in Fig. 7.5(b). The inflow from the corners to the interior part of the box at the mid-plane, as discussed previously, is apparent from this frame. The flow behaviour in the face planes is shown in Figs. 7.5(c) and 7.5(d), which also indicates a large-scale structure. Note that the presence of corner rolls is reflected even in the face planes, though their size has reduced substantially from the diagonal plane (with LSC). The horizontal planes near the top and bottom plates [see Figs. 7.5(e) and 7.5(g)] clearly show

the horizontal motion along the diagonal direction. The rising hot plumes hit the cold plate, from where the velocity vectors apparently diverge to horizontal directions, as shown in see Fig. 7.5(e). The flow primarily spreads horizontally towards the opposite corner (along the diagonal direction), while some fluid also moves to other corners. The horizontal flow towards the nearest corner results in a recirculating vortex discussed above. The red colour identifies (corresponding to hot fluid) the region of impingement of the hot plumes onto the top plate, where magnitude of the velocity vectors is nearly zero. Similar behaviour is observed near the bottom plate (blue coloured region), as shown in Fig. 7.5(g). In the horizontal mid-plane $y = 0.5H$, the presence of the four-roll structure and LSC across the two diagonals are clearly reflected [refer Fig. 7.5(f)]. Along the LSC diagonal flow occurs normal to the horizontal plane. However, in the opposite diagonal, the hot and cold fluid coming from the bottom and top plates, respectively, collide onto each other, resulting in a strong inflow towards the interior of the cell. These coherent structures are interconnected, and they change their orientations, resulting in reorientations. More discussions on which will be carried out in the following sections. After identifying the orientation of LSC and flow behaviour in different flow planes, we investigate the characteristics of LSC and its association with the heat transfer, dissipation rates, and boundary layer thickness.

7.3 Characterization of LSC

Recall that in chapters 3 and 4, we characterized LSC and its reorientations inside a cylindrical cells using Fourier mode decomposition. Similarly, we carry out the Fourier analysis of the vertical velocity recorded along the azimuthal direction at the mid-vertical plane ($y = 0.5H$). Fourier transform of the velocity signal is defined as

$$\hat{u}_k = \sum_{j=1}^{N} u_j e^{-i2\pi kj/N}, \tag{7.1}$$

where u_j is the velocity signal from the previously mentioned $N(= 8)$ data points [see figure 7.2(a)] and $\hat{u_k}$ is the k^{th} Fourier mode. Based on the formalism proposed by Kunnen *et al.* [128], Weiss and Ahlers [201] and Xi *et al.* [156], we have characterized the LSC using the frac-

tion of energy contained in the k^{th} mode E_k/E_{tot}, where $E_k = |\hat{u}_k|^2$ and $E_{tot} = \sum_{k=1}^{N/2} E_k$. The evidence of LSC is often ascertained from the energy fraction of first Fourier mode (E_1/E_{tot}). Figure 7.6(a) shows the variation of the energy fraction of first three Fourier modes with Ra. It is evident that energy content of the first mode E_1/E_{tot} increases steadily with Ra only to reach 0.8 asymptotically at $Ra \approx 2 \times 10^8$ while influence of all the higher modes are on the wane.

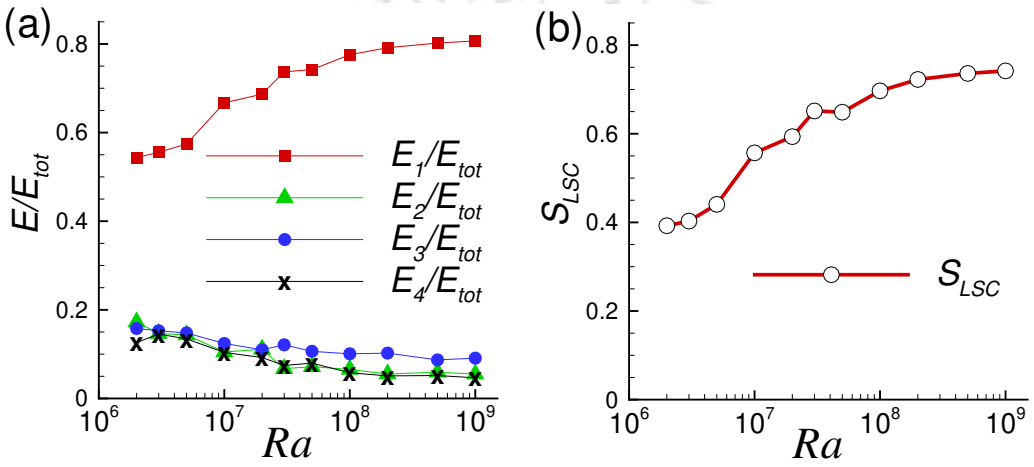

Figure 7.6: The variation of (a) energy fraction of first four Fourier modes (E_k/E_{tot}) and (b) the strength of LSC (S_{LSC}) with Ra.

Further, we compute the strength of LSC [202, 281], S_{LSC}, defined as

$$S_{LSC} = Max\left[\left(\frac{E_1}{E_{tot}} - \frac{1}{N_s}\right)/\left(1 - \frac{1}{N_s}\right), 0\right] \tag{7.2}$$

where $N_s = N/2$ and N is the total number of probes in the azimuthal direction. The value of S_{LSC} lies between 0 and 1. The strength close to unity indicates that most of the energy is contained in the first Fourier mode, i.e., $E_1/E_{tot} \approx 1$ and the azimuthal vertical velocity profile is close to a cosine fit, thus indicating LSC. On the other hand, a value near to zero implies that the energy fraction of first Fourier mode is smaller ($E_1/E_{tot} << 1$), in effect most of the energy is contained in the higher modes and the flow behaviour is far from LSC structure. Similar to the energy fraction, the strength of LSC also increases with the increase in Ra and settles at a somewhat smaller value ($S_{LSC} \approx 0.75$) as shown in Fig. 7.6(b). Thus, we observe that with the increase in Ra, the LSC structure becomes more prominent, and the higher flow modes become weaker, which effectively reduces the frequency of flow reversals. This indicates that

high-resolution studies of LSC are not practically viable as at higher Ra, a prohibitively long time integration is required.

7.3.1 Vertical velocity profiles

The time-averaged vertical velocity at the mid-height ($y = 0.5H$) along the LSC and non-LSC planes are shown in Fig. 7.7(a). It is apparent that the flow is dominant in the diagonal plane containing LSC and nominal in the opposite diagonal. Further, the wall-bounded nature of the flow is evident from Fig. 7.7(a). The maximum velocity is observed near the lateral walls and is negligibly small near the bulk region. Figure 7.7(b) shows the average velocity profile along the LSC diagonal compared with that observed in the LES study by Foroozani *et al.* [65]. The profiles match well in the bulk region, but the LES under predicts the peak velocity near the walls, which might be due to insufficient near-wall resolution.

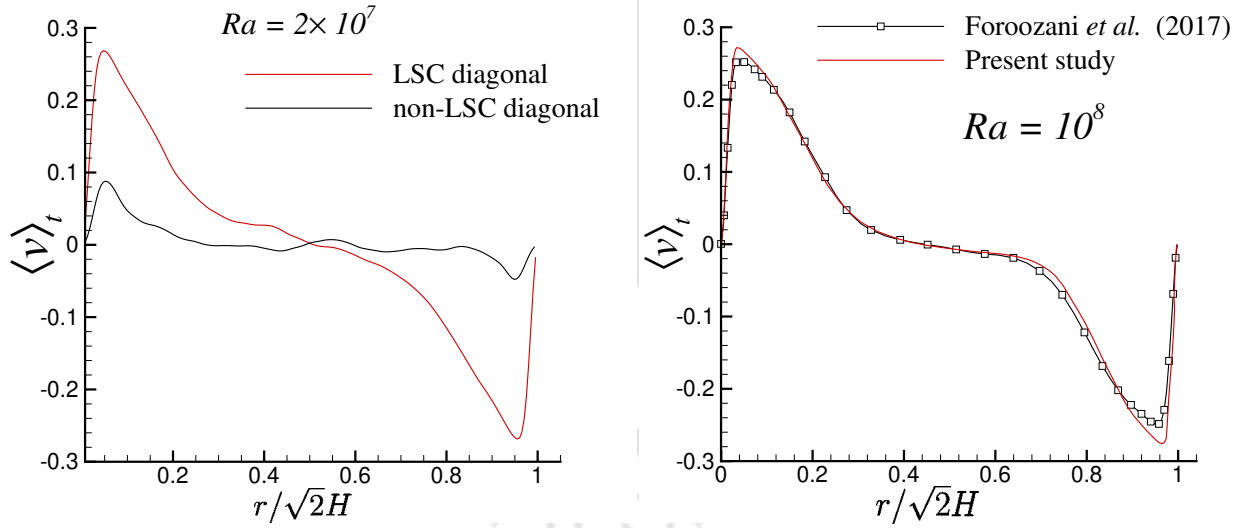

Figure 7.7: (a) The temporal averaged vertical velocity profile along the LSC and non-LSC planes at mid-height $y = 0.5H$ for $Ra = 2 \times 10^7$. (b) Time-averaged vertical velocity along the LSC plane compared with the LES study by Foroozani *et al.* [65].

The time-averaged velocity profile along the LSC plane for different Ra is shown in Fig. 7.8. With the increase in Ra, the peak velocity shifts towards the corners as the flow become more wall-bounded. This is because, at higher Ra, the LSC becomes more "squarish" in shape with unidirectional motion near the horizontal and vertical walls. Detailed discussion on the change in flow behaviour of LSC with increase in Ra is carried out in the following sections

(refer Fig. 7.21). Further, as the LSC becomes more wall-bounded, the bulk region becomes homogeneous, which is indicated by the flat vertical velocity profiles with $v \approx 0$ in the bulk. The maximum value of the vertical velocity increases with Ra, which also indicates the rise in the strength of the large-scale flow. This is in good agreement with the quantitative description defined using the strength of LSC, discussed previously (see Fig. 7.6), which also increases with increase in Rayleigh number.

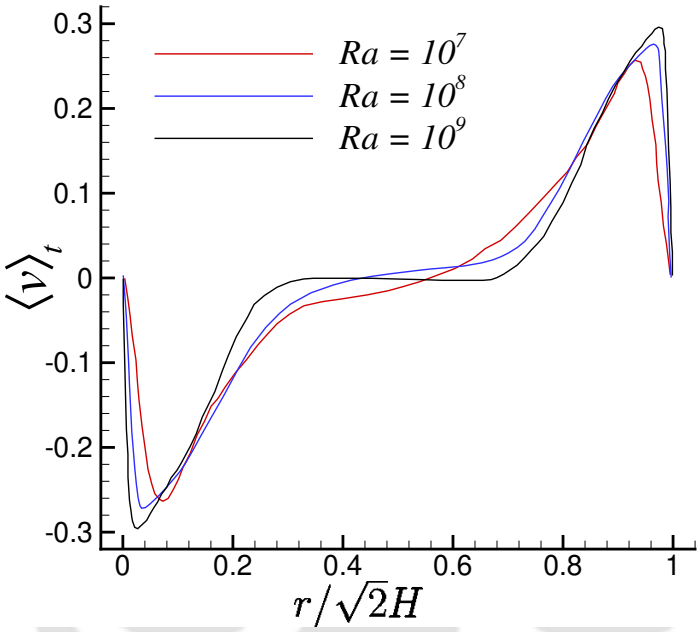

Figure 7.8: The temporal averaged vertical velocity profile along the LSC plane at mid-height $y = 0.5H$ for $Ra = 2 \times 10^7$, 10^8 and 10^9. With increase in Ra, the peak velocity increases and shifts towards the corners of the box.

7.3.2 Effect of LSC on the boundary layer

As the presence and evolution of spatial boundary layer is central to the classical 1/3 law based heat transfer regime, effect of the LSC on the boundary layers is in order [69, 203]. At this point, we are interested to see how the boundary layer thickness varies along and perpendicular to the plane containing LSC. Figure 7.9(a) shows instantaneous temperature iso-surfaces for $Ra = 10^7$ indicating LSC structure, where the dashed line indicates the diagonal plane containing LSC. The time-averaged flow structure for the same is shown in Fig. 7.9(b), which is used to compute the thermal boundary layer thickness. Here averaging is performed within a time-span

at which LSC persists along a particular diagonal plane. The thermal boundary layer thickness is computed by the slope method, as discussed in chapter 3. The contours of boundary layer thickness at the bottom and top are shown in Figs. 7.9(c) and 7.9(d), respectively. Close to the bottom plate, the thermal boundary layer is thicker near the region where hot plumes rise and is thinner near the opposite side of the lateral wall where the cold plumes plunge into the boundary layer, as shown in Fig. 7.9(c). A similar observation is made near the top plate [Fig. 7.9(d)].

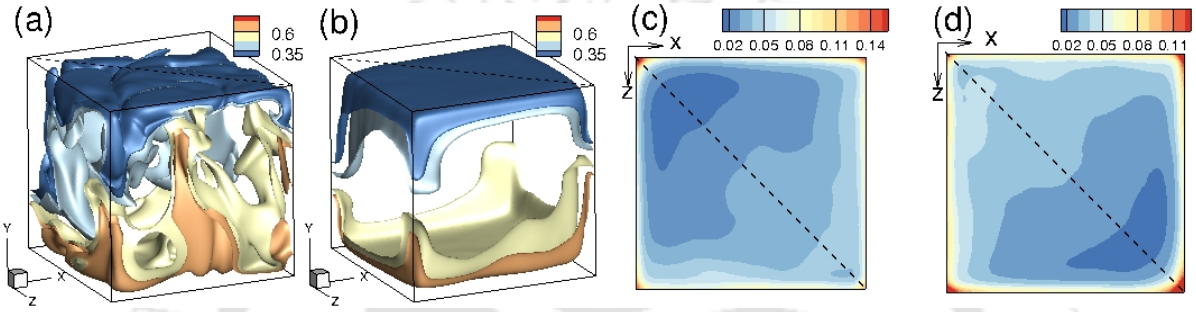

Figure 7.9: (a) Instantaneous temperature iso-surfaces for $Ra = 10^7$ indicating LSC. The dotted lines indicate the diagonal plane containing LSC. (b) Time averaged (within a span of LSC) temperature iso-surfaces for the same configuration. The contours of boundary layer thickness at the (c) bottom and (d) top.

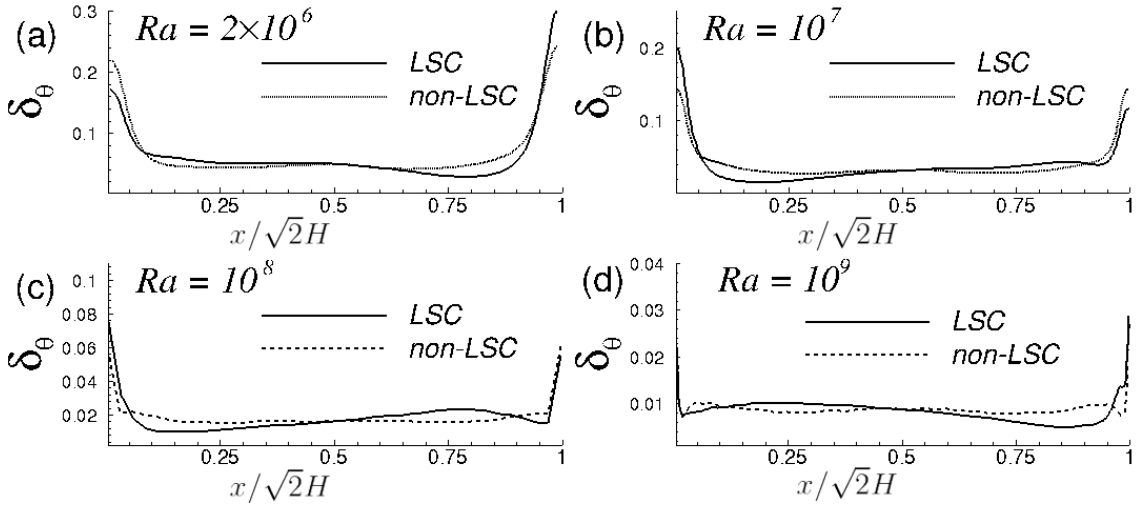

Figure 7.10: Average thermal boundary layer thickness along the LSC plane and non-LSC plane for (a) $Ra = 2 \times 10^6$, (b) $Ra = 10^7$, (c) $Ra = 10^8$, and (d) $Ra = 10^9$. Time averaging is carried out within a time span during which LSC persists along a particular diagonal.

The variation of δ_θ along the LSC and non-LSC planes are shown in Fig. 7.10 for different Ra. Note that along the non-LSC plane, the boundary layer thickness varies almost symmetrically. However, along the LSC plane, δ_θ shows an asymmetric trend, as it is thicker at one

side and thinner near the opposite side of the lateral wall. These observations are consistent with the time traces of the vertical velocity discussed in the previous subsection (refer Fig. 7.2), wherein, the signal shows high variance fluctuation along the transverse direction of LSC with zero-mean value, and fluctuation about finite mean value along the LSC direction. The fluctuation about the finite-mean value along LSC direction can be associated with asymmetric behaviour of boundary layer width near the lateral wall. Recall that similar dependence of the orientation of LSC on the spatial structure of the thermal boundary layer thickness was observed in the cylindrical domain also, discussed in chapter 4.

7.3.3 Effect of LSC on the thermal dissipation rate

Here we analyze the thermal dissipation rate in connection with the orientation of LSC. The contours of thermal dissipation rate in the diagonal planes d_1 and d_2 are shown in Figs. 7.11(a) and 7.11(b), respectively. As the magnitude of dissipation is much higher near the horizontal plates compared to the bulk region, the contours are shown in logarithmic dissipation rate for better visualization. The LSC is aligned along d_1, where the direction of circulation is indicated by the dashed line. Note that though maximum dissipation occurs near the top and bottom plates (inside the boundary layers), significant amount of dissipation is apparent near the regions where the LSC interacts with the corner-rolls. The nature of the thermal plumes (hot or cold) and the flow direction of the corner rolls are always opposite to that of the primary large-scale roll. As a result, the regions where these corner vortices interact with the primary large-scale flow are associated with high gradients of temperature and hence, generates high thermal dissipation rate. Similarly, in the other diagonal plane, dissipation becomes considerable at the mid-plane, where the hot and cold plumes collide onto each other. This is more evident from the horizontal mid-plane $y = 0.5H$, as shown in Figs. 7.11(d), where the azimuthal orientation of LSC is represented by the dashed line. Here the dissipation is negligible along the LSC region (along the dashed line) due to nearly uniform motion, while significant dissipation is noted near the four-roll structure due to the intermixing of hot and cold plumes. The contours of the thermal dissipation rate near the top and bottom plates are shown in Figs. 7.11(c) and 7.11(e), respectively. We observe that the dissipation rate varies significantly along the direction of LSC. The thermal dissipation is maximum in the regions

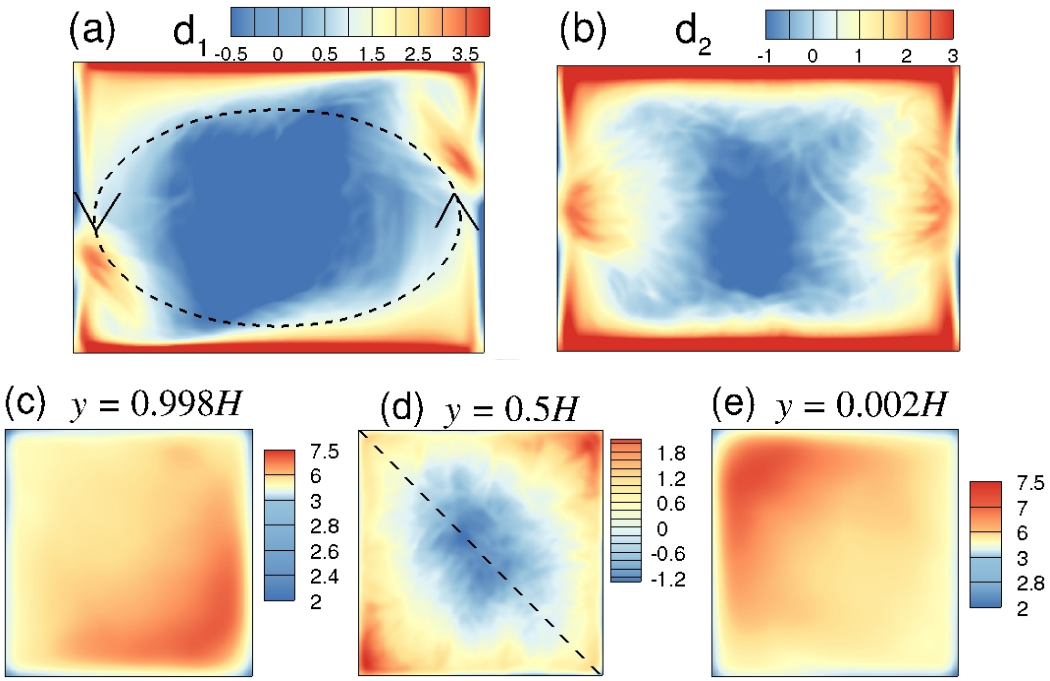

Figure 7.11: Contours of logarithm of thermal dissipation rate at the diagonal planes (a) containing LSC and (b) four-roll structure, and three horizontal planes, (c) $y = 0.998H$ (close to top plate), (d) $y = 0.5H$ (mid-plane), and (e) $y = 0.002H$ (close to bottom plate), for $Ra = 10^7$. The dotted lines indicate the alignment of LSC.

where the plumes collide with the boundary layer. For example, in Fig. 7.11(c), the red colour indicate regions associated with high dissipation rate where the hot plumes collide on to the top plate. Similar high-amplitude dissipation events associated with the collision of thermal plumes were observed by Schumacher and Scheel [204].

7.4 Reorientations of LSC

Previous numerical and experimental works have shown that in cubic domain, LSC has four preferable orientations: along the two diagonals with clockwise and anti-clockwise circulation [65, 66, 282]. These states switch between one another by lateral shift, which is a multiple of $\pi/2$. In most of these studies the reorientations were predominantly due to the rotation of the plane containing LSC, i.e., rotation-led reorientation [61, 65, 282]. It is interesting to note that the cessation-led reorientations that are observed in cylindrical domains are rarely seen in cubic configuration. Further, previous studies indicate that the partial reversal of LSC, i.e., reorientation of one diagonal plane to another is a more probable event than the complete reversal of

the LSC plane. Vasiliev *et al.* [283] proposed a new approach to identify the reorientations of LSC, where instead of the conventional single-roll along the diagonal plane, they introduced a superposition of a pair of large-scale orthogonal (to the faces) two-dimensional rolls. During the reorientation of LSC from one diagonal to another, one of these planar LSCs (PLSCs) stops and reappears in the same or opposite direction, and the mechanism is called "planar cessation-led reversal." Additionally, they observed complete reversals of LSC where both the PLSCs reverse the direction of flow and as a result, the LSC remains in a single diagonal, but the direction of circulation changes. This is identified as a complete flow reversal where the LSC drifts azimuthally by $\Delta\Phi \approx \pi$. In the present study also, we observe similar large-scale convection rolls along the faces [see Figs. 7.5(c) and 7.5(d)] with the direction of circulation associated with the LSC along the diagonal plane. The different possible orientations of LSC in the diagonal planes along with the circulation direction are shown schematically in Fig. 7.12. Here different colour shades are used to identify the two diagonal planes of the box, while arrows indicate the direction of the large-scale flow in the corresponding plane. A and B shows the orientations along the diagonal plane d_1 with CW and CCW rotation, respectively, while C and D shows the alignment along the opposite diagonal d_2.

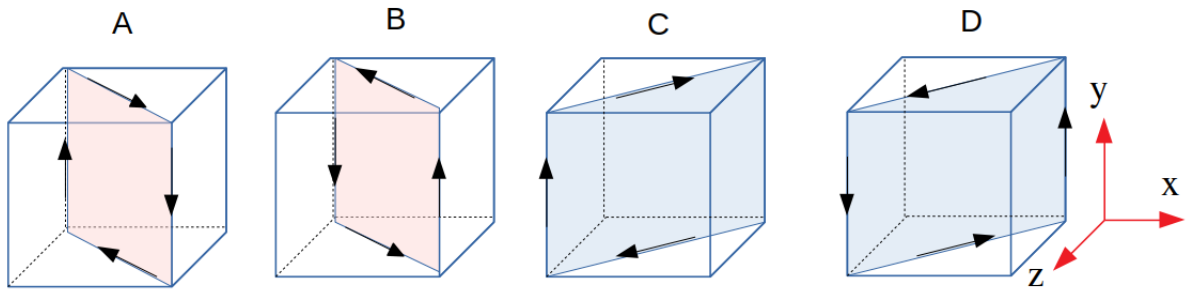

Figure 7.12: Schematic representation of four possible orientations of LSC in the diagonal planes with CW and CCW rotation.

The existence and transition of LSC between these states are examined using the global angular momentum ($\boldsymbol{L} = \boldsymbol{r_0} \times \boldsymbol{u}$) about the center of the cell, where $\boldsymbol{r_0} = (0.5, 0.5, 0.5)$. In Fig. 7.13, L_x, L_y and L_z are the components of angular momentum in x, y, and z directions, respectively. The top panel shows the time signals of vertical velocity from probes located at the diagonal planes, where A, B, and C correspond to the respective flow states shown in Fig. 7.12 with the same notations. The locations of the numerical probes are shown in Fig. 7.2(a). Note that the vertical component (L_y) is essentially zero suggesting the mean wind is always aligned

along the vertical planes. However, the components L_x and L_z show quasi-stable periods with fluctuations around mean value close to ± 0.25 and switch their signs at irregular intervals of time. Such changes in the magnitudes of L_x and L_z are associated with the reorientation of LSC. A change in sign of any one of these components corresponds to the lateral shift of LSC by $\pi/2$, i.e., a partial reversal. In Fig. 7.13 the switching from C to A (at $t \approx 8500$, identified by the red window) and B to C (at $t \approx 9100$) show such reorientations. Note that here the LSC shifts from one diagonal plane to the other. However, the simultaneous change in the sign of both L_x and L_z indicates a complete reversal, where the LSC remains in the same plane while the direction of circulation reverses. In Fig. 7.13, the reorientation from A to B at $t \approx 8800$, marked by the blue window, represents a complete reversal. Note that complete reversals are rarely observed.

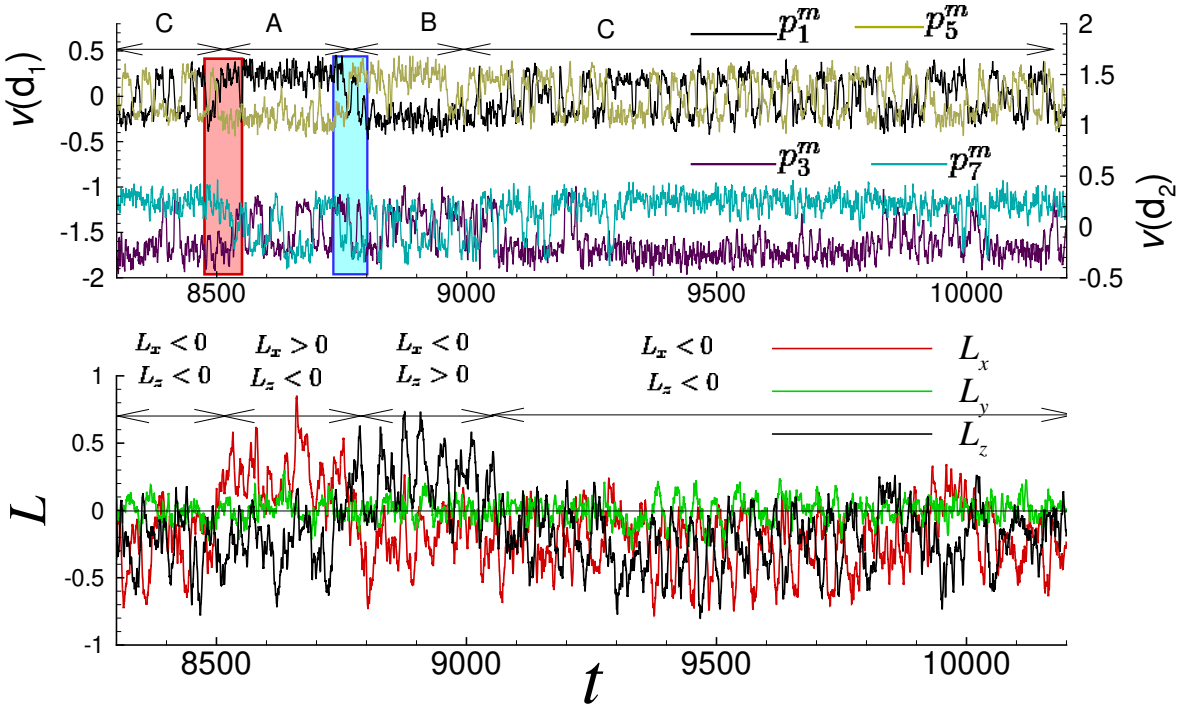

Figure 7.13: Top panel: The time signals of vertical velocity from probes located in the diagonal planes. The notations A, B, and C correspond to the different orientations of LSC, which are shown in Fig. 7.12. Bottom panel: The components of global angular momentum about the centre of the flow domain.

Next, we characterize the reorientations based on the formalism used in chapter 4, which dealt with convection inside a cylindrical cell. Reorientations are generally quantified using the amplitude $A_k = |\hat{u_k}|$ and phase $\Phi_k = \tan^{-1}(\mathbf{Im}\ \hat{u_k}/\mathbf{Re}\ \hat{u_k})$ of the k-th Fourier mode. During

cessation-led reorientations the amplitude of the first Fourier mode (A_1) almost drops to zero while in rotation-led ones the LSC rotates azimuthally without significant change in A_1 [54]. Although these events are well explored experimentally in a cylindrical cell [56, 206], their occurrence in a Cartesian box is rare.

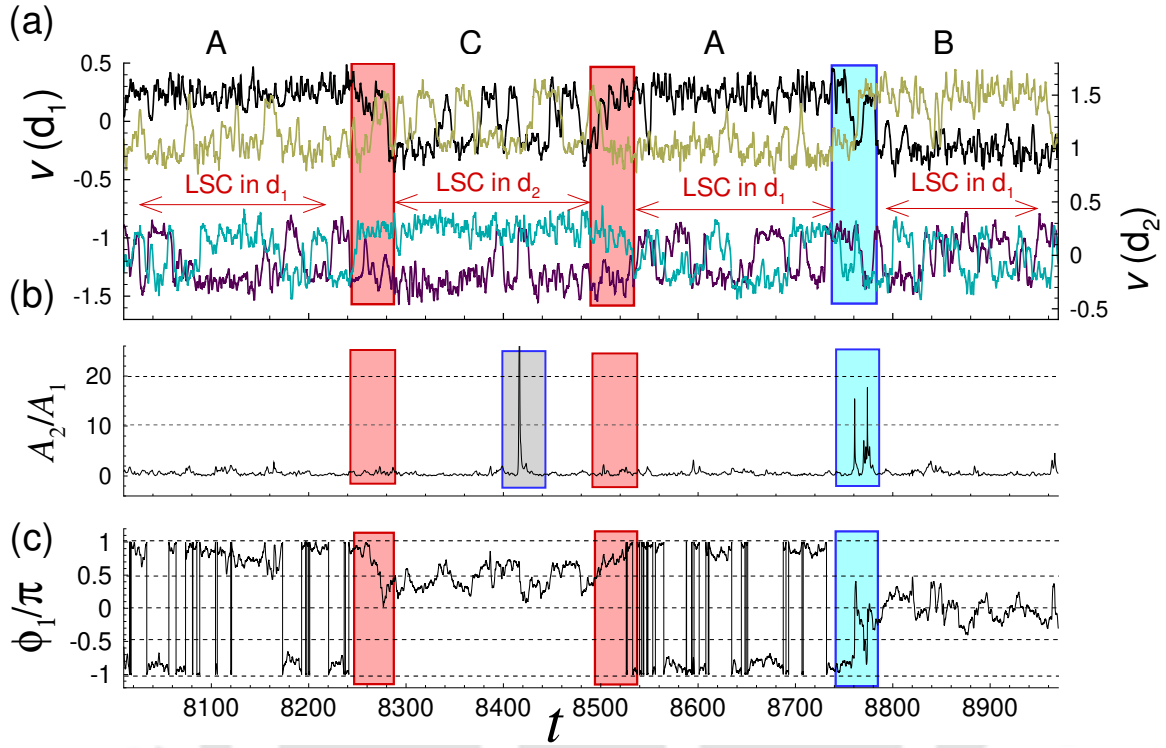

Figure 7.14: Time signals of (a) vertical velocity, (b) amplitude fraction A_2/A_1, and (c) phase of the first Fourier mode Φ_1 for $Ra = 2 \times 10^6$. The notations A, B, and C correspond to the different orientations of LSC, shown in Fig. 7.12.

Time evolution of vertical velocity, amplitude ratio of the first two Fourier modes (A_2/A_1), and phase of the first Fourier mode (Φ_1) are shown in Fig. 7.14. The corresponding orientations of LSC (following the notations in Fig. 7.12) are also shown in the top panel. Note that A and B are orientations along the diagonal d_1, while C represents the alignment along d_2, as discussed earlier. Initially LSC is observed along d_1 where it stays for about $t \approx 230$ time units. Then it switches to d_2 (see red windows) accompanied by a change in phase $\Delta\Phi_1 \approx \pi/2$ [see frame (c)] which represents a partial reversal (A to C). Note that the amplitude fraction remains negligibly small [frame (b)] during this event, and thus it is identified as a rotation-led reorientation. A similar occurrence is observed at $t \approx 8515$ where the LSC switches back from d_2 to d_1 (C to A). However, at $t \approx 8760$, a different reorientation is observed as A_2/A_1 shows a spike accompanied with a phase change of $\Delta\Phi_1 \approx \pi$ (blue window). Here, the amplitude

of the first Fourier mode drops considerably ($A_1 \rightarrow 0$) and that of the second rises, and is identified as cessation-led reorientation. Note, though LSC persists along d_1 before and after the reorientation, the sense of rotation reverses with a phase shift of $\Delta\Phi_1 \approx \pi$, resulting in a complete reversal (A to B). We have observed many such partial and complete reversals for $Ra = 2 \times 10^6$, while for higher Ra the reversals are restricted to partial ones only, as seen Fig. 7.15.

Interestingly, at $t \approx 8410$, a similar spike in the amplitude fraction is observed [see Fig. 7.14 (b)], but the time signals show that LSC persists in d_2 without any change in orientation. Here the LSC ceases and restarts in the same diagonal with the same sense of rotation resulting in no effective change in angular measure, $\Delta\Phi_1 \approx 0$. This is identified as a cessation, but not as a reorientation since there is no change in the orientation of LSC. Note that similar event was observed in the cylindrical domain also, which is discussed in chapter 4. In all previous studies of LSC dynamics in cubic configuration, the reorientations were predominantly rotation-led [61, 65, 282]. It is interesting to note that the cessation-led reorientations that are observed in cylindrical domains are rarely seen in cubic configuration. In the present study, we observe several cessations resulting in partial, complete or no reversal at $Ra = 2 \times 10^6$, while for $Ra = 10^7$ very few cessation events are observed (see Figs. 7.15 and 7.16).

The complete time histories of vertical velocity, amplitude fraction of the Fourier modes A_2/A_1, and phase of the first mode Φ_1, up to 8000 free-fall time units for $Ra = 10^7$ and 2×10^6 are shown in Figs. 7.15 and 7.16. Note that the vertical velocity signals are extracted from probes located across the diagonals (p_1^m, p_5^m, p_3^m and p_7^m) and faces (p_2^m, p_6^m, p_4^m and p_8^m). The locations of the numerical probes are shown at the bottom right corner for reference. Similar to the diagonals, the probes located at the faces also show anti-correlated behaviour [frame (b)], although their mean value is comparatively less than the signals from the diagonal planes. This is in accordance with the single-roll structures observed in the face planes, as shown in Fig. 7.5. Similar flow behaviour was observed by Valencia *et al.* [282], where they identified these single-roll structures as planar LSCs or PLSCs. Note that both the faces always show a mean flow, irrespective of the alignment of LSC in any of the diagonal planes. During a partial reversal, as the LSC drifts from one diagonal plane to the another, the flow reverses in one of the faces, while in the other it remains the same. For $Ra = 10^7$, only partial reversals are observed (see Fig. 7.15), where the phase changes by $\Delta\Phi_1 \approx \pi/2$ [see frame (d)]. Effectively, the flow

behaviour in face f_1 remains the same during the entire simulation run, while that in f_2 changes accordingly, as shown in frame (b). For $Ra = 2 \times 10^6$, both partial and complete reversals are realized, as shown in Fig. 7.16. For instance, at $t \approx 6800$ and $t \approx 7000$, complete reversals are observed, where the LSC remains in diagonal plane d_2, but its direction of circulation changes and thus resulting in an azimuthal change of $\Delta\Phi_1 \approx \pi$. Note that during this event, the mean flow switches in both the faces, while high variance fluctuations persist in the diagonal plane d_1.

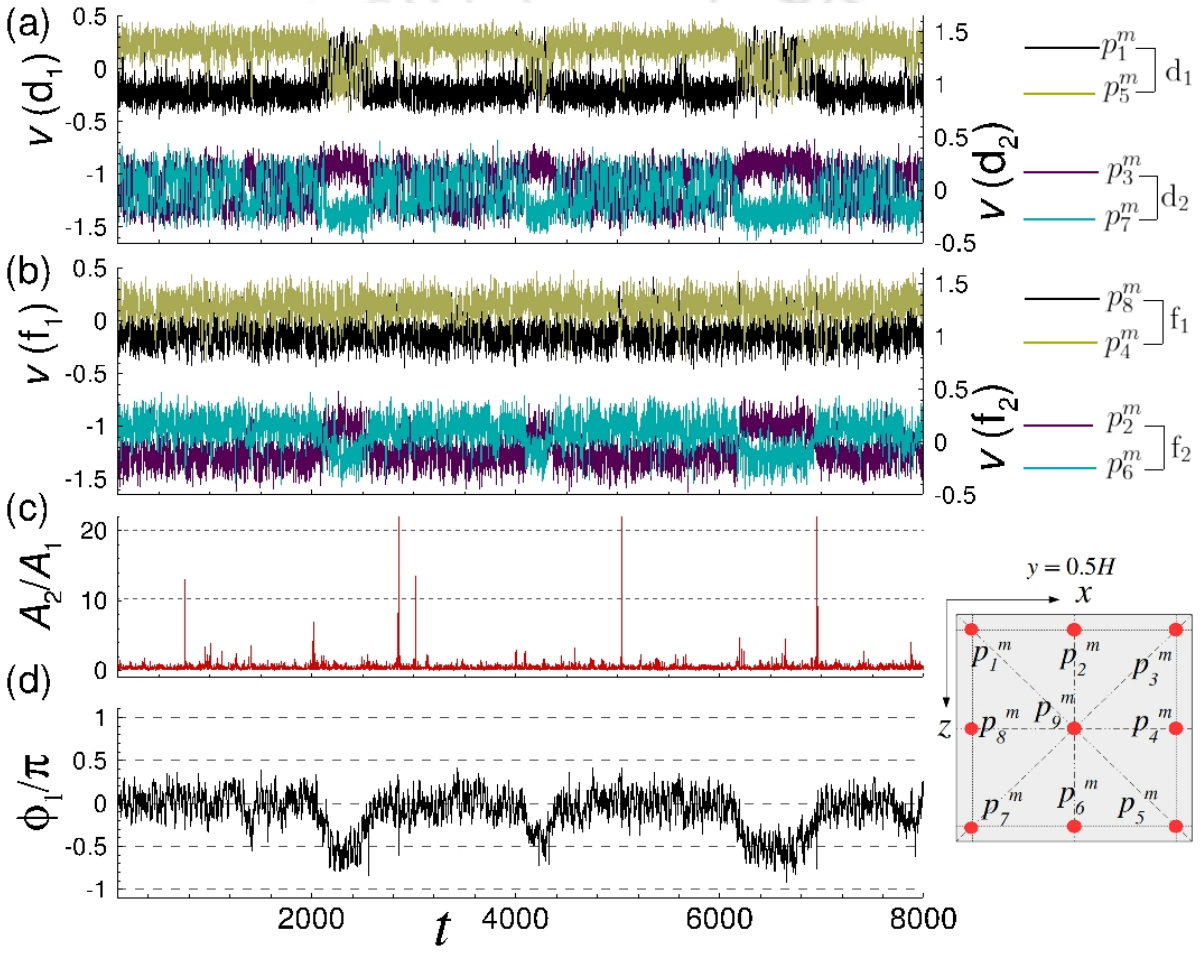

Figure 7.15: Time signals of (a,b) vertical velocity along the two diagonals and faces, (c) amplitude fraction A_2/A_1, and (d) phase of the first Fourier mode for $Ra = 10^7$. The location of the numerical probes is shown at the bottom right corner.

Dynamics and interplay between the Fourier modes can be evaluated by computing cross-correlation between them. Figure 7.17 shows correlations between the first and second mode, $C_{1,2}$. At lower Ra, the first and second modes are negatively correlated and as the Rayleigh number increases they become nearly uncorrelated. This suggests that for lower Ra, a drop in

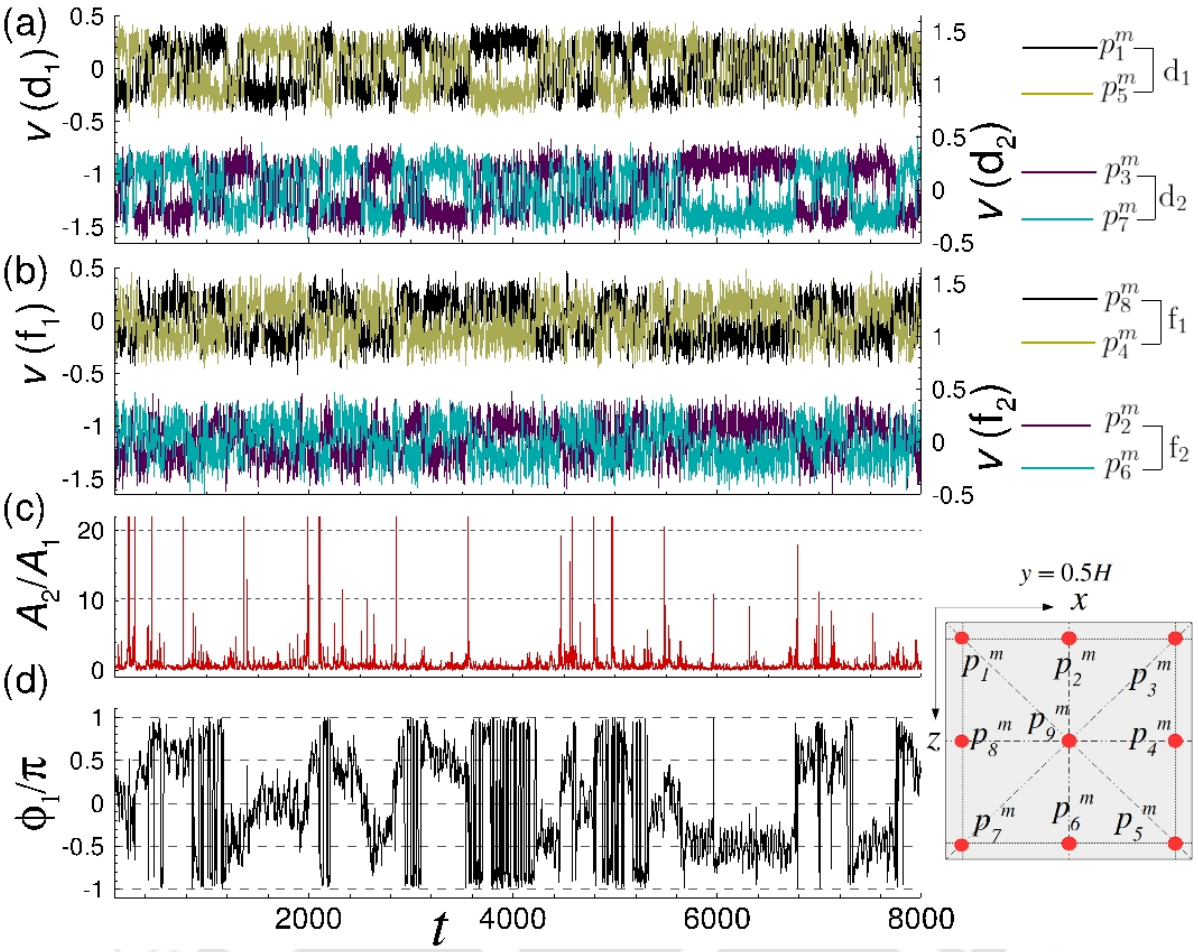

Figure 7.16: Time signals of (a,b) vertical velocity along the diagonals and faces, (c) amplitude fraction A_2/A_1, and (d) phase of the first Fourier mode for $Ra = 2 \times 10^6$. The location of the numerical probes is shown at the bottom right corner.

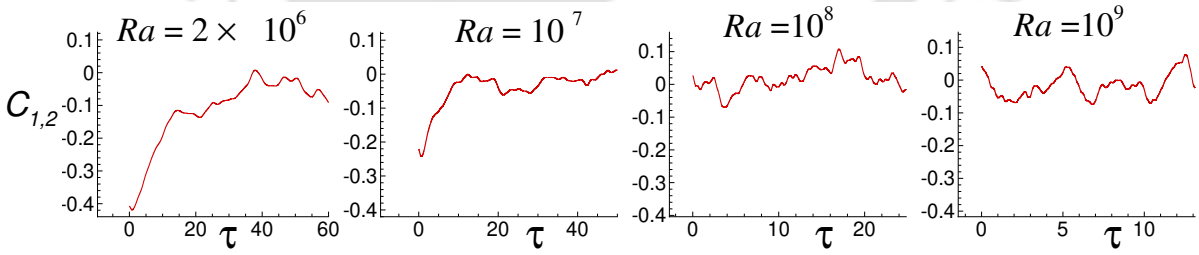

Figure 7.17: Cross-correlation between the first two Fourier modes at different Ra. The first and second modes are negatively correlated at low Ra, while at higher Ra they become nearly uncorrelated.

E_1 is accompanied by a gain in E_2, which is a signature of cessation events. However, at higher Ra no such correlation is observed. This indicates that at lower Ra, cessation-led reorientations are more probable than at higher Ra, and consistently the cessations are observed only for lower Ra.

7.4.1 Mechanism of flow reversals

So far, we have observed that the LSC is locked in one diagonal plane, accompanied by a four-roll structure in the other, and these patterns switch intermittently with time. Here we attempt to explore the mechanism that leads to the change in flow topology in different planes. In this section, we analyse the flow during the reorientation of LSC. Previous 2D/quasi-2D studies [274, 275] on the dynamics of LSC have emphasized the role of corner rolls in flow reversals, though in such a set-up, LSC is forced to coexist with the rolls at all times in a plane with no possibility of rotation-led reversal. Alleviating such limitations, we discuss dynamics and reversal of the mean wind in a 3D Cartesian box.

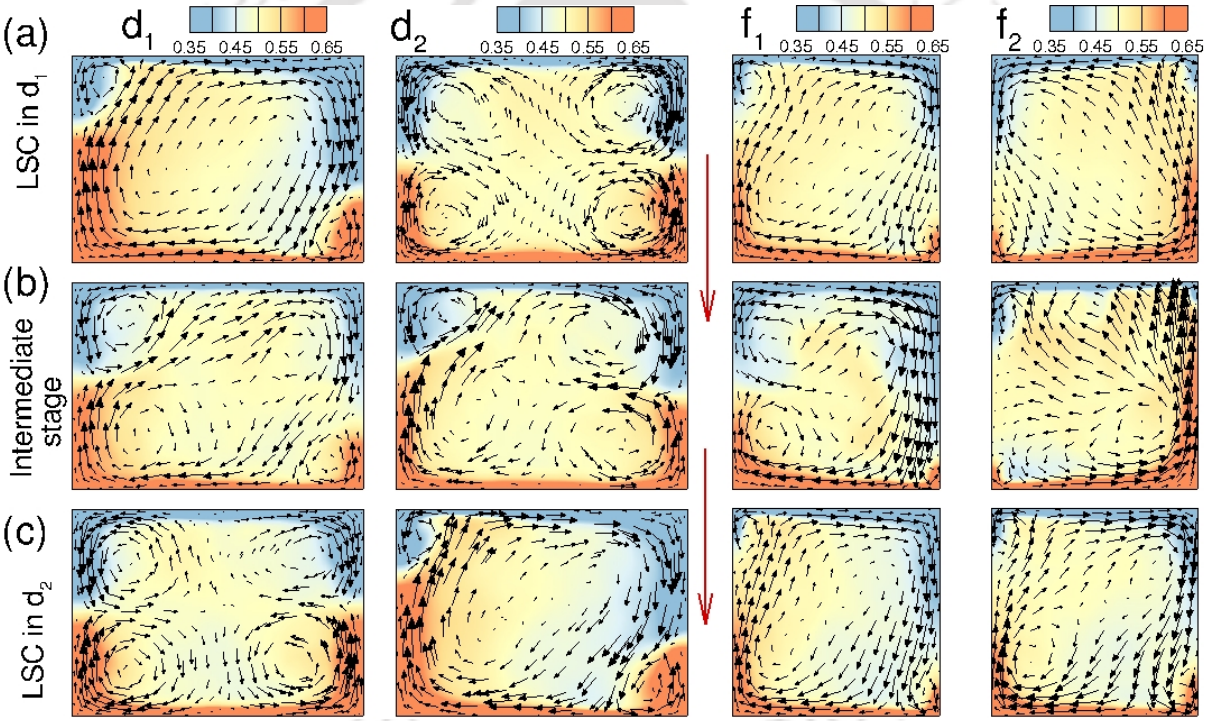

Figure 7.18: Time-averaged velocity vectors superimposed on the temperature contours at diagonal (d_1 and d_2) and face (f_1 and f_2) planes (a) before, (b) during, and (c) after a partial reversal of LSC for $Ra = 2 \times 10^6$.

The series of events that lead to a partial reversal for $Ra = 2\times10^6$ is pictorially summarized in Fig. 7.18 where time-averaged (5-10 convective time units for the transition and 150-200 for stable persistence) velocity vectors are superimposed on temperature contours. At the outset, LSC is oriented along d_1 [see frame (a)] as a clockwise primary roll accompanied by two counter-clockwise secondary rolls near the corners, while in d_2 a four-roll structure is noticed. During reversal, the corner rolls in d_1 grow in size [refer frame (b)] while they induce the

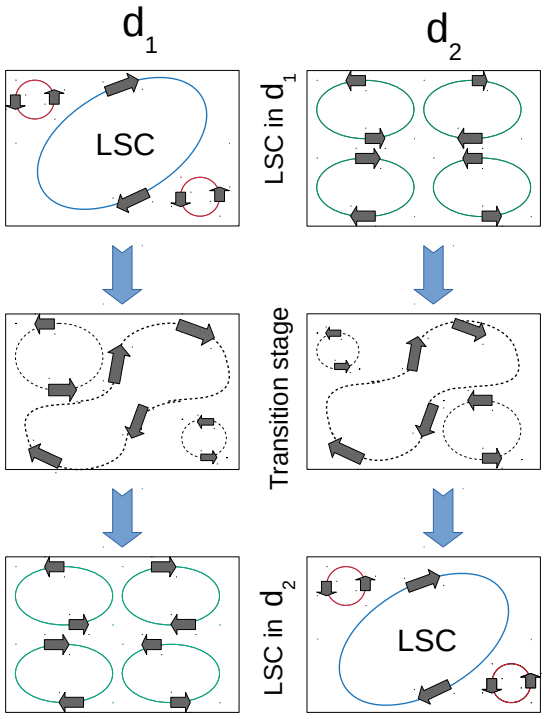

Figure 7.19: Schematic representation of the LSC and corner-rolls in the LSC plane and four-roll structure in the non-LSC plane before, during, and after a partial reversal. The intermediate stage clearly shows that the corner-rolls grow sequentially in the LSC plane.

primary roll to break into two, which results in a four-roll structure in frame (c). Note that the corner rolls do not grow simultaneously, rather sequentially, and they maintain the same sense of rotation before the reversal. On the other hand, only a set of rolls with the same sense of rotation appear to grow and merge in d_2 only to form an LSC retaining the sense of rotation. This effectively shrinks the remaining two rolls towards the corners. Thus, the LSC and four-roll structure switch between the diagonal planes during a partial reversal. Interestingly, flow topologies in both the diagonal planes are similar during the transition stage. In contrast to the diagonal planes, we observe a single-roll structure accompanied by two substructures inside the primary roll in the faces f_1 and f_2. This flow topology is almost similar to the abnormal single-roll state (ASRS) reported in the recent experimental study by Chen *et al.* [284]. After the reversal, the sense of circulation in one face reverses, while it remains the same in the other. For better representation of the partial reversal, a schematic representation of the flow topology in the diagonal planes are shown in Fig. 7.19, where the arrows show the direction of flow circulation. The solid lines indicate the roll behaviour before and after the reversal, while the dotted lines indicate the transition stage during the reversal. The intermediate stage clearly

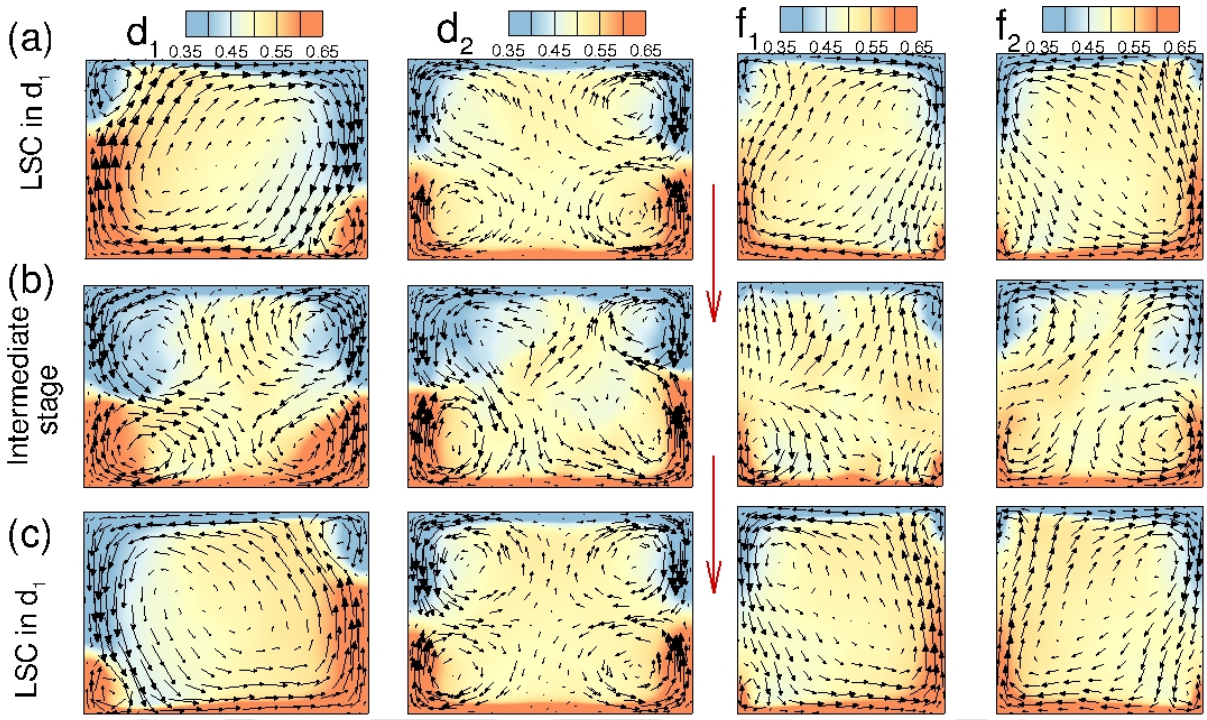

Figure 7.20: Time-averaged velocity vectors superimposed on the temperature contours at diagonal (d_1 and d_2) and face (f_1 and f_2) planes (a) before, (b) during, and (c) after a complete reversal of LSC for $Ra = 2 \times 10^6$.

shows that the corner-rolls grow sequentially in the LSC plane. After the reversal the LSC and four-roll structure switch between the diagonal planes.

The flow topologies in the diagonal and face planes before, during, and after a complete reversal is shown in Fig. 7.20. In the case of a complete reversal, corner rolls in the diagonal plane containing LSC grow in size to yield a four-roll structure, which further merges to produce an LSC with opposite sense of rotation. However, on the other diagonal plane, the same four-roll structure is maintained during the entire reversal process. Note that the direction of circulation reverses in both the faces during complete reversal, as shown in Fig. 7.20. Interestingly, the sequence of flow structures and vortex reconnection in the LSC-plane during a complete reversal is very much similar to that observed in 2D/quasi-2D [274, 275] cases. On the contrary, partial reversals which can occur due to a CW or CCW rotation of the LSC are impossible to appear in 2D. Thus, the confinement in 2D reduces the possible flow configurations of LSC and its reversals by half.

Time-averaged velocity streamlines superimposed on temperature contours in the diagonal (containing LSC and four-roll structure) and the face planes are shown in Figs. 7.21(a)-7.21(d)

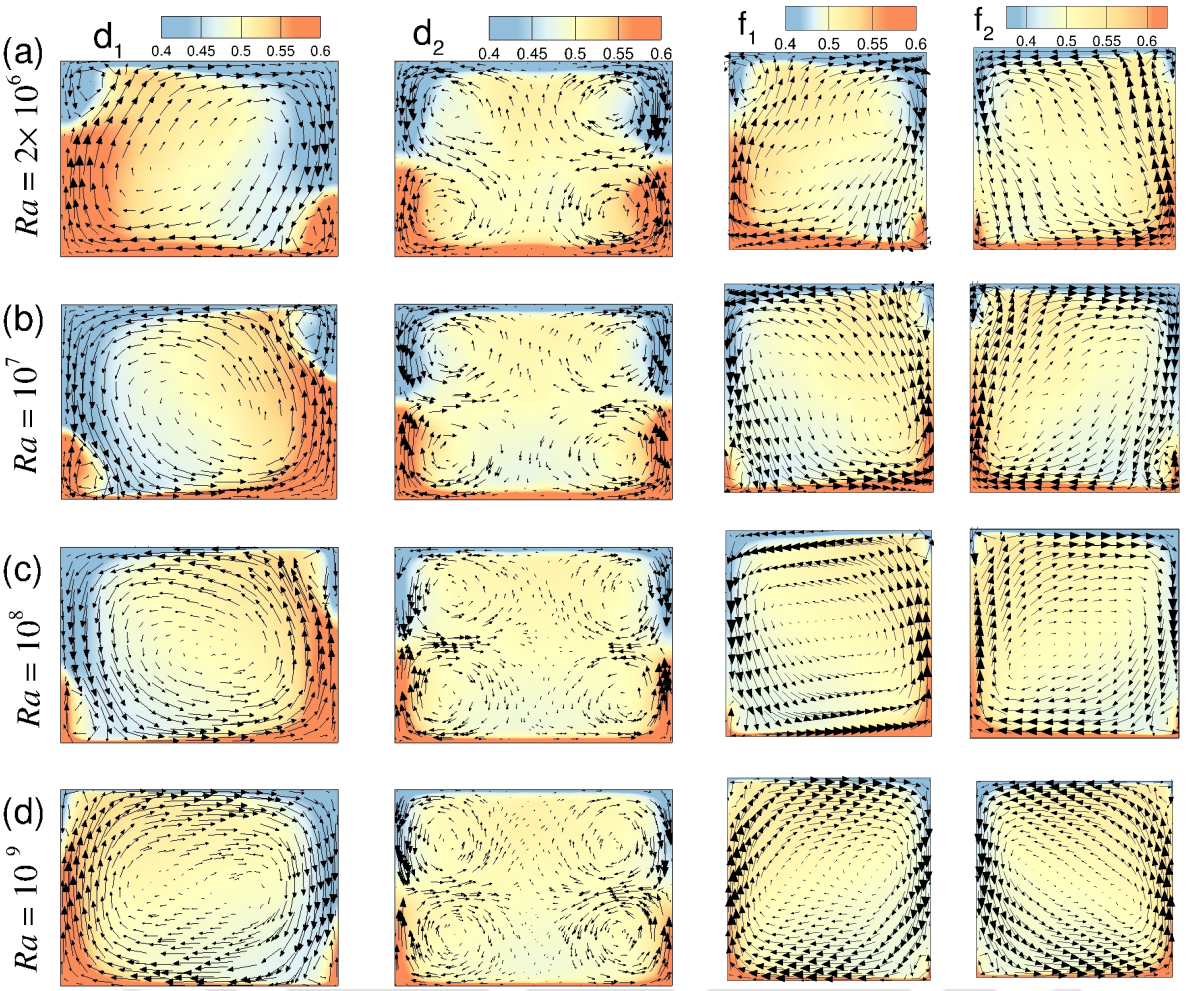

Figure 7.21: Time-averaged velocity vectors superimposed on the temperature contours at diagonal (d_1 and d_2) and face (f_1 and f_2) planes for (a) $Ra = 2\times10^6$, (b) $Ra = 10^7$, (c) $Ra = 10^8$, and (d) $Ra = 10^9$. With increase in Ra, the LSC becomes more dominant and the corner-rolls get suppressed.

for different Rayleigh numbers. With increase in Ra, the LSC structure becomes more prominent and "domain-filling," which effectively suppresses the corner-rolls. This observation is in line with increase in the strength of LSC with Ra. At higher Ra, the LSC becomes aligned with the horizontal direction causing nearly unidirectional motion along its path. Similar observations were made by Niemela and Sreenivasan [285] in their experimental study with helium gas in a cylindrical container. They reported that the LSC changed from a tilted and nearly elliptical shape at low Rayleigh numbers to a squarish shape at high Rayleigh numbers. We observe that, in contrast to the LSC, four-roll structure on the other diagonal remains geometrically similar across all Ra. As the corner vortices play a pivotal role in flow reversals, a decrease in the frequency of reversals at higher Ra can thus be attributed to the suppression of these corner rolls.

Note the presence of substructures inside the single roll in the face plane for $Ra = 2 \times 10^6$, which is absent at higher Ra. Recent study by Chen *et al.* [284] has shown that the emergence of substructures inside the LSC makes it less stable and thus increases the probability of re-orientations. Hence, in addition to the corner-rolls, the structure and stability of LSC are also critical to its reorientations. With the increase in Ra, the LSC becomes more dominant and the corner-rolls get suppressed. This effectively reduces the occurrence of reorientations. To show the 3D perspective of the corner vortices the time-averaged Q structures are shown in Fig. 7.22 for different Ra. The levels are shown at about 10% of the corresponding global maximum of Q. As discussed earlier, the corner vortices extend along the adjacent faces sharing the diagonal plane to yield a "boomerang" shape. Note that as the Rayleigh number increases, these corner vortices shrinks in size considerably though they retain their spread and orientation.

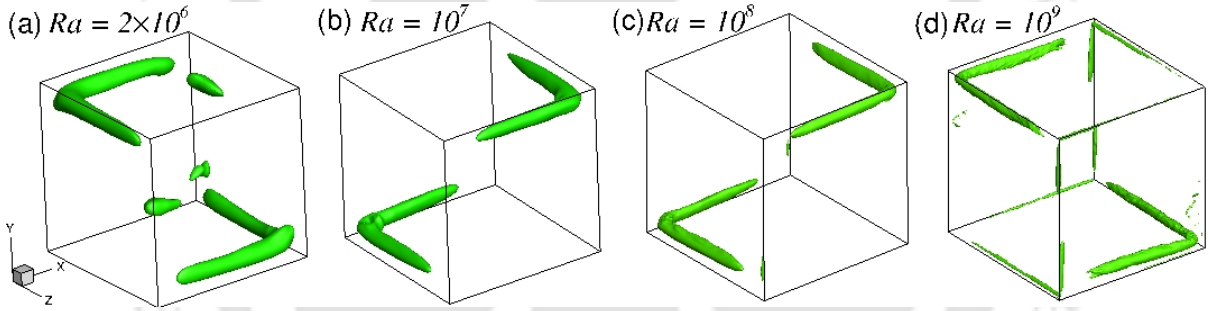

Figure 7.22: Time-averaged Q structures for (a) $Ra = 2 \times 10^6$, (b) $Ra = 10^7$, (c) $Ra = 10^8$, and (d) $Ra = 10^9$, drawn at about 10% of the global maximum of Q. The corner vortices diminish with increase in Ra.

7.5 Effect of LSC on the turbulent kinetic energy budget

Dynamical coupling between the activities in the diagonal planes is crucial to understand the reorientations of LSC. In order to address this aspect, we investigate the mechanism of energy transport by looking at the contributions coming from different terms in the turbulent kinetic energy (TKE) budget equation. Recall that the TKE budget equation is written as

$$\underbrace{\frac{\partial}{\partial t}\left(\frac{1}{2}\overline{u_i'u_i'}\right)+U_j\frac{\partial}{\partial x_j}\left(\frac{1}{2}\overline{u_i'u_i'}\right)}_{A_k}=\underbrace{-\frac{\partial}{\partial x_j}\left(\overline{u_j'p'}-2\sqrt{\frac{Pr}{Ra}}\overline{u_i's_{ij}'}+\frac{1}{2}\overline{u_i'u_i'u_j'}\right)}_{T_k}$$
$$\underbrace{-\overline{u_i'u_j'}S_{ij}}_{P_S}+\underbrace{\overline{u_i'\theta'}\delta_i y}_{P_B}\underbrace{-2\sqrt{\frac{Pr}{Ra}}\overline{s_{ij}'s_{ij}'}}_{\epsilon}. \tag{7.3}$$

As discussed in the previous chapter, the terms are cast as advection (A_k), transport (T_k), production by shear (P_S) and buoyancy (P_B), and dissipation (ϵ) of turbulent kinetic energy to facilitate a systematic discussion.

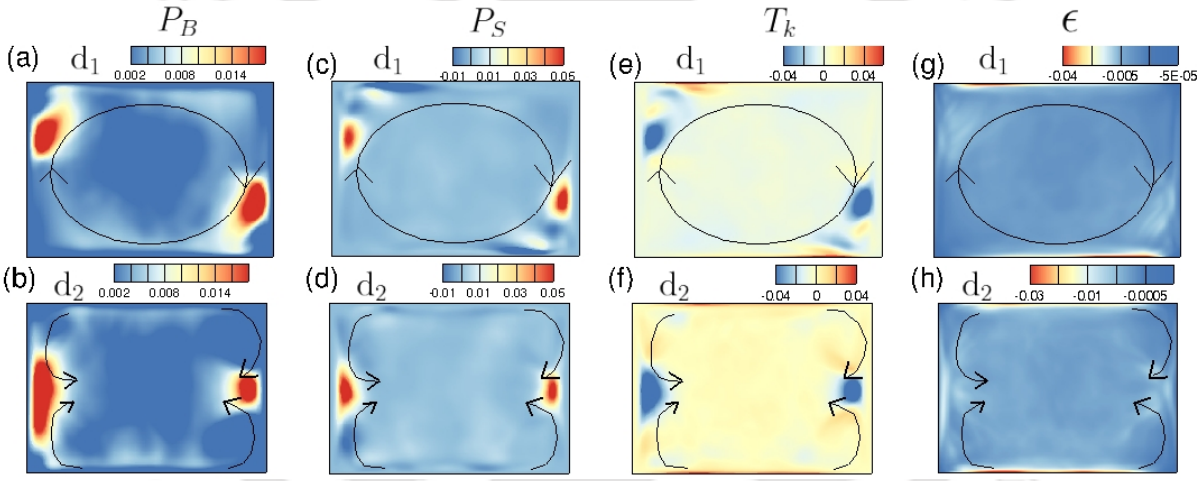

Figure 7.23: Contours of (a,b) buoyancy production, (c,d) shear production, (e,f) transport and (g,h) dissipation of TKE in the diagonal planes d_1 (top row) and d_2 (bottom row) when the LSC is oriented along d_1. The arrows indicate the direction of circulation of the mean flow and the four-roll structure.

Contours of production, transport, and dissipation of TKE in the diagonal planes are shown in Fig. 7.23, when the LSC is aligned along d_1. Here the top and bottom rows show the contours in diagonal plane d_1 and d_2, respectively, while the arrows indicate the corresponding direction of circulation of the mean flow and four-roll structure in these planes. We observe that, in the LSC plane, production by both buoyancy and shear occurs mainly near the regions where the corner-rolls interact with LSC [see frames (a) and (c)]. However, in the non-LSC plane, production occurs primarily where the counter-rotating rolls of the four-roll structure interact with each other, as shown in frames (b) and (d). Note that these regions are associated with large negative values of transport [see frames (e) and(f)], which indicate the extraction of

Table 7.1: Columns from left to right represents the average advection (A_k), transport (T_k), dissipation (ϵ), shear production (P_s), and buoyancy production (P_b) of TKE, along with the imbalance ($I_k = \epsilon + P_S + P_B$) in the diagonal planes d_1 and d_2.

Plane	$A_k(\times 10^{-4})$	$T_k(\times 10^{-4})$	$\epsilon(\times 10^{-4})$	$P_S(\times 10^{-4})$	$P_B(\times 10^{-4})$	$I_k(\times 10^{-4})$
(a) d_1: LSC in d_1	2.48	−5.39	−42.9	12.8	39.1	8.99
(b) d_2: LSC in d_1	3.75	−13.4	−39.7	21.9	35.9	18.1
(c) d_1: Transient	4.52	−7.33	−33.4	14.1	20.8	1.56
(d) d_2: Transient	0.33	−2.63	−28.4	14.7	17.5	3.71
(e) d_1: LSC in d_2	5.32	−11.5	−35.5	25.2	28.0	17.7
(f) d_2: LSC in d_2	3.16	5.57	−38.7	7.40	29.6	−1.71

TKE. The dissipation of TKE is shown in frames (g) and (h), which indicate that dissipation is negligible in the bulk region and mostly restricted to the boundary layers.

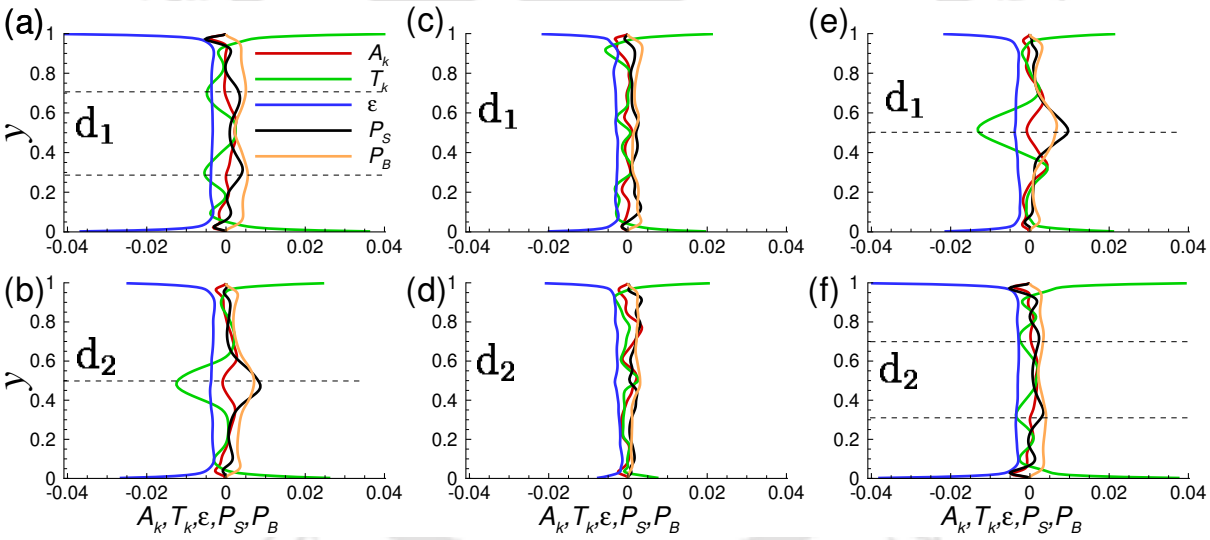

Figure 7.24: Vertical profiles of TKE constituents in the diagonal planes, (a,b) before, (c,d) during and (e,f) after reversal. The top row shows the TKE profiles in the diagonal plane d_1, while the bottom row corresponds to d_2.

Next, we evaluate the vertical variation of different energy budget terms (Eq.7.3) before, during, and after a reorientation with top and bottom rows correspond to the diagonal plane d_1 and d_2, respectively, as shown in Fig. 7.24. Here, time and horizontal direction averaging (in d_1 and d_2) is used as the ensemble in order to obtain vertical profiles. It is important to note that the pairs (a,b), (c,d) and (e,f) indicate alignment of the LSC along d_1, transient stage from d_1 to d_2, and alignment along d_2, respectively. Overall [considering all frames (a)-(f)], the buoyancy production remains small near the wall and increases as we move away from the wall to attain

its maximum value. However, dissipation exhibits an opposite trend with maximum near the wall, which asymptotically drops across the boundary layer. To sum up, we observe that the energy is mainly produced in the bulk, transported through large-scale structures and finally dissipated near the walls.

Now we concentrate on the situation in which the LSC is aligned along d_1 [see Figs. 7.24(a) and 7.24(b)]. The dashed lines in d_1 show the approximate location ($y = 0.3H$ and $0.7H$) of the regions where the corner-rolls interact with the LSC (also refer to Fig. 7.23). Similarly, in d_2, the dashed lines indicate the mid-height region ($y = 0.5H$) where counter-rotating rolls of the four-roll structure interact with each other. In the LSC plane d_1, shear and buoyancy production are significant at the interface of LSC and corner-rolls, identified by positive bulge in P_S and P_B, as shown in Fig. 7.24(a). This is accompanied by a negative peak in the transport term near the same location, which indicate the extraction of TKE. Thus, unlike homogeneous shear flow turbulence, as fluctuations are largely sustained by buoyancy, a different mechanism than a simple $P_S \approx \epsilon$ is anticipated here. To make the energy transfer more quantitative, we also compute the planar averaged quantities along with the imbalance between total production and dissipation, as shown in Table 7.1, where different rows (a-f) are identified based on the plane and orientation of LSC corresponding to that mentioned in Fig. 7.24. As LSC is aligned along d_1, here the buoyancy production is apparently dominant over shear (39.1 over 12.8). However, in d_2, both P_B and P_S are nearly comparable, and maximum shear production is observed in the bulk at the interface of the counter rotating rolls [see Fig. 7.24(b)]. Interestingly, shear production dominates over P_B in the bulk unlike the LSC plane due to strong friction between the counter-acting plumes. Here, the imbalance (marked in red) is seen much higher than the LSC plane (18.1 over 8.99), which is mainly balanced by the transport term, that redistributes TKE in the domain. Note the negative bulge in the transport term, which shows the extraction of TKE, as shown in Fig. 7.24(b). Thus, the excess TKE generated in the bulk is extracted and carried towards the walls, where it is finally dissipated.

The TKE profiles during the transient stage is shown in Figs. 7.24(c) and 7.24(d). In both the diagonal planes, buoyancy and shear production are comparable which are balanced by dissipation rendering a trivial transport process. Note that the imbalance of TKE is minimal during the transient stage in both d_1 and d_2, as shown in Table 7.1. During reorientation, the LSC makes transition from d_1 to d_2 resulting in interchange of TKE profiles between the

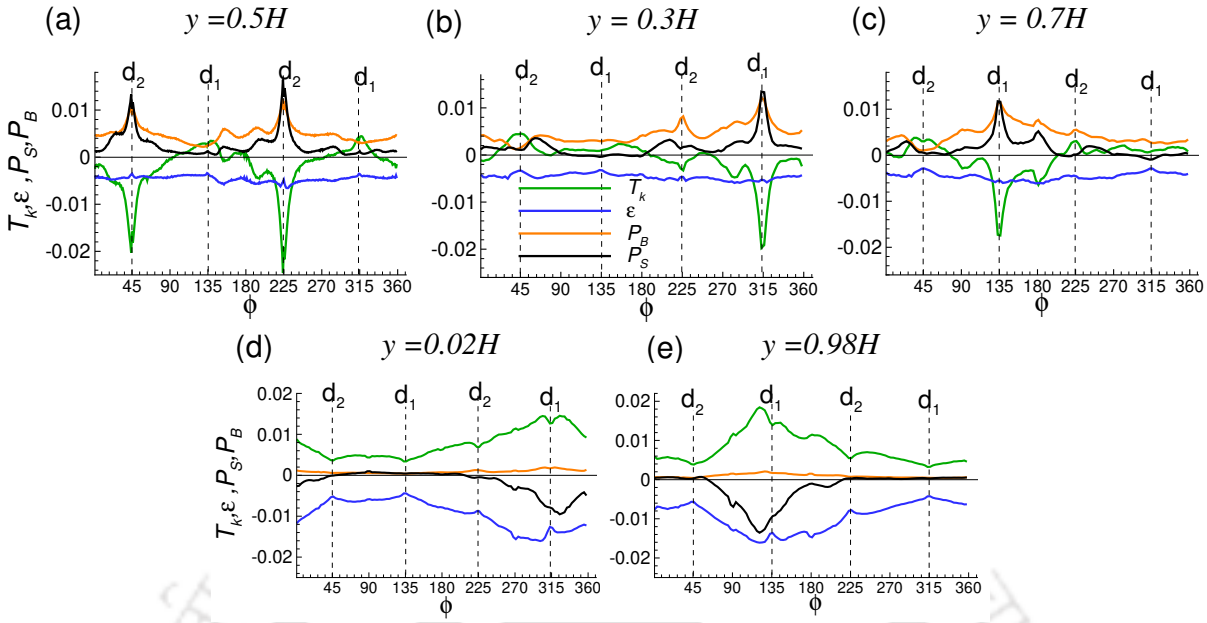

Figure 7.25: Lateral variation of TKE constituents at (a) $y = 0.5H$, (b) $y = 0.3H$, (c) $y = 0.7H$, (d) $y = 0.02H$, and (e) $y = 0.98H$, when the LSC is oriented along d_1. The dotted lines indicate the azimuthal locations of d_1 and d_2.

diagonal planes. Figures 7.24(e) and 7.24(f) correspond to the situation in which LSC is aligned along d_2. This leads to dominance of buoyancy in d_2 and maximum imbalance in d_1 (17.7 in Table 7.1) with a typical bulge in T_k, as shown in Fig. 7.24(e).

Next, we turn our attention to the process of energy transfer across these planes. To this end, we compute the azimuthal variation of different energy budget terms (Eq. 7.3) at various vertical heights, namely, bulk ($y = 0.5H$), boundary layer ($y = 0.98H$ and $0.02H$), and near the corner rolls ($y = 0.3H$ and $0.7H$), during the time span when LSC is oriented along d_1, as shown in Fig. 7.25. Here dashed lines indicate the azimuthal locations of d_1 and d_2. At the mid-plane [Fig. 7.25(a)], both shear and buoyancy produce kinetic energy in d_2 owing to a chaotic mixing, identified by positive peaks in their respective profiles. This TKE is in turn extracted by the transport mechanism (note the -ve sign). Similar high amplitude production events are observed at horizontal planes $y = 0.3H$ and $0.7H$, near the corner-rolls at d_1, as shown in frames (b) and (c). Note that production of TKE occurs at localized pockets, seen as spikes in the P_S and P_B profiles. These are primarily the regions where two counter-rotating convective rolls interact with each other [see the red spots in Figs. 7.23(a)-7.23(d)]. In the LSC-plane, these cells comprise of the LSC and corner-rolls, while in the non-LSC plane they constitute two counter-rotating rolls of the four-roll structure.

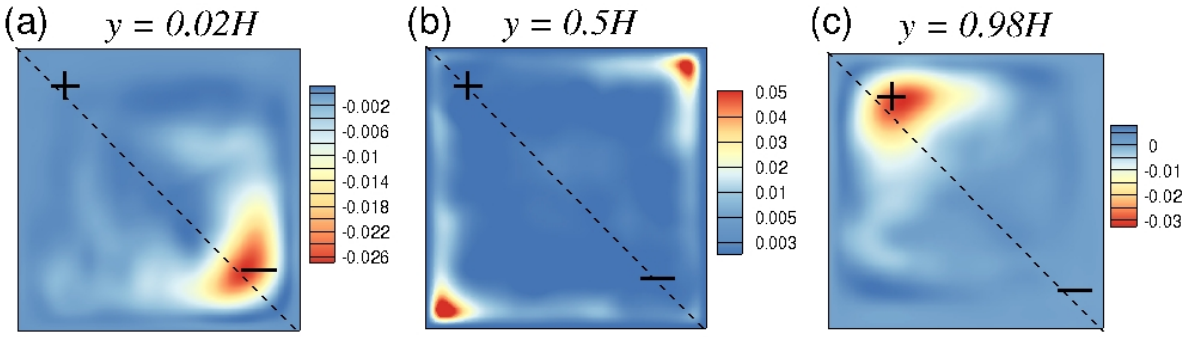

Figure 7.26: Contours of production of TKE by shear in the horizontal planes (a) $y = 0.02H$, (b) $y = 0.5H$, and (c) $y = 0.98H$. The dashed lines indicate the orientation of LSC, while $+$ve and $-$ve signs represent rising and dipping plumes.

Azimuthal variation of the TKE constituents in the boundary layer is shown in Figs. 7.25(d) and 7.25(e). It is apparent that dissipation is dominant in the boundary layers, especially in the diagonal plane d_1. This is accompanied by large positive values of transport, which indicates the supply of TKE. The buoyancy production is trivial inside the boundary layers, while shear production shows a negative peak near d_1. It is a common understanding that the shear production indicates the correlation between Reynolds stress and the mean strain rate tensor. Positive value of P_S represents the transfer of kinetic energy from the mean flow to turbulence [286]. Commonly, the energy exchange involves a loss to the mean flow and gain to turbulence. However, here we observe negative peaks in P_S which suggests a source of mean kinetic energy at the expense of the fluctuating field [269, 286]. Figure 7.26 shows the contours of shear production in horizontal planes at the bulk and boundary layer regions. Here dashed lines indicate the orientation of LSC (along d_1), while $+$ve and $-$ve signs represent rising and dipping plumes. We observe that in the bulk region, shear production is positive as shown in frame (b). However, inside the boundary layers [see frames (a) and (c)], P_S is negative with maximum near the regions where rising (dipping) thermal plumes collide onto the top (bottom) plate. Hence inside the boundary layers, the LSC (mean flow) derives energy from the turbulent fluctuations. Note that although negative P_S is observed inside the boundary layer region, the integral of P_S over the whole domain always remains positive [287].

For better evaluation of the distribution of dissipation, the contours of ϵ are plotted at horizontal planes in the boundary layer and mid-plane region, as shown in Fig. 7.27, where dashed lines indicate the orientation of LSC. As discussed previously, dissipation of TKE is negligible in the bulk [see frame (b)] and dominant inside the boundary layers [frames (a) and (c)].

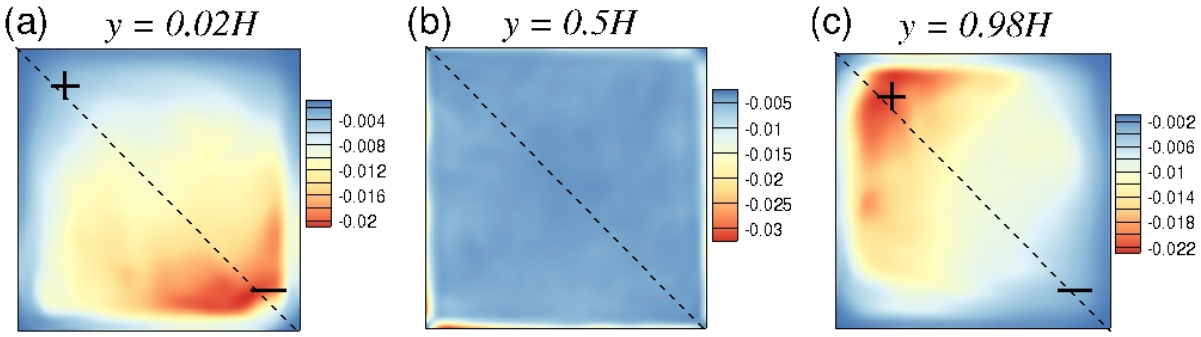

Figure 7.27: Contours of dissipation of TKE in horizontal planes (a) $y = 0.02H$, (b) $y = 0.5H$, and (c) $y = 0.98H$. The dashed lines indicate the orientation of LSC, while $+$ve and $-$ve signs represent rising and dipping plumes.

Further, the maximum dissipation of TKE is observed in the regions where the plumes collide with the top or bottom plates.

Overall, we observe that the production of TKE occurs at localized pockets in both the diagonal planes where two counter-rotating rolls interact with each other. The turbulent transport mechanism extracts TKE from these locations and feeds it to the boundary layers where the energy is finally dissipated. Our analysis show that the dissipation of TKE largely happens near the diagonal plane containing LSC at regions where thermal plumes collide with the horizontal plates. The mean flow (LSC) derives this energy from the turbulent fluctuations inside the boundary layers, while in the bulk region it losses energy which is identified as the positive production of TKE. Redistribution of TKE along the diagonals at different heights, thus, plays a crucial role in sustaining the LSC as well as the turbulent fluctuations.

7.6 Summary

In this chapter, dynamics of LSC in turbulent RBC inside a cubic box has been investigated for $2 \times 10^6 \leq Ra \leq 10^9$. LSC is primarily aligned along one of the diagonal planes accompanied by a four-roll structure in the other diagonal. The Fourier mode analysis of velocity signals in the mid-plane revealed the presence of rotation-led as well as cessation-led reorientations. Further, stronger negative cross-correlation between the first two Fourier modes at low Ra becomes nearly uncorrelated as Ra increases. This explains the observation that at lower Ra, cessation-led reorientations are more probable than at higher Ra. Switching of LSC from one

diagonal to other, defined as partial reversal, marked by a lateral shift $\Delta\Phi \approx \pi/2$, is seen as common occurrence across all Ra. In contrast, complete reversals, where LSC only switches its sense of rotation staying in the same diagonal, is a rare occurrence and restricted to low Ra. Further, we have analyzed the flow topology in different planes and proposed a mechanism of the reorientations. During a partial reversal, the LSC weakens at the expense of growth of the corner-rolls to form a four-roll structure, while in the opposite plane two rolls merge together to form LSC. In the case of a complete reversal, corner rolls in the diagonal plane containing LSC grow in size to yield a four-roll structure, which further merges to produce an LSC with opposite sense of rotation. However, on the other diagonal plane, the same four-roll structure is maintained during the entire reversal process. Using kinetic energy budget, we have analyzed the energy transfer mechanism that connects the dynamics between these planes. This analysis highlights the importance of shear production and transport of TKE, as shear and buoyancy produced energy is extracted via transport mechanism to feed its drainage largely along the LSC plane. With the increase in Ra, the LSC becomes more dominant and suppresses the corner-rolls. This effectively reduces the occurrence of reorientations at higher Ra.

8

Conclusions and future scope

In this thesis, using direct numerical simulations, we have studied various aspects of turbulent Rayleigh-Bénard convection inside cylindrical and cubic enclosures. We have mainly focused on LSC, its characteristics and dynamics in these two geometries. In addition, a detailed investigation on the effect of rotation, Prandtl number and statistics of thermal plumes have also been carried out. The principal findings from each part of the thesis are summarized in this chapter. Finally, we present a brief overview of the prospects for future research on turbulent RBC.

8.1 Conclusions

The novelty of the work lies in the profound analysis of LSC and its dynamics in turbulent RBC inside cubic and cylindrical enclosures. In the cylindrical domain, we have been able to study some of the statistical features of reorientations which were previously reported only in experimental works. Further, for the first time, we have observed a rare phenomenon of multiple-cessation. In Cartesian box, we have been able to attain a high Rayleigh number range, up to $Ra = 10^9$, which is rarely attempted in numerical studies. In addition, by evaluating the topology of the flow in different planes, we have been able to propose a novel mechanism of flow reversal. The main findings of the thesis are summarized below.

For rotating RBC inside a cylindrical cell, we have been able to identify different flow regimes based on the flow structure and Fourier modes. At low rotation rates, we observe an

LSC dominated flow structure (regime I), while with an increase in rotation the coherence at large scale is lost. At intermediate rotation rates, marked by regime II, no specific flow structure is observed as the Fourier modes share almost equal energy. However, at higher rotation rates (regime III), the larger Fourier modes dominate (second or third), and as a result, we observe wall-bounded, multiple roll structures such as quadrupole and sextupole. The behaviour of the Nusselt number and dissipation rates at these regimes have been evaluated. Overall, the flow statistics remain almost unchanged in the low rotation rate regime, while significant changes are observed in regimes II and III. Both the Nusselt number and dissipation rates show a power-law behaviour at the rotation dominated regime. At high rotation rates, the fluctuations in velocity are reduced, and the mean temperature profile approaches a linear one, which indicates the suppression of convective motion due to rotation.

We have studied the effect of Prandtl number on the flow structure and heat transfer rate in RRBC. We have shown that there is an intermediate Pr regime where the increase in heat transfer occurs at low rotation rates. For all Pr, a reduction in heat transfer rate is observed with the increase in rotation rate. However, for intermediate Pr regime, an increase in Nu of about $4-6\%$, from the non-rotating case is observed at low rotation rates. The rise in heat transfer rate is observed in the region where the flow structure changes from quadrupolar to dipolar state. At extremely high rotation rate, the fluctuations in the flow are damped out, and the flow attains a conduction stage. The results show that higher Prandtl number delays the attainment of conduction stage. The critical rotation rate for which transition to the conduction state occurs exhibits a power-law dependence on Prandtl number as $1/Ro_c \propto Pr^{0.5}$.

One of the major accomplishments of our study has been the identification and characterization of LSC, its dynamics and statistics. Figure 8.1 shows a flow chart of the novel findings of the present work, along with the already known facts. The reorientations have been identified as rotation-led and cessation-led based on their nature of occurrence, and as partial and complete reversal depending on the azimuthal drift. In addition to the previously reported rare events like cessations and double-cessation, an interesting event of multiple-cessation has been observed in cylindrical geometry. Further, we have shown that the orientation of LSC significantly affects the heat transfer, dissipation rates, and the boundary layer thickness. We have been able to study some of the statistical features of reorientations, and the results are in good agreement with previous experimental works. As observed in the case of non-rotating RBC,

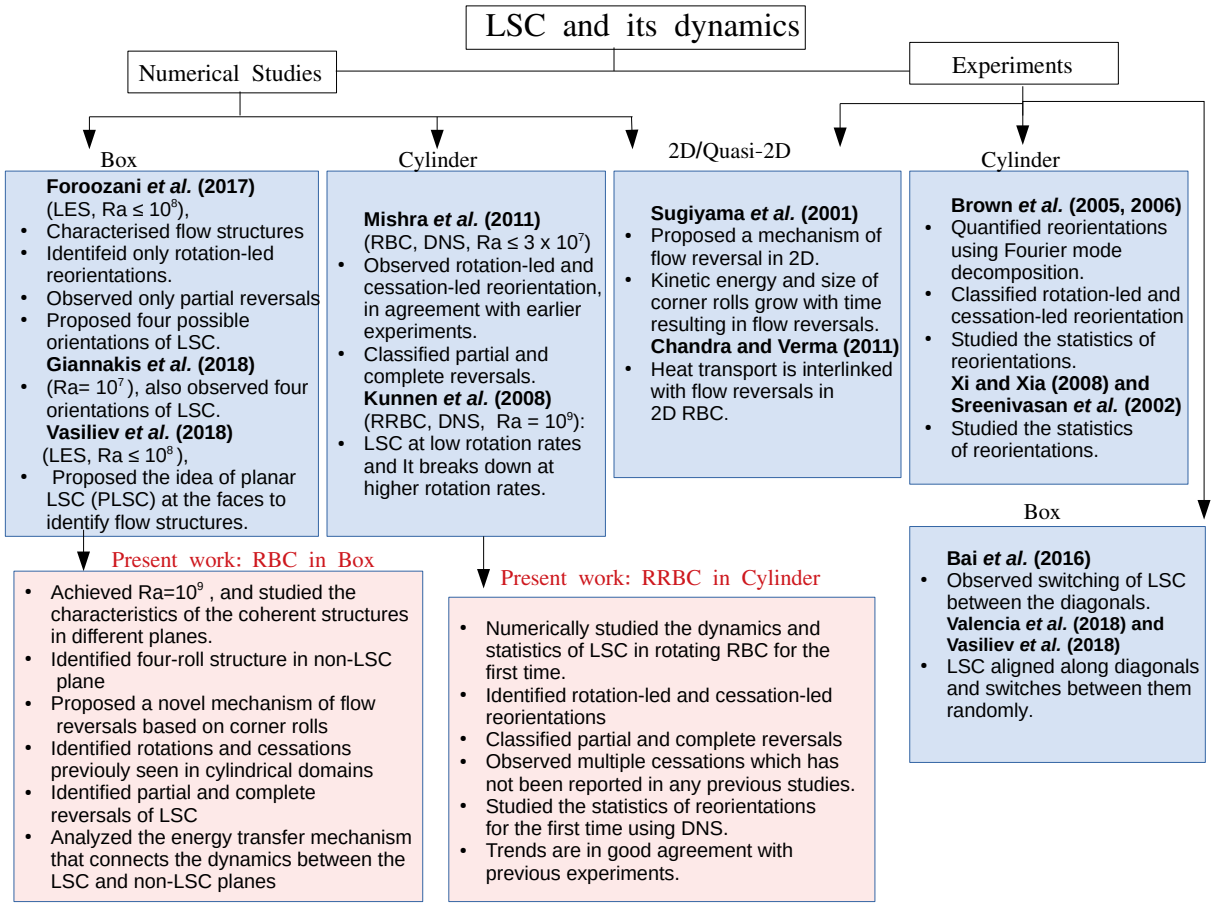

Figure 8.1: Flow chart showing the novel findings of the present work along with previous studies on LSC and its dynamics.

we find that cessation-led reorientations are rare events compared to the rotation-led ones for RRBC. Double-cessations are even rarer, and multiple-cessations are the rarest of all reorientations. As the rotation rate increases, a significant increase in the number of reorientations is observed. Similar to non-rotating RBC, we find that the probability distribution of the reorientations exhibits a power-law distribution.

For turbulent RBC inside a Cartesian box, we have been able to attain a high Rayleigh number range, up to $Ra = 10^9$, and study various characteristics of the flow, especially thermal plumes and LSC. We have identified plume and turbulent background regions and showed that the volume fraction of the plume decreases with Ra, while the background fraction increases. Further, we have computed the contribution of thermal dissipation rate from the plume and background regions and found that both contributions exhibit a decreasing trend with Ra. Comparisons with the theoretical predictions show that the dissipation from the plume region

follows the Grossmann-Lohse (GL) scaling at lower cutoffs, while considerable deviations are observed in the background contribution. Turbulent statistics like variance, skewness, and flatness of velocity and temperature have been evaluated to study different characteristics of the flow. We observe that the PDFs of both viscous and thermal dissipation rates compare well with a stretched exponential function and their tails get more extended with the increase in Ra. The evaluation of kinetic energy budget shows that TKE is mainly produced in the bulk region; from there, it is transported towards the walls and dissipated in the boundary layers.

One of the principal achievements of the thesis has been the investigation of LSC and its dynamics inside a cubic cell at a high Rayleigh number range. LSC is primarily aligned along one of the diagonal planes accompanied by two corner rolls, while in the other diagonal a four-roll structure is noticed. Similar to that obtained in cylindrical confinement, we have identified both rotation-led and cessation-led reorientations of LSC. However, due to the lack of symmetry in the azimuthal direction, the azimuthal drift of the LSC is restricted to $\Delta\Phi_1 \approx \pi/2$ and $\Delta\Phi_1 \approx \pi$, which are characterized as partial and complete reversals, respectively. Our analysis shows that partial reversals are a common occurrence across all Ra, while complete reversals are rare and restricted to low Ra. By evaluating the topology of the flow in different planes, we have been able to propose a mechanism of flow reversal in the box geometry. During a partial reversal, the LSC weakens at the expense of growth of the corner-rolls to form a four-roll structure, while in the opposite plane, two rolls merge together to form LSC. In the case of a complete reversal, corner rolls in the diagonal plane containing LSC grow in size to yield a four-roll structure, which further merges to produce an LSC with opposite sense of rotation. With the increase in Ra, the LSC becomes more dominant and suppresses the corner-rolls. This effectively reduces the occurrence of reorientations at higher Ra. Using kinetic energy budget, we have analyzed the energy transfer mechanism that connects the dynamics between the LSC and non-LSC planes. Our analysis shows that the production of TKE occurs at localized pockets in both the diagonal planes, while its dissipation largely occurs near the diagonal plane containing LSC. The transport mechanism redistributes energy between these planes. It thus, plays a crucial role in sustaining the LSC and four-roll structure.

8.2 Future scope

Based on the observations made during the present work, here we list some of the avenues of future research in turbulent convection. Some of the critical issues that we are presently looking forward to are discussed below.

- Effect of surface roughness on turbulent RBC: We have observed that thermal plumes organize to form LSC in cylindrical and cubic enclosures. Introduction of surface roughness is expected to significantly affect the pattern of plume emissions and, thus, the formation and dynamics of LSC [288]. These aspects are of our prime future interests. It is generally believed that surface roughness enhances the heat transport [289–294], which depends on both the height and wavelength of the roughness elements [295–297]. The interaction of these surface elements with the boundary layers and their association with the behaviour of thermal plumes and overall heat transfer dynamics are important areas to focus on. Attainment of the so-called ultimate regime [81] is another aspect that has been of recent research interest. We aim to attain the ultimate regime by introducing surface roughness and thereby perturbing the boundary layers [57]. Note that most of the numerical studies on surface roughness have been carried out in 2D systems. It will be interesting to explore these avenues using 3D simulations, although, introducing random 3D roughness elements is a challenge in its own.

- Effect of tilt on turbulent RBC: Tilting the flow domain can significantly affect the flow structures, heat transport and various other characteristics of the system [298–300]. In a tilted convection cell, the symmetry of the system is broken, and the orientation of the LSC is locked, which allows the analysis of LSC and its dynamics more convincingly. Recall that in chapter 7, we have seen that with increase in Ra, the LSC becomes more squarish. Similar observations were made in the experimental study by Guo *et al.* [301], where they observed that the LSC changes from oblique elliptic-like to squarish-like structure with the increase in tilt angle. Thus, with the introduction of tilt, we might see some specific aspects of LSC that are generally seen at higher Ra. The effect of tilt angle on the structure and dynamics of LSC and its association with global heat transport are also interesting aspects to explore.

- Large-eddy simulations of turbulent RBC: In chapter 7, we have shown that with the increase in Ra, the frequency of reorientations of LSC reduces considerably. This makes DNS investigation of the dynamics of LSC a strenuous task, as the LSC stays in a particular plane for a very long time without reversing. We find that to study the dynamics of LSC at very high Rayleigh numbers, large-eddy simulation (LES) is the way forward. LES is a better choice than DNS in terms of computational cost and is superior to Reynolds averaged Navier-Stokes (RANS) in terms of dynamic approximation of the flow. As our prime focus has been on large-scale structures, their dynamics and global quantities, LES provides the best balance between computational cost and numerical resolution. We aim to investigate different kinds of reorientations of LSC and study their statistics using LES in future.

Appendix

Calculation of Nusselt number

To get the estimate of global heat transport in Rayleigh-Bénard convection, the Nusselt number is computed. Now let us consider non-dimensional energy equation

$$\frac{\partial \theta}{\partial t} + \nabla \cdot (\boldsymbol{u}\theta) = \alpha_T \nabla^2 \theta, \tag{8.1}$$

where $\theta = (T - T_C)/(T_H - T_C)$ is the normalized temperature having values 1 and 0 at bottom and top plates, respectively. Above equation can be cast into the heat flux form as

$$\frac{\partial \theta}{\partial t} + \nabla \cdot \boldsymbol{q} = 0 \tag{8.2}$$

where $q = (\boldsymbol{u}\theta - \alpha_T \nabla\theta)$ is the total heat flux (sum of the conductive and convective fluxes) and α_T depends on the choice of velocity scale (V^{ref}). Considering heat transport in vertical direction (let it be z), Nu, which is the ratio of convective and conductive heat fluxes, is estimated as

$$Nu = \frac{q_{conv}}{q_{cond}} = \frac{w\theta - \alpha_T \frac{\partial \theta}{\partial z}}{-\alpha_T (\frac{\partial \theta}{\partial z}_{cond})} \tag{8.3}$$

In the conduction state, non-dimensional temperature θ varies linearly in vertical direction (z) as $\theta_{cond} = 1 - z$. Thus, $\frac{\partial \theta}{\partial z}_{cond} = -1$. This implies

$$Nu = \frac{1}{\alpha_T}(w\theta) - \frac{\partial \theta}{\partial z} \tag{8.4}$$

If we consider the diffusive velocity $V^{ref} = \alpha/H$, then α_T = 1. However, on using the buoyancy scale $V^{ref} = \sqrt{g\beta\Delta TH}$, then $\alpha_T = \sqrt{1/(RaPr)}$. Thus, the Nusselt number is obtained as

$$Nu = w\theta - \frac{\partial\theta}{\partial z} \qquad \text{(for } `V^{ref} = \alpha/H) \tag{8.5}$$

$$Nu = \sqrt{RaPr}(w\theta) - \frac{\partial\theta}{\partial z} \qquad \text{(for } V^{ref} = \sqrt{g\beta\Delta TH}) \tag{8.6}$$

Further, the volume and time averaged Nusselt number, $\langle Nu\rangle$, is written as

$$\langle Nu\rangle = \langle w\theta\rangle - \left\langle \frac{\partial\theta}{\partial z} \right\rangle \qquad \text{(for } `V^{ref} = \alpha/H) \tag{8.7}$$

$$\langle Nu\rangle = \sqrt{RaPr}\langle w\theta\rangle - \left\langle \frac{\partial\theta}{\partial z} \right\rangle \qquad \text{(for } V^{ref} = \sqrt{g\beta\Delta TH}) \tag{8.8}$$

Now, when $\partial\theta/\partial z$ is summed up over the volume, the intermediate values get cancelled out, and thus reduces to -1 as shown below.

$$\left\langle \frac{\partial\theta}{\partial z} \right\rangle = \overline{\frac{1}{V}\int_V \frac{\partial\theta}{\partial z} dv} = \frac{1}{V}\left\{ \frac{\theta|_{z=1} - \theta|_{z=0}}{(z=1)-(z=0)} \right\} V = -1$$

This implies

$$\langle Nu\rangle = 1 + \langle w\theta\rangle \qquad \text{(for } `V^{ref} = \alpha/H) \tag{8.9}$$

$$\langle Nu\rangle = 1 + \sqrt{RaPr}\langle w\theta\rangle \qquad \text{(for } V^{ref} = \sqrt{g\beta\Delta TH}) \tag{8.10}$$

Nusselt number based on thermal and viscous dissipation rates

The thermal and viscous dissipation rates play an important role in the local and global heat transport process. If the Eq. 8.1 is multiplied by θ, each term is simplified as

$$\theta\partial\theta/\partial t = \partial(1/2\theta^2)/\partial\theta \tag{8.11}$$

$$\theta\nabla\cdot(\boldsymbol{u}\theta) = \theta\boldsymbol{u}\cdot\nabla\theta = \boldsymbol{u}\cdot\nabla(1/2\theta^2) = \nabla\cdot(1/2\boldsymbol{u}\theta^2) \tag{8.12}$$

$$\theta\nabla^2\theta = \theta\nabla\cdot(\nabla\theta) = \nabla\cdot(\theta\nabla\theta) - |\nabla\theta|^2 \tag{8.13}$$

Thus,

$$\frac{\partial(\frac{1}{2}\theta^2)}{\partial t} + \nabla \cdot (\frac{1}{2}\boldsymbol{u}\theta^2) = \alpha_T\{\nabla \cdot (\theta\nabla\theta) - |\nabla\theta|^2\}$$

Integrating it over the volume V (surrounded by the surface S) gives

$$\int_V \frac{d}{dt}(\frac{1}{2}\theta^2)dv + \int_V \nabla \cdot (\frac{1}{2}\boldsymbol{u}\theta^2)dv = \alpha_T\left\{\int_V \nabla \cdot (\theta\nabla\theta)dv - \int_V |\nabla\theta|^2 dv\right\}$$

Assuming that the volume V does not change with time and using the divergence theorem, the above equation further reduces to

$$\frac{d}{dt}\int_V (\frac{1}{2}\theta^2)dv + \int_S (\frac{1}{2}\boldsymbol{u}\theta^2)\cdot\hat{n}ds = \alpha_T\int_S (\theta\nabla\theta)\cdot\hat{n}ds - \alpha_T\int_V |\nabla\theta|^2 dv \tag{8.14}$$

Note that $\boldsymbol{u} = 0$ on the no-slip walls. Further, for periodic boundaries $\boldsymbol{u}\theta^2$ is same on opposite walls but $\hat{n}$ is in opposite direction. Thus we obtain

$$\int_S (\frac{1}{2}\boldsymbol{u}\theta^2)\cdot\hat{n}ds = 0$$

Also on adiabatic wall $\nabla\theta\cdot\hat{n} = 0$. For periodic walls, $\nabla\theta\cdot\hat{n}$ is same on opposite sides but $\hat{n}$ is in opposite direction. Thus, the first integral on the right hand side reduces to the surface integrals at top and bottom walls.

$$\int_S (\theta\nabla\theta)\cdot\hat{n}ds = \theta|_{z=1}\int_{z=1}\frac{\partial\theta}{\partial z}ds + \theta|_{z=0}\int_{z=0}\frac{\partial\theta}{\partial z}ds = \int_{z=0}\frac{\partial\theta}{\partial z}ds$$

Owing to the normalization, $\theta|_{z=0} = 1$ and $\theta|_{z=1} = 0$. Thus, Eq. 8.14 becomes

$$\frac{d}{dt}\int_V (\frac{1}{2}\theta^2)dv = \alpha_T\int_{z=0}\frac{\partial\theta}{\partial z}ds - \alpha_T\int_V |\nabla\theta|^2 dv \tag{8.15}$$

Now, on multiplying Eq. 8.1 by z, the resulting terms are

$$\begin{aligned} z\partial\theta/\partial t &= \partial(z\theta)\partial t \\ z\nabla\cdot(\boldsymbol{u}\theta) &= \nabla\cdot(z\boldsymbol{u}\theta) - (\boldsymbol{u}\theta)\cdot\nabla z = \nabla\cdot(z\boldsymbol{u}\theta) - w\theta \\ z\nabla^2\theta &= z\nabla\cdot(\nabla\theta) = \nabla\cdot(z\nabla\theta) - \nabla z\cdot\nabla\theta = \nabla\cdot(z\nabla\theta) - \partial\theta/\partial z \end{aligned}$$

Thus, we obtain

$$\frac{\partial(z\theta)}{\partial t} + \nabla \cdot (z\boldsymbol{u}\theta) - w\theta = \alpha_T\{\nabla \cdot (z\nabla\theta) - \frac{\partial\theta}{\partial z}\} \tag{8.16}$$

Integrating Eq. 8.16 over the volume V yields

$$\int_V \frac{\partial(z\theta)}{\partial t}dv + \int_V \nabla \cdot (z\boldsymbol{u}\theta)dv - \int_V w\theta dv = \alpha_T\Big\{\int_V \nabla \cdot (z\nabla\theta)dv - \int_V \frac{\partial\theta}{\partial z}dv\Big\}$$

Applying divergence theorem, the above equation reduces to

$$\frac{d}{dt}\int_V z\theta dv + \int_S (z\boldsymbol{u}\theta)\cdot\hat{n}ds - \int_V w\theta dv = \alpha_T\Big\{\int_S (z\nabla\theta)\cdot\hat{n}ds - \int_V \frac{\partial\theta}{\partial z}dv\Big\} \tag{8.17}$$

By the virtue of no-slip boundary condition on the horizontal plates and no-slip/periodic boundary condition on the lateral walls,

$$\int_S (z\boldsymbol{u}\theta)\cdot\hat{n}ds = 0.$$

Now, as S is a piece-wise continuous surface and owing to adiabatic or periodic boundary conditions, $\nabla\theta\cdot\hat{n} = 0$ on the lateral walls. Thus, we obtain

$$\int_S (z\nabla\theta)\cdot\hat{n}ds = 1\int_{z=1}\frac{-\partial\theta}{\partial z}ds + 0\int_{z=0}\frac{\partial\theta}{\partial z}ds = -\int_{z=1}\frac{\partial\theta}{\partial z}ds$$

Thus, Eq. 8.17 reduces to

$$\frac{d}{dt}\int_V z\theta dv - \int_V w\theta dv = -\alpha_T(\int_{z=1}\frac{\partial\theta}{\partial z}ds + \int_V \frac{\partial\theta}{\partial z}dv) \tag{8.18}$$

On integrating energy equation (Eq. 8.1) over the volume and applying the divergence theorem, it results in

$$\frac{d}{dt}\int_V \theta dv + \int_S (\boldsymbol{u}\theta)\cdot\hat{n}ds = \alpha_T\int_S \nabla\theta\cdot\hat{n}ds \tag{8.19}$$

Owing to no-slip boundary condition on horizontal plates and no-slip/periodic boundary condition on the lateral walls, $\int_S (\boldsymbol{u}\theta)\cdot\hat{n}ds = 0$. Thus, Eq. 8.19 reduces to

$$\frac{d}{dt}\int_V \theta dv = \alpha_T\int_{z=0}\frac{\partial\theta}{\partial z}ds - \alpha_T\int_{z=1}\frac{\partial\theta}{\partial z}ds \tag{8.20}$$

Adding Eq. 8.15 and Eq. 8.18 and subtracting from the above Eq. 8.20 results in

$$\frac{d}{dt}\int_V(\theta-\frac{1}{2}\theta^2-z\theta)dv+\int_V w\theta dv=\alpha_T\int_V\frac{\partial\theta}{\partial z}dv+\alpha_T\int_V|\nabla\theta|^2dv \tag{8.21}$$

Now let u consider a bounded function $f(t)$ such that $|f(t)|\leq C<\infty$, where C is any real constant. Time average of derivative of the bounded function $f(t)$ can be written as

$$\overline{\frac{df}{dt}}=\lim_{T\to\infty}\frac{1}{T}\int_t^{t+T}\frac{df(t')}{dt'}dt'=\lim_{T\to\infty}\frac{1}{T}(f(t+T)-f(t))$$

Maximum value of this function can be obtained as

$$max\{f(t+T)-f(t)\}=max\{f(t+T)\}-min\{f(t)\}=C-(-C)=2C.$$

Thus,

$$\overline{\frac{df}{dt}}\leq\lim_{T\to\infty}\frac{2C}{T}=0 \tag{8.22}$$

On taking time average of the Eq. 8.21,

$$\overline{\frac{d}{dt}\int_V(\theta-\frac{1}{2}\theta^2-z\theta)dv}+\overline{\int_V w\theta dv}=\alpha_T\overline{\int_V\frac{\partial\theta}{\partial z}dv}+\alpha_T\overline{\int_V|\nabla\theta|^2dv} \tag{8.23}$$

where,

$\overline{\frac{d}{dt}\int_V(\theta-\frac{1}{2}\theta^2-z\theta)dv}=0$ (using Eq.8.22) and $\overline{\int_v\frac{\partial\theta}{\partial z}dv}=\overline{\frac{\theta|_{z=1}-\theta|_{z=0}}{(z=1)-(z=0)}V}=-V$

$\partial\theta/\partial z$ when summed up over the volume reduces to the above as the intermediate values get cancelled out. Thus, Eq. 8.23 can be written as

$$\overline{\int_V w\theta dv}=\alpha_T\overline{(-V)}+\alpha_T\overline{\int_V|\nabla\theta|^2dv} \tag{8.24}$$

Dividing by V on both sides of Eq. 8.24 gives

$$\frac{1}{V}\overline{\int_V w\theta dv}=\alpha_T(-1+\frac{1}{V}\overline{\int_V|\nabla\theta|^2dv}) \tag{8.25}$$

$$\langle w\theta\rangle=\alpha_T(-1+\langle|\nabla\theta|^2\rangle) \tag{8.26}$$

If the reference velocity is $V^{ref} = \alpha/H$ (diffusion scale) then $\alpha_T = 1$ and $Nu = 1 + \langle w\theta \rangle$. Thus,

$$Nu = 1 - 1 + \langle |\nabla\theta|^2 \rangle = \langle |\nabla\theta|^2 \rangle \tag{8.27}$$

On the other hand, for buoyancy scale $V^{ref} = \sqrt{g\beta\Delta TH}$, $\alpha_T = (RaPr)^{-1/2}$ and $Nu = 1 + (RaPr)^{1/2}\langle w\theta \rangle$. Thus,

$$Nu = 1 + (RaPr)^{-1/2}(RaPr)^{1/2}(-1 + \langle |\nabla\theta|^2 \rangle) = \langle |\nabla\theta|^2 \rangle \tag{8.28}$$

Now consider the non-dimensional momentum equation

$$\frac{\partial \boldsymbol{u}}{\partial t} + \boldsymbol{u} \cdot \nabla(\boldsymbol{u}) = -\nabla p + \alpha_u \nabla^2 \boldsymbol{u} + \alpha_b \theta \delta_{iZ} \tag{8.29}$$

Note that for diffusion scale $V^{ref} = \alpha/H$, $\alpha_u = Pr$ and $\alpha_b = RaPr$. Similarly for buoyancy scale $V^{ref} = \sqrt{g\beta\Delta TH}$, $\alpha_u = (Pr/Ra)^{1/2}$ and $\alpha_b = 1$. Here δ is the Kronecker delta. On contracting the above equation by $\boldsymbol{u}$, the different terms become

$$\begin{aligned}
\boldsymbol{u} \cdot \frac{\partial \boldsymbol{u}}{\partial t} &= \frac{\partial(\frac{1}{2}U^2)}{\partial t} \\
\boldsymbol{u} \cdot \{\boldsymbol{u} \cdot \nabla \boldsymbol{u}\} &= \nabla \cdot (\frac{1}{2}U^2 \boldsymbol{u}) \\
\boldsymbol{u} \cdot \nabla P &= \nabla \cdot (\boldsymbol{u}p) - p\nabla \cdot \boldsymbol{u} = \nabla \cdot (\boldsymbol{u}p) \\
\boldsymbol{u} \cdot \nabla^2 \boldsymbol{u} &= \nabla \cdot (\boldsymbol{u} \cdot \nabla \boldsymbol{u}) - |\nabla \boldsymbol{u}|^2 \\
\boldsymbol{u} \cdot \alpha_b \theta \delta_{iz} &= \alpha_b w\theta
\end{aligned}$$

Here U is the magnitude of the velocity vector $\boldsymbol{u}$. Thus, we obtain

$$\frac{\partial(\frac{1}{2}U^2)}{\partial t} + \nabla \cdot (\frac{1}{2}U^2 \boldsymbol{u}) = -\nabla \cdot (\boldsymbol{u}p) + \alpha_u \nabla \cdot (\boldsymbol{u} \cdot \nabla \boldsymbol{u}) - \alpha_u |\nabla \boldsymbol{u}|^2 + \alpha_b w\theta$$

Integrating the above equation over the entire volume V gives

$$\begin{aligned}
\int_V \frac{\partial(\frac{1}{2}U^2)}{\partial t} dv + \int_V \nabla \cdot (\frac{1}{2}U^2 \boldsymbol{u}) dv = &- \int_V \nabla \cdot (\boldsymbol{u}p) dv + \int_V \alpha_u \nabla \cdot (\boldsymbol{u} \cdot \nabla \boldsymbol{u}) dv \\
&- \int_V \alpha_u |\nabla \boldsymbol{u}|^2 dv + \int_V \alpha_b w\theta dv
\end{aligned}$$

Assuming constant volume and using the divergence theorem, we get

$$\frac{d}{dt}\int_V (\frac{1}{2}U^2)dv + \int_S (\frac{1}{2}U^2\boldsymbol{u})\cdot\hat{n}ds = -\int_S (\boldsymbol{u}p)\cdot\hat{n}ds + \int_S \alpha_u(\boldsymbol{u}\cdot\nabla\boldsymbol{u})\cdot\hat{n}ds - \int_V \alpha_u|\nabla\boldsymbol{u}|^2dv + \int_V \alpha_b w\theta dv \tag{8.30}$$

Owing to no-slip boundary condition on horizontal plates and no-slip/periodic boundary condition on the lateral walls,

$$\int_S (\frac{1}{2}U^2\boldsymbol{u})\cdot\hat{n}ds = 0$$
$$\int_S (\boldsymbol{u}p)\cdot\hat{n}ds = 0$$
$$\int_S \alpha_u(\boldsymbol{u}\cdot\nabla\boldsymbol{u})\cdot\hat{n}ds = 0$$

Thus,

$$\frac{d}{dt}\int_V (\frac{1}{2}U^2)dv = -\int_V \alpha_u|\nabla\boldsymbol{u}|^2dv + \int_V \alpha_b w\theta dv \tag{8.31}$$

Taking time average and subsequently dividing it by the volume results in

$$\overline{\frac{1}{V}\frac{d}{dt}\int_V (\frac{1}{2}U^2)dv} = \overline{-\frac{1}{V}\int_V \alpha_u|\nabla\boldsymbol{u}|^2dv} + \overline{\frac{1}{V}\int_V \alpha_b w\theta dv} \tag{8.32}$$

Using the result from Eq. 8.22, we obtain

$$\overline{\frac{1}{V}\frac{d}{dt}\int_V (\frac{1}{2}U^2)dv} = 0$$

This implies,

$$\langle w\theta\rangle = \frac{\alpha_u}{\alpha_b}\langle|\nabla\boldsymbol{u}|^2\rangle \tag{8.33}$$

For $V^{ref} = \alpha/H, \alpha_u = Pr, \alpha_b = RaPr$, and using Eq. 8.9, the Nusselt number becomes

$$\langle Nu\rangle = 1 + \frac{1}{Ra}\langle|\nabla\boldsymbol{u}|^2\rangle \tag{8.34}$$

Similarly, for $V^{ref} = \sqrt{g\beta\Delta TH}, \alpha_u = (Pr/Ra)^{1/2}, \alpha_b = 1$, and using Eq. 8.10

$$\langle Nu\rangle = 1 + Pr\langle|\nabla\boldsymbol{u}|^2\rangle \tag{8.35}$$

References

[1] Ingersoll A. P. Atmosphere dynamics of the outer planets. *Science*, **248**:2308–315, 1990.

[2] Heimpel M. & Aurnou J. Turbulent convection in rapidly rotating spherical shells: a model for equatorial and high latitude jets on jupiter and saturn. *Icarus*, **187**:540–557, 2007.

[3] Pirajno F. & Huston D. L. *Earth's Oldest Rocks*. Elsevier, 2019.

[4] Holmes A. Radioactivity and Earth movements. *Transactions of the Geological Society of Glasgow*, **18**:559–606, 1931.

[5] Coltice N., Gérault M., & Ulvrová M. A mantle convection perspective on global tectonics. *Earth Sci. Rev.*, **165**:120–150, 2017.

[6] Davies G. F. Whole-mantle convection and plate tectonics. *Geophys. J. Int.*, **49**:459–486, 1977.

[7] Morgan W. J. Deep mantle convection plumes and plate motions. *AAPG Bull.*, **56**:203–213, 1972.

[8] Turcotte D. L. & Oxburgh E. R. Mantle convection and the new global tectonics. *Ann. Rev. Fluid Mech.*, **4**:33–66, 1972.

[9] Hartmann D. L., Moy L. A., & Fu Q. Convection and the energy balance at the top of the atmosphere. *J. Climate*, **14**:4495–4511, 2001.

[10] Incropera F.P. *Liquid Cooling of Electronic Devices by Single-phase Convection*. John Wiley & Sons, 1999.

[11] Plate tectonics convergent boundaries. https://www.tes.com/lessons/iqQjEVZQzwerAg/plate-tectonics-convergent-boundaries, . Accessed: 2020-03-01.

[12] What are convection cells and how do they work? https://sciencestruck.com/what-are-convection-cells-how-do-they-work, . Accessed: 2020-03-01.

[13] Examine global surface currents. http://www.pbslearningmedia.org/resource/ess05.sci.ess.earthsys.globalsurf/, . Accessed: 2020-03-01.

[14] Internal structure of the sun, illustration. https://www.sciencephoto.com/media/947202/view/internal-structure-of-the-sun-illustration, . Accessed: 2020-03-01.

[15] Busse F.H. Convection driven zonal flows and vortices in the major planets. *Chaos*, **4**:123–134, 1994.

[16] Miesch M.S. The coupling of solar convection and rotation. *Solar Phys.*, **192**:59–89, 2000.

[17] King E. M. & Aurnou J. M. Turbulent convection in liquid metal with and without rotation. *Proc. Natl. Acad. Sci. U.S.A*, **110**:6688–6693, 2013.

[18] King E. M., Stellmach S., Noir J., Hansen U., & Aurnou J. M. Boundary layer control of rotating convection systems. *Nature*, **457**:301–304, 2009.

[19] Hassler D., Dammascha I., Lemaire P., Brekke P., Curdt W., Mason H., Vial J.-C., & Wilhelm K. Solar wind outflow and the chromospheric magnetic network. *Science*, **283**:810–813, 1999.

[20] Marshall J. & Schott F. Open-ocean convection: Observations, theory, and models. *Rev. Geophys.*, **37**:1–64, 1999.

[21] Rahmstorf S. The thermohaline ocean circulation: A system with dangerous thresholds. *Climate Change*, **46**:247–256, 2000.

[22] Hadley G. Concerning the cause of the general trade-windstropical. *Phil. Trans. R. Soc. Lond.*, **39**:58–62, 1735.

[23] Johnston J. P. Effects of system rotation on turbulence structures: a review relevant to turbomachinery flows. *Int. J. Rot. Mach.*, **4**:97–112, 1998.

[24] Wissen van R., Golombok M., & Brouwers J. J. H. Gas centrifugation with wall condensation. *AIChE Journal*, **52**:1271–1274, 2006.

[25] Chandrasekhar S. *Hydrodynamic and Hydromagnetic Stability*. Oxford University Press, 1961.

[26] Benard H. Les tourbillons cellulaires dans une nappe liquide. -Méthodes optiques d'observation et d'enregistrement. *Journal de Physique Théorique*, **10**:254–266, 1901.

[27] Rayleigh Lord. On convection currents in a horizontal layer of fluid, when the higher temperature is on the under side. *Philosophical Magazine and Journal of Science: Series 6*, **32**:529–546, 1916.

[28] Charlson G. S. & Sani R. L. Thermoconvective instability in a bounded cylindrical fluid layer. *Int. J. Heat Mass Transf.*, **13**:1479–1496, 1970.

[29] Buell J. & Catton I. The effect of wall conduction on the stability of a fluid in a right circular cylinder heated from below. *J. Heat Transfer*, **105**:255–260, 1983.

[30] Schmidt R. J. & Milverton S. W. On the instability of a fluid when heated from below. *Proc. Royal Soc. Lond. A*, **152**:586–594, 1935.

[31] Jeffreys H. The stability of a layer of fluid heated from below. *Philosophical Magazine and Journal of Science: Series 7*, **2**:833–844, 1926.

[32] Jeffreys H. Some cases of instability in fluid motion. *Proc. Royal Soc. Lond. A*, **118**:195–208, 1928.

[33] Low A. R. On the criterion for stability of a layer of viscous fluid heated from below. *Proc. Royal Soc. Lond. A*, **125**:180–195, 1929.

[34] Touihri R., Hadid H. Ben, & Henry D. On the onset of convective instabilities in cylindrical cavities heated from below. i. pure thermal case. *Phys. Fluids*, **11**:2078–2088, 1999.

[35] Ma D. J., Sun D. J., & Yin X. Y. Multiplicity of steady states in cylindrical Rayleigh-Bénard convection. *Phys. Rev. E*, **74**:2815–2817, 2006.

[36] Borońska K. & Tuckerman L. S. Extreme multiplicity in cylindrical Rayleigh-Bénard convection: I. time-dependence and oscillations. *Phys. Rev. E*, **81**:036–320, 2010.

[37] Neumann G. Three-dimensional numerical simulation of bouyancy-driven convection in vertical cylinder heated from below. *J. Fluid Mech.*, **214**:559–578, 1990.

[38] Hof B., Lucas P. G. J., & Mullin T. Flow state multiplicity in convection. *Phys. Fluids*, **11**: 2815–2817, 1999.

[39] Mutabazi I., Wesfreid J. E., & Guyon E. *Dynamics of spatio-temporal cellular structures*. Springer, New York, NY, 2006.

[40] Krishnamurthi R. & Howard L. N. Large-scale flow generation in turbulent convection. *Proc. Natl Acad. Sci. USA*, **78**:1981–1985, 1981.

[41] Li Y. R., Ouyang Y. Q., Peng L., & Wu S. Y. Direct numerical simulation of Rayleigh Bénard convection in a cylindrical container of aspect ratio 1 for moderate Prandtl number fluid. *Phys. Fluids*, **24**:1–16, 2012.

[42] D'Orazio M. C., Cianfrini C., & Corcione M. Rayleigh Bénard convection in tall rectangular enclosures. *Phys. Fluids*, **24**:1–16, 2012.

[43] Cioni S., Ciliberto S., & Sommeria J. Strongly turbulent Rayleigh-Bénard convection in mercury: comparison with results at moderate Prandtl number. *J. Fluid Mech.*, **335**:111–140, 1997.

[44] Niemela J. J., Skrbek L., Sreenivasan K. R., & Donnelly R. J. The wind in confined thermal convection. *J. Fluid Mech.*, **449**:169–178, 2001.

[45] Sreenivasan K. R., Bershadskii A., & Niemela J. J. Mean wind and its reversal in thermal convection. *Phys. Rev. E*, **65**:056306, 2002.

[46] Puthenveettil B. A. & Arakeri J. H. Plume structure in high-Rayleigh number convection. *J. Fluid Mech.*, **542**:217–249, 2005.

[47] Sun C., Xia K.-Q., & Tong P. Three-dimensional flow structures and dynamics of turbulent thermal convection in a cylindrical cell. *Phys. Rev. E*, **72**:026302, 2005.

[48] Daya Z. A. & Ecke R. E. Does turbulent convection feel the shape of the container? *Phys. Rev. Lett.*, **87**:184501, 2001.

[49] Wagner S., Shishkina O., & Wagner C. *Influence of geometry on Rayleigh-Bénard convection*. Springer International Publishing, 2014.

[50] Wagner S., Shishkina O., & Wagner C. Boundary layers and wind in cylindrical Rayleigh-Bénard cells. *J. Fluid Mech.*, **697**:336–366, 2012.

[51] Mishra P. K., De A. K., Verma M. K., & Eswaran V. Dynamics of reorientations and reversals of large-scale flow in Rayleigh-Bénard convection. *J. Fluid Mech.*, **668**:480–499, 2011.

[52] Verzicco R. & R.Camussi . Numerical experiments on strongly turbulent thermal convection in a slender cylindrical cell. *J. Fluid Mech.*, **477**:19–49, 2003.

[53] Lakharaju R., Stevens R. J. A. M., Verzicco R., Grossman S., Prosperetti A., Sun C., & Lohse. D. Spatial distribution of heat flux and fluctuations in turbulent Rayleigh-Bénard convection. *Phys. Rev. E*, **86**:056315, 2012.

[54] Brown E., Nikolaenko A., & Ahlers G. Reorientation of the large-scale circulation in turbulent Rayleigh-Bénard convection. *Phys. Rev. Lett.*, **95**:084503, 2005.

[55] Hansen U., Yuen D. A., & Kroening S. E. Mass and heat transport in strongly time-dependent thermal convection at infinite Prandtl number. *Geophys. Astrophys. Fluid Dyn.*, **63**:67–89, 1992.

[56] Brown E. & Ahlers G. Rotations and cessations of the large-scale circulation in turbulent Rayleigh-Bénard convection. *J. Fluid Mech.*, **568**:351–386, 2006.

[57] Ahlers G., Grossmann S., & Lohse D. Heat transfer and large scale dynamics in turbulent Rayleigh-Bénard convection. *Rev. Mod. Phys.*, **81**:503, 2009.

[58] Funfschilling D. & Ahlers G. Plume motion and large-scale circulation in a cylindrical Rayleigh-Bénard cell. *Phys. Rev. Lett.*, **92**:194502, 2004.

[59] Xi H.-D & Xia K.-Q. Cessations and reversals of the large-scale circulation in turbulent thermal convection. *Phys. Rev. E*, **75**:066307, 2007.

[60] Xi H.-D & Xia K.-Q. Azimuthal motion, reorientation, cessation, and reversal of the large-scale circulation in turbulent thermal convection: A comparative study in aspect ratio one and one-half geometries. *Phys. Rev. E*, **78**:036326, 2008.

[61] Bai K., Ji D., & Brown E. Ability of a low-dimensional model to predict geometry-dependent dynamics of large-scale coherent structures in turbulence. *Phys. Rev. E*, **93**:023117, 2016.

[62] Zocchi G., Moses E., & Libchaber A. Coherent structures in turbulent convection, an experimental study. *Physica A*, **166**:387–407, 1990.

[63] Qiu X.-L. & Xia K.-Q. Viscous boundary layers at the sidewall of a convection cell. *Phys. Rev. E*, **58**:486–491, 1998.

[64] Sun C., Chan T. S., & Xia K.-Q. Experimental studies of the viscous boundary layer properties in turbulent Rayleigh-Bénard convection. *J. Fluid Mech.*, **605**:79–113, 2008.

[65] Foroozani N., Niemela J. J., Armenio V., & Sreenivasan K. R. Reorientations of the large-scale flow in turbulent convection in a cube. *Phys. Rev. E*, **95**:033107, 2017.

[66] Giannakis D., Kolchinskaya A., Krasnov D., & Schumacher J. Koopman analysis of the long-term evolution in a turbulent convection cell. *J. Fluid Mech.*, **847**:735–767, 2018.

[67] Wang J. & Xia K.-Q. Spatial variations of the mean and statistical quantitiesin the thermal boundary layers of turbulent convection. *Eur. Phys. J. B*, **32**:127–136, 2003.

[68] Werne J. Structure of hard-turbulent convection in two dimensions: Numerical evidence. *Phys. Rev. E*, **48**:1020(16), 1993.

[69] Lui S. L. & Xia K. Q. Spatial structure of the thermal boundary layer in turbulent convection. *Phys. Rev. E*, **57**:5494–5503, 1998.

[70] Qiu X.-L. & Xia K.-Q. Spatial structure of the viscous boundary layer in turbulent convection. *Phys. Rev. E*, **58**:5816–5820, 1998.

[71] Foroozani N., Niemela J. J., Armenio V., & Sreenivasan K. R. Influence of container shape on scaling of turbulent fluctuations in convection. *Phys. Rev. E*, **90**:063003, 2014.

[72] Chandra M. & Verma M. K. Dynamics and symmetries of flow reversals in turbulent convection. *Phys. Rev. E*, **83**:067303, 2011.

[73] Malkus M. V. R. The heat transport and spectrum of thermal turbulence. *Proc. Royal Soc. Lond. A*, **225**:196–212, 1954.

[74] Casting B., Gunaratne G., Heslot F., Kadanoff L., Libchaber A., Thomae S., Wu X.-Z., Zaleski S., & Zanetti G. Scaling of hard thermal turbulence in Rayleigh-Bénard convection. *J. Fluid Mech.*, **204**:1–30, 1989.

[75] Shraiman B. I. & Siggia E. D. Heat transport in high-Rayleigh number convection. *Phys. Rev. A*, **42**:3650–3653, 1990.

[76] Grossmann S. & Lohse D. Scaling in thermal convection: a unifying theory. *J. Fluid Mech.*, **407**:27–56, 2000.

[77] Grossmann S. & Lohse D. Thermal convection for large Prandtl numbers. *Phys. Rev. Lett.*, **86**: 3316–3319, 2001.

[78] Grossmann S. & Lohse D. Prandtl and Rayleigh number dependence of the Reynolds number in turbulent thermal convection. *Phys. Rev. E*, **66**:016305, 2002.

[79] Siggia E. D. High-Rayleigh number convection. *Annu. Rev. Fluid Mech.*, **26**:137–168, 1994.

[80] Iyer K. P., Scheel J. D., Schumacher J., & Sreenivasan K. R. Classical 1/3 scaling of convection holds up to Ra= 10^{15}. *Proc. Natl. Acad. Sci.*, **117**:7594–7598, 2020.

[81] Kraichnan R. H. Turbulent thermal convection at arbitrary Prandtl number. *Phys. Fluids*, **5**: 1374–1389, 1962.

[82] Lohse D. & Toschi F. The ultimate state of thermal convection. *Phys. Rev. Lett.*, **90**:034502, 2003.

[83] Calzavarini E., Lohse D., Toschi F., & R.Tripiccione . Rayleigh and Prandtl number scaling in the bulk of Rayleigh-Bénard turbulence. *Phys. Fluids*, **17**:055107, 2005.

[84] Cholemari M. R. & Arakeri J. H. Experiments and a model of turbulent exchange flow in a vertical pipe. *Int. J. Heat Mass Transfer*, **48**:4467–4473, 2005.

[85] Cholemari M. R. & Arakeri J. H. Axially homogeneous, zero mean flow buoyancy-driven turbulence in a vertical pipe. *J. Fluid Mech.*, **621**:69–102, 2009.

[86] Chillà F., Rastello M., Chaumat S., & Castaing B. Ultimate regime in Rayleigh-Bénard convection: The role of plates. *Phys. Fluids*, **16**:2452–2456, 2004.

[87] Moses E., Zocchi G., & Libchaber A. An experimental study of laminar plumes. *J. Fluid Mech.*, **251**:581–601, 1993.

[88] E E. Kaminski & Jaupart C. Laminar starting plumes in high-Prandtl-number fluids. *J. Fluid Mech.*, **478**:287–298, 2003.

[89] Xi H.-D., Lam S., & Xia K.-Q. From laminar plumes to organized flows: the onset of large-scale circulation in turbulent thermal convection. *J. Fluid Mech.*, **503**:47–56, 2004.

[90] Belmonte A. & Libchaber A. Thermal signature of plumes in turbulent convection: The skewness of the derivative. *Phys. Rev. E.*, **53**:4893–4898, 1996.

[91] Julien K., Legg S., MacWilliams J., & Werne J. Plumes in rotating convection. part 1. ensemble statistics and dynamical balances. *J. Fluid Mech.*, **391**:151–187, 1999.

[92] Zhou S. O. & Xia K. Q. Plume statistics in thermal turbulence: mixing of an active scalar. *Phys. Rev. Lett.*, **89**:184502, 2002.

[93] Alexandre P. B., Falasca F., Hardenberg J. V., & Provenzale A. Plume dynamics in rotating Rayleigh-Bénard convection. *Phys. Lett. A*, **380**:1363–1367, 2016.

[94] Shishkina O. & Wagner C. Analysis of thermal dissipation rates in turbulent Rayleigh-Bénard convection. *J. Fluid Mech.*, **546**:51–60, 2006.

[95] Emran M. S. & Schumacher J. Conditional statistics of thermal dissipation in turbulent Rayleigh-Bénard convection. *Eur. Phys. J. E*, **35**:108, 2012.

[96] Poel van der E. P., Verzicco R., Grossmann S., & Lohse D. Plume emission statistics in turbulent Rayleigh-Bénard convection. *J. Fluid Mech.*, **772**:5–15, 2015.

[97] Parodi A., Hardenberg von J., Passoni G., Provenzale A., & Spiegel E. A. Clustering of plumes in turbulent convection. *Phys. Rev. Lett.*, **92**:194503, 2004.

[98] Zhou S.-Q., Xie Y.-C., Sun C., & Xia K.-Q. Statistical characterization of thermal plumes in turbulent thermal convection. *Phys. Rev. Fluids*, **1**:054301, 2016.

[99] Chandrasekhar S. The instability of a layer of fluid heated below and subject to coriolis forces. *Proc. Royal Soc. Lond. A*, **217**:306–327, 1953.

[100] Fultz D. & Nakagawa Y. Experiments on over-stable thermal convection in mercury. *Proc. Royal Soc. Lond. A*, **235**:211–225, 1955.

[101] Taylor G. I. Experiments on the motion of solid bodies in rotating fluids. *Proc. Royal Soc. Lond. A*, **104**:213–218, 1923.

[102] Proudman J. On the motion of solids in a liquid possessing vorticity. *Proc. Royal Soc. Lond. A*, **92**:408–424, 1916.

[103] Tritton D. J. *Physical Fluid Dynamics*. Van Nostrand Reinhold(UK) Co. Ltd, 1982.

[104] Veronis G. Cellular convection with finite amplitude in a rotating fluid. *J. Fluid Mech.*, **5**: 401–435, 1959.

[105] Veronis G. Large-amplitude Bénard convection in a rotating fluid. *J. Fluid Mech.*, **31**:113–139, 1968.

[106] Lucas P. J., Pfotenhauer J., & Donnelly R. Stability and heat transfer of rotating cryogens. part 1. influence of rotation on the onset of convection in liquid 4 he. *J. Fluid Mech.*, **129**:245–264, 1983.

[107] Pfotenhauer J., Lucas P. J., & Donnelly R. Stability and heat transfer of rotating cryogens. part 2. effects of rotation on heat-transfer properties of convection in liquid he. *J. Fluid Mech.*, **145**: 239–252, 1984.

[108] Pfotenhauer J., Niemela J., & Donnelly R. Stability and heat transfer of rotating cryogens.part 3. effects of finite cylindrical geometry and rotation on the onset of convection. *J. Fluid Mech.*, **175**:85–96, 1987.

[109] Zhong F., Ecke R., & Steinberg V. Rotating Rayleigh-Bénard convection: asymmetric modes and vortex states. *J. Fluid Mech.*, **249**:135–159, 1993.

[110] Lopez J. M., Marques F., Mercader I., & Batiste O. Onset of convection in a moderate aspect-ratio rotating cylinder: Eckhaus-Benjamin-Feir instability. *J. Fluid Mech.*, **72**:36307–36315, 2007.

[111] Marques F. & Lopez J. M. Influence of wall modes on the onset of bulk convection in a rotating cylinder. *Phys. Fluids*, **20**:024109, 2008.

[112] Lopez J., Rubio A., & Marques F. Travelling circular waves in axisymmetric rotating convection. *J. Fluid Mech.*, **569**:331–348, 2006.

[113] Lopez J. & Marques F. Centrifugal effects in rotating convection: nonlinear dynamics. *J. Fluid Mech.*, **628**:269–297, 2009.

[114] Lopez J. & Marques F. Onset of Küppers-Lortz-like dynamics in finite rotating thermal convection. *J. Fluid Mech.*, **644**:337–357, 2010.

[115] Rossby H. T. A study of Bénard convection with and without rotation. *J. Fluid Mech.*, **36**: 309–335, 1969.

[116] Julien K., Legg S., MacWilliams J., & Werne J. Rapidly rotating turbulent Rayleigh-Bénard convection. *J. Fluid Mech.*, **322**:243–273, 1996.

[117] Vorobieff P. & Ecke R. Turbulent rotating convection: an experimental study. *J. Fluid Mech.*, **458**:191–218, 2002.

[118] Liu Y. & Ecke R. E. Heat transport measurements in turbulent rotating Rayleigh-Bénard convection. *Phys. Rev. E*, **80**:036314, 2009.

[119] Niemela J. J., Babuin S., & Sreenivasan K. R. Turbulent rotating convection at high Rayleigh and taylor numbers. *J. Fluid Mech.*, **649**:509–522, 2010.

[120] Stevens R. J. A. M., Clercx H. J. H., & Lohse D. Heat transport and flow structures in rotating Rayleigh-Bénard convection. *Eur. J. Mech. B Fluids*, **40**:41–49, 2013.

[121] Vishnu R. & Sameen A. Heat transport in rotating-lid Rayleigh-Bénard convection. *Physica D*, **94**:054004, 2019.

[122] Novi L., Hardenberg von J., Hughes D. W., Provenzale A., & Spiegel E. A. Rapidly rotating Rayleigh-Bénard convection with a tilted axis. *Phys. Rev. E*, **99**:053116, 2019.

[123] Julien K., Legg S., MacWilliams J., & Werne J. Hard turbulence in rotating Rayleigh-Bénard convection. *Phys. Rev. E*, **53**:R5557–R5560, 1996.

[124] Kunnen R. P. J., Geurtz B. J., & Clercx H. J. H. Direct numerical simulation of turbulent rotating Rayleigh-Bénard convection. In *Direct and Large-Eddy Simulation VI*, volume 10, pages 233–240, 2006.

[125] Kunnen R. P. J., Clercx H. J. H., & Geurtz B. J. Heat flux intensification by vortical flow localization in rotating convection. *Phys. Rev. E*, **74**:056306,1–4, 2006.

[126] Kunnen R. P. J., Geurtz B. J., & Clercx H. J. H. Turbulence statistics and energy budget in rotating rotating Rayleigh-Bénard convection. *Eur. J. Mech. B Fluids*, **28**:578–589, 2009.

[127] Stevens R. J. A. M., Clercx H. J. H., & Lohse D. Numerical simulations of rotating Rayleigh-Bénard convection. In *Direct and Large-Eddy Simulation VIII*, volume 15, pages 359–364, 2011.

[128] Kunnen R. P. J., Geurtz B. J., & Clercx H. J. H. Breakdown of large-scale circulation in turbulent rotating convection. *Europhys. Lett.*, **84**:24001:1–6, 2008.

[129] Kunnen R. P. J., Geurtz B. J., & Clercx H. J. H. Experimental and numerical investigation of turbulent convection in a rotating cylinder. *J. Fluid Mech.*, **642**:445–476, 2010.

[130] Kunnen R. P. J., Geurtz B. J., & Clercx H. J. H. Vortex statistics in turbulent rotating convection. *Phys. Rev. E*, **82**:036306, 2010.

[131] Oresta P., Stringano G., & Verzicco R. Transitional regimes and rotation effects in Rayleigh-Bénard convection in a slender cylindrical cell. *Eur. J. Mech. B Fluids*, **26**:1–14, 2007.

[132] Schmitz S. & Tilgner A. Heat transport in rotating convection without Ekman layers. *Phys. Rev. E*, **80**:015305, 1990.

[133] Schmitz S. & Tilgner A. Transitions in turbulent rotating Rayleigh-Bénard convection. *Geophysical and Astrophysical Fluid Dynamics*, **104**:481–489, 2020.

[134] Zhong J. Q. & Ahlers G. Heat transport and the large-scale circulation in rotating turbulent Rayleigh-Bénard convection. *J. Fluid Mech.*, **665**:300–333, 2010.

[135] Zhong J. Q., Stevens R. J. A. M., Clercx H. J. H., Verzicco R., Lohse D., & Ahlers G. Prandtl-, Rayleigh-, and Rossby-number dependence of heat transport in turbulent rotating Rayleigh-Bénard convection. *Phys. Rev. Lett.*, **102**:044502:1–4, 2009.

[136] Kunnen R. P. J., Stevens R. J. A. M., Overkamp J., Sun C., Heijst van G. F., & Clercx H. J. H. The role of Stewartson and Ekman layers in turbulent rotating Rayleigh-Bénard convection. *J. Fluid Mech.*, **688**:422–442, 2011.

[137] Weiss S. & Ahlers G. Heat transport by turbulent rotating Rayleigh-Bénard convection and its dependence on the aspect ratio. *J. Fluid Mech.*, **684**:407–426, 2011.

[138] Stevens R. J. A. M., Clercx H. J. H., & Lohse D. Optimal Prandtl number for heat transfer in rotating Rayleigh-Bénard convection. *New J. Phys*, **12**:359–364, 2010.

[139] Horn S. & Shishkina O. Toroidal and poloidal energy in rotating Rayleigh-Bénard convection. *J. Fluid Mech.*, **762**:232–255, 2015.

[140] King E. M., Stellmach S., & Buffett B. Scaling behavior in Rayleigh-Bénard convection with and without rotation. *J. Fluid Mech.*, **717**:449–471, 2013.

[141] Geurtz B. J. & Kunnen R. P. J. Intensified heat transfer in modulated rotating Rayleigh-Bénard convection. *Int. J. Heat Fluid Flow*, **49**:62–68, 2014.

[142] De A. K. & Dalal A. Numerical simulation of unconfined flow past a triangular cylinder. *Int. J. Numer. Meth. Fluids*, **52**:801–821, 2006.

[143] De A. K. An implicit non-staggered cartesian grid methodfor incompressible viscous flows in complex geometriesy. *Sadhana*, **39**:1071–1094, 2014.

[144] Peter S. & De A. K. A parallel implementation of the ghost-cell immersed boundarymethod with application to stationary and moving boundary problems. *Sadhana*, **41**:441–450, 2016.

[145] Ferziger J. H. & Peric M. *Computational methods for fluid dynamics*. Springer, 2002.

[146] Saad Y. *Iterative Methods for Sparse Linear systems*. Siam, 2003.

[147] Stone H. L. Iterative solution of implicit approximation of multidimensional partial differential equations. *SIAM J Numer Anal*, **5**:530–558, 1968.

[148] Zhang & Shao-Liang . Gpbi-cg: Generalized product-type methods based on bi-cg for solving nonsymmetric linear systems. *SIAM J Sci Comput*, **18**(2):537–551, 1997.

[149] Anderson D. A., Tannehill J. C., & Pletcher R. H. *Computational Fluid Mechanics and Heat Transfer*. Taylor an Francis, 1997.

[150] Rudiger S. & Knobloch E. Mode interaction in rotating Rayleigh-Bénard convection. *Fluid Dyn. Res.*, **33**:477–492, 2003.

[151] Kaczorowski M. & Xia K.-Q. Turbulent flow in the bulk of Rayleigh-Bénard convection: small-scale properties in a cubic cell. *J. Fluid Mech.*, **722**:596–617, 2013.

[152] Grotzbach G. Spatial resolution requirements for direct numerical simulation of the Rayleigh-Bénard convection. *J. Comput. Phys*, **49**:241–264, 1983.

[153] Stevens R. J. A. M., Verzicco R., & Lohse D. Radial boundary layer structure and Nusselt number in Rayleigh-Bénard convection. *J. Fluid Mech.*, **643**:495–507, 2010.

[154] Russo G. P. *Aerodynamic Measurements*. Woodhead Publishing, 2011.

[155] Venugopal V. T. & De A. K. Flow periodicity and convection modes in rotating Rayleigh-Bénard convection at low Rayleigh numbers. *Sadhana*, **44**:27, 2019.

[156] Xi H.-D., Zhang Y.-B., Hao J.-T, & Xia K.-Q. Higher-order flow modes in turbulent Rayleigh-Bénard convection. *J. Fluid Mech.*, **805**:31–51, 2016.

[157] Vishnu V. T., De A. K., & Mishra P. K. Significance of Prandtl number on the heat transport and flow structure in rotating Rayleigh-Bénard convection. *ASME J. Heat Transfer*, **142**:012501, 2019. doi: DOI:10.1115/1.4045062.

[158] Bai X.-D., Zhang W., Fang Q.-H., Wang Y., Zheng J.-H, & Guo A.-X. The visualization of turbulent coherent structure in open channel flow. *J. Hydrodyn*, **31(2)**:266–273, 2019.

[159] Hussain A. K. M. F. Role of coherent structures in turbulent shear flows. *Prec. Indian Acad. Sci*, **4**:129–175, 1981.

[160] Fiedler H. E. Coherent structures in turbulent flows. *Prog. Aerospace Sci.*, **25**:231–269, 1988.

[161] Rockwood M., Huang Y., & Green M. Tracking coherent structures in massively-separated and turbulent flows. *Phys. Rev. Fluids*, **3**:014702, 2018.

[162] Stevens R. J. A. M., Clercx H. J. H., & Lohse D. Effect of plumes on measuring the large scale circulation in turbulent Rayleigh-Bénard convection. *Phys. Fluids*, **23**:095110, 2011.

[163] Xi H.-D., Zhou S.-Q., Zhou Q., Chan T. S., & Xia K.-Q. Origin of the temperature oscillation in turbulent thermal convection. *Phys. Rev. Lett.*, **102**:044503, 2009.

[164] Cheng J. S., Stellmach S., Ribeiro A., Grannan A., King M., & Aurnou M. Laboratory-numerical models of rapidly rotating convectionin planetary cores. *Geophys. J. Int.*, **201**:1–17, 2015.

[165] De A. K., Eswaran V., & Mishra P. K. Scalings of heat transport and energy spectra of turbulent Rayleigh-Bénard convection in a large-aspect-ratio box. *Int. J. Heat Fluid Flow*, **67**:111–124, 2017.

[166] Kooij G. L., Botchev M. A., & Geurts B. J. Direct numerical simulation of Nusselt number scaling in rotating Rayleigh-Bénard convection. *Int. J. Heat Fluid Flow*, **55**:26–33, 2015.

[167] Grossmann S. & Lohse D. Fluctuations in turbulent Rayleigh-Bénard convection:the role of plumes. *Phys. Fluids*, **16**:4462–4471, 2004.

[168] Kolmogorov A. N. A refinement of previous hypotheses concerning the local structure of turbulence in a viscous incompressible fluid at high Reynolds number. *J. Fluid Mech.*, **13**:82–85, 1962.

[169] Zhang Y., Zhou Q., & Sun C. Statistics of kinetic and thermal energy dissipation rates in two-dimensional turbulent Rayleigh-Bénard convection. *J. Fluid Mech.*, **814**:165–184, 2017.

[170] Emran M. S. & Schumacher J. Fine-scale statistics of temperature and its derivatives in convective turbulence. *J. Fluid Mech.*, **611**:13–34, 2008.

[171] Schumacher J. & Sreenivasan K. R. Statistics and geometry of passive scalars in turbulence. *Phys. Fluids*, **17**:125107, 2005.

[172] Kaczorowski M. & Wagner C. Analysis of the thermal plumes in turbulent Rayleigh-Bénard convection based on well-resolved numerical simulations. *J. Fluid Mech.*, **618**:89–112, 2009.

[173] Kerr R. Rayleigh number scaling in numerical convection. *J. Fluid Mech.*, **310**:139–179, 1996.

[174] Fernando H., Chen R., & Boyer D. Effects of rotation on convective turbulence. *J. Fluid Mech.*, **228**:513–547, 1991.

[175] Priestley C. H. B. *Turbulent Transfer in the Lower Atmosphere*. University of Chicago Press, 1959.

[176] Priestley C. H. B. *Buoyancy Effects in Fluid*. Cambridge University Press, 1973.

[177] Zhou Q. O. & Xia K.-Q. Thermal boundary layer structure in turbulent Rayleigh-Bénard convection in a rectangular cell. *J. Fluid Mech.*, **721**:199–224, 2013.

[178] Grossmann S. & Lohse D. Multiple scaling in the ultimate regime of thermal convection. *Phys. Fluids*, **23**:045108, 2011.

[179] Belmonte A., Tilgner A., & Libchaber A. Temperature and velocity boundary layers in turbulent convection. *Phys. Rev. E.*, **50**:269–280, 1994.

[180] Verzicco R. & R.Camussi . Prandtl number effects in convective turbulence. *J. Fluid Mech.*, **383**: 55–73, 1999.

[181] Zhou S. O., Sugiyama K., Stevens R. J. A. M., Grossmann S., Lohse D., & Xia K. Q. Horizontal structures of velocity and temperature boundary layers in two-dimensional numerical turbulent Rayleigh-Bénard convection. *Phys. Fluids*, **23**:125104, 2011.

[182] Ekman V. W. On the influence of the Earth's rotation on ocean currents. *Ark. Mat. Astron. Fys.*, **2**:1–53, 1905.

[183] Tilgner A., Belmonte A., & Libchaber A. Temperature and velocity profiles of turbulent convection in water. *Phys. Rev. E.*, **47**:R2253–R2256, 1993.

[184] Xin Y.-B., Xia K.-Q., & Tong P. Measured velocity boundary layers in turbulent convection. *Phys. Rev. Lett.*, **77**:1266, 1996.

[185] Sano M., Wu X.-Z., & Libchaber A. Turbulence in helium gas free convection. *Phys. Rev. A*, **40**: 6421–6430, 1989.

[186] Cioni S., Ciliberto S., & Sommeria J. Large-scale flow properties of turbulent thermal convection. *Phys. Rev. E*, **54**:R5901–R5904, 1996.

[187] Qiu X.-L. & Tong P. Large-scale velocity structures in turbulent thermal convection. *Phys. Rev. E*, **64**:036304–1 – 036304–13, 2001a.

[188] Sun C., Xi H.-D, & Xia K.-Q. Azimuthal symmetry, flow dynamics, and heat transport in turbulent thermal convection in a cylinder with an aspect ratio of 0.5. *Phys. Rev. Lett*, **95**:074502, 2005.

[189] Tsuji Y., Mizuno T, Mashiko T., & Sano M. Mean wind in convective turbulence of mercury. *Phys. Rev. Lett*, **94**:034501–1 – 034501–4, 2005.

[190] Brown E. & Ahlers G. Large-scale circulation model for turbulent Rayleigh-Bénard convection. *Phys. Rev. Lett.*, **98**:134501, 2007.

[191] Dabbagh F., Trias F. X., Gorobets A., & Oliva A. On the evolution of flow topology in turbulent Rayleigh-Bénard convection. *Phys. Fluids*, **28**:115105, 2016.

[192] Keller J. B. Periodic oscillations in a model of thermal convection. *J. Fluid Mech.*, **26**:599–606, 1966.

[193] Welander P. On the oscillatory instability of a differentially heated fluid loop. *J. Fluid Mech.*, **29**:17–30, 1967.

[194] Creveling H. F., DePaz J. F., Baladi J. Y., & Schoenhals R. J. Stability characteristics of a single-phase free convection loop. *J. Fluid Mech.*, **67**:65–84, 1975.

[195] Gorman M., Widmann P. J., & Robbins K. A. Chaotic flow regimes in a convection loop. *Phys. Rev. Lett*, **52**:2241–2244, 1984.

[196] Doorn van E., Dhruva B., Sreenivasan K. R., & Cassella V. Statistics of wind direction and its increments. *Phys. Fluids*, **12**:1529, 2000.

[197] Mishra P., Gissinger C., Dormy E., & Fauve S. Energy transfers during dynamo reversals. *Europhys. Lett.*, **104**:69002, 2013.

[198] Stringano G. & Verzicco R. Mean flow structure in thermal convection in a cylindrical cell of aspect ratio one half. *J. Fluid Mech.*, **548**:1–16, 2006.

[199] Benzi R. & Verzicco R. Numerical simulations of flow reversal in Rayleigh-Bénard convection. *Europhys. Lett.*, **81**:64008, 2008.

[200] Hart J. E., Kittelman S., & Ohlsen D. R. Mean flow precession and temperature probability density functions in turbulent rotating convection. *Phys. Fluids*, **14**:955–962, 2002.

[201] Weiss S. & Ahlers G. The large-scale flow structure in turbulent rotating Rayleigh-Bénard convection. *J. Fluid Mech.*, **688**:461–492, 2011.

[202] Stevens R. J. A. M., Clercx H. J. H, & Lohse D. Breakdown of the large-scale circulation in Γ=1/2 rotating Rayleigh-Bénard flow. *Phys. Rev. E*, **86**:056311, 2012.

[203] Puits du R. & Willert C. The evolution of the boundary layer in turbulent Rayleigh-Bénard convection in air. *Phys. Fluids*, **28**:044108, 2016.

[204] Schumacher J. & Scheel J. D. Extreme dissipation event due to plume collision in a turbulent convection cell. *Phys. Rev. E*, **94**:043104, 2016.

[205] Verma M. K. *Physics of Buoyant Flows: From Instabilities to Turbulence*. World Scientific, Singapore,, 2018.

[206] Xi H. D., Zhou Q., & Xia K. Q. Azimuthal motion of the mean wind in turbulent thermal convection. *Phys. Rev. E*, **73**:056312, 2006.

[207] Newman M. E. J. Power laws, Pareto distributions and Zipf's law. *Contemp. Phys.*, **46**:323–351, 2005.

[208] Bevington P. R. & Robinson D. K. *Data Reduction and Error Analysis for the Physical Sciences*. McGraw-Hil, 1992.

[209] Weiss S., Wei P., & Ahlers G. Heat-transport enhancement in rotating turbulent Rayleigh-Bénard convection. *Phys. Rev. E*, **93**:043102(16), 2016.

[210] Poel van der E. P., Stevens R. J. A. M., & Lohse D. Connecting flow structures and heat flux in turbulent Rayleigh-Bénard convection. *Phys. Rev. E*, **84**:045303(R), 2011.

[211] Pharasi H. K., Kannan R., Kumar K., & K. Bhattacharjee j. . Turbulence in rotating Rayleigh-Bénard convection in low-Prandtl-number fluids. *Phys. Rev. E*, **84**:047301, 2011.

[212] Guzman A. Aguirre, Ostilla-Monica R., Clercx H. J. H., & Kunnen R. P. J. Rotating Rayleigh-Bénard convection at low Prandtl number. In *APS Meeting of Fluid Dynamics*, volume 62, 2017.

[213] Verzicco R. & Camussi R. Transitional regimes of low-Prandtl thermal convection in a cylindrical cell. *Phys. Fluids*, **9**:1287–1294, 1997.

[214] Silano G., Sreenivasan K. R., & Verzicco R. Numerical simulations of Rayleigh-Bénard convection for Prandtl numbers between 10^{-1} and 10^{4} and Rayleigh numbers between 10^{5} and 10^{9}. *J. Fluid Mech.*, **662**:409–446, 2010.

[215] Ning L. & Ecke R. Rotating Rayleigh-Bénard convection: Aspect-ratio dependence of the initial bifurcations. *Phys. Rev. E*, **47**:3326–3333, 1993.

[216] Roche P. E., Castaing B., Chabaud B., & Hebral B. Prandtl and Rayleigh numbers dependences in Rayleigh-Bénard convection. *Europhys. Lett.*, **58**:693–698, 2002.

[217] Chillà F., Rastello M., Chaumat S., & Castaing B. Long relaxation times and tilt sensitivity in Rayleigh-Bénard turbulence. *Eur. Phys. J. B*, **40**:223–227, 2004.

[218] Nikolaenko A., Brown E., Funfschilling D., & Ahlers G. Heat transport by turbulent Rayleigh-Bénard convection in cylindrical cells with aspect ratio one and less. *J. Fluid Mech.*, **523**:251–260, 2005.

[219] Weiss S. & Ahlers G. Turbulent Rayleigh-Bénard convection in a cylindrical container with aspect ratio Γ=0.5 and Prandtl number Pr =4.38. *J. Fluid Mech.*, **676**:5–40, 2011.

[220] Chillà F. & Schumacher J. New perspectives in turbulent Rayleigh-Bénard convection. *Eur. Phys. J. E*, **58**:35–59, 2012.

[221] Sparrow E. M., Husar R. B., & Goldstein R. J. Observations and other characteristics of thermals. *J. Fluid Mech.*, **41**:793–800, 1970.

[222] Shishkina O. & Wagner C. Analysis of sheet-like thermal plumes in turbulent Rayleigh-Bénard convection. *J. Fluid Mech.*, **599**:383–404, 2008.

[223] Zhang J., Childress S., & Libchaber A. Non-boussinesq effect: thermal convection with broken symmetry. *Phys. Fluids*, **9**:1034–1042, 1997.

[224] Zhou Q. & Xia K.-Q. Physical and geometrical properties of thermal plumes in turbulent Rayleigh-Bénard convection. *New J. Phys.*, **12**:075006, 2010.

[225] Gluckman B. J., Willaime H., & Gollub J. P. Geometry of isothermal and isoconcentration on surfaces in thermal turbulence. *Phys. Fluids A*, **5**:647–61, 1993.

[226] Tanaka H. & Miyata H. Turbulent natural convection in a horizontal water layer heated from below. *Int. J. Heat Mass Transfer*, **23**:1273–1281, 1980.

[227] Haramina T. & Tilgner A. Coherent structures in boundary layers of Rayleigh-Bénard convection. *Phys. Rev. E*, **69**:056306, 2004.

[228] Zhou Q., Sun C., & Xia K.-Q. Morphological evolution of thermal plumes in turbulent Rayleigh-Bénard convection. *Phys. Rev. Lett.*, **98**:074501, 2007.

[229] Funfschilling D., Brown E., & Ahlers G. Torsional oscillations of the large-scale circulation in turbulent Rayleigh-Bénard convection. *J. Fluid Mech.*, **607**:119–139, 2008.

[230] Bosbach J., Weiss S., & Ahlers G. Plume fragmentation by bulk interactions in turbulent Rayleigh-Bénard convection. *Phys. Rev. Lett.*, **108**:054501, 2012.

[231] Grossmann S. & Lohse D. On geometry effects in Rayleigh-Bénard convection. *J. Fluid Mech.*, **486**:105–114, 2003.

[232] He X.-Z., Ching E. S. C., & Tong P. Locally averaged thermal dissipation rate in turbulent Rayleigh-Bénard convection: a decomposition into contributions from different temperature gradient components. *Phys. Fluids*, **23**:025106, 2011.

[233] Bhattacharya S., Pandey A., Kumar A., & Verma M. K. Complexity of viscous dissipation in turbulent thermal convection. *Phys. Fluids*, **30**:031702, 2018.

[234] Pandey A., Scheel J. D., & Schumacher J. Turbulent superstructures in Rayleigh-Bénard convection. *Nature Commun.*, **9**:2118, 2018.

[235] Dennis D. J. C. Coherent structures in wall-bounded turbulence. *Anais da Academia Brasileira de Ciencias*, **87**:1161–93, 2015.

[236] Chong M. S., Perry A. E., & Cantwell . A general classification of three-dimensional flow field. *Phys. Fluids A*, **2**:765–777, 1990.

[237] Hunt J. C. R., Wray A. A., & Moin P. Eddies, stream, and convergence zones in turbulent flows. *Center for Turbulence Research Report CTR-S88*, :193–208, 1988.

[238] Jeong J. & Hussain F. On the identification of a vortex. *J. Fluid Mech.*, **285**:69–94, 1995.

[239] Stevens R. J. A. M., Poel van der E.P., Grossmann S., & Lohse D. The unifying theory of scaling in thermal convection: The updated prefactors. *J. Fluid Mech.*, **736**:177–194, 2013.

[240] Chu T. Y. & Goldstein J. R. Turbulent convection in a horizontal layer of water. *J. Fluid Mech.*, **60**:141–159, 1973.

[241] Wu X. Z. & Libchaber A. Scaling relations in thermal turbulence: The aspect-ratio dependence. *Phys. Rev. A*, **45**:842–845, 1992.

[242] Ahlers G. & Xu X. Prandtl-number dependence of heat trans-port in turbulent Rayleigh-Bénard convectio. *Phys. Rev. Lett.*, **86**:3320, 2001.

[243] Kaczorowski M. & Wagner C. Direct numerical simulation of turbulent convection in a rectangular Rayleigh-Bénard cell. *Proceedings of* 5^{th} *International Symposium on Turbulence and Shear Flow Phenomena, Garching*, **2**:499–504, 2007.

[244] Monica R. O., Yang Y., Poel van der E. P., Lohse D., & Verzicco R. A multiple-resolution strategy for direct numerical simulation of scalar turbulence. *J. Comput. Phys*, **301**:308–321, 2015.

[245] Shang X.-D., Qiu X.-L., Tong P., & Xia K.-Q. Measurements of the local convective heat flux in turbulent Rayleigh-Bénard convection. *Phys. Rev. E*, **70**:026308, 2004.

[246] Lulff J. Describing the heat transport of turbulent Rayleigh-Bénard convection by POD methods. *Physics. Flu-dyn*, **arXiv**, 2015.

[247] Lohse D. & Grossmann S. Intermittency in turbulence. *Physica A*, **194**:519–531, 1993.

[248] Debue P., Shukla V., Kuzzay D., Faranda D., Saw E.-W., Daviaud F., & Dubrulle B. Dissipation, intermittency, and singularities in incompressible turbulent flows. *Phys. Rev. E*, **97**:53101, 2018.

[249] Staicu A.D. *Intermittency in turbulence*. Ph.D. thesis, Department of Applied Physics, Technische Universiteit Eindhoven, 2002.

[250] Overholt M. R. & Pope S. B. Direct numerical simulation of a passive scalar with imposed mean gradient in isotropic turbulence. *Phys. Fluids*, **8**:3128–3148, 1996.

[251] Obukhov A. M. Some specific features of atmospheric turbulence. *J. Geophys. Res.*, **67**:3011, 1962.

[252] Ching E. S. C., Guo H., Shang X.-D., Tong P., & Xia K.-Q. Extraction of plumes in turbulent thermal convection. *Phys. Rev. Lett.*, **93**:124501–1, 2004.

[253] Sugiyama K., Calzavarini E., Grossmann S., & Lohse D. Flow organization in two-dimensional non-Oberbeck-Boussinesq Rayleigh-Bénard convection in water. *J. Fluid Mech.*, **637**:105–135, 2009.

[254] Celani A., Matsumoto T., Mazzino A., & Vergassola M. Scaling and universality in turbulent convection. *Phys. Rev. Lett.*, **88**:054503, 2002.

[255] Gastine T., Wicht J., & Aurnou J. M. Turbulent Rayleigh-Bénard convection in spherical shells. *J. Fluid Mech.*, **778**:721–764, 2015.

[256] Ng C. S., Ooi , Lohse D., & Chung D. Vertical natural convection: application of the unifying theory of thermal convection. *J. Fluid Mech.*, **764**:349–361, 2015.

[257] Heslot F., Casting B., & Libchaber A. Transition to turbulence in helium gas. *Phys. Rev. A*, **36**: 5870–5873, 1987.

[258] Solomon T. H. *Transport and boundary layers in Rayleigh-Bénard convection*. Ph.D. thesis. Department of Physics, University of Pennsylvania, 1990.

[259] Deluca E. E., Werne J., Rosner R., & Cattaneo F. Numerical simulations of soft and hard turbulence: Preliminary results for two-dimensional convection. *Phys. Rev. Lett.*, **64**:2370–2373, 1990.

[260] Solomon T. H. & Gollub J. P. Thermal boundary layers and heat flux in turbulent convection: The role of recirculating flows. *Phys. Rev. A*, **43**:6683–6693, 1991.

[261] Qiu X.-L., Shang X. D., Tong P., & Xia K. Q. Velocity oscillations in turbulent Rayleigh-Bénard convection. *Phys. Fluids*, **16**:41–423, 2004.

[262] Lam S., Shang X.-D., Zhou S.-Q., & Xia K.-Q. Prandtl number dependence of the viscous boundary layer and the Reynolds numbers in Rayleigh-Bénard convection. *Phys. Rev. E*, **65**: 066306, 2002.

[263] Willis G. E. & Deardorff J. W. A laboratory model of diffusion into the convective planetary boundary layer. *Q. J. R. Met. Soc.*, **102**:427–445, 1974.

[264] Petschel K., Stellmach S., Wilczek M., Lúlff J., & Hansen U. Kinetic energy transport in Rayleigh-Bénard convection. *J. Fluid Mech.*, **772**:395–417, 2015.

[265] Deardorff J. W. & Willis G. E. Investigation of turbulent thermal convection between horizontal plates. *J. Fluid Mech.*, **28**:675–704, 1967.

[266] Kerr R. Energy budget in Rayleigh-Bénard convection. *Phys. Rev. Lett*, **87**:22502, 2001.

[267] Kim J., Moin P., & Moser R. Turbulent statistics in fully developed channel flow at low Reynolds number. *J. Fluid Mech.*, **177**:133–166, 1987.

[268] Petschel K., Stellmach S., Wilczek M., Lúlff J., & Hansen U. Dissipation layers in Rayleigh-Bénard convection: a unifying view. *Phys. Rev. Lett.*, **110**:114502, 2013.

[269] Tennekes H. & Lumley J. L. *A first course on turbulence*. The MIT Press, 1972.

[270] Chand K., Sharma M., Vishnu V. T., & De A. K. Statistics of coherent structures in two-dimensional turbulent Rayleigh-Bénard convection. *Phys. Fluids*, **31**:115112, 2019.

[271] Breuer M. & Hansen U. Turbulent convection in the zero Reynolds number limit. *Europhys. Lett.*, **86**:24004, 2009.

[272] Paul S., Kumar K., Verma M. K., Carati D., De A., & Eswaran V. Chaotic travelling rolls in Rayleigh-Bénard convection. *Pramana*, **74**:75–82, 2010.

[273] Hansen U., Yuen D. A., & Kroening S. E. Transition to hard turbulence in thermal convection at infinite Prandtl number. *Phys. Fluids A*, **2(12)**:2157–2163, 1990.

[274] Sugiyama K., Ni R., Stevens R. J. A. M., Chan T. S., Zhou S.-Q., Xi H.-D., Sun C., Grossmann S., Xia K. Q., & Lohse D. Flow reversals in thermally driven turbulence. *Phys. Rev. Lett.*, **105**: 034503, 2010.

[275] Chandra M. & Verma M. K. Flow reversals in turbulent convection via vortex reconnections. *Phys. Rev. Lett.*, **110**:114503, 2013.

[276] Vasiliev A. & Frick P. G. Reversals of large-scale circulation in turbulent convection in rectangular cavities. *JETP Lett.*, **93**:330–334, 2011.

[277] Yanagisawa T., Yamagishi Y., Hamano Y., Tasaka Y., & Takeda Y. Spontaneous flow reversals in Rayleigh-Bénard convection of a liquid metal. *Phys. Rev. E*, **83**:036307, 2011.

[278] Wagner C. & Shishkina O. Aspect-ratio dependency of Rayleigh-Bénard convection in box-shaped containers. *Phys. Fluids.*, **25**:085110, 2013.

[279] Ni R., Huang S.-D., & Xia K.-Q. Reversals of the large-scale circulation in quasi-2D Rayleigh-Bénard convection. *J. Fluid Mech.*, **778**:R5, 2015.

[280] Brown E. & Ahlers G. A model of diffusion in a potential well for the dynamics of the large-scale circulation in turbulent Rayleigh-Bénard convection. *Phys. Fluids*, **20**:075101, 2008.

[281] Vishnu V. T., De A. K., & Mishra P. K. Dynamics and statistics of reorientations of large-scale circulation in turbulent rotating Rayleigh-Bénard convection. *Phys. Fluids*, **31**:055112, 2019. doi: 10.1.1/jpb001. URL https://doi.org/10.1063/1.5093948.

[282] Valencia L., Pallares J., Cuesta I., & Grau F. Xavier. Turbulent Rayleigh-Bénard convection of water in cubical cavities: a numerical and experimental study. *Int. J. Heat Mass Transf.*, **50**: 3203–3215, 2007.

[283] Vasiliev A., Frick P., Kumar A., Stepanov R., Sukhanovskii A., & Verma M. K. Mechanism of reorientations of turbulent large-scale convective flow in a cubic cell. *arXiv:1805.06718v1.*, , 2018.

[284] Chen X., Huang S-D., Xia K-Q., & Xi H-D. Emergence of substructures inside the large-scale circulation induces transition in flow reversals in turbulent thermal convection. *J. Fluid Mech.*, **877**:R1–11, 2019.

[285] Niemela J. J. & Sreenivasan K. R. Rayleigh-number evolution of large-scale coherent motion in turbulent convection,. *Europhys. Lett.*, **62**:829–833, 2003.

[286] Cimarelli A., Leonforte A., Angelis E. De, Crivellini A., & Angeli D. On negative turbulence production phenomena in the shear layer of separating and reattaching flows. *Phys. Lett. A*, **383**: 1019–1026, 2019.

[287] Liberzon A., Luthi B., Guala M., & Kinzelbach W. Experimental study of the structure of flow regions with negative turbulent kinetic energy production in confined three-dimensional shear flows with and without buoyancy. *Phys. Fluids*, **17**:095110, 2005.

[288] Foroozani N., Niemela J. J., Armenio V., & Sreenivasan K. R. Turbulent convection and large scale circulation in a cube with rough horizontal surfaces. *Phys. Rev. E*, **99**:033116, 2019.

[289] Shen Y., Tong P., & Xia K.-Q. Turbulent convection over rough surfaces. *Phys. Rev. Lett.*, **76**: 908–911, 1996.

[290] Du Y.-B. & Tong P. Enhanced heat transport in turbulent convection over a rough surface. *Phys. Rev. Lett.*, **81**:987–990, 1998.

[291] Shishkina O. & Wagner C. Modelling the influence of wall roughness on heat transfer in thermal convection. *J. Fluid Mech.*, **686**:568–582, 2011.

[292] Wagner S. & Shishkina O. Heat flux enhancement by regular surface roughness in turbulent thermal convection. *J. Fluid Mech.*, **763**:109–135, 2015.

[293] Salort J., Liot O., Rusaouen E., Seychelles F., Tisserand J. C., Creyssels M., Castaing B., & Chillà F. Thermal boundary layer near roughnesses in turbulent Rayleigh-Bénard convection: Flow structure and multistability. *Phys. Fluids*, **26**:015112, 2014.

[294] Salort J., Rusaouen E., Liot O., Seychelles F., Tisserand J. C., Creyssels M., Castaing B., & Chillà F. Roughness-enhanced heat flux in turbulent thermal convection. In *Proceedings of the* 14^{th} *European Turbulence Conference*, 2013.

[295] Toppaladoddi S., Succi S., & Wettlaufer J. S. Roughness as a route to the ultimate regime of thermal convection. *Phys. Rev. Lett.*, **118**:074503, 2017.

[296] Zhu X., Stevens R. J. A. M., Verzicco R., & Lohse D. Roughness facilitated local 1/2 scaling does not imply the onset of the ultimate regime of thermal convection. *Phys. Rev. Lett.*, **119**: 154501, 2017.

[297] Zhang Y., Sun C., Bao Y., & Zhou Q. How surface roughness reduces heat transport for small roughness heights in turbulent Rayleigh-Bénard convection. *J. Fluid Mech.*, **836**:R2, 2017.

[298] Wei P. & Xia K.-Q. Viscous boundary layer properties in turbulent thermal convection in a cylindrical cell: the effect of cell tilting. *J. Fluid Mech.*, **720**:140–168, 2013.

[299] Zwirner L., Khalilov R., Kolesnichenko I., Mamykin A., Mandrykin S., Pavlinov A., Shestakov A., Teimurazov A., Frick P., & Shishkina O. The influence of the cell inclination on the heat transport and large-scale circulation in liquid metal convection. *J. Fluid Mech.*, **884**:A18, 2019.

[300] Shishkina O. & Horn S. Thermal convection in inclined cylindrical containers. *J. Fluid Mech.*, **790**:R3, 2015.

[301] Guo S., Zhou S., Cen X., Qu L., Lu Y., Sun L., & Shang X. The effect of cell tilting on turbulent thermal convection in a rectangular cell. *J. Fluid Mech.*, **762**:273–287, 2015.

Publications

Journals

1. Dynamics and statistics of reorientations of large-scale circulation in turbulent rotating Rayleigh-Bénard convection, V. T. Vishnu, A. K. De and P. K Mishra, *Phys. Fluids*, 31 (2019) 055112.

2. Significance of Prandtl number on the heat transport and flow structure in rotating Rayleigh-Bénard convection, V. T. Vishnu, A. K. De and P. K Mishra, *ASME J. Heat Transfer.*, 142 (2019) 012501.

3. Flow periodicity and convection modes in rotating Rayleigh-Bénard convection at low Rayleigh numbers, V. T. Vishnu and A. K. De, *Sadhana*, 44 (2019) 14.

4. Dynamics of large-scale circulation and energy transfer mechanism in turbulent Rayleigh-Bénard convection in a cubic cell, V. T. Vishnu, A. K. De and P. K Mishra, Phys. Fluids, 32, (2020) 095115.

5. Statistics of thermal plumes and dissipation rate in turbulent Rayleigh-Bénard convection, V. T. Vishnu, A. K. De and P. K Mishra (*under review*)

Conference proceedings

1. Rotating Rayleigh-Bénard convection in unit aspect-ratio container at low Rayleigh numbers, V. T. Vishnu and Arnab Kumar De, *The 6^{th} International and 43^{rd} National Conference on Fluid Mechanics and Fluid Power*, MNNIT Allahabad, India, (2016).

2. Analysis of periodic Rayleigh-Bénard convection with moderate rotation rates at low Rayleigh numbers, V. T. Vishnu and A. K. De, *The 24^{th} National and 2^{nd} International ISHMT-ASTFE Heat and Mass Transfer Conference*, BITS Pilani Hyderabad campus and IIT Hyderabad, (2017).

3. Mode transitions in rotating Rayleigh-Bénard convection at low Rayleigh numbers, V. T. Vishnu and A. K. De, *The 44^{th} National Conference on Fluid Mechanics and Fluid Power*, Amrita University, Amritapuri Campus, Kerala, (2017).

4. The effect of rotation on the heat transport and flow structures in turbulent rotating Rayleigh-Bénard

convection, V. T. Vishnu, A. K. De and P. K. Mishra, *The 7^{th} International and 45^{th} National Conference on Fluid Mechanics and Fluid Power*, IIT Bombay, (2018).

5. Rotation influenced reorientations of large-scale circulations in Rayleigh-Bénard convection, V. T. Vishnu, A. K. De and P. K. Mishra, *International Conference on Rayleigh-Bénard Turbulence*, Enschede, The Netherlands, (2018).

6. Dynamics and statistics of thermal plumes in turbulent Rayleigh-Bénard convection, V. T. Vishnu, A. K. De and P. K. Mishra, *The 25^{th} National and 3^{rd} International ISHMT-ASTFE Heat and Mass Transfer Conference*, IIT Roorkee, (2019).

7. Dynamics of large-scale circulation in turbulent rotating Rayleigh-Bénard convection, V. T. Vishnu, A. K. De and P. K. Mishra, *The 25^{th} National and 3^{rd} International ISHMT-ASTFE Heat and Mass Transfer Conference*, IIT Roorkee, (2019).

8. Mean-wind and its characteristics in turbulent Rayleigh-Bénard convection in a cubic cell, V. T. Vishnu, A. K. De and P. K. Mishra, *The 8^{th} International and 47^{th} National Conference on Fluid Mechanics and Fluid Power*, IIT Guwahati, (2020)

9. Dynamics of corner vortices and flow reversals in turbulent Rayleigh-Bénard convection, V. T. Vishnu, A. K. De and P. K. Mishra, *The 25^{th} International Congress of Theoretical and Applied Mechanics*, Milano, Italy, (2021) (*to attend*).